

THESIS FOR THE DEGREE OF LICENTIATE OF ENGINEERING

Converter interactions in VSC-based HVDC systems

GEORGIOS STAMATIOU



Department of Energy and Environment
CHALMERS UNIVERSITY OF TECHNOLOGY
Gothenburg, Sweden, 2015

Converter interactions in VSC-based HVDC systems
GEORGIOS STAMATIOU

© GEORGIOS STAMATIOU, 2015.

Division of Electric Power Engineering
Department of Energy and Environment
Chalmers University of Technology
SE-412 96 Gothenburg
Sweden
Telephone +46 (0)31-772 1000

Printed by Chalmers Reproservice
Gothenburg, Sweden, 2015

To my beloved family...

Converter interactions in VSC-based HVDC systems
GEORGIOS STAMATIOU
Department of Energy and Environment
Chalmers University of Technology

Abstract

The main objective of this thesis is to perform stability and control studies in the area of VSC-HVDC. A major part of the investigation focuses on the explanation of poorly-damped conditions and instability that are linked to dc-side resonances. Initially, a frequency domain approach is considered, applied to a two-terminal VSC-HVDC connection that is modeled as a Single-Input Single-Output (SISO) feedback system, where the VSC-system and dc-grid transfer functions are defined and derived. The passivity analysis and the net-damping criterion are separately applied, demonstrating the superiority of the latter as an analysis tool. Furthermore, it was discovered that the net-damping of a system and the damping factor of its poorly-damped dominant poles are correlated in an almost linear way.

The occurrence of poorly-damped conditions is further analyzed from an analytical perspective, where the eigenvalues of a two-terminal VSC-HVDC system are approximated by closed-form expressions. This offers the benefit of a deeper understanding in the way selected parameters of the system can affect the frequency and damping characteristics of its eigenvalues. The *Similarity Matrix Transformation* (SMT) method is introduced in this thesis and applied to the reduced 4th order state-space model of a two-terminal VSC-HVDC system. The results show that the *SMT* offers improved accuracy in approximating the actual eigenvalues of the system, compared to the already established *LR* method.

Finally, studies are performed in VSC-MTDC grids, with the main objective of proposing advanced control strategies that can offer robust performance during steady-state and transient conditions, with improved power flow and direct-voltage handling capabilities. The advantageous properties of the proposed controllers are proven through simulations of four- and five-terminal MTDC grids, in which their benefits compared to their conventional counterparts are shown.

Index Terms: VSC, HVDC, Poor damping, Frequency Domain Analysis, Net damping, Passivity Analysis, Symbolic eigenvalue expressions, MTDC, Droop control.

Acknowledgments

My sincere gratitude goes to my supervisor and friend Prof. Massimo Bongiorno for his invaluable guidance and support throughout the course of this project. Thank you very much for your endless effort and dedication through the challenging times encountered, and for the fruitful discussions that provided substance to this thesis. I would also like to thank my examiner Prof. Ola Carlson for supporting this project.

I want to use the opportunity to address my gratitude to Yujiao Song and Prof. Claes Breitholtz from the department of Signals and Systems, for their great contribution in tackling major problems in the objectives of this thesis. In this context, I would like to thank Senior Lecturer Thomas Ericsson from the department of Mathematical Sciences, for his thorough assistance in numerical analysis issues. Furthermore, I want to thank Prof. Torbjörn Thiringer for his encouragement and assistance in bringing this thesis to its final shape.

This work was carried out within the project "DC grids for integration of large scale wind power - OffshoreDC" and funded by the Nordic Energy Research, through their Top-level Research Initiative. ABB is also a partner and funding member of the project. A special thanks goes to the project leader Dr. Nicolaos Antonio Cutululis for his administrative support, as well as the other members of the OffshoreDC project for the interesting discussions that we shared. Finally, I would like to thank Dr. Georgios Demetriades from ABB Corporate Research, for his encouragement and useful feedback throughout the course of this thesis.

At this point, I would like to thank Prof. Pericle Zanchetta at the University of Nottingham, UK, for his support and offering me the opportunity to come to Sweden and change my life forever. What a journey...

Special thanks go to my friends in the division for the fun time we have been having and my officemates Poopak Roshanfekr, Shemsedin Nursebo and Ingemar Mathiasson, who made the office a pleasurable place to work in.

Finally, I would like to thank my father, mother and brother for being the best family I could ever have and for setting the best examples on how to live my life. Thank you for your endless love and support!

Georgios Stamatou
Gothenburg, Sweden
May, 2015

List of Acronyms

APC	Active-Power Controller
CPL	Constant Power Load
DVC	Direct-Voltage Controller
D-DVC	Droop-based Direct-Voltage Controller
HVDC	High Voltage Direct Current
LCC	Line Commutated Converter
LHP	Left Hand of the s-Plane
MMC	Modular Multilevel Converter
MTDC	Multi-terminal High Voltage Direct Current
NPC	Neutral-Point Clamped
PD-DVC	Power-Dependent Direct-Voltage Controller
PCC	Point of Common Coupling
PLL	Phase-Locked Loop
pu	Per Unit
PWM	Pulse-Width Modulation
RHP	Right Hand of the s-Plane
SCR	Short Circuit Ratio
SISO	Single-Input Single-Output
SMT	Similarity Matrix Transformation
SPWM	Sinusoidal Pulse-Width Modulation
VSC	Voltage Source Converter
VSC-HVDC	Voltage Source Converter based High Voltage Direct Current
VSC-MTDC	Voltage Source Converter based Multi-terminal High Voltage Direct Current

Contents

Abstract	v
Acknowledgments	vii
List of Acronyms	ix
Contents	xi
1 Introduction	1
1.1 Background and motivation	1
1.2 Purpose of the thesis and main contributions	3
1.3 Structure of the thesis	3
1.4 List of publications	4
2 VSC-HVDC operation and control	7
2.1 Introduction to VSC-HVDC	7
2.2 Main components of a VSC-HVDC transmission system	8
2.2.1 AC-side transformer	9
2.2.2 Phase reactor	9
2.2.3 AC-side filters	10
2.2.4 DC-side capacitor	10
2.2.5 DC-lines	11
2.3 VSC principle of operation	12
2.3.1 Converter structure, switching and modulation	12
2.3.2 Sinusoidal Pulse-Width Modulation	14
2.3.3 Power-transfer capabilities and limitations	16
2.3.4 Advances in converter topologies	18
2.4 VSC control	21
2.4.1 Vector current control	22
2.4.2 Phased-Locked Loop	26
2.4.3 Direct-voltage control	27
2.4.4 Active-power control	29
2.4.5 Reactive-power control	29
2.4.6 AC-voltage regulation	30
2.5 Control strategy in two-terminal VSC-HVDC systems	30

Contents

2.6	Summary	32
3	Poorly-damped oscillations in systems	35
3.1	Damping of systems	35
3.2	DC-side oscillations in industrial systems	37
3.2.1	Effect of Constant Power Loads	37
3.2.2	Traction and industrial systems	38
3.2.3	LCC-HVDC	42
3.2.4	VSC-HVDC	43
3.3	Example of dc-side oscillations in two-terminal VSC-HVDC	44
3.3.1	Poorly-damped conditions	44
3.3.2	Unstable conditions	46
3.4	Summary	48
4	Stability in two-terminal VSC-HVDC systems: frequency-domain analysis	49
4.1	Stability analysis based on a frequency-domain approach	49
4.1.1	Passivity of closed-loop transfer function	49
4.1.2	Net-damping stability criterion	50
4.2	System representation	52
4.2.1	DC-grid transfer function	53
4.2.2	AC-side transfer function	55
4.2.3	Closed-loop SISO feedback representation	58
4.3	Frequency-domain analysis: Passivity approach	59
4.3.1	DC-grid subsystem for passivity studies	59
4.3.2	VSC subsystem	60
4.3.3	Analysis	60
4.3.4	Altered system configuration	63
4.4	Frequency-domain analysis: Net-damping approach	63
4.4.1	Open-loop resonances	64
4.4.2	Non-apparent cases	66
4.5	Correlation between net-damping and damping factor	68
4.5.1	Damping in a multi-pole system	68
4.5.2	Net-damping in poorly-damped configurations	68
4.6	Stability improvement	71
4.6.1	Notch filter in the control structure	71
4.6.2	Damping effect of the notch filter	72
4.7	Summary	76
5	Stability in two-terminal VSC-HVDC systems: analytical approach	77
5.1	Analytical investigation of dynamic stability	77
5.1.1	Cubic equation	78
5.1.2	Quartic equation	79
5.1.3	Alternative solutions	81
5.2	Approximating methods	81
5.2.1	Similarity Matrix Transformation	82

5.2.2	The LR algorithm	86
5.3	State-space modeling of systems under investigation	93
5.3.1	Investigated system	93
5.3.2	DC-link transmission model	94
5.3.3	Two-terminal VSC-HVDC model	95
5.3.4	Validity of VSC-HVDC model simplifications	100
5.4	Summary	105
6	Applications of the analytical approach	107
6.1	Application of Similarity Matrix Transformation	107
6.1.1	Parameter values	108
6.1.2	Matrix simplification	108
6.1.3	Similarity transformation	110
6.1.4	Results	113
6.2	Application of the LR algorithm to a VSC-HVDC system	122
6.2.1	General expression of eigenvalues	123
6.2.2	Convergence of eigenvalue expressions	123
6.2.3	Analytical eigenvalues expressions	125
6.2.4	Results	127
6.3	Application of the LR algorithm to an HVDC transmission system	134
6.3.1	General expression of eigenvalues	136
6.3.2	Convergence of eigenvalue expressions	136
6.3.3	Analytical eigenvalues expressions	138
6.3.4	Results	139
6.4	Investigation on the accuracy of the approximating methods	145
6.4.1	Accuracy of the Similarity Matrix Transformation	145
6.4.2	Accuracy of the convergence of the LR algorithm	148
6.5	Summary	150
7	Control investigation in Multiterminal VSC-HVDC grids	153
7.1	Multiterminal HVDC grids	153
7.1.1	Technologies and initial projects	154
7.1.2	Visions	155
7.2	Key components for future large scale Multiterminal connections	156
7.2.1	DC-breaker	156
7.2.2	DC-DC converter	157
7.3	MTDC-grid topologies	159
7.4	Control of MTDC grids	161
7.4.1	Voltage-margin control	161
7.4.2	Voltage-droop control	162
7.4.3	Control strategy for connections to renewable power plants	165
7.5	Controller offering direct-voltage support in MTDC grids	166
7.5.1	Direct-voltage support in MTDC grids	167
7.5.2	Controller for direct-voltage support in MTDC grids	167

Contents

7.5.3	Comments on the PD-DVC	170
7.5.4	MTDC model-setup	171
7.5.5	Power-flow studies	171
7.5.6	Dynamic performance under fault conditions	174
7.6	Control strategy for increased power-flow handling	178
7.6.1	Comparison with standard strategies	178
7.6.2	Proposed Controller	179
7.6.3	Application of the proposed controller	181
7.6.4	Dynamic performance during ac-faults	187
7.7	Summary	189
8	Conclusions and future work	191
8.1	Conclusions	191
8.2	Future work	193
	References	195
A	Transformations for three-phase systems	203
A.1	Introduction	203
A.2	Transformation of three-phase quantities to vectors	203
A.2.1	Transformation between fixed and rotating coordinate systems	204
B	Per-unit Conversion	207
B.1	Per-unit conversion of quantities	207

Chapter 1

Introduction

1.1 Background and motivation

The use of Voltage Source Converter based High Voltage Direct Current (VSC-HVDC) systems is considered to be a major step in facilitating long distance power transfer and integrating remotely located renewable energy sources to major consumption centers. First introduced in 1997, with the commissioning of a 3 MW technology demonstrator at Hellsjön, Sweden [1], VSC technology has improved drastically over the years, in terms of power and voltage rating, harmonic performance and losses [2, 3]. VSC-HVDC is a fairly recent technology, free of several constraints associated with the thyristor-based Line Commutated Converter (LCC) technology, with added degrees of freedom such as independent control of active and reactive power. The VSC eliminates the need for telecommunication links between stations (at least in a point-to-point configuration), which is otherwise a necessity in LCC-HVDC to perform the reversal of power flow. Additionally, VSC stations can be connected to weak ac grids and even perform black-start, in contrast to LCC stations that can only be connected to relatively strong ac grids. This also represents a limitation for the LCC-based technology when it comes to integration of large renewable power generation units (e.g. large scale wind farms), which usually comprise weak grids. These features render the VSC as an ideal candidate for implementation in Multi-terminal HVDC (MTDC) systems, with numerous stations connected in a variety of ways.

The introduction of power electronics in power systems has offered a breakthrough in terms of controllability and stability. In turn, this has led to an increased possibility of interactions between the system components. Potential resonances might appear that, if become poorly damped, can degrade the effective damping of the system and increase the risk of instability. Such occurrences have often been described in traction [4–7] and classical HVDC applications [8–13]. Poorly-damped resonances between the converter stations and the transmission cables can appear both in two-terminal VSC-HVDC connections [14] and VSC-MTDC grids [15, 16].

Stability studies are typically approached by using numerical analysis to determine the actual values of the system's poles [17]. Alternative solutions may however offer a different perspec-

Chapter 1. Introduction

tive to the understanding of stability and poor damping. A frequency domain approach is proposed in [9, 18] and further utilized in [19, 20], where the passivity analysis of a system is used to derive design criteria. This concept has however limitations as it cannot provide answers for non-passive systems, where other methods should be further used. A different frequency domain tool is the net-damping criterion, used in [21–24] to facilitate a subsynchronous torsional interaction analysis of turbine-generator sets. There, the system was modeled as a Single-Input Single-Output (SISO) feedback process, comprising of an open-loop and a feedback subsystem. The assessment of the accumulated subsystem *damping* at the open-loop resonant frequencies offered direct and consistent conclusions, regarding the closed-loop stability. Nevertheless, this method has never been used in VSC-HVDC studies.

An analytical approach to the stability of a system offers the benefit of a deeper understanding in the way selected parameters of a system can affect the frequency and damping characteristics of its eigenvalues. Hence, it is valuable if such symbolic descriptions can be obtained for a poorly-damped VSC-HVDC link, highlighting the relationship between the system's parameters and its poorly-damped poles. A major problem in this process is the fact that the analytical description of a high-order system is challenging and in many cases impossible. Modeling a VSC-HVDC connection while maintaining a sufficient level of complexity, can lead to a system whose order can easily surpass the tenth order. It is therefore important and interesting to significantly minimize the order of such systems, in such a way that most of the information on the dynamic response is preserved.

Relevant research in the analytical approach area has taken place mostly in electric drives and traction systems [25, 26], where a rectifier and an inverter are connected via dc lines. However, the analytical description considers only the resonance of the dc cable, disregarding the effect of the converter controllers on the overall performance. In [14], the analytical eigenvalues of the dc-link in a two-terminal VSC-HVDC connection is provided, but is only applicable for zero power transfer. Approximate symbolic eigenvalues in VSC-MTDC grids are provided in [27] but require significant simplifications, influencing the validity of the final expressions. In [28, 29] the approximate analytical eigenvalue solutions of analogue electronic circuits are computed by the semi-state equations of the investigated system. The proposed process may not always be successful and could lead to a significant loss of information. The poles of an analogue circuit are calculated through the time constant matrix of the system in [30]. However, this kind of approach allows analytic computation of the first two dominant poles only with major system simplifications being required in order to compute the other poles. In [31–33], the *LR* iterative method is used to calculate the symbolic poles and zeros of analogue electronic circuits, based on their state matrix. However the implemented approach incurs a heavy computational burden and numerous simplifications are still required to produce compact final solutions. Consequently, the development of analytical methods that are more computationally efficient and provide sufficient accuracy in the approximation of a plurality of eigenvalues, is considered of great value.

The concept of MTDC grids as counterpart to the very well established High Voltage AC grids is an interesting approach when it comes to high power transmission over long distances. Relevant research in the field used to strictly consider LCC-HVDC stations [34, 35], but recently there has been a shift of interest towards VSC technology. Different types of control strate-

1.2. Purpose of the thesis and main contributions

gies for VSC-MTDC grids have been suggested, e.g. the voltage-margin control [36, 37], or droop-based control [38–40]. In [41], a comprehensive analysis on the control and protection of MTDC grids has been carried out, while other works such as [16, 17] deal with the study of the stability in such systems. Further development is required for control strategies that offer robust performance during steady-state and transient conditions, with improved power flow and direct-voltage handling capabilities.

1.2 Purpose of the thesis and main contributions

The main purpose of this thesis is to perform studies on the stability of VSC-HVDC systems and investigate the interaction between the control structures, passive components and operating points. The ultimate goal is to develop methodologies and tools that will allow the explanation and understanding of poorly-damped conditions that may appear in such systems. Furthermore, the potential of using VSC technology in large scale MTDC grids, requests a robust control structure with exceptional handling characteristics of the power-flow and direct-voltage management. This is an area to which this thesis attempts to contribute accordingly.

To the best of the author’s knowledge, the main contributions of this thesis are the following:

1. An approach is proposed to explain the origin of dc-side instability and poorly-damped conditions in a two-terminal VSC-HVDC system, based on the frequency domain analysis of the subsystems that constitute the latter. Furthermore, an almost linear correlation between the net-damping of a system and the damping factor of the poorly-damped closed-loop dominant poles has been discovered.
2. A new method to derive the analytical eigenvalue expressions of a 4th order two-terminal VSC-HVDC model, was developed and its effectiveness was demonstrated. This enables the extraction of eigenvalues in a closed form, making it possible to understand how a certain system parameter or operational point contributes to the placement of a pole and can therefore assist in understanding how a system can be simplified for easier further analysis.
3. Two new types of droop-based control strategies for application in MTDC grids, are developed and analyzed. The associated controllers offer steady-state and dynamic enhancement in the handling of relatively stiff- or constant-power controlled VSC stations connected to the grid, compared to conventional controllers.

1.3 Structure of the thesis

The thesis is organized into eight chapters with Chapter 1 describing the background information, motivation and contribution of the thesis. Chapter 2 provides a theoretical base for the understanding of the VSC-HVDC technology and presents the VSC control structure and its limitations, the components of a realistic VSC-station and information on the latest advances

Chapter 1. Introduction

in converter topologies. Chapter 3 functions as a general introduction to the concept of damping in dynamic systems and focuses on poorly-damped conditions that may appear. Examples are provided in the areas of traction, electric drives, classical HVDC and VSC-HVDC, along with the main contributing factors to such conditions in each case. In Chapter 4, the dynamic behavior of two-terminal VSC-HVDC transmission systems is analyzed through a frequency domain approach. The *passivity* approach and the *net-damping* criterion are utilized to explain poorly-damped conditions and occasions of instability, as well as to describe the way certain interventions to the VSC control can improve the dynamic performance of the complete system. Following the frequency domain analysis, Chapter 5 focuses on an analytical approach to the description of poorly-damped conditions in two-terminal VSC-HVDC systems, by means of deriving analytical eigenvalue expressions that contain all the parameters of the control and passive components of the system, as well as the nominal operating points. As tools to accomplish this objective, the chapter introduces the *Similarity Matrix Transformation* (SMT) method and provides an overview of the *LR* iterative method. The chapter concludes with the derivation of state-space models for a generic two-terminal VSC-HVDC transmission system and the dc-transmission link that connects the two VSC stations. The eigenvalues of these models are analytically extracted using the SMT and LR methods in Chapter 6, where the accuracy and the validity of the final expressions is thoroughly analyzed and comments on the capabilities and limitations of each method are made. Chapter 7 provides an insight to MTDC grids regarding the technologies involved, grid topologies and control strategies. Within the context of direct-voltage droop control in MTDC grids, the chapter introduces two proposed droop-based control methods with advantageous properties in the handling of relatively stiff- or constant-power controlled VSC stations connected to the grid. Finally the thesis concludes with a summary of the results achieved and plans for future work in Chapter 8.

1.4 List of publications

The publications originating from the project are:

- I. G. Stamatiou and M. Bongiorno, "Decentralized converter controller for multiterminal HVDC grids," in *Proc. of the 15th European Conference on Power Electronics and Applications (EPE 2013)*, Sept. 2013, pp. 1-10.
- II. L. Zeni, T. Haileselassie, G. Stamatiou, G. Eriksen, J. Holbøll, O. Carlson, K. Uhlen, P. E. Sørensen, N. A. Cutululis, "DC Grids for Integration of Large Scale Wind Power," in *Proc. of EWEA Offshore 2011*, 29 Nov. - 1 Dec. 2011, Amsterdam.
- III. N. A. Cutululis, L. Zeni, W. Z. El-Khatib, J. Holbøll, P. E. Sørensen, G. Stamatiou, O. Carlson, V. C. Tai, K. Uhlen, J. Kiviluoma and T. Lund, "Challenges Towards the Deployment of Offshore Grids: the OffshoreDC Project," in *Proc. of 13th International Workshop on Large-Scale Integration of Wind Power into Power Systems as well as on Transmission Networks for Offshore Wind Power (WIW 2014)*, 2014.

1.4. List of publications

- IV. G. Stamatiou, Y. Song, M. Bongiorno and C. Breitholtz, "Analytical investigation of poorly damped resonance conditions in HVDC systems," *submitted for publications in IEEE Trans. on Power Del., special issue: HVDC transmission systems for large offshore wind power plants.* [second review]
- V. G. Stamatiou and M. Bongiorno, "A novel decentralized control strategy for MultiTerminal HVDC transmission grids," *accepted for presentation at the 7th annual IEEE Energy Conversion Congress & Exposition (ECCE 2015), Montreal, Quebec, Canada.*

Chapter 1. Introduction

Chapter 2

VSC-HVDC operation and control

The use of VSC in HVDC applications and the analysis of the behavior of the associated systems require an understanding of the fundamental properties and functionalities of the VSC technology. The intention of this chapter is to provide a basic but detailed background information on VSC-HVDC systems. The main structure and components of a VSC-HVDC system are initially described, followed by an introduction to the operational principles of a VSC. Thus, the interconnected layers of control that allow the VSC to operate as a controllable voltage source are presented. This will provide the basis for the understanding of the dynamic behavior of VSC-HVDC systems, as will be investigated in the following chapters. Finally, the control strategy of a typical two-terminal VSC-HVDC transmission link is presented and demonstrated via simulations.

2.1 Introduction to VSC-HVDC

The typical configuration of a two-terminal VSC-HVDC transmission link is illustrated in Fig. 2.1, where two VSC stations connect two ac systems via a dc-transmission system. The two ac systems can be independent networks, isolated from each other, or nodes of the same ac system where a flexible power transmission link is to be established. The interconnection point between a VSC station and its adjacent ac system is called the Point of Common Coupling (PCC). The main operating mechanism of a VSC station considers the ability of the VSC

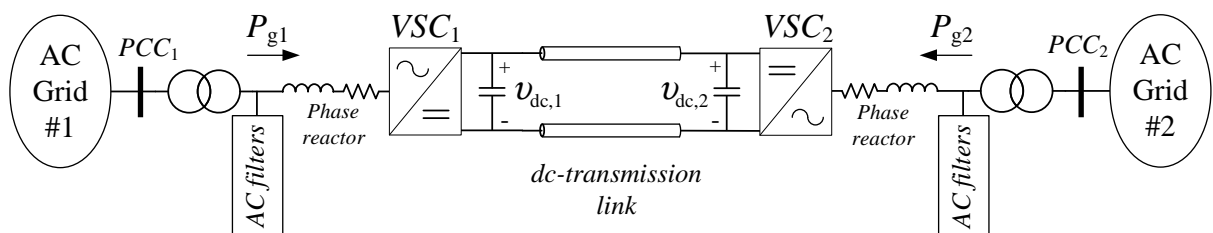


Fig. 2.1 Two-terminal VSC-HVDC transmission link. The controlled power is the power entering the phase reactor with a positive direction towards the VSC station.

Chapter 2. VSC-HVDC operation and control

to function as a controllable voltage source that can create an alternating voltage of selected magnitude and phase, allowing the exchange of a predetermined amount of active and reactive power between itself and the ac system. This is achieved by operating the stations as active rectifiers that can create a voltage waveform. In order to ensure that, the dc side of the converters must maintain a fairly stiff direct voltage. For this reason and as explained later in Section (2.5), one of the VSC stations bears the duty of controlling the voltage in the dc transmission to a designated value while the other station handles the control of the active power flow that will be exchanged between the two ac nodes. In parallel to that, each station can regulate the reactive power exchange with its interconnected ac system, independently from the active power handling. This is a major feature that the LCC-HVDC lacks. Additionally, the presence of diodes connected in anti-parallel with the IGBTs provides bidirectional power capabilities to the VSC, without the need to invert the polarity of the dc-link voltage, unlike in LCC-HVDC. The desired power exchange in a VSC station is imposed at the connection point of the phase reactor, connecting the VSC main valves to the transformer, shown in Fig. 2.1.

The dc-transmission link may consist of overhead or cable type of conductors, based on the operational characteristics of the transmission system. A very common arrangement of the dc link, used extensively in classical HVDC, is the asymmetric monopole, with or without metallic return. In this way only one pole is energized while the other is either a grounded conductor or isolated ground connections at each station, respectively. For these arrangements, the transformers have to be designed for dc stresses and there is no redundancy if the single energized pole is lost. The bipolar connection solves the redundancy issue by connecting two identical asymmetric monopole systems in parallel, in such a way that the grounded parts of the stations are connected to each other and there is a positively and negatively charged pole completing the system. This arrangement is more costly, but if an energized pole is lost, the VSC-HVDC can keep operating with the remaining pole, at a reduced power rating. The last type of VSC connection is the symmetric monopole, as shown in Fig. 2.1, constituted by two conductors connecting the VSC stations and operated at opposite voltages. This is achieved by splitting the dc-side capacitor into two identical parts with a grounded midpoint. In this way, the transformer does not suffer from dc stresses and redundancy is still offered at 50% of the rated power. This arrangement is going to be used in the present thesis. This convention will be used in the rest of the thesis as well.

The following sections provide a detailed overview on the key components of a VSC transmission system, the operating principles and the control systems involved.

2.2 Main components of a VSC-HVDC transmission system

The complete description of a VSC-HVDC transmission system is presented in Fig. 2.2. The main part of the station, comprising of the switching valves, is surrounded by a number of key components that are necessary for the proper operation of the converter. These are the dc-side capacitor, ac-side filters, the phase reactor, the coupling transformer and the dc-transmission lines. These components are further described in this section.

2.2. Main components of a VSC-HVDC transmission system

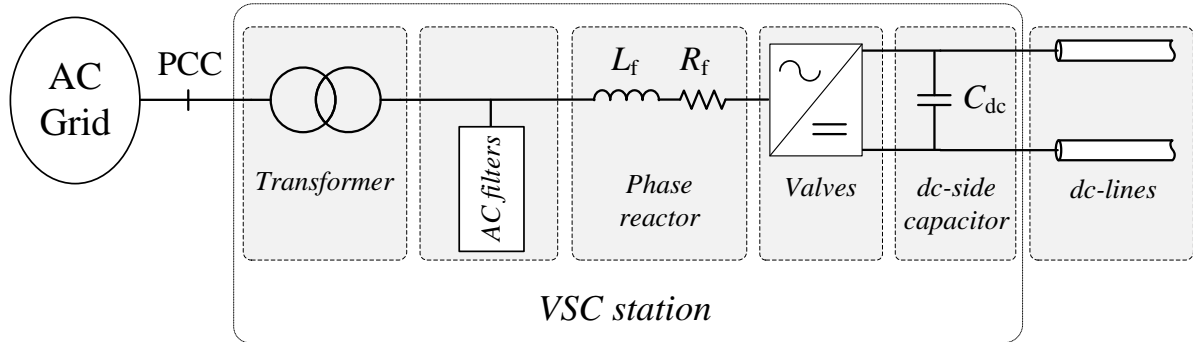


Fig. 2.2 Components of a VSC-HVDC station.

2.2.1 AC-side transformer

A VSC station is usually connected to an ac grid via a converter transformer. Its main function is to facilitate the connection of the converter to an ac system whose voltage has a different rated value. Furthermore, the transformer blocks the propagation of third-order harmonics and multiples to the main ac system, while at the same time provides galvanic isolation between the latter and the VSC station. The transformer is a three-phase ac power-transformer, equipped with a tap changer. For large power ratings, the size and weight of a three-phase transformer can be forbidding from a structural and transportation point of view and is, therefore, built as separate single-phase transformers. For asymmetrical dc-transmission configurations, the transformer will be exposed to a dc-offset in the valve-side ac voltages, which will result in a slightly more complicated transformer design [2].

2.2.2 Phase reactor

The phase reactor is one of the key components of a VSC station. Its main function is to facilitate the active and reactive power transfer between the station and the rest of the ac system. With the one side of the reactor connected to the ac system, the VSC is able to apply a fully controlled voltage to the other side of the reactor. The magnitude and phase difference of the latter, compared to the ac-system voltage will induce a controlled amount of active and reactive power transfer over the reactor.

A secondary function of the phase reactor is to filter higher harmonic components from the converter's output current and also limit short-circuit currents through the valves. The phase reactor impedance, in combination with the transformer impedance, defines the short circuit current for the valve diodes [2]. According to [42], the typical short-circuit impedance of this type of phase reactor is 0.15 pu. The phase reactor is modeled as an inductor in series with a small resistance, which takes into account the reactor losses. The authors in [43] consider a reactor inductance of 0.25 pu.

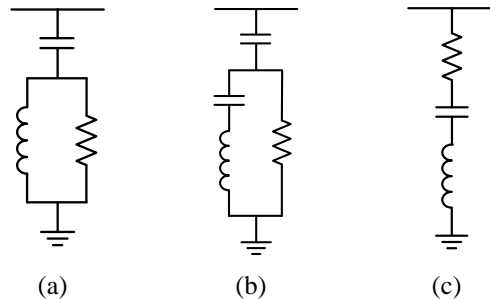


Fig. 2.3 AC-side filters. (a) 2nd order filter, (b) 3rd order filter and (c) Notch filter.

2.2.3 AC-side filters

The voltage output of the HVDC converters is not purely sinusoidal but contains a certain amount of harmonics, due to the commutation valve switching process. This causes the current in the phase reactor to also contain harmonics at the same frequencies, apart from the desired sinusoidal component at the grid frequency. These currents are not desired to flow in the rest of the ac grid as they could cause additional losses in other components and distorted voltage waveforms.

When using PWM modulation, a high frequency ratio m_f , shown later in Section (2.3.2), shifts the switching harmonics to the high-frequency range, where the reactance of any inductors on the ac side (including the phase reactor) becomes high. As a result, the generated harmonic currents have low amplitude and the waveform of the resulting converter current propagating to the rest of the grid approaches the sinusoidal form, while the harmonic losses are simultaneously decreased. However, this choice forces the valves to switch at a higher frequency and the switching losses are increased.

Aiming to maintain m_f at a reasonably low value but also reduce the harmonic content of the VSC output, a range of passive filters are used, connected between the phase reactor and the transformer [2, 44]. Typical examples are 2nd order filters, 3rd order filters or notch filters, as depicted in Fig. 2.3. Depending on the converter topology and its switching levels, the harmonic content of the converter output can be reduced to a level where the necessary ac-side filters can be reduced in number and size or even neglected.

2.2.4 DC-side capacitor

The main function of the dc-side capacitor is to reduce the voltage ripple on the dc-side and provide a sufficiently stable direct-voltage from which alternating voltage will be generated on the ac-side of the converter. Furthermore, the capacitor acts as a sink for undesired high-frequency current components that are generated by the switching action of the converter and are injected to the dc-side. These currents are prevented from propagating to the rest of the dc-transmission link, being filtered by the inductance and resistance of the dc lines. Additionally, the dc-side capacitor acts as a temporary energy storage where the converters can momentarily store or absorb energy, keeping the power balance during transients.

2.2. Main components of a VSC-HVDC transmission system

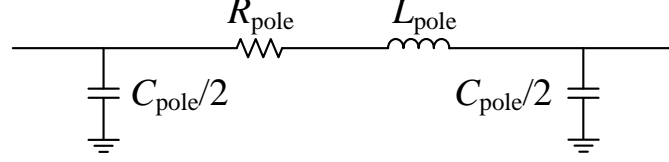


Fig. 2.4 Π -model of a single pole for a dc-transmission link.

The capacitor sizing is usually performed considering the amount of power to be stored. Consequently, the capacitor is characterized by the *capacitor time constant*, defined as

$$\tau = \frac{C_{dc} v_{dc,N}^2}{2 \cdot P_N} \quad (2.1)$$

where C_{dc} is the capacitance, $v_{dc,N}$ is the rated pole-to-pole direct voltage and P_N is the rated active power of the VSC. The time constant is equal to the time needed to charge the capacitor of capacitance C_{dc} from zero to $v_{dc,N}$, by providing it with a constant amount of power P_N [45]. A time constant of 4 ms is used in [46] and 2 ms in [2].

2.2.5 DC-lines

The transmission of power between VSC-HVDC stations is performed using dc-lines. Each dc-pole can be modeled as a Π -model, with resistance R_{pole} , inductance L_{pole} and two identical capacitors with capacitance $C_{pole}/2$ each. This is depicted in Fig. 2.4. Transmission lines are normally described in terms of resistance/km/pole r , inductance/km/pole l and capacitance/km/pole c . With the length of the dc-transmission system being provided in km units, the previous cable elements are defined as

- $R_{pole} = r \cdot (\text{transmission line length})$
- $L_{pole} = l \cdot (\text{transmission line length})$
- $C_{pole} = c \cdot (\text{transmission line length})$

It is possible to use two different types of dc-transmission lines: cables or overhead lines. Cable-poles are normally laid very close to each other and therefore have a relatively high capacitance and low inductance per km. On the contrary, overhead transmission line poles are located in a relative distance from each other and as a result they have a relatively high inductance and low capacitance per km. The values that are going to be used in the present thesis are presented in Table 2.1.

TABLE 2.1. PHYSICAL PROPERTIES FOR MODELING DC-TRANSMISSION LINES

Type of dc-transmission line	r (Ω /km/pole)	l (mH/km/pole)	c (μ F/km/pole)
Cable	0.0146	0.158	0.275
Overhead line	0.0178	1.415	0.0139

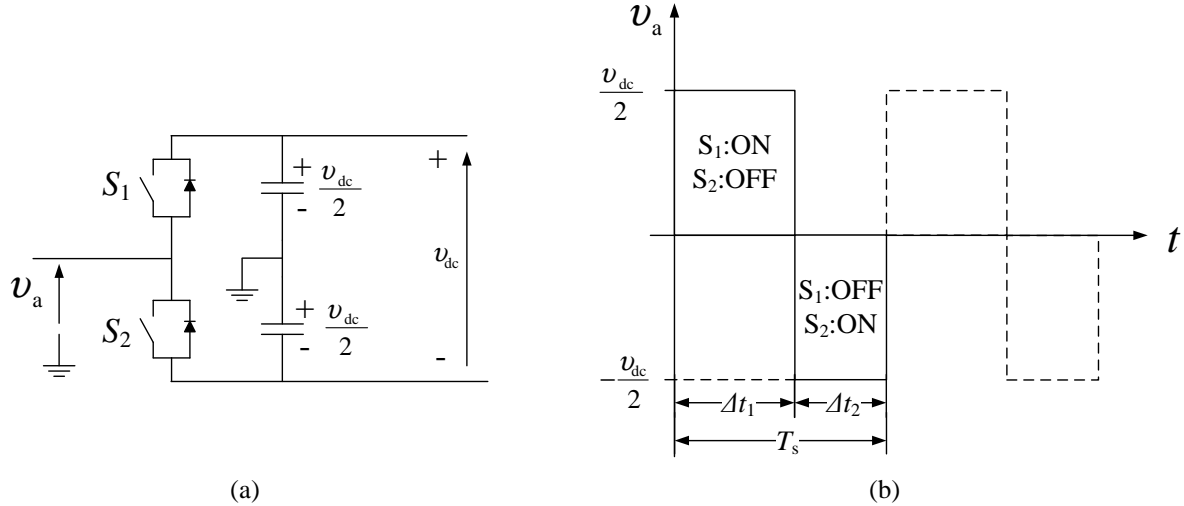


Fig. 2.5 Half-bridge converter: (a) Converter topology and (b) Output voltage waveform.

2.3 VSC principle of operation

In contrast to the *line-commutated converters*, the VSC belongs to the *self-commutated converter* category, being able to switch its power electronic valves at any desired current flowing through them. This feature allows the VSC to generate a desired alternating voltage at its ac-side and produce a bi-directional power flow. This section describes how the VSC operates and provides a brief introduction to the application of the Pulse-Width Modulation (PWM) method. Observe that other modulation strategies can be applied in actual installations in order to reduce the system losses, but most of them share common traits with the (PWM) method. Finally, the operational limitations of the VSC are analyzed and a number of existing and future VSC-HVDC converter topologies are presented.

2.3.1 Converter structure, switching and modulation

The explanation of how a VSC operates starts from the fundamental half-bridge converter in Fig. 2.5(a). The dc-side is connected to a dc-source of voltage v_{dc} , which is in turn divided equally among two series-connected identical capacitors. Each of them bears a direct voltage of $v_{dc}/2$. The two switches S_1 and S_2 are operated with the following sequence of actions

1. The switching pattern is periodic with frequency ω_0 and period T_s .
2. For a duration Δt_1 , switch S_1 is kept at on-state and S_2 at off-state. The output voltage v_a is equal to $+v_{dc}/2$.
3. For a duration $\Delta t_2 = T_s - \Delta t_1$, switch S_1 is kept at off-state and S_2 at on-state. The output voltage v_a is equal to $-v_{dc}/2$.

2.3. VSC principle of operation

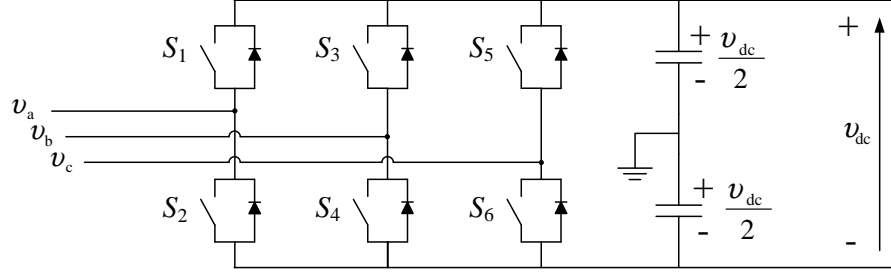


Fig. 2.6 Three-phase six-bridge VSC converter.

The resulting periodic waveform of v_a is shown in Fig. 2.5(b), fluctuating between $+v_{dc}/2$ and $-v_{dc}/2$. The Fourier series of this waveform can be expressed as

$$v_a = \frac{v_{a,0}}{2} + v_{a,1} \sin(\omega_0 t + \phi_1) + \sum_{n=2}^{\infty} v_{a,n} \sin(n\omega_0 t + \phi_n) \quad (2.2)$$

where the terms $v_{a,n}$ and ϕ_n are the Fourier coefficients and angles, respectively. For a switching duty-cycle of 0.5 (or $\Delta t_1 = T_s/2$), the dc-offset term $v_{a,0}/2$ becomes equal to zero and (2.2) becomes

$$v_a = v_{a,1} \sin(\omega_0 t + \phi_1) + \sum_{n=2}^{\infty} v_{a,n} \sin(n\omega_0 t + \phi_n) \quad (2.3)$$

This implies that there is a fundamental sinusoidal harmonic of amplitude $v_{a,1}$ with a frequency ω_0 , along with higher harmonics. An n -th order harmonic will have a frequency $n \cdot \omega_0$ and amplitude $v_{a,n}$. For this type of square waveform, the amplitude of the sinusoidal components are defined as

$$\begin{aligned} v_{a,n} &= \frac{2 \cdot v_{dc}}{\pi \cdot n}, \quad n = 1, 3, 5, \dots \\ v_{a,n} &= 0, \quad n = 0, 2, 4, \dots \end{aligned} \quad (2.4)$$

with $v_{a,n} < v_{a,n-1}$ for every odd n . This means that the fundamental component has the largest amplitude. Consequently, under the considered switching pattern, the half-bridge leg is able to behave as a voltage source, generating an alternating output voltage that comprises of a fundamental sinusoidal component of fixed amplitude and varying phase (achieved by delaying the whole switching pattern over time), together with higher-order harmonics of smaller magnitude.

If three half-bridge legs are connected to the same voltage source and dc-side capacitors as in Fig. 2.6, a three phase VSC converter is created, with each leg being able to independently produce its own alternating voltage v_a , v_b or v_c . In this case, if the three legs are provided with the same square wave switching pattern of 0.5 duty-cycle and frequency ω_0 , but consecutively phase shifted by $2\pi/3$ rad from one leg to the next, the VSC acts as a three-phase voltage source with voltages of equal magnitudes and phase-shifted by $2\pi/3$ rad.

2.3.2 Sinusoidal Pulse-Width Modulation

The previously described square-waveform modulation applied on a half-bridge converter has several disadvantages. As mentioned earlier, even though it is possible to control the phase of the resulting output voltage waveform, it is not possible to modulate the amplitude of the sinusoidal components if v_{dc} is fixed, with the fundamental component being the object of interest. Furthermore, relation (2.4) indicates that there are harmonics in the low-frequency range with significant amplitude and bulky filtering equipment would be required to ensure that the output voltage is mainly represented by the fundamental component. A number of alternative modulating techniques are used in practice to solve these problems e.g. the pulse-width modulation, the space-vector modulation, or the selective-harmonic elimination. The first of these methods is further described here.

Considering the half-bridge converter of Fig. 2.5(a), the PWM method dictates that switches S_1 and S_2 do not necessarily have to be switched with a fixed duty cycle. A selected sequence of alternating switchings with different time durations can create an output voltage whose fundamental component can have controllable amplitude, while the amplitude of higher harmonics can be significantly reduced. A version of the PWM is the Sinusoidal Pulse-Width Modulation (SPWM) and its concept is presented in Fig. 2.7, applied on the half-bridge converter of Fig. 2.5(a).

The main idea behind this method, applied to a VSC, considers the sampling of a desired reference signal in order to recreate it as an output voltage. A periodic triangular-wave carrier signal is used for the sampling, with amplitude A_c and frequency f_c . The value of A_c is chosen equal to $v_{dc}/2$ with reference to the converter of Fig. 2.5(a). Assume that the desired reference voltage output of the VSC is

$$v_{a,ref} = A_r \sin(2\pi f_r t + \phi) \quad (2.5)$$

where A_r is the amplitude of the reference and f_r is its frequency. The *Modulation index* m_a and the *Frequency ratio* m_f are defined below.

$$m_a = \frac{A_r}{A_c} \quad (2.6)$$

$$m_f = \frac{f_c}{f_r} \quad (2.7)$$

In order to apply the SPWM to the half-bridge converter of Fig. 2.5(a), amplitudes A_c and A_r are normalized by the value $v_{dc}/2$, resulting in $A_{c,norm}=1$ while the reference signal of (2.5) becomes

$$(v_{a,ref})_{norm} = A_{r,norm} \sin(\omega_0 t + \phi) = \frac{A_r}{v_{dc}/2} \sin(\omega_0 t + \phi) \quad (2.8)$$

with the Modulation index becoming

$$m_a = \frac{A_r}{v_{dc}/2} \quad (2.9)$$

The top graph of Fig. 2.7 shows the superposition of a normalized referenced signal at a frequency of $f_r=50$ Hz, corresponding to a reference voltage with an amplitude A_r slightly smaller than $v_{dc}/2$, and a carrier signal at $f_c=1500$ Hz. The SPWM method follows the rules

2.3. VSC principle of operation

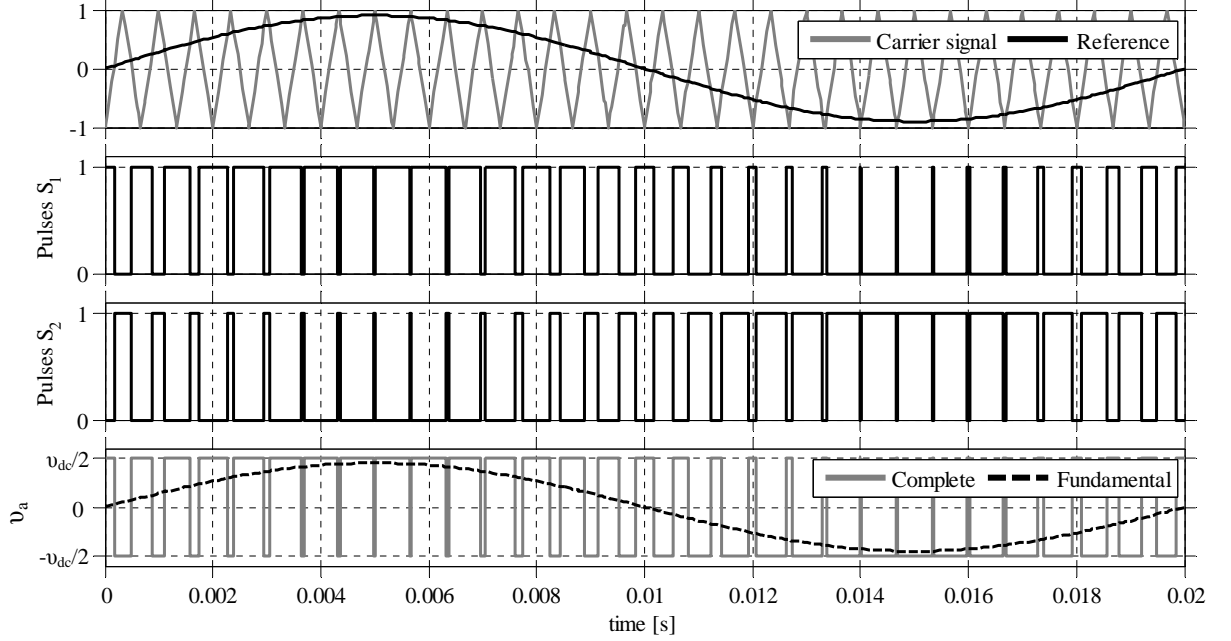


Fig. 2.7 Application of SPWM to a half-bridge converter. The graphs show the carrier and reference waves, the pulses to the active switches and the output voltage waveforms.

- If at any instance the reference signal has a higher value than the carrier signal, then S_1 is set at on-state and S_2 is kept at off-state.
- If at any instance the reference signal has a lower value than the carrier signal, then S_1 is kept at off-state and S_2 is set at on-state.

The resulting switching pulses for S_1 and S_2 are shown in Fig. 2.7, with values 1 and 0 corresponding to on- and off-state, respectively. Following these switching patterns, the resulting step-wise waveform of the half-bridge converter is presented in the lower graph. In this case, and considering that the waveform varies between $-v_{dc}/2$ and $v_{dc}/2$, the amplitude $v_{a,1}$ of the fundamental is given as

$$v_{a,1} = m_a \cdot \frac{v_{dc}}{2} = \frac{A_r}{v_{dc}/2} \cdot \frac{v_{dc}}{2} = A_r \quad (2.10)$$

This indicates that the resulting waveform has a fundamental component which is identical to the reference voltage in (2.5). The converter is thus able to reproduce a reference with varying amplitude while keeping v_{dc} constant, unlike the square-waveform modulation. The same principle applies to the three-phase VSC in Fig. 2.6.

As long as $m_a \leq 1$, the VSC operates in its linear region and relation (2.10) applies. For $m_a > 1$ (the reference signal has higher amplitude than the carrier signal), the VSC enters the over-modulation region where (2.10) does no longer apply. In this case, the amplitude of the fundamental is no longer equal to the amplitude of the reference and can reach a maximum value of $2v_{dc}/\pi$, defined by (2.4), and that corresponds to a fully square waveform of the VSC output voltage.

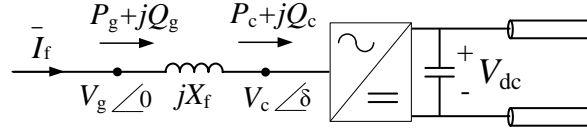


Fig. 2.8 Steady-state power transfer on the ac-side of a VSC-HVDC converter.

An added benefit of the SPWM method is the fact that when the VSC is operated in its linear region, the high-order harmonics of the voltage output primarily appear at the close vicinity of frequencies that are integer multiples of f_c . The higher the frequency ratio m_f , the further these harmonics are relocated towards higher frequencies, where associated passive filters can have small dimensions and cost. However, a high f_c implies that there are more converter switchings per reference period and this leads to higher switching losses. It is thus necessary to find a compromise in terms of cost/size of passive filters and switching losses.

2.3.3 Power-transfer capabilities and limitations

Having described how the VSC can produce a fully controllable output alternating voltage, it is possible to examine the power-transfer capabilities of a VSC-HVDC station. Figure 2.8 shows the portion of an HVDC transmission link with a VSC station and the phase reactor. The associated ac system, transformer and ac-side filters are considered by an equivalent Thevenin model that is connected to the phase reactor, with the connection point having a voltage phasor $\bar{V}_g = V_g \angle 0$. For simplicity purposes, the phase reactor and the valves of the station are considered to be lossless.

The VSC can produce an output voltage $\bar{V}_c = V_c \angle \delta$ with a desired magnitude and an angle difference δ , compared to \bar{V}_g . For such a system, the steady-state per-unit complex power absorbed by the VSC at the connection point of the phase reactor to the rest of the ac system is equal to

$$S_g = \bar{V}_g [\bar{I}_f]' = V_g \left[\frac{V_g - V_c \angle \delta}{jX_f} \right]' = -\frac{V_g V_c}{X_f} \sin(\delta) + j \frac{V_g^2}{X_f} - j \frac{V_g V_c}{X_f} \cos(\delta) \quad (2.11)$$

where the active and reactive power are

$$P_g = -\frac{V_g V_c}{X_f} \sin(\delta) \quad (2.12)$$

$$Q_g = \frac{V_g^2}{X_f} - \frac{V_g V_c}{X_f} \cos(\delta) \quad (2.13)$$

Considering that the phase shift angle δ is usually very small, the Taylor approximation of $\sin(\delta)$ and $\cos(\delta)$ gives δ and 1, respectively. As such, equations (2.12) and (2.13) are rewritten as

$$P_g = -\frac{V_g V_c}{X_f} \delta \quad (2.14)$$

$$Q_g = \frac{V_g - V_c}{X_f} V_g \quad (2.15)$$

2.3. VSC principle of operation

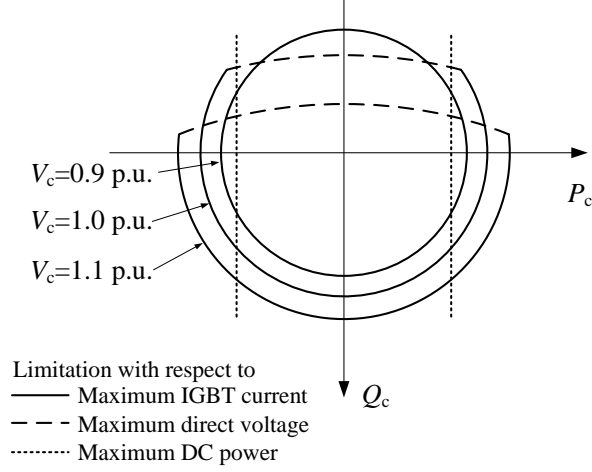


Fig. 2.9 Capability curve of a VSC-HVDC station.

Taking into account that V_g is expected to be relatively stiff and the variation range of V_c is normally small (0.9-1.1 p.u.), it can be seen that δ is the dominant term in (2.14) in defining the allowable P_g . Likewise, the term δ is absent in (2.15), indicating that the magnitude difference $V_g - V_c$ is dominant in defining the amount of Q_g . For this reason, it can be claimed that the active power P_g is controlled by the angle difference of the voltages across the phase reactor, and the reactive power Q_g is controlled by the magnitude difference of the voltage phasors. Given that the VSC can independently control the magnitude and phase of its output voltage, it can be claimed that the VSC is able to control the active and reactive power transfer independently.

However, the power-transfer capabilities of a VSC station are not unlimited and care should be taken so that certain limitations are not exceeded. There are mainly three factors that limit the power capability, seen from a power system stability perspective [47] and their effect is presented in Fig. 2.9. The first one is the maximum current through the IGBTs of the converter valves. The maximum apparent power $|S_{\max}|$ that the VSC can output at its ac-side is

$$|S_{\max}| = |P_c + jQ_c|_{\max} = \sqrt{(P_c^2 + Q_c^2)_{\max}} = V_c \cdot I_{f,\max} \quad (2.16)$$

where $I_{f,\max}$ is the maximum allowed current through the IGBTs, dictated by the design of the latter. Relation (2.16) defines a circle of maximum MVA, with radius $V_c \cdot I_{f,\max}$. Therefore, for a given $I_{f,\max}$ and varying V_c , the maximum allowed MVA limit of the VSC changes as well. Three such circles are drawn in Fig. 2.9 for V_c equal to 0.9, 1.0 and 1.1 pu.

The second limit is the maximum steady-state direct-voltage level $V_{dc,\max}$. The reactive power is mainly dependent on the voltage difference between the alternating voltage that the VSC can generate from the direct voltage on its dc side (with the amplitude of the fundamental being directly related to V_{dc}), and the grid ac voltage. If the grid ac voltage is high, the difference between the $V_{dc,\max}$ and the ac voltage will be low. The reactive power capability is then moderate but increases with decreasing ac voltage. The third limit is the maximum direct current through the cable. This affects only the active power and is drawn by a straight line in Fig. 2.9. The enclosed area between the previous limits defines the allowed operational area of the VSC. If these limits are to be considered for powers P_g and Q_g , small adjustments need to be made to

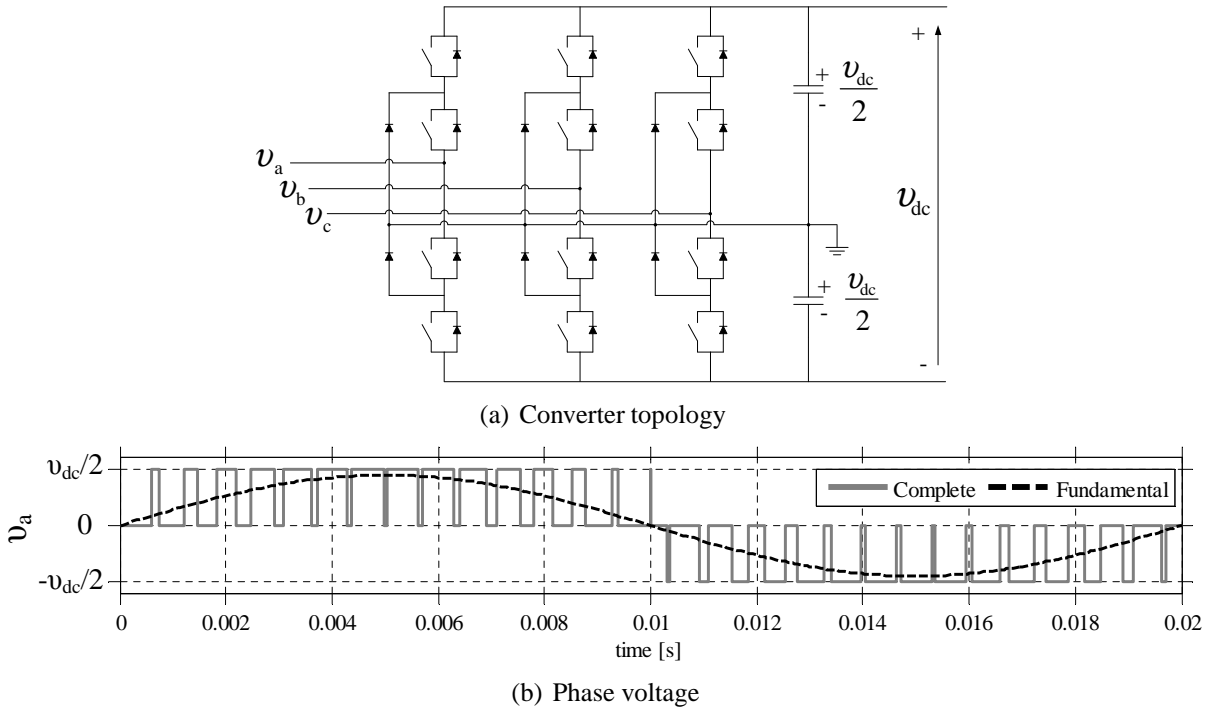


Fig. 2.10 Three-level Neutral-Point-Clamped converter.

the curves of the figure, to account for the active-power losses and reactive-power absorption, owing to the presence of the phase reactor.

2.3.4 Advances in converter topologies

Even though numerous designs for potential HVDC converters exist, only a few are considered realistic for commercial use and even less have been implemented in practice. The great majority of all VSC-HVDC connections having been built to date [3] are based on the two-level converter of Fig. 2.6. However, the produced two-level ac-side voltage has a high harmonic content and the use of filters is necessary, with losses being high due to the high switching frequency at which the valves are operated.

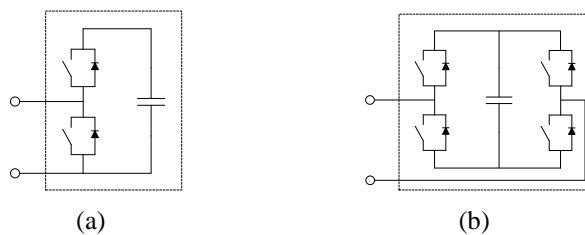


Fig. 2.11 Module cells for a Modular Multilevel Converter: (a) Half-bridge cell and (b) Full-bridge cell.

2.3. VSC principle of operation

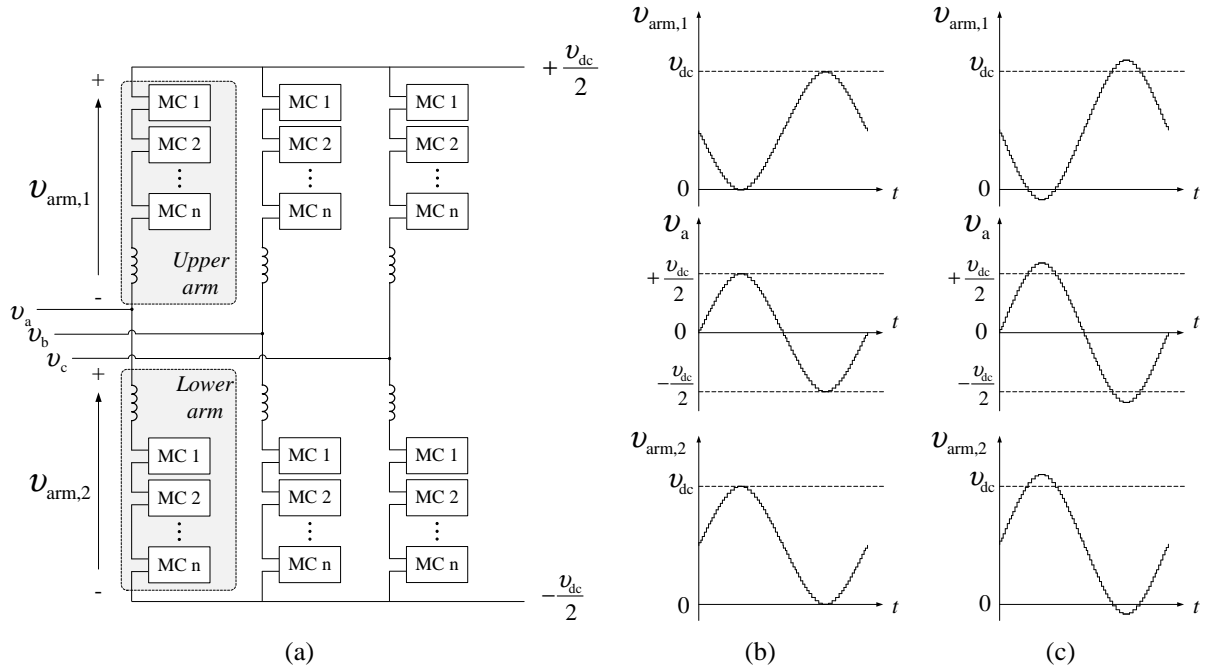


Fig. 2.12 Modular Multilevel Converter: (a) Converter topology, (b) Voltage waveforms with half-bridge cells and (c) Voltage waveforms with full-bridge cells.

A first effort towards multilevel ac voltage has been performed by adapting the Neutral-Point-Clamped (NPC) converter to HVDC standards. This converter is presented in Fig. 2.10(a) in its three-phase arrangement and the resulting phase voltage is depicted in Fig. 2.10(b). The converter can now switch to three levels ($+\frac{v_{dc}}{2}$, 0 and $-\frac{v_{dc}}{2}$), leading to less total harmonic distortion, reduced losses and filter requirements but at the cost of high mechanical complexity, increased converter size, challenges in balancing the dc-side capacitors and uneven loss distribution among the valves. An actively clamped topology that solves the loss distribution problem of the NPC was introduced, called Active NPC (ANPC), with the clamping diodes being replaced by transistors [3, 48].

The major breakthrough in VSC-HVDC however was provided by the introduction of the Modular Multilevel Converter (MMC) [49]. Overall, the MMC resembles a two-level converter where the series IGBT valve is replaced by a chain of series connected, identical and isolated cells each providing fundamental voltage levels. The MMC is shown in Fig. 2.12(a). Cumulatively, the whole chain produces a voltage consisting of a very finely-shaped ac waveform with a dc-offset of equal magnitude to the direct voltage of the adjacent dc cable. Eventually the phase voltage will consist of only the alternating part. In its simplest form, the MMC uses the half bridge cell (Fig. 2.11(a)) where a capacitor is either inserted or bypassed, providing two possible voltage levels; V_{cap} or 0, where V_{cap} is the voltage of the cell capacitor. The arm- and phase-voltage waveforms at one leg of the converter are plotted in Fig. 2.12(b). Other cell topologies can also be used, like the full bridge cell in Fig. 2.11(b), providing voltage levels of V_{cap} , 0 or $-V_{cap}$. MMC with full bridge cells, with the associated arm- and phase-voltage waveforms shown in Fig. 2.12(c), can produce higher magnitude alternating voltage and even suppress dc-faults [50]

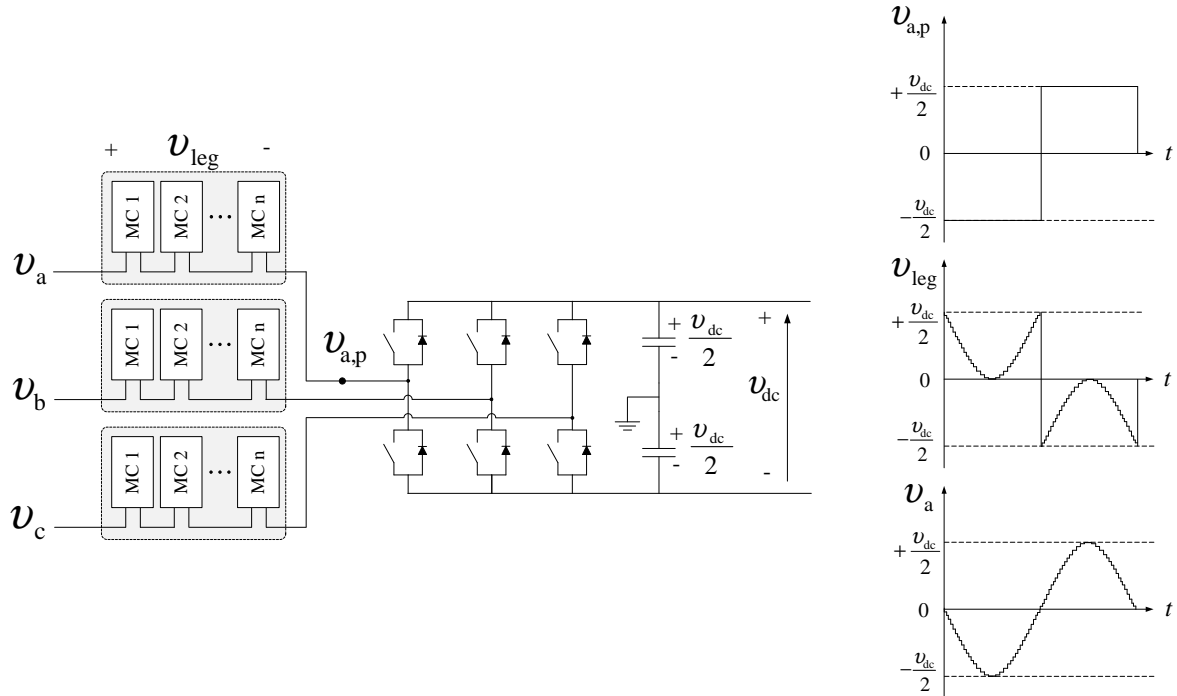


Fig. 2.13 Series hybrid with wave-shaping on the ac side.

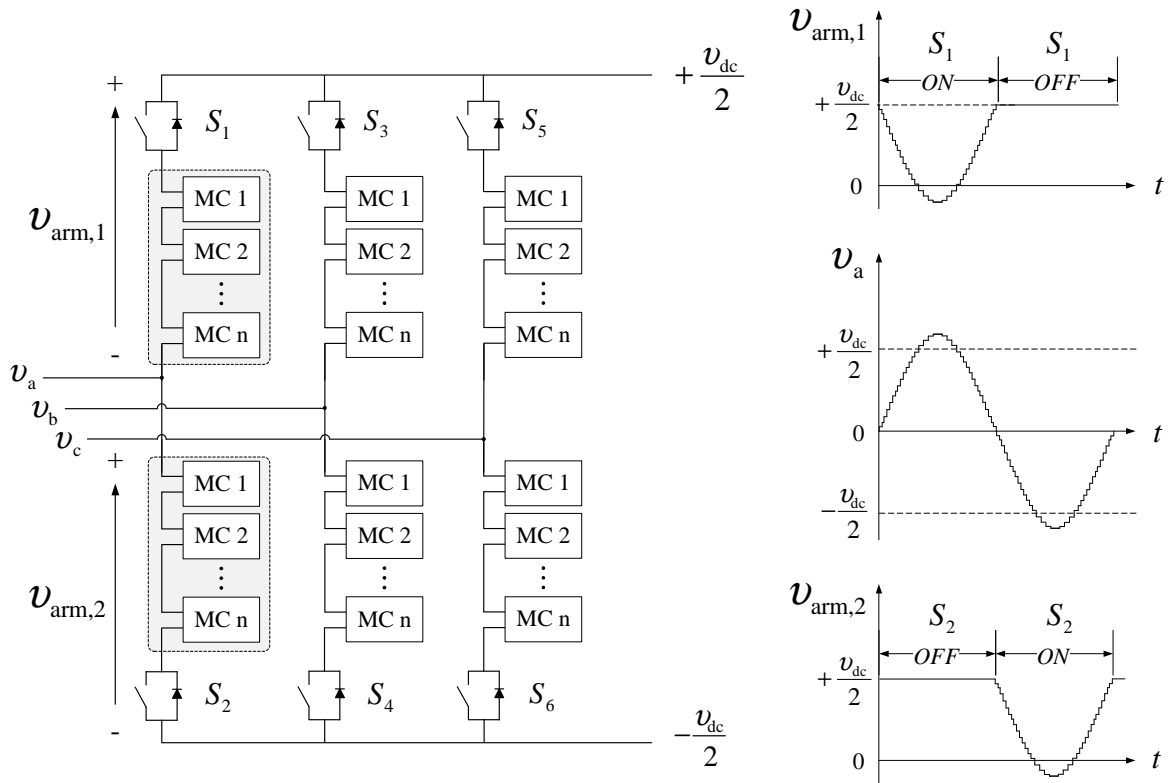


Fig. 2.14 Series hybrid with wave-shaping on the dc side.

at the expense of higher IGBT numbers. Overall the MMC offers very low losses, low effective switching frequency and minimization of ac-side filters.

Very recently, a number of proposed alterations to the original MMC concepts have been proposed and seriously considered for the next generation of MMC [50]. One very interesting example is the "Series hybrid with wave shaping on the ac side" shown in Fig. 2.13. This is a combination of the two-level converter and the MMC. The idea is that the six-bridge converter provides a two-level voltage while a series connected chain of cells creates a complex waveform which, when superimposed to the former, results in a fine multilevel sinusoidal waveform. The main benefit of this topology are the reduced switching losses since the cells of every arm need to switch and produce a sinusoidal arm voltage for only half of the period of the fundamental.

Another proposed design is the "Series hybrid with wave shaping on the dc side" (Fig. 2.14) which is also considered by Alstom as its next generation HVDC solution [51]. Each arm of the converter consists of an IGBT-stack in series with a chain of cells. The main principle of operation is that each arm is responsible for creating only half the sinusoidal waveform. This results in chains of cells rated at approximately only half the total dc-side voltage. The IGBT valves are needed to isolate the arm that is complementary to the one connected to the ac-phase terminal at any time. Even though the MMC technology has only few commissioned examples to present, the technology trend points towards the domination of the MMC form in VSC-HVDC applications, mostly due to the very low losses that can be achieved and the possibility to suppress dc-faults if full-bridge cells are used.

2.4 VSC control

The dominant method in the control of VSC in various applications is the vector control. Having been widely applied in machine drives for the control of VSC-driven electrical machines, the vector control is also highly applied in VSC-HVDC applications, as mentioned in [42]. The main idea of the vector control involves the representation of a three-phase alternating quantity of the ac system as a vector with dc-type of properties, positioned on a rotating dq -rotating frame. The resulting vector can then be controlled in a similar manner as the voltage and current of a dc system, and finally restored to its three-phase alternating representation to be applied to the ac system.

The typical structure of a VSC-HVDC control system is illustrated in Fig. 2.15. Its backbone is the Vector Current Controller (VCC). This control structure receives as inputs the currents references $i_f^d^*$ and $i_f^q^*$, with a role of producing a pair of voltage reference $v_c^d^*$ and $v_c^q^*$. These are transformed into three-phase quantities and provided as modulating signals to the PWM block, which will generate appropriate firing signals for the VSC valves. The resulting current on the phase reactor should ideally match the current references. As mentioned in Section (2.3.2), the modulating voltage signal to the PWM is internally normalized by the value of the direct voltage of the dc-side capacitor in the VSC.

A Phase-Locked Loop (PLL) is used to synchronize the dq -rotating frame of the converter to the rotating vector $\underline{v}_g^{(\alpha\beta)}$ vector in $\alpha\beta$ -coordinates, providing a reliable reference frame for any

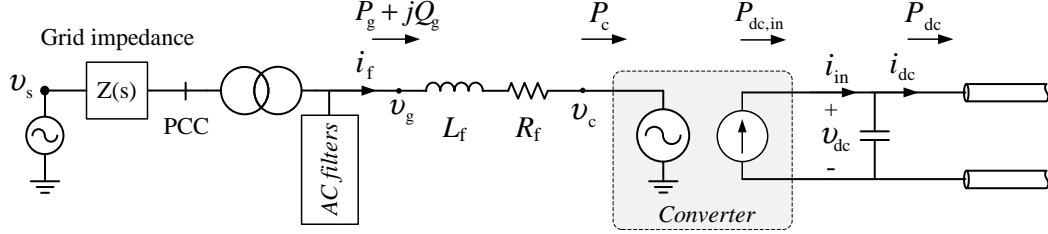


Fig. 2.16 Equivalent model of the VSC.

plied across the phase reactor, the following combined description of differential equations can be obtained for the three phases

$$\underline{v}_g^{(abc)} - \underline{v}_c^{(abc)} = L_f \frac{d\underline{i}_f^{(abc)}}{dt} + R_f \underline{i}_f^{(abc)} \quad (2.17)$$

By applying Clarke's transformation (described in the Appendix), (2.17) can be expressed in the fixed $\alpha\beta$ -coordinate system as

$$\underline{v}_g^{(\alpha\beta)} - \underline{v}_c^{(\alpha\beta)} = L_f \frac{d\underline{i}_f^{(\alpha\beta)}}{dt} + R_f \underline{i}_f^{(\alpha\beta)} \quad (2.18)$$

A further step is to apply the Park transformation (see Appendix). The PLL of the VSC is synchronized with the voltage vector $\underline{v}_g^{(dq)}$. The considered voltage and current vectors can then be expressed as

$$\underline{v}_g^{(\alpha\beta)} = \underline{v}_g^{(dq)} e^{j\theta_g} \quad (2.19)$$

$$\underline{v}_c^{(\alpha\beta)} = \underline{v}_c^{(dq)} e^{j\theta_g} \quad (2.20)$$

$$\underline{i}_f^{(\alpha\beta)} = \underline{i}_f^{(dq)} e^{j\theta_g} \quad (2.21)$$

Equation (2.18) can thus be transformed into

$$\begin{aligned} \underline{v}_g^{(dq)} e^{j\theta_g} - \underline{v}_c^{(dq)} e^{j\theta_g} &= L_f \frac{d(\underline{i}_f^{(dq)} e^{j\theta_g})}{dt} + R_f \underline{i}_f^{(dq)} e^{j\theta_g} \Rightarrow \\ \underline{v}_g^{(dq)} e^{j\theta_g} - \underline{v}_c^{(dq)} e^{j\theta_g} &= j \frac{d\theta_g}{dt} L_f \underline{i}_f^{(dq)} e^{j\theta_g} + L_f e^{j\theta_g} \frac{d\underline{i}_f^{(dq)}}{dt} + R_f \underline{i}_f^{(dq)} e^{j\theta_g} \Rightarrow \\ \underline{v}_g^{(dq)} e^{j\theta_g} - \underline{v}_c^{(dq)} e^{j\theta_g} &= j \omega_g L_f \underline{i}_f^{(dq)} e^{j\theta_g} + L_f e^{j\theta_g} \frac{d\underline{i}_f^{(dq)}}{dt} + R_f \underline{i}_f^{(dq)} e^{j\theta_g} \end{aligned} \quad (2.22)$$

where ω_g is the angular frequency of the dq -rotating frame. Usually, the variations in $\omega_g(t)$ are very small over time and it can then be considered as constant. Under this condition and eliminating the term $e^{j\theta_g}$, (2.22) can be re-written as

$$L_f \frac{d\underline{i}_f^{(dq)}}{dt} = -R_f \underline{i}_f^{(dq)} - j \omega_g L_f \underline{i}_f^{(dq)} + \underline{v}_g^{(dq)} - \underline{v}_c^{(dq)} \quad (2.23)$$

Chapter 2. VSC-HVDC operation and control

which can be expanded to its real and imaginary part as

$$L_f \frac{di_f^d}{dt} = -R_f i_f^d + \omega_g L_f i_f^q + v_g^d - v_c^d \quad (2.24)$$

$$L_f \frac{di_f^q}{dt} = -R_f i_f^q - \omega_g L_f i_f^d + v_g^q - v_c^q \quad (2.25)$$

These are two cross-coupled first-order subsystems, with the cross-coupling being initiated by the terms $\omega_g L_f i_f^q$ and $\omega_g L_f i_f^d$.

The complex power S_g is calculated as

$$\begin{aligned} S_g &= \underline{v}_g^{(dq)} \left[\underline{i}_f^{(dq)} \right]' = \left(v_g^d + j v_g^q \right) \left(i_f^d - j i_f^q \right) \Rightarrow \\ S_g &= \left(v_g^d i_f^d + v_g^q i_f^q \right) + j \left(v_g^q i_f^d - v_g^d i_f^q \right) \end{aligned} \quad (2.26)$$

where the active and reactive power are

$$P_g = v_g^d i_f^d + v_g^q i_f^q \quad (2.27)$$

$$Q_g = v_g^q i_f^d - v_g^d i_f^q \quad (2.28)$$

Considering that the PLL performs the synchronization by aligning the d -axis of the dq -rotating frame to the vector $\underline{v}_g^{(dq)}$, the q -component of the latter will be zero in steady-state, thus

$$\underline{v}_g^{(dq)} = v_g^d \quad (2.29)$$

Applying (2.29) to (2.27) and (2.28) gives

$$P_g = v_g^d i_f^d \quad (2.30)$$

$$Q_g = -v_g^d i_f^q \quad (2.31)$$

which means that the active power can be controlled via the d component of the current, i_f^d , while the reactive power with the q component of the current, i_f^q . If the two currents can be controlled independently, the VSC could have an independent and decoupled control of the active and reactive power.

Regarding the active-power balance at the two sides of the valves of the VSC (as reactive power does not propagate to the dc-side) and assuming that the losses on the valves are negligible, the following relation applies

$$\begin{aligned} P_c = P_{dc,in} &\Rightarrow \text{Real} \left\{ \underline{v}_c^{(dq)} \left[\underline{i}_f^{(dq)} \right]' \right\} = v_{dc} i_{in} \Rightarrow v_c^d i_f^d + v_c^q i_f^q = v_{dc} i_{dc} \Rightarrow \\ i_{in} &= \frac{v_c^d i_f^d + v_c^q i_f^q}{v_{dc}} \end{aligned} \quad (2.32)$$

which is the direct current propagating to the dc side of the VSC, as shown in Fig. 2.16. In steady-state, the current i_{in} becomes equal to i_{dc} , assuming a lossless dc capacitor and neglecting harmonics due to switching.

Observing (2.23)-(2.25), the only manner in which the VSC can affect the dynamics of the reactor current and attempt to set it to a desired reference $i_f^{(dq)*}$, is by changing its output voltage $\underline{v}_c^{(dq)}$ accordingly. Therefore a control law must be applied providing a reference $\underline{v}_c^{(dq)*}$, which the VSC will apply with ideally no delay.

Equation (2.23) can be transformed in the Laplace domain as

$$sL_f \mathbf{i}_f = -R_f \mathbf{i}_f - j\omega_g L_f \mathbf{i}_f + \mathbf{v}_g - \mathbf{v}_c \quad (2.33)$$

where the bold font indicates the Laplace transformation of a corresponding dq -coordinate vector. If the current i_f and the voltage v_g are perfectly measured, the following control law is suggested in [52], which eliminates the cross-coupling of the current dq -components and compensates for the disturbance caused by v_g

$$\mathbf{v}_c^* = -F(s) (\mathbf{i}_f^* - \mathbf{i}_f) - j\omega_g L_f \mathbf{i}_f + \mathbf{v}_g \quad (2.34)$$

where, $F(s)$ is the controller transfer function applied to the current error. If the controller computational delay and the PWM switching are modeled as a delay time T_d , then $\mathbf{v}_c = e^{-sT_d} \mathbf{v}_c^*$, [43]. However, for simplification purposes, the delay time can be neglected and then $\mathbf{v}_c = \mathbf{v}_c^*$. Under this condition, the control law (2.34) is replaced in (2.33) and provides

$$\begin{aligned} sL_f \mathbf{i}_f &= -R_f \mathbf{i}_f + F(s) (\mathbf{i}_f^* - \mathbf{i}_f) \Rightarrow \mathbf{i}_f = \frac{1}{sL_f + R_f} F(s) (\mathbf{i}_f^* - \mathbf{i}_f) \Rightarrow \\ \mathbf{i}_f &= G_e(s) F(s) (\mathbf{i}_f^* - \mathbf{i}_f) \Rightarrow \\ \mathbf{i}_f &= \frac{G_e(s) F(s)}{1 + G_e(s) F(s)} \mathbf{i}_f^* \end{aligned} \quad (2.35)$$

where $G_e(s) = 1/(sL_f + R_f)$, representing the electrical dynamics in the phase reactor. Let G_{cc} be the closed-loop transfer function from \mathbf{i}_f^* to \mathbf{i}_f . G_{cc} can be shaped as a low-pass filter, as follows

$$G_{cc}(s) = \frac{a_{cc}}{s + a_{cc}} = \frac{\frac{a_{cc}}{s}}{1 + \frac{a_{cc}}{s}} \quad (2.36)$$

where a_{cc} is the closed-loop bandwidth. From (2.35), it is

$$G_{cc}(s) = \frac{G_e(s) F(s)}{1 + G_e(s) F(s)} \quad (2.37)$$

so if $G_e(s) F(s) = a_{cc}/s$, the desired closed-loop system in (2.36) is obtained. This yields

$$F(s) = \frac{a_{cc}}{s} G_e^{-1}(s) = \frac{a_{cc}}{s} (sL_f + R_f) = a_{cc} L_f + \frac{a_{cc} R_f}{s} \quad (2.38)$$

which indicates that $F(s)$ is a PI controller with proportional gain $K_{p,cc} = a_{cc} L_f$ and integral gain $K_{i,cc} = a_{cc} R_f$.

The block diagram of the complete current controller based on relation (2.34) is provided in Fig. 2.17. Several improvements can be implemented in the current controller such as

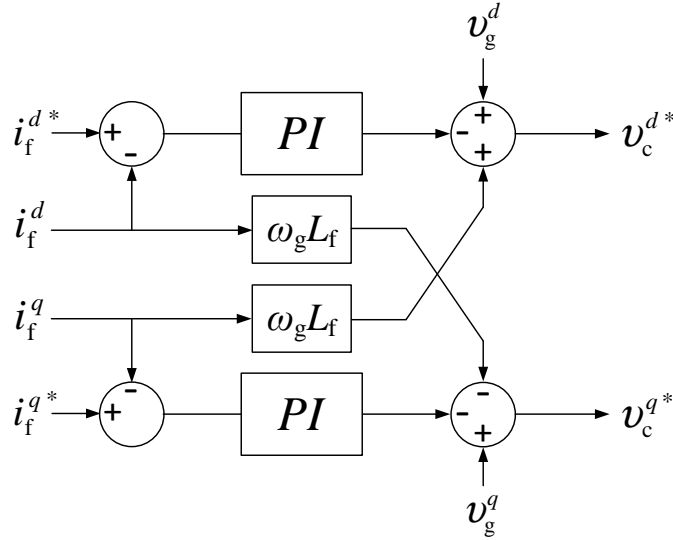


Fig. 2.17 Current Controller of the VSC.

- anti-windup functionalities in case of voltage saturation
- active damping capabilities to reject undesired disturbances
- filtering of signals before they are fed-forward into the control process

2.4.2 Phased-Locked Loop

The duty of the PLL in the VSC control structure is to estimate the angle of rotation θ_g of the measured voltage vector $\underline{v}_g^{(\alpha\beta)}$. Fig. 2.18 shows $\underline{v}_g^{(\alpha\beta)}$, along with the $\alpha\beta$ -stationary frame, the ideally aligned d_iq_i frame (rotating with angular speed ω_g and angle θ_g) and the converter dq -rotating frame (rotating with angular speed $\hat{\omega}_g$ and an angle $\hat{\theta}_g$). The latter is the frame that is in the knowledge of the PLL, which tries to position it so that the d -axis is aligned with the rotating vector.

As it can be seen, as long as the PLL's dq frame rotates with $\hat{\theta}_g$ and is still not properly aligned with $\underline{v}_g^{(\alpha\beta)}$, the dq -decomposition of the vector is going to produce a non-zero q -component v_g^q . The PLL must thus increase or decrease $\hat{\omega}_g$ speed (and thus $\hat{\theta}_g$) until the calculated v_g^q becomes equal to zero. This means that from a control perspective, the term v_g^q can be used as an error signal, which when fed to a PI controller will lead to the creation of such an $\hat{\omega}_g$ and $\hat{\theta}_g$ that eventually will set v_g^q to zero.

The structure of the adopted PLL is depicted in Fig. 2.19. The voltage $v_g^{(abc)}$ is transformed into $\underline{v}_g^{(\alpha\beta)}$ and using the PLL's estimation $\hat{\theta}_g$, calculates $\underline{v}_g^{(dq)}$. Based on the "error" v_g^q , the PLL's PI controller is outputting a correction signal $\Delta\omega$ which is added to a constant pre-estimation of the vector's angular speed $\omega_{g,0}$. This provides the converter angular speed $\hat{\omega}_g$ and is integrated to produce the updated version of $\hat{\theta}_g$, which is fed back to the $\alpha\beta$ -to- dq block and produces the

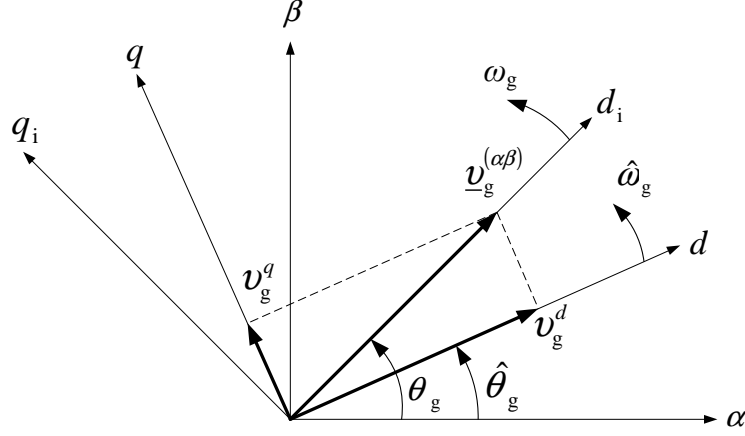


Fig. 2.18 Decomposition of the voltage vector $\underline{v}_g^{(\alpha\beta)}$ into the converter dq frame and the ideal dq frame.

new v_g^q . In steady-state, $\hat{\omega}_g$ and $\hat{\theta}_g$ become equal to ω_g and θ_g , respectively. The gains $K_{p,PLL}$ and $K_{i,PLL}$ are selected as suggested in [53] as

$$K_{p,PLL} = 2a_{PLL}, \quad K_{i,PLL} = a_{PLL}^2 \quad (2.39)$$

In [54], a bandwidth a_{PLL} for the closed-loop system of 5 Hz is selected and in [55] a range of 3 to 5 Hz is mentioned as typical bandwidth for grid-connected applications. In this thesis, a_{PLL} is selected to be 5 Hz (provided to the controller in rad/s units).

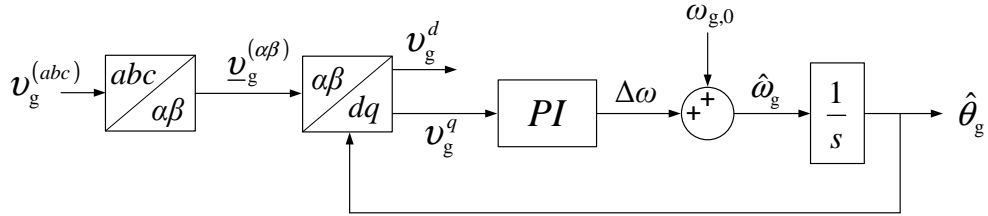


Fig. 2.19 Block diagram of PLL.

2.4.3 Direct-voltage control

The portion of the complete VSC model that describes the dynamics of the direct voltage controller is presented in Fig. 2.20. The energy stored in the dc capacitor C_{dc} of the direct-voltage controlled VSC is $C_{dc}W/2$, with the value $W = v_{dc}^2$ being proportional to the energy of that capacitor. The dynamics of the dc capacitor become

$$\frac{1}{2}C_{dc} \frac{dW}{dt} = P_{dc,in} - P_{dc} \quad (2.40)$$

The direct-voltage controller can be a simple PI controller $F(s)$ with proportional gain K_p and integral gain K_i . The output of the controller is a reference P_g^* . Assuming no losses on the phase reactor (neglect R_f) and a lossless converter, we have

$$P_g \approx P_c \approx P_{dc,in} \quad (2.41)$$

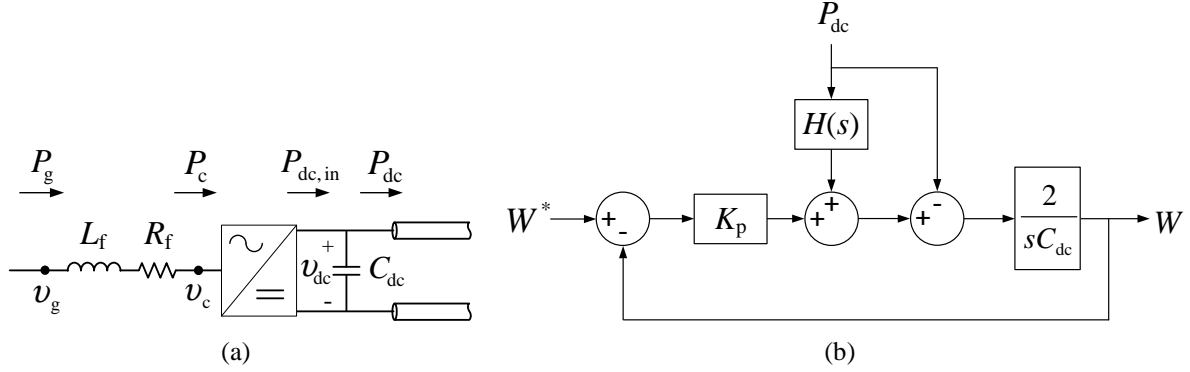


Fig. 2.20 Direct-voltage regulation in a VSC: (a) Power flow across the converter and (b) Closed-loop direct-voltage control process.

Therefore, P_g can be considered as the power that is drawn from the ac grid and directly injected to the dc-side capacitor to keep it charged, as in Fig. 2.20(a). From a control point of view, P_{dc} represents a disturbance. Therefore a dc-power feedforward term is added to cancel its effect in the closed-loop system. Consequently, $F(s)$ can be represented solely by K_p , still maintaining a zero state error [43]. If losses were considered, K_i should be maintained, providing a trimming action and removing steady-state errors. In the present analysis however, the previous losses are neglected and $K_i=0$. The expression of the direct-voltage controller can then be written as

$$P_g^* = F(s)(W^* - W) + P_f = K_p(W^* - W) + P_f \Rightarrow$$

$$P_g^* = K_p(W^* - W) + H(s)P_{dc} \quad (2.42)$$

where W^* is the reference "energy" stored in the capacitor, $H(s)$ is the transfer function of a low-pass filter $a_f/(s + a_f)$ having bandwidth a_f , and P_f represents the power-feedforward term of the direct-voltage controller, equal to the filtered value of P_{dc} . Given equation (2.30), the current reference i_f^{d*} could then be equal to $i_f^{d*} = P_g^*/v_g^d$, where v_g^d could optionally be filtered as well through a low-pass filter of bandwidth a_f , as suggested in [43].

Observe that the voltage control is not controlling v_{dc} itself but rather the square of the latter, W . If the controller were to operate directly on the error $v_{dc}^* - v_{dc}$, the voltage control process would be non-linear and the small-signal closed-loop dynamics of the system would be dependent on the steady-state operating point $v_{dc,0}$. This inconvenience is avoided by prompting the controller to alternatively operate on the error $W^* - W$ [43].

Assuming perfect knowledge of the grid-voltage angle and an infinitely fast current-control loop, the requested active power P_g^* can be immediately applied, thus $P_g = P_g^*$. Substituting (2.42) to (2.40) and considering (2.41), gives

$$W = \frac{2K_p}{2K_p + sC_{dc}}W^* + \frac{2[H(s) - 1]}{2K_p + sC_{dc}}P_{dc} = \frac{\frac{2K_p}{C_{dc}}}{s + \frac{2K_p}{C_{dc}}}W^* + \frac{2[H(s) - 1]}{2K_p + sC_{dc}}P_{dc} \Rightarrow$$

$$W = G_{cp}W^* + Y_{cp}P_{dc} \quad (2.43)$$

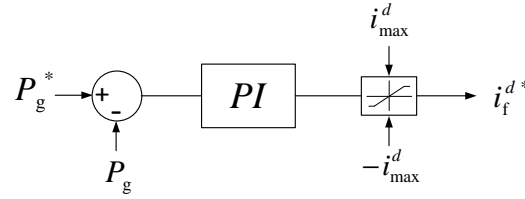


Fig. 2.21 Active-power controller of the VSC.

where G_{cp} is the closed-loop transfer function of the voltage controller for $P_{dc}=0$. If the proportional gain is selected as $K_p = a_d C_{dc}/2$, the transfer function G_{cp} is now equal to $a_d/(s + a_d)$ which is a first-order low-pass filter with bandwidth a_d . This serves as a valuable designing tool for the prediction of the closed-loop performance of the direct-voltage controller.

2.4.4 Active-power control

The role of the active-power controller is to induce the flow of active power equal to a certain reference. The point of the VSC circuit where the active power is measured and controlled, is usually the connection point between the phase reactor and the ac-side filters. If the considered station is in power-control mode, i.e. it is the receiving-end station, the controlled power corresponds to the power P_g that enters the phase reactor towards the valves of the VSC, with regards to Fig. 2.15. As shown in (2.30), the active power depends only on the current i_f^d and the voltage v_g^d . The latter experiences only small variations in practice and its contribution to P_g is considered to be constant. The active power will then be essentially decided by i_f^d . Hence, an active power controller as in Fig. 2.21 can be used where a PI controller is used to generate the current reference i_f^{d*} that will be fed to the current controller and finally imposed to the phase reactor.

The PI can have an anti-windup function where the reference i_f^{d*} is limited to a maximum value i_{max}^d equal to a rated property i_N . This can be the rated ac current of the converter or a value close to the maximum allowed valve current, both turned into an appropriate dq -current quantity.

2.4.5 Reactive-power control

In an almost identical way as the active-power control, the reactive-power control is normally applied at the connection point between the phase reactor and the ac-side filters, controlling the active power Q_g that enters the phase reactor, with a direction towards the VSC valves. Equation (2.31) shows that the reactive power at the selected measurement point is proportional to the relatively stiff voltage value v_g^d and the current i_f^q . Consequently, Q_g can be considered a function of i_f^q only. The PI-based reactive-power controller in Fig. 2.22 can then regulate Q_g to follow a reference Q_g^* by creating an appropriate current i_f^{q*} to be provided to the current controller and finally imposed to the phase reactor. Notice that Q_g^* and Q_g are added with opposite signs than P_g^* and P_g in the previous section, because of the minus sign in (2.31).

The controller can have an anti-windup function where the reference i_f^{q*} is limited to a max-

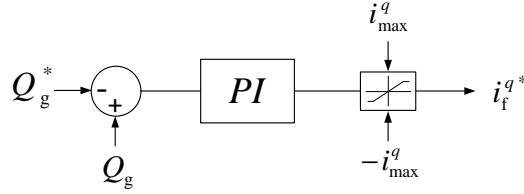


Fig. 2.22 Reactive-power controller of the VSC.

imum value i_{\max}^q . Considering the previous maximum current limitation i_N and a strategy that gives priority to the establishment of the separately requested i_{\max}^d current, the limit of the reactive current reference can be varied during operation by the relation

$$i_{\max}^q = \sqrt{i_N^2 - (i_f^{d*})^2} \quad (2.44)$$

2.4.6 AC-voltage regulation

When the VSC is connected to a weak grid, the PCC voltage can be regulated and stiffened. A weak grid connected to the PCC has by definition a relatively large grid impedance. The flow of current between such a grid and the VSC would cause significant voltage drop across the grid impedance and drastically change the voltage magnitude at the PCC, and thus the voltage v_g of the phase reactor as in Fig. 2.16. Considering a mostly inductive equivalent impedance of the grid, if the VSC absorbs reactive power, the magnitude of v_g is going to decrease, with the opposite phenomenon occurring for an injection of reactive power from the VSC. Therefore, since the reactive power is regulated through i_f^q , a PI controller can be used as an alternating voltage controller, as in Fig. 2.23. Observe that the signs of adding $|v_g|^*$ and $|v_g|$ are in such a way so that a positive error $|v_g|^* - |v_g|$, (demand for increase of voltage magnitude) should cause a demand for negative reactive power and therefore positive i_f^{q*} .

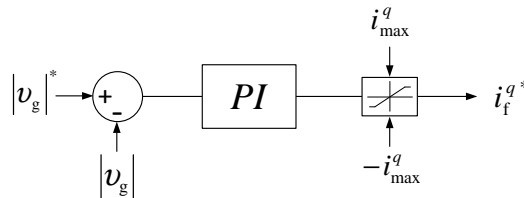


Fig. 2.23 Alternating-voltage controller of the VSC.

2.5 Control strategy in two-terminal VSC-HVDC systems

In a typical configuration of a two-terminal VSC-HVDC link as the one in Fig. 2.1, if power is transmitted from Station 1 to Station 2, then Station 1 is a direct-voltage controlled station

2.5. Control strategy in two-terminal VSC-HVDC systems

and Station 2 is active-power controlled. In case of power flow reversal, the previous control duties are swapped between the stations. The purpose of following such a control strategy is to allow the direct-voltage controlled station to control the position on the dc-transmission link with the highest voltage. Once there is power flow through the dc lines, a voltage drop will develop on the resistance of the lines. The highest voltage will occur at the dc terminals of the station that injects power to the dc link. Therefore, for safety purposes, this station is set to direct-voltage control, ensuring that the highest voltage on the lines is firmly controlled and the physical voltage limitations of the overall equipment are not exceeded.

An example of such a strategy, including power reversal, is presented here. The control algorithm of the stations follows the following logic

- Both station receive the same direct-voltage reference v_{dc}^* but each of them receives an individual power reference P_g^* .
- A station is initially set to direct-voltage control mode.
- If a station is provided with a negative power reference (power being injected to the ac side of the VSC), the station is set to active-power control mode. A command for a positive power reference (power being injected to the dc side of the VSC) will not be followed.
- If a station receives a positive or zero power reference and used to be in active-power control mode, it will remain in this mode until its measured transferred power drops to zero. After this event, it will switch to direct-voltage control mode.

The last step is set so that a potential swapping of the control duties between the stations occurs only when there is zero actual power flow on the lines, and not only when the power reference crosses zero. This will prevent sudden power reactions from stations whose control duties change abruptly. The simulation scenario follows the next steps

1. Both stations start with $v_{dc}^* = 640$ kV and $P_{g,1}^* = P_{g,2}^* = 0$ MW (zero power transfer).
2. Between $t=1$ s and $t=1.5$ s, $P_{g,1}^*$ is linearly decreased to -800 MW and remains constant until $t=4$ s. It is then linearly increased, reaching 0 MW at $t=4.5$ s.
3. Between $t=6$ s and $t=6.5$ s, $P_{g,2}^*$ is linearly decreased to -800 MW and remains constant until $t=8$ s. It is then linearly increased, reaching 0 MW at $t=8.5$ s.

The VSC-HVDC model has the same structure as in Fig. 2.1, having a transmission link comprised of 100 km cable-type of lines, with physical characteristics provided in Table 2.1. The ac grids to which the VSC stations are connected, are considered infinitely strong and are therefore represented by 400 kV voltage sources. The characteristics of the VSC stations are provided in Table 2.2. Regarding the ac-side filtering, the model uses a notch filter centered at the switching frequency f_s (since the PWM voltage waveform inherits most of its high-frequency components from the carrier wave that oscillates at f_s and forces the converter to switch at roughly the same frequency), in parallel with a capacitor.

TABLE 2.2. RATED VALUES OF THE VSC-HVDC STATIONS

P_N	VSC rated power	1000 MW
$U_{dc,N}$	rated direct voltage	640 kV
$U_{s,N}$	rated voltage at transformer's ac-grid side	400 kV
$U_{g,N}$	rated voltage at transformer's converter side	320 kV
S_N	ac side rated power	1000 MVA
X_l	transformer leakage inductance	0.05 pu
L_f	phase reactor inductance	50.0 mH (0.153 pu)
R_f	phase reactor resistance	1.57 Ω (0.1 $\times X_f$)
C_{dc}	dc-side capacitor	20 μ F
a_d	bandwidth of the closed-loop direct-voltage control	300 rad/s (0.96 pu)
a_f	bandwidth of the power-feedforward filter	300 rad/s (0.96 pu)
a_{cc}	bandwidth of the closed-loop current control	3000 rad/s (9.6 pu)
f_s	switching frequency	1500 Hz
f_{notch}	notch-filter frequency	1500 Hz
C_{filter}	ac-side filter capacitor	5 μ F

The simulation results are presented in Fig. 2.24. As it can be seen, initially both stations are in direct-voltage control mode and maintain the dc grid voltage at the reference value. Once Station 1 receives negative power reference $P_{g,1}^*$, it switches to active-power control mode and follows it while Station 2 is still in direct-voltage control mode, maintaining the voltage at its terminals at 640 kV. When $P_{g,1}^*$ ascends to zero, Station 1 remains in active-power control mode and when the actual power $P_{g,1}$ reaches zero, it will safely return to direct-voltage control mode. After $t=6$ s, the previously direct-voltage controlled Station 2 receives a negative power reference $P_{g,2}^*$ and becomes active power controlled, until $P_{g,2}^*$ drops to zero and the actual power $P_{g,2}$ is zero. In the same time, Station 1 remained in direct voltage control mode.

2.6 Summary

This chapter served as an introduction to the concept of the VSC technology and focused on its application to HVDC transmission systems. The main parts of a VSC-HVDC station were presented, followed by the explanation of the VSC operating principles that provide this type of converter with unique power transfer handling capabilities. A range of interlinked controllers that perform the operation of a typical VSC station were presented, within the general context of vector control. Added details were provided on the derivation and tuning of the current controller and the direct-voltage controller. Finally, the operational strategy of a two-terminal VSC-HVDC system was presented and demonstrated through a simple simulation result.

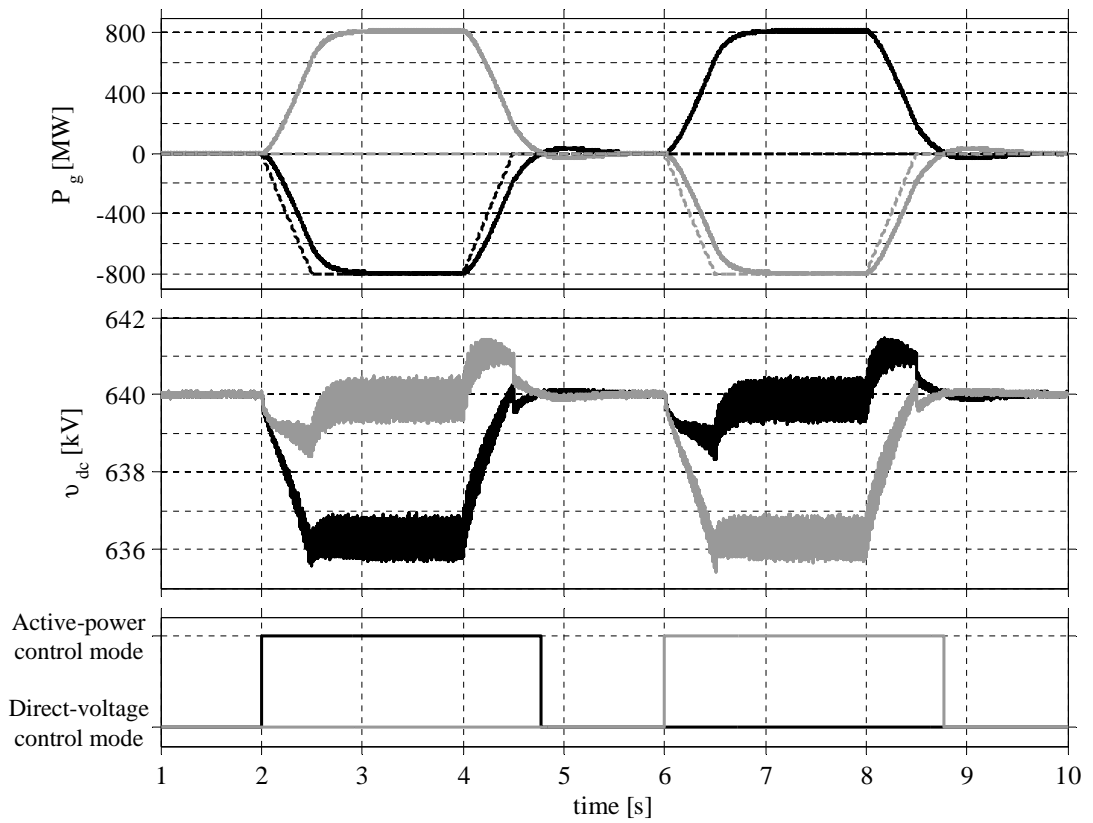


Fig. 2.24 Power reversal in a two-terminal VSC-HVDC system. The properties of Station 1 and Station 2 are indicated by black and gray color, respectively. Power references are indicated by dashed lines.

Chapter 2. VSC-HVDC operation and control

Chapter 3

Poorly-damped oscillations in systems

One of the problems that can generally be observed in dynamic systems is the potential occurrence of poorly-damped oscillations following disturbances. This is of great concern for HVDC applications, where the ratings and complexity level demand strict avoidance of such events. The introduction of VSC technology has undoubtedly offered great controllability to the applications used, but has also influenced their dynamic performance and therefore their ability to damp potentially hazardous oscillations.

The intention of this chapter is to develop a background on poorly-damped oscillations that may occur in systems and in particular those encompassing VSC-HVDC. A general description of damping in systems is provided, followed by the influence of the VSC and constant power loads in the system. This is followed by examples, description and possible ways to mitigate poorly-damped oscillations in the areas of traction, drives, LCC-HVDC and VSC-HVDC. Finally, simulations scenarios illustrate the occurrence of poor damping and instability in a two-terminal VSC-HVDC system.

3.1 Damping of systems

Most systems in nature can be well-represented by a 2nd order system, generically described as

$$G(s) = \frac{n(s)}{s^2 + 2\zeta\omega_n s + \omega_n^2} \quad (3.1)$$

where $n(s)$ is a polynomial of a maximum order of two. In this case, the characteristic polynomial of the system is $p(s) = s^2 + 2\zeta\omega_n s + \omega_n^2$, where ω_n is the *natural frequency* and ζ is the *damping factor*. The natural frequency ω_n determines the speed of the response while the damping factor ζ determines the degree of overshoot in a step response, as well as the maximum amplification from input to output. If

- $\zeta > 1$ the characteristic polynomial factorizes into two real poles
- $\zeta = 1$ gives two equal real poles (critical damping)

Chapter 3. Poorly-damped oscillations in systems

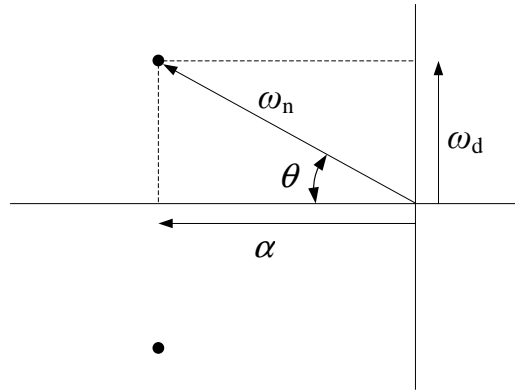


Fig. 3.1 Complex conjugate pole pair of a 2nd order system.

- $0 < \zeta < 1$ gives a pair of complex conjugate poles (damped oscillations)
- $\zeta = 0$ gives a pair of complex conjugate poles on the imaginary axis of the s -plane (pure oscillations without damping)
- $\zeta < 0$ response unstable

A pair of complex conjugate pole pair is plotted in the s -plane as in Fig. 3.1.

The poles can be written in Cartesian form as $\alpha \pm j\omega_d$ or in polar form $\omega_n \angle \theta$, where ω_d is the *damped natural frequency*. The following relationships hold

$$\zeta = \cos \theta \quad (3.2)$$

$$a = \omega_n \cos \theta = \omega_n \zeta \quad (3.3)$$

$$\omega_d = \omega_n \sin \theta = \omega_n \sqrt{1 - \zeta^2} \quad (3.4)$$

In a strict sense, poles having ζ less than 0.707 (or $\theta > 45^\circ$) are considered to have a response which is too oscillatory and are characterized as *poorly-damped* poles. Conversely, values of ζ greater than 0.707 (or $\theta < 45^\circ$) indicate a behavior with sufficient damping of any oscillatory components and the corresponding poles are addressed to as *well-damped* poles. The damping factor ζ is also regarded as the *damping* of the system.

In a multi-pole system, any complex conjugate pole pairs can be defined by the expressions (3.2)-(3.4), with the poles being characterized by their individual damping factor. However, the definition of a universal damping in a multi-pole system cannot be given since all the poles contribute in a non-straightforward manner to the final response. Nevertheless, poorly-damped complex conjugate poles are not desirable in a multi-pole system and could be responsible for poorly-damped oscillations. If their damping becomes very small, approaching zero, the concerned pole pair could become the closest to the imaginary axis among all the poles of the system; thus becoming *dominant* poles and their poorly-damped behavior then dominating the complete system response.

3.2 DC-side oscillations in industrial systems

The introduction of power electronic converters in power systems has offered a breakthrough in the controllability and stability impact of systems. In turn, this has led to an increased possibility of interactions between the system components. Consequently, potential resonances might appear that, if become poorly damped, can degrade the effective damping of the system and increase the risk of instability. Areas where related problems may or have already appeared are presented in this section.

3.2.1 Effect of Constant Power Loads

The concept of a Constant Power Load (CPL) in power electronic applications, considers a drive system that is controlled in such a way that it exchanges a constant amount of power with a system e.g. a motor or a grid. This can be viewed in Fig. 3.2(a) where an inverter is fed from a dc source through a filtering stage. R_f and L_f also include possible line impedances. The converter is in turn providing power P_L to a load, which is in this case set constant.

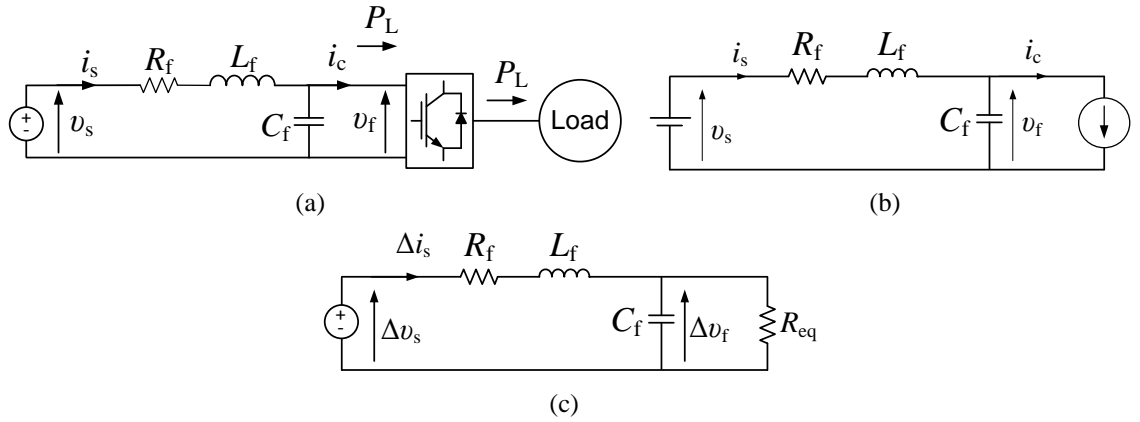


Fig. 3.2 CPL load and modeling. (a) Full-model description, (b) Equivalent current-source model, (c) Linearized model.

If the losses in the converter are disregarded, the load power can be assumed equal to the dc-link power as

$$P_L = v_f i_c \quad (3.5)$$

and the whole drive can then be modeled as a simple controlled current-source $i_c = P_L/v_f$. The equivalent circuit can be seen in Fig. 3.2(b). The behavior of this system can then be analyzed with the hypothesis of a small variation around the nominal operating point. Linearizing the capacitor dynamics around the operating point of load power P_L and capacitor voltage $v_{f,0}$ gives

$$C_f \frac{dv_f}{dt} = i_s - i_c \Rightarrow$$

$$C_f \frac{d\Delta v_f}{dt} = \Delta i_s - \Delta i_c \Rightarrow C_f \frac{d\Delta v_f}{dt} = \Delta i_s - \Delta \left(\frac{P_L}{v_f} \right) \Rightarrow$$

Chapter 3. Poorly-damped oscillations in systems

$$C_f \frac{d\Delta v_f}{dt} = \Delta i_s + \frac{P_L}{v_{f,0}^2} \Delta v_f \quad (3.6)$$

The fact that $\Delta i_c = -\frac{P_L}{v_{f,0}^2} \Delta v_f$ dictates that the small signal impedance of the converter is

$$Z_{inv} = \frac{\Delta v_s}{\Delta i_c} = -\frac{v_{f,0}^2}{P_L} = R_{eq} < 0 \quad (3.7)$$

implying that for small variations around the steady-state nominal point, the drive acts as a negative resistance R_{eq} , when power is provided to the load. Taking into account the linearized line dynamics

$$L_f \frac{di_s}{dt} = v_s - v_f - i_s R_f \Rightarrow L_f \frac{d\Delta i_s}{dt} = \Delta v_s - \Delta v_f - R_f \Delta i_s \quad (3.8)$$

the linearized model of the complete system can be seen in Fig. 3.2(c), with the presence of the negative resistance R_{eq} . The state-space model of the system becomes

$$\frac{d}{dt} \begin{bmatrix} \Delta i_s \\ \Delta v_f \end{bmatrix} = \begin{bmatrix} -\frac{R_f}{L_f} & -\frac{1}{L_f} \\ \frac{1}{C_f} & \frac{P_L}{v_{f,0}^2 C_f} \end{bmatrix} \begin{bmatrix} \Delta i_s \\ \Delta v_f \end{bmatrix} + \begin{bmatrix} \frac{1}{L_f} \\ 0 \end{bmatrix} \Delta v_s \quad (3.9)$$

From the Routh theorem, the stability conditions of (3.9) are

$$\frac{v_{f,0}^2}{P_L} > R_f \quad (3.10)$$

$$\frac{R_f}{L_f} > \frac{P_L}{v_{f,0}^2 C_f} \quad (3.11)$$

Usually, condition (3.10) is satisfied but the same does not always apply in (3.11). Additionally, in many common applications, the parameters of the system are such that the two eigenvalues of (3.9) are a pair of complex-conjugate poles with a real part of

$$\text{Re}[p] = -\frac{R_f}{2L_f} + \frac{P_L}{2v_{f,0}^2 C_f} \quad (3.12)$$

It is evident that for fixed passive components, an increased steady-state power transfer P_L , brings the complex poles closer to the imaginary axis and decreases their damping, with a possibility of crossing to the Right-Hand s-Plane (RHP) and becoming unstable. Consequently, the use of converters in a system that operate as CPL causes stability concerns and are mainly responsible for poorly-damped oscillations.

3.2.2 Traction and industrial systems

A typical and well-documented field where dc-side resonances and poorly-damped conditions are recorded, is electrified traction. The most common example are electrical locomotives as

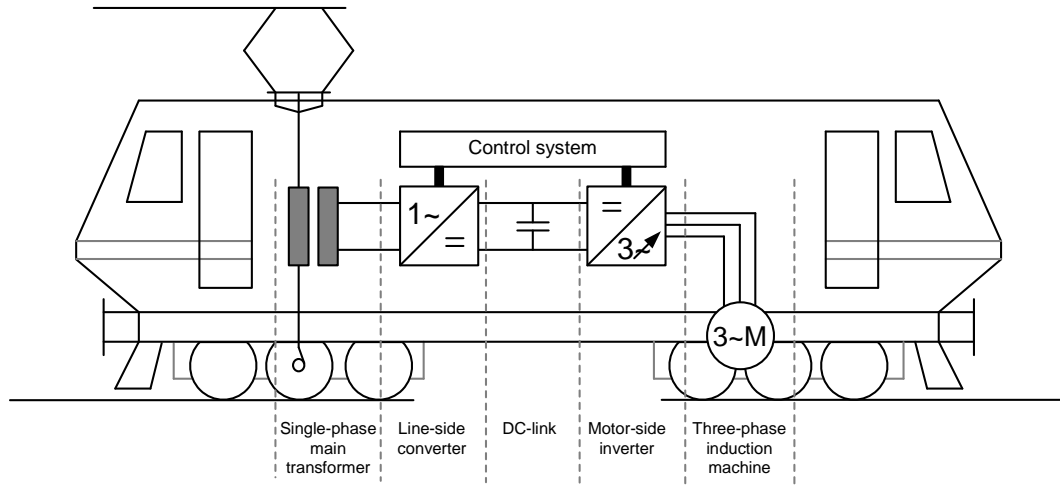


Fig. 3.3 Rail vehicle with its main electrical components

the one presented in Fig. 3.3, which shows a motorized wagon fed with alternating voltage. On-board the wagon there is a single-phase transformer connected to a rectifier (which can be active or non-controlled) that charges the dc-link. A motor-side inverter is providing the necessary power to an ac-machine, which serves as the prime mover of the wagon. The single-phase alternating voltage provided to the wagon is typically a 15 kV, 16 2/3 Hz supply (in the Swedish, Norwegian, German, Austrian and Swiss systems) and is created by rotary synchronous- synchronous frequency converters, as well as static converters. The former are discrete motor-generator sets, consisting of one single-phase 16 2/3 Hz synchronous generator that is driven directly by a three-phase 50 Hz, which in turn is fed from the three-phase public distribution medium voltage supply. Danielsen in [4], investigates the properties of such systems in the Norwegian and Swedish railway. It was found that for the investigated system, a low-frequency (1.6 Hz) poorly-damped mode can be excited when a low-frequency eigenmode of the mechanical dynamics of the rotary converter is close to the low bandwidth of the direct-voltage control loop used in the wagon's active rectifier. This led to a poorly-damped resonance on the dc-link voltage.

It is however often that direct voltage is provided directly in traction. In this case, the internal electrifying system of the wagons is as in Fig. 3.4. Two types of resonances can be excited in such systems, as documented in [5]. Figure 3.4(a) shows that the RLC circuit created by the dc-filter of the inverter and the impedance of the transmission lines between the wagon and the remote substation, may create a resonance at a critical frequency. Another problem may occur on the wagon itself, if it is using multiple inverters to power multiple wheels. As shown in Fig. 3.4(b), the filters of different converters are fed from the same dc-link, causing closed resonant circuits to appear.

A common way in which such resonances are treated in traction is by using active-damping control [5, 56]. Figure 3.5 shows an inverter, connected to a direct voltage source v_s via an RLC filter, feeding a 3-phase motor. The converter is assumed to provide constant power P_{out} to the ac-motor. As shown in Section (3.2.1), this system has two complex-conjugate poles which

Chapter 3. Poorly-damped oscillations in systems

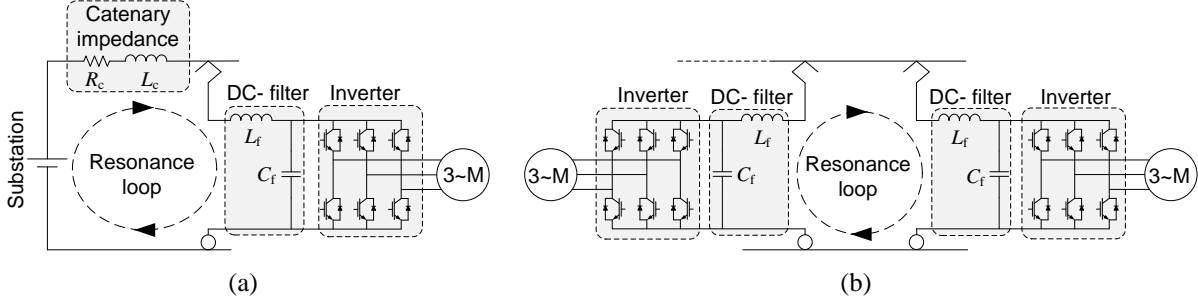


Fig. 3.4 System of traction drives considering resonance of input filter. (a) Resonance between substation and traction drive (b) Resonance between multiple traction drives located on the same cart.

can be poorly damped. The idea of active damping implies that when a resonating imbalance is measured on capacitor C_f , an alternating current i_{damp} of the same frequency and with a selected phase is injected to the capacitor, reducing the fluctuations of its charge. The active-damping control involves the filtering of v_s through a low-pass filter $F(s) = a_f/(s + a_f)$, with bandwidth a_f , producing the signal v_{cf} . The constant K , transforms the dc-side i_{damp} into a dq -frame quantity. According to the arrangement of Fig. 3.5, the system can be described by the circuit in Fig. 3.6(a), where the converter is replaced by a current source. The dynamics at the dc-capacitor are

$$C_{dc} \frac{dv_f}{dt} = i_s - i_c \Rightarrow C_{dc} \frac{dv_f}{dt} = i_s - \left(\frac{P_{out}}{v_f} + i_{damp} \right) \Rightarrow C_{dc} \frac{dv_f}{dt} = i_s - \frac{P_{out}}{v_f} - \frac{v_f - v_{cf}}{R_{damp}} \Rightarrow$$

$$\frac{d\Delta v_f}{dt} = \frac{1}{C_{dc}} \Delta i_s + \frac{P_{out}}{C_{dc} v_{f,0}^2} \Delta v_f - \frac{1}{C_{dc} R_{damp}} \Delta v_f + \frac{1}{C_{dc} R_{damp}} \Delta v_{cf} \quad (3.13)$$

The dynamics on the filter are

$$L_{dc} \frac{di_s}{dt} = v_s + v_f - i_s R_{dc} \Rightarrow \frac{d\Delta i_s}{dt} = \frac{1}{L_{dc}} \Delta v_s + \frac{1}{L_{dc}} \Delta v_f - \frac{R_{dc}}{L_{dc}} \Delta i_s \quad (3.14)$$

and on the filter

$$\frac{dv_{cf}}{dt} = a_f (v_f - v_{cf}) \Rightarrow \frac{d\Delta v_{cf}}{dt} = a_f \Delta v_f - a_f \Delta v_{cf} \quad (3.15)$$

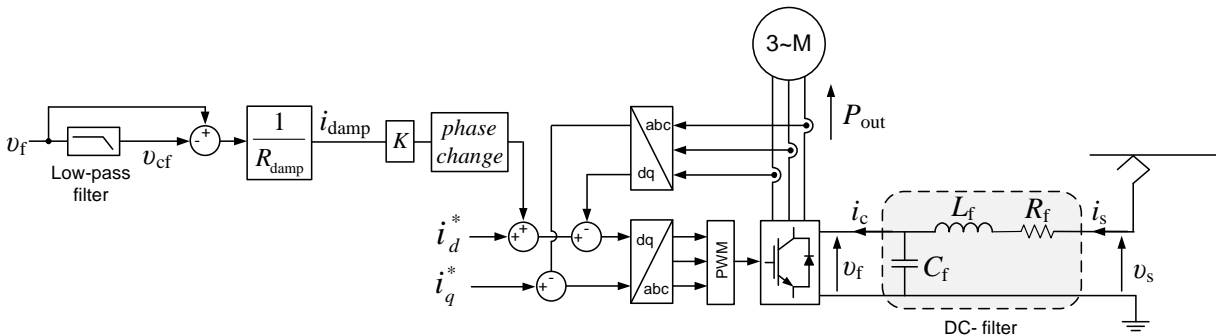


Fig. 3.5 Active damping controller

3.2. DC-side oscillations in industrial systems

The state space representation of this system is

$$\frac{d}{dt} \begin{bmatrix} \Delta i_s \\ \Delta v_f \\ \Delta v_{cf} \end{bmatrix} = \begin{bmatrix} -\frac{R_{dc}}{L_{dc}} & \frac{1}{L_{dc}} & \frac{1}{L_{dc}} \\ \frac{1}{C_{dc}} & \frac{P_{out}}{C_{dc}v_{f,0}^2} - \frac{1}{C_{dc}R_{damp}} & \frac{1}{C_{dc}R_{damp}} \\ 0 & a_f & -a_f \end{bmatrix} \begin{bmatrix} \Delta i_s \\ \Delta v_f \\ \Delta v_{cf} \end{bmatrix} + \begin{bmatrix} \frac{1}{L_{dc}} \\ 0 \\ 0 \end{bmatrix} \Delta v_s \quad (3.16)$$

The visualization of (3.13) and (3.14) as an electrical circuit can be seen in Fig. 3.6(b), where R_{eq} is the negative resistance due to constant load $-P_{out}/v_{f,0}^2$. As it can be seen, the active-damping control has added a virtual resistance of value R_{damp} in the circuit, which if chosen large enough can not only cancel the negative resistance R_{eq} , but also provide a sufficiently positive resistance to the system, damping currents that may be caused by a fluctuating Δv_s and without adding actual losses. In this way, Δv_f can be minimized, meaning that the voltage of v_f of the dc-link of the converter can be almost immune to fluctuations of the feeding voltage v_s . In terms of eigenvalues, the state matrix in (3.16) has a real pole in the far left of the Left-Hand s-Plane (LHP) and two complex conjugate poles. These have almost the same frequency as the poles of the system without active-damping, but their real part has become much more negative, implying that their damping has increased.

This type of active damping control is used extensively to damp dc-side resonances and poorly-damped poles not only in traction, but in any application with controlled VSC converters connected to a dc-link. A relevant damping control method for suppression of resonances in DC power networks is presented in [57], while a more elaborate non-linear control strategy to mitigate negative-impedance instability issues in direct-voltage fed induction machines is investigated in [6]. A virtual-resistance based method is presented in [7] where the rectifier-inverter drives equipped with small (film) dc-link capacitors may need active stabilization. The impact of limited bandwidth and switching frequency in the inverter-motor current control loop is considered as well. A different concept of introducing a virtual capacitor parallel to the actual dc-capacitor of the inverter is introduced in [58], causing a similar effect as the virtual resistance-based active damping.

The use of active filtering is another well-known method with large applicability. Tanaka et. al in [25] consider large-capacity rectifier-inverter systems, such as in rapid-transit railways, with single or multiple inverters connected to a single rectifier through dc-transmission lines. The active method proposed is shown in Fig. 3.7, where a small-rated voltage source single-phase PWM converter is connected in series to the dc-capacitor C_{dc1} through a matching transformer. This acts as a damping to the dc-capacitor current i_{c1} . Within this context, a variation of the

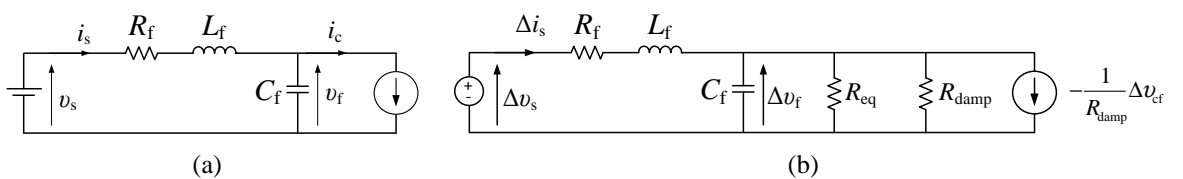


Fig. 3.6 (a) Current-source equivalent circuit of the inverter and filter system (b) Linearized model of the system with the active-damping control.

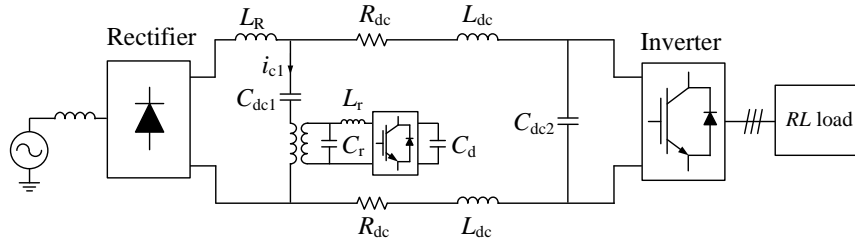


Fig. 3.7 Active filtering in Rectifier-Inverter systems

depicted active filter is presented in the same publication with the PWM converter using the power of the capacitor C_{dc1} to operate in a regenerative manner.

3.2.3 LCC-HVDC

The origin and nature of the dc-side resonances in LCC-HVDC installations varies greatly compared to the dc-side resonances of VSC-HVDC systems or generally DC networks with VSC converters. The ac- and dc-side of a thyristor converter are not decoupled as in a VSC, due to the non-linear switching action of the thyristor converter that causes a frequency transformation of voltages and currents between the two sides. This frequency transformation is important when analyzing dc-resonances for two reasons [10]. Firstly, excitation sources of a certain frequency on the ac-side drive oscillations on the dc-side at different frequency. Secondly, the impedances involved are at different frequencies at the ac- and dc-side. The thyristor converter acts as a modulator of dc-side oscillations when transforming them to the ac-side. If the carrier frequency f_c is the fundamental frequency of the commutating voltage and the modulation frequency f_m is that of the dc-side oscillation, then new side-band frequencies at $f_c \pm f_m$ are generated in the ac-phase currents. Ac-side voltages that excite dc-oscillations can be attributed to system disturbances or by harmonic sources in the ac-network. Examples are

1. initial transformer energization with an inrush of magnetization inrush current;
2. transformer saturation;
3. single-line to ground faults near the converter resulting in unbalanced phase voltages which generate second order dc-side harmonics;
4. persistent commutation failures generate fundamental frequency dc-oscillations.

On the dc-side, the harmonic voltages superimposed on the direct voltage produce harmonic currents that enter the dc line. The amplitude of these depends on the inductance of the normally large smoothing reactor and the impedance of dc-filters. These harmonic currents may, for instance, induce interference in telephone lines, in close proximity to the dc lines. This has been a major concern in LCC-HVDC installations, with strict specifications from the network operators on mitigating actions. As a results, an increased presence of dc-side filters is required, whose only function is to reduce harmonic currents.

Traditional passive dc-side filters have been the norm for years, but their increasing size and cost has led to the consideration of active filtering. An early mentioning of the concept in LCC is being made in [11], where active filtering similar to the one in Fig. 3.7 is described. Possible locations of implementation within the dc-circuit are discussed and a proof of concept is demonstrated with the actual installation in the Konti-Skan dc-link at the Lindome converter Station, Sweden. More information on actual concepts and applications is presented in [12] where the interaction between multiple active filters of a dc-link is discussed, stating that long transmission lines weaken the coupling between the active filters so that interactions among them do not disturb the harmonic control. Aspects in the specification and design of dc-side filtering (both passive and active) in multiterminal LCC-HVDC, are presented in [13] suggesting that active filters are ideal. Changes in the dc-grid topology can alter the position of dc-resonances and an adaptive control of the active filters can keep tracking them.

3.2.4 VSC-HVDC

The problem of dc-side resonances can also appear in VSC-HVDC links. A typical two-terminal VSC-HVDC system is depicted in Fig. 3.8 where each of the transmission poles has been replaced with its equivalent Π -section, as seen earlier in Chapter 2. A first observation is that the dc-link is effectively a closed RLC resonant-circuit. If the converter capacitors are considered equal, $C_{dc1} = C_{dc2} = C_{conv}$, the resonant frequency of the circuit will be

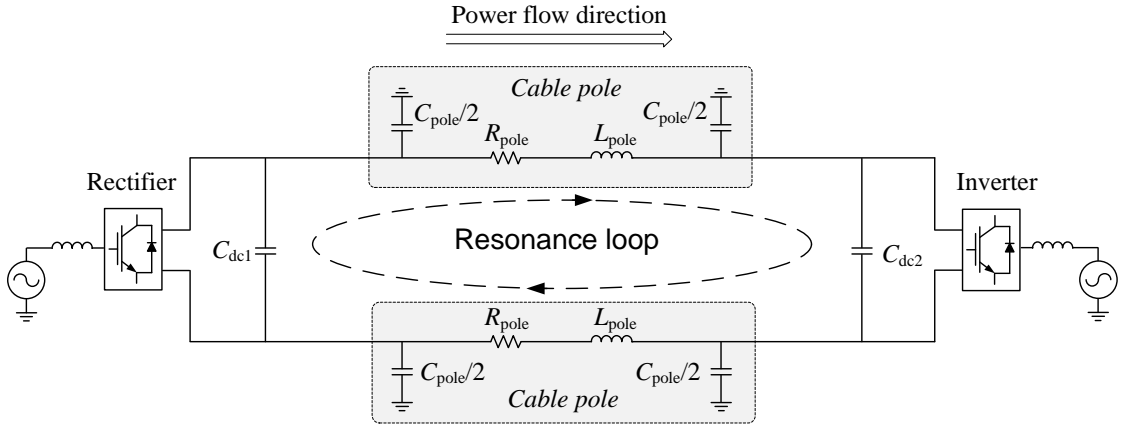


Fig. 3.8 DC-link resonance loop in a two-terminal VSC-HVDC connection

$$\omega_{\text{res}} = \frac{1}{\sqrt{L_{\text{pole}} \left(C_{\text{conv}} + \frac{C_{\text{pole}}}{4} \right)}} \quad (3.17)$$

When power is imported from the rectifier-side and exported from the inverter-side, the transmission link is naturally unstable as will be investigated later in Sections (5.3) and (6.3). The rectifier station is operating in direct-voltage control mode with a certain controller speed, stabilizing the transmission link and bringing a power balance. The interaction between the dynamics

of the direct-voltage controller and the dc-link, lead to a closed-loop system whose properties are not always predictable. It can be shown in Section (3.3) that the system may have poorly-damped poles (most often those associated with the resonant frequency of the dc-link) or even become unstable. The contribution of the CPL small signal deterioration of the systems stability characteristics should also be taken into account.

In [15], the authors investigate the transient stability of a dc grid comprising of clusters of off-shore wind-turbine converters connected through HVDC-cables to a large onshore VSC inverter. Using the traveling wave theory on long cables, it was demonstrated that choosing equal lengths for the cluster cables was a worst case scenario in terms of grid stability. A two-terminal VSC-HVDC connection between two weak ac grids is presented in [14] using Power-Synchronization control on the converters, where it was also claimed that the resistance of the dc-link plays a destabilizing role. A poorly-damped resonance was demonstrated to exist and a notch filter was used in the control strategy to reduce the dc resonant peak. Investigation of the dynamic stability has also been performed in multiterminal VSC-HVDC connections as in [16], where the impact of the droop setting k_{droop} in the direct-voltage controller of the stations was assessed. It was found that high values of k_{droop} could turn a point-to-point droop controlled connection unstable.

3.3 Example of dc-side oscillations in two-terminal VSC-HVDC

Instances of poorly-damped behavior and instability are demonstrated in this section, with a two-terminal VSC-HVDC system being considered the object under testing. The objective is to highlight the effect of the system's properties and operating points on its stability. The model of the system is exactly the same as in Section (2.5) and visualized in Fig. 2.1, with full switching VSC stations, ac filters and transformers. The characteristics of the VSC stations are provided in Table 2.2. The only difference is the use of overhead lines in the dc-transmission link instead of cables. As explained in Section (2.2.5), overhead lines normally have much higher inductance per km (almost an order of magnitude greater) than cables of the same voltage and power rating. A higher inductance in the dc-transmission link tends to decrease the damping of the system, as will be seen in the analysis that will follow in the next chapters. The overhead line used in this section have physical properties provided in Table 2.1.

3.3.1 Poorly-damped conditions

Two cases are considered to highlight potentially poorly-damped phenomena

- **Case 1:** The active-power controlled station imposes a steady-state power transfer of $P_{\text{out}} = 0$ MW. At $t = 1$ s, the voltage reference to the direct-voltage controller is increased from 640 kV to 645 kV. At $t = 1.5$ s, the voltage reference is set back at 640 kV.
- **Case 2:** The active-power controlled station imposes a steady-state power transfer of $P_{\text{out}} = -900$ MW. Identically to **Case 1**, the voltage reference to the direct-voltage con-

3.3. Example of dc-side oscillations in two-terminal VSC-HVDC

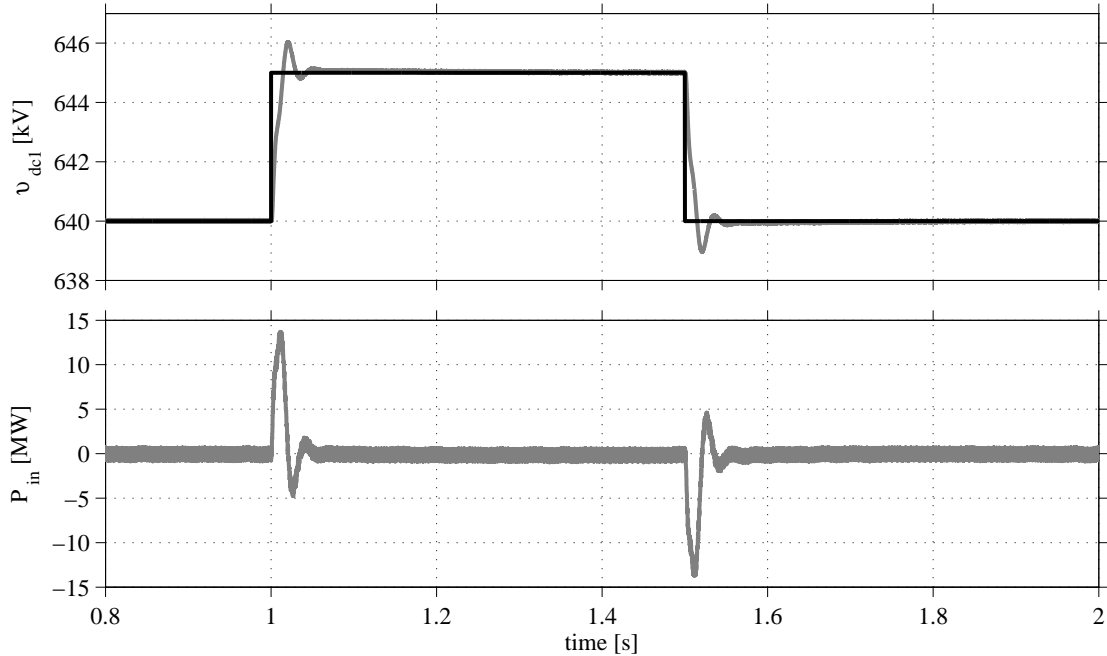


Fig. 3.9 Power and voltage response of the system in **Case 1**. Upper figure: v_{dc1} (gray line) and v_{dc}^* (black line). Lower figure: P_{in} .

troller is increased from 640 kV to 645 kV at $t = 1$ s and then set back to 640 kV at $t = 1.5$ s.

The length of the overhead-transmission line is 200 km. For both of the examined cases, the voltage v_{dc1} at the dc-terminal of the direct-voltage controlled station and the input power P_{in} of the same station are plotted.

Figure 3.9 shows the results for the **Case 1** scenario. The response of v_{dc1} to the new reference v_{dc}^* seems to be sufficiently damped with only a small overshoot. This behavior is equally reflected on the response of P_{in} . Both responses show that the excited oscillations are practically fully damped 70 ms after the step request in v_{dc}^* . Regarding the same system but under the conditions of **Case 2**, the response of the same entities are presented in Fig. 3.10. The simulation shows that the response of v_{dc1} has a higher overshoot, compared to Fig. 3.9, and features a poorly-damped oscillation. Likewise, the response of P_{in} is dynamically similar to v_{dc1} . It presents a slightly higher overshoot than its counterpart in Fig. 3.9 (considering the absolute power deviation) and suffers from a poorly-damped oscillatory component of the same frequency as in v_{dc1} .

This example demonstrated that operating the system under different steady-state conditions (power transfer in this case), an identical excitation may cause significantly different dynamic response, without changing any physical or controller parameter in the process.

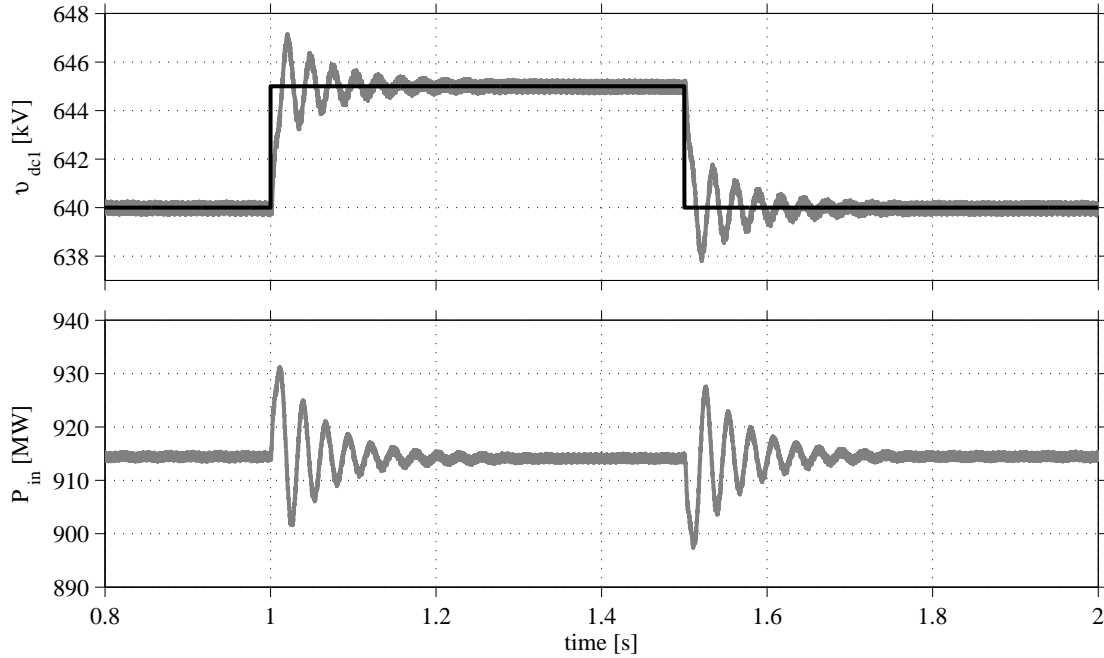


Fig. 3.10 Power and voltage response of the system in **Case 2**. Upper figure: v_{dc1} (gray line) and v_{dc}^* (black line). Lower figure: P_{in} .

3.3.2 Unstable conditions

The length of the dc-transmission link in the previous system is increased to 300 km and a specific pattern of active-power reference is provided to the active-power controlled station, while the direct-current controller receives a constant reference $v_{dc}^* = 640$ kV. The sequence of events is as follows

1. $P_{out}^* = 0$ MW until $t = 5$ s.
2. P_{out}^* is linearly ramped from 0 to -500 MW until $t = 5.5$ s.
3. P_{out}^* remains unchanged until $t = 6.5$ s.
4. P_{out}^* is linearly ramped from -500 to -900 MW until $t = 7$ s and then remains constant until $t = 8.5$ s.
5. P_{out}^* is linearly ramped from -900 to -500 MW until $t = 9$ s and then remains constant until then end of the simulation.

The response of the system can be observed in Fig. 3.11. In the first 7 seconds of the simulation, the system manages to follow the active-power reference without any problems, with the direct-voltage controller performing seamlessly at all instances. However after $t = 7$ s and when the power reaches approximately 900 MW, the system experiences an oscillation of 199.4 Hz which constantly increases in magnitude as evidently observed in the P_{in} and v_{dc1} responses. This

3.3. Example of dc-side oscillations in two-terminal VSC-HVDC

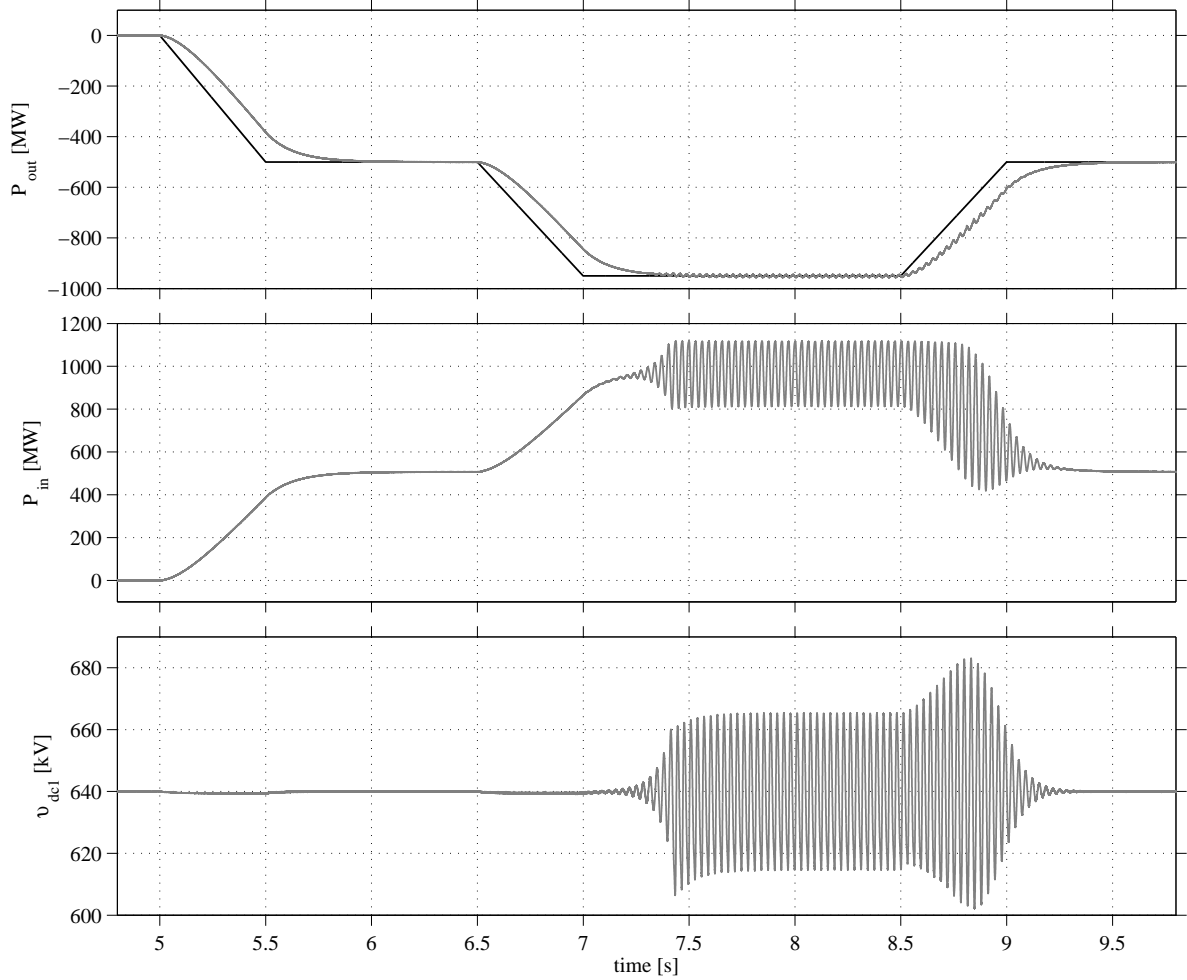


Fig. 3.11 Power and voltage response of the system in instability conditions. Upper figure: P_{out}^* (black line) and P_{out} (gray line). Middle figure: P_{in} . Lower figure: v_{dc1}

oscillation quickly becomes unstable but the system integrity is sustained due to the existence of limiters in the control structures, limiting the input i_d^* at the current controllers of both VSC stations to 1.1 pu in the examined scenario. As such, P_{in} never exceeds 1100 MW in magnitude and the theoretically unstable oscillation is now contained in a bounded region. It should be noted that even during this event, the active power controller manages to impose the request P_{out}^* on its ac side. Only small signs of the oscillation can be traced on P_{out} . This is attributed to the fact that the corrected modulation wave of the PWM process is calculated and applied only at the switching events. For a higher switching frequency, the oscillation is much smaller until it disappears completely for non-switching converter models.

Once P_{out}^* is ramped to -500 MW, the system gradually goes out of instability and becomes stable and fully operational again after $t=9.4$ s. This demonstrates how the level of power transfer had a fundamental impact on the dynamic stability of the system. The instability exhibited in the example of this section will be further investigated in the following chapter.

3.4 Summary

In this chapter, an effort was made to establish a background on poor damping in dynamic systems, focusing mostly on VSC-HVDC applications. Initially it was identified that even though it is not possible to specify the term of damping in a high-order system, it is acceptable to closely identify it with the damping factor of its dominant poles, which mainly characterize the dynamic response of the system. Following this, it was shown how constant-power loads, fed by VSCs, can decrease the damping factor of complex poles of the system they are part of, leading to the potential appearance of poorly-damped oscillations. This is a commonly experienced phenomenon in traction, where electrical machines are operated to supply constant traction power. Existing control methods can improve the damping characteristics of such systems by means of active damping.

Oscillation phenomena were later identified in LCC-HVDC transmission links. There, the increased harmonic content of the dc-side voltage is inevitably expanded to the ac side as well, as the LCC cannot decouple its two sides. Some of these harmonics may become poorly damped and the presence of large passive or active filters is necessary on both ac and dc sides of the converter station. Oscillations may also be experienced in VSC-HVDC systems and resonances, mostly associated with the characteristic frequency of the dc-transmission link, could appear under specific conditions, e.g. long transmission-line length. This was further investigated by simulating a two-terminal VSC-HVDC system, where a combination of long transmission lines and high power transfer gave rise to poorly-damped resonances and even instability.

The present chapter laid the foundations for the understanding of the analysis that will be performed in the next three chapters, where the poor-damping characteristics of two-terminal VSC-HVDC transmission systems are analyzed in the frequency domain and analytically.

Chapter 4

Stability in two-terminal VSC-HVDC systems: frequency-domain analysis

In this chapter, a two-terminal VSC-HVDC system is modeled in detail and its stability characteristics are examined from a frequency analysis perspective. The aim is to develop a methodology pattern, which can describe and possibly predict the occurrence of poorly-damped phenomena or instances of instability. For analysis purposes, the system is divided into two subsystems: one describing the dc-transmission link receiving power from the rectifier station and the other describing the dynamics of the VSC rectifier station which injects a controlled amount of power to the dc grid in an effort to stabilize the direct voltage. The two subsystems are initially examined from a *passivity* point of view with relevant comments being drawn for the overall stability using the Nyquist criterion. However, the conditions under which the passivity approach is applicable can be limited. A different frequency analysis tool is thus later applied, using the *net-damping* approach. Finally, an initially unstable system is stabilized by altering the control structure of the VSC rectifier and an explanation is provided, observing the impact of the system parameters to the overall net damping.

4.1 Stability analysis based on a frequency-domain approach

If a system can be represented by a closed-loop SISO feedback system, as in Fig. 4.1, its stability can be evaluated by examining the frequency response of the distinct transfer functions $F(s)$ and $G(s)$. Two main methods are considered in this chapter: the passivity approach and the net-damping stability criterion.

4.1.1 Passivity of closed-loop transfer function

A linear, continuous-time system described by a transfer function $R(s)$ is defined as *passive* if and only if, the following conditions apply at the same time [59]

1. $R(s)$ is stable

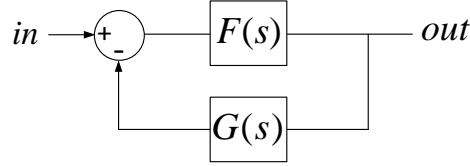


Fig. 4.1 SISO system with negative feedback.

$$2. \operatorname{Re}\{R(j\omega)\} \geq 0, \forall \omega \geq 0$$

From a complex-vector point of view, the latter is equivalent to the condition of $-\pi/2 \leq \arg\{R(j\omega)\} \leq \pi/2$, implying that the real part of the transfer function is non-negative. Additionally, if $R(s)$ is stable and $\operatorname{Re}\{R(j\omega)\} > 0, \forall \omega \geq 0$, the corresponding system is defined as *dissipative*. As an example, the typical second-order low-pass filter function

$$R(s) = \frac{\omega_n^2}{s^2 + 2\zeta\omega_n s + \omega_n^2} \quad (4.1)$$

represents a dissipative system for $\zeta > 0$, with a step response that contains either no oscillations ($\zeta \geq 1$), or a damped oscillation ($0 > \zeta > 1$). However, if $\zeta = 0$, the represented system is only passive with a step response that contains a sustained oscillation of constant magnitude and frequency ω_n , without ever being damped.

The passivity concept can be expanded to closed-loop systems, as the SISO in Fig. 4.1. If both the open-loop transfer function $F(s)$ and the feedback transfer function $G(s)$ are passive, then the closed-loop transfer function of the complete system

$$R_c(s) = \frac{F(s)}{1 + F(s)G(s)} \quad (4.2)$$

is stable and passive [60]. The opposite is however not true. If either $F(s)$, or $G(s)$, or both of them, are non-passive then $R_c(s)$ is not necessarily non-passive or unstable.

The previous statements are very important from a control point of view. If a controlled process can be represented by the SISO form of Fig. 4.1, the passivity characteristic of the subsystems $F(s)$ and $G(s)$ can either guarantee the stability of the closed loop, or provide a hint for instability and there is a need for further investigation using alternative tools, e.g. the Nyquist criterion, which can provide a definite answer.

4.1.2 Net-damping stability criterion

A useful tool in the frequency analysis of the stability of a system is the *Net-Damping* stability criterion. Its applicability can be investigated on SISO systems, identical to the one depicted in Fig. 4.1, where the frequency functions of the open-loop and feedback dynamics are expressed as

$$\frac{1}{F(j\omega)} = D_F(\omega) + jK_F(\omega) \quad (4.3)$$

4.1. Stability analysis based on a frequency-domain approach

and

$$G(j\omega) = D_G(\omega) + jK_G(\omega) \quad (4.4)$$

Canay in [21] and [22] used such a SISO representation in order to introduce the complex torque coefficients method for subsynchronous torsional interaction analysis of turbine-generator sets. In that case, $F(s)$ represented the turbine's mechanical dynamics and $G(s)$ the generator's electrical dynamics. Addressing $D_F(\omega)$ and $D_G(\omega)$ as damping coefficients and $K_F(\omega)$ and $K_G(\omega)$ as spring coefficients, the introduced method involves the evaluation of the net damping $D(\omega) = D_F(\omega) + D_G(\omega)$. If at each resonance of the closed-loop system applies

$$D(\omega) = D_F(\omega) + D_G(\omega) > 0 \quad (4.5)$$

then according to [21], there is no risk for detrimental torsional interaction. Several examples were provided as proof of the statement but no strict mathematical proof. The method was shown in [23] not to correctly predict closed-loop oscillatory modes and instabilities. However, a mathematical proof of the positive-net-damping criterion (4.5) was provided in [24], using the Nyquist criterion. There, in agreement with [23], it was clarified that the net damping should be evaluated for the open-loop (not closed-loop) resonances, as well as for low frequencies where the loop gain exceeds unity.

As part of the proof process in [24], the Nyquist criterion is applied to the transfer function $F(s)G(s)$ with

$$F(j\omega)G(j\omega) = \frac{D_F(\omega)D_G(\omega) + K_F(\omega)K_G(\omega)}{D_F^2(\omega) + K_F^2(\omega)} + j\frac{D_F(\omega)K_G(\omega) - D_G(\omega)K_F(\omega)}{D_F^2(\omega) + K_F^2(\omega)} \quad (4.6)$$

To determine whether the Nyquist curve encircles -1, the imaginary part of (4.6) is set to zero, yielding

$$F(j\omega_N)G(j\omega_N) = \frac{D_G(\omega_N)}{D_F(\omega_N)} \quad (4.7)$$

where ω_N is the frequency where the Nyquist curve intersects with the real axis. Usually, resonant frequencies are very close to events of intersections with the real axis and therefore constitute points where an encirclement of -1 could occur (thus instability of the closed loop) [24]. If (4.7) is larger than -1 then $D_F(\omega_N) + D_G(\omega_N) > 0$, giving (4.5) in the vicinity of a potential resonant frequency. However, this accounts only for $D_F(\omega_N) > 0$, as examined in the previous references. If $D_F(\omega_N) < 0$, relation (4.7) would give the following in order to avoid an instability

$$\begin{aligned} \frac{D_G(\omega_N)}{D_F(\omega_N)} > -1 \xrightarrow{D_F(\omega_N) < 0} D_G(\omega_N) < -D_F(\omega_N) \Rightarrow \\ D(\omega_N) = D_F(\omega_N) + D_G(\omega_N) < 0 \end{aligned} \quad (4.8)$$

showing that extra attention should be given when applying the net-damping criterion, taking into account the nature of $D_F(\omega)$ close to the resonant frequencies.

Compared to the passivity analysis, a benefit of analyzing the stability of a SISO system via the positive-net-damping criterion is that there is no need for each of the $F(s)$ and $G(s)$ to be passive or even stable. In fact it is not uncommon that one or both of the two transfer functions are

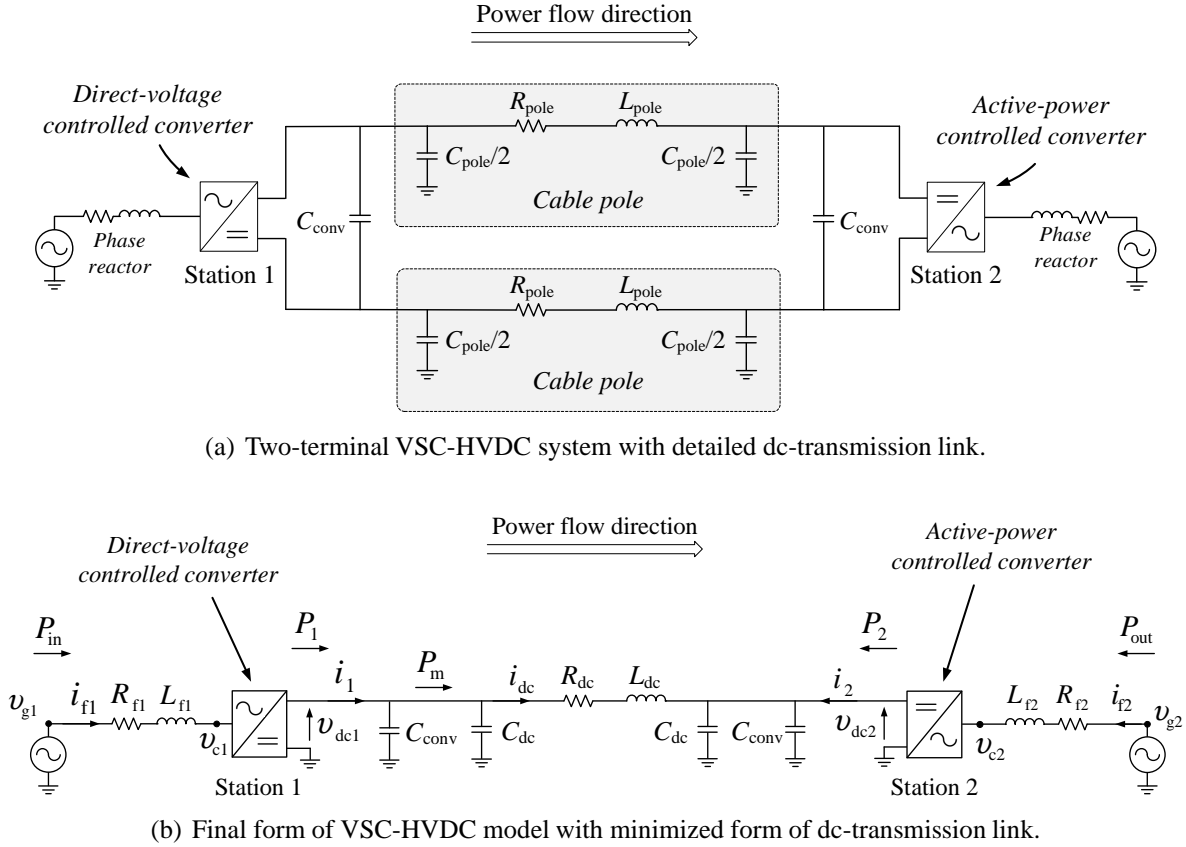


Fig. 4.2 Two-terminal VSC-HVDC model.

individually unstable, but closing the loop through the negative feedback stabilizes the system. In such cases, the passivity analysis cannot be used, unlike the positive-net-damping criterion which can still be applied.

4.2 System representation

The objective of this section is to derive a SISO representation of the two-terminal VSC-HVDC model, compatible to the depiction of Fig. 4.1. This will allow a further investigation of the system in terms of passivity and net damping. The model under consideration is shown in Fig. 4.2(a). The ac grids are assumed to be infinitely strong and are thus modeled as voltage sources, to which each VSC station is connected via a filter inductor (with inductance L_f and resistance R_f). The dc terminals of each station are connected to a dc capacitor with a capacitance C_{conv} . Each dc cable is modeled as a Π -model, in the way described in Section (2.2.5). Given the physical characteristics of the symmetrical monopole configuration and considering balanced conditions, the model in Fig. 4.2(a) can be equated to the asymmetrical monopole model in Fig. 4.2(b). This model retains the same power and voltage ratings as the one in Fig. 4.2(a) and has the same dynamics. It is however simplified in form, assisting the later description of the

4.2. System representation

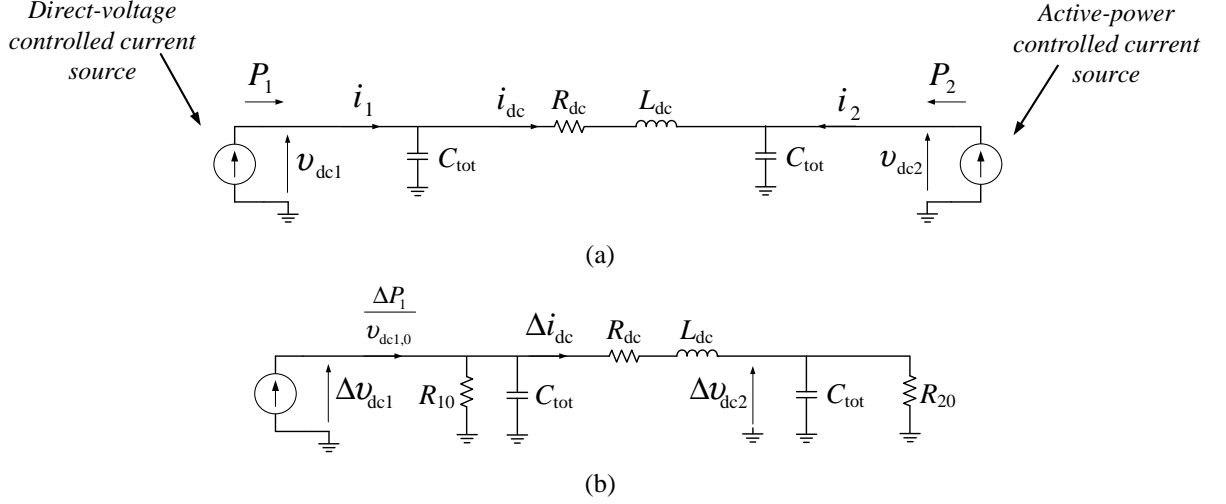


Fig. 4.3 DC-side consideration of the system: (a) detailed current-source equivalent model, (b) linearized model.

model through equations. The transmission link values are defined as

$$R_{dc} = 2 \cdot R_{pole}, \quad L_{dc} = 2 \cdot L_{pole}, \quad C_{dc} = C_{pole}/4 \quad (4.9)$$

This model will be used further on in this chapter. Choosing the correct type of input and output for the SISO representation of the system is not straightforward. It will be shown in the following section that the choice of the small signal deviation ΔW^* as input and ΔP_1 as output, allows a SISO formulation of the considered model, similar to the closed-loop form of Fig. 4.1.

4.2.1 DC-grid transfer function

The part of the model to the right of the dc terminals of VSC Station 1 in Fig. 4.2, can be treated separately for dynamic purposes. For this analysis, the two VSC stations can be represented as controllable current sources with the rectifier injecting current $i_1 = P_1/v_{dc1}$ and the inverter injecting $i_2 = P_2/v_{dc2}$, as depicted in Fig. 4.3(a). The capacitors C_{conv} and C_{dc} in Fig. 4.2 have been replaced with their lumped value C_{tot} .

Considering the capacitor at the rectifier side, the direct-voltage dynamics are

$$\begin{aligned} C_{tot} \frac{dv_{dc1}}{dt} &= \frac{P_1}{v_{dc1}} - i_{dc} \Rightarrow C_{tot} \frac{d\Delta v_{dc1}}{dt} = \frac{1}{v_{dc1,0}} \Delta P_1 - \frac{P_{1,0}}{v_{dc1,0}^2} \Delta v_{dc1} - \Delta i_{dc} \Rightarrow \\ C_{tot} \frac{d\Delta v_{dc1}}{dt} &= \frac{1}{v_{dc1,0}} \Delta P_1 - \frac{1}{R_{10}} \Delta v_{dc1} - \Delta i_{dc} \end{aligned} \quad (4.10)$$

where the term $v_{dc1,0}^2/P_{1,0}$ has been replaced with R_{10} , since it acts as a fictive resistance which under a voltage drop of Δv_{dc1} causes a current $\Delta v_{dc1}/R_{10}$. The subscript "0" denotes the steady-state value of an electrical entity, around which the latter is linearized, and is consistently used in the rest of the analysis in the thesis.

Chapter 4. Stability in two-terminal VSC-HVDC systems: frequency-domain analysis

As mentioned earlier, the power-controlled station is set to a fixed power reference and therefore P_2 is assumed to be constant. In this case, the dynamics of the capacitor voltage on the inverter side become

$$\begin{aligned} C_{\text{tot}} \frac{d v_{\text{dc}2}}{dt} &= i_{\text{dc}} + \frac{P_2}{v_{\text{dc}2}} \Rightarrow C_{\text{tot}} \frac{d \Delta v_{\text{dc}2}}{dt} = \Delta i_{\text{dc}} - \frac{P_{2,0}}{v_{\text{dc}2,0}^2} \Delta v_{\text{dc}2} \Rightarrow \\ C_{\text{tot}} \frac{d \Delta v_{\text{dc}2}}{dt} &= \Delta i_{\text{dc}} - \frac{1}{R_{20}} \Delta v_{\text{dc}2} \end{aligned} \quad (4.11)$$

Similarly as earlier, the term $v_{\text{dc}2,0}^2/P_{2,0}$ has been replaced with R_{20} , since it acts as a fictive resistance which under a voltage drop of $\Delta v_{\text{dc}2}$ causes a current $\Delta v_{\text{dc}2}/R_{20}$. Finally, the dynamics of the current i_{dc} are

$$L_{\text{dc}} \frac{d i_{\text{dc}}}{dt} = -R_{\text{dc}} i_{\text{dc}} - v_{\text{dc}2} + v_{\text{dc}1} \Rightarrow L_{\text{dc}} \frac{d \Delta i_{\text{dc}}}{dt} = \Delta v_{\text{dc}1} - R_{\text{dc}} \Delta i_{\text{dc}} - \Delta v_{\text{dc}2} \quad (4.12)$$

The differential equations (4.10)-(4.12) constitute the linearized model of the dc-transmission link and are represented in Fig. 4.3(b) as an equivalent small-signal electrical circuit. The physical meaning of the terms R_{10} and R_{20} can now become clear. It is interesting to notice that due to the steady-state properties of the circuit

$$i_{\text{dc},0} = \frac{P_{1,0}}{v_{\text{dc}1,0}} = -\frac{P_{2,0}}{v_{\text{dc}2,0}} \quad (4.13)$$

and then

$$\begin{aligned} R_{\text{dc}} &= \frac{v_{\text{dc}1,0} - v_{\text{dc}2,0}}{i_{\text{dc},0}} = \frac{v_{\text{dc}1,0}}{i_{\text{dc},0}} - \frac{v_{\text{dc}2,0}}{i_{\text{dc},0}} = \frac{v_{\text{dc}1,0}}{P_{1,0}/v_{\text{dc}1,0}} - \frac{v_{\text{dc}2,0}}{-P_{2,0}/v_{\text{dc}2,0}} = \frac{v_{\text{dc}1,0}^2}{P_{1,0}} + \frac{v_{\text{dc}2,0}^2}{P_{2,0}} \Rightarrow \\ R_{\text{dc}} &= R_{10} + R_{20} \end{aligned} \quad (4.14)$$

The state-space model of the considered dc-transmission system is created by considering (4.10)-(4.12). The states of the system are $x_1 = \Delta v_{\text{dc}1}$, $x_2 = \Delta i_{\text{dc}}$ and $x_3 = \Delta v_{\text{dc}2}$. The only input is $u_1 = \Delta P_1$. For $W = v_{\text{dc}1}^2$, the output of the system is $y = \Delta W = 2v_{\text{dc}1,0} \Delta v_{\text{dc}1}$. The resulting state-space model is

$$\begin{aligned} \mathbf{A}_{\text{dc-link}} &= \begin{bmatrix} -\frac{1}{C_{\text{tot}} R_{10}} & -\frac{1}{C_{\text{tot}}} & 0 \\ \frac{1}{L_{\text{dc}}} & -\frac{R_{\text{dc}}}{L_{\text{dc}}} & -\frac{1}{L_{\text{dc}}} \\ 0 & \frac{1}{C_{\text{tot}}} & -\frac{1}{C_{\text{tot}} R_{20}} \end{bmatrix} \\ \mathbf{B}_{\text{dc-link}} &= \begin{bmatrix} \frac{1}{C_{\text{tot}} v_{\text{dc}1,0}} \\ 0 \\ 0 \end{bmatrix}, \mathbf{C}_{\text{dc-link}} = [2v_{\text{dc}1,0} \quad 0 \quad 0], \mathbf{D}_{\text{dc-link}} = 0 \end{aligned} \quad (4.15)$$

denoting as

$$\omega_1 = \frac{1}{C_{\text{tot}} R_{10}}, \quad \omega_2 = \frac{1}{C_{\text{tot}} R_{20}}, \quad \omega_3 = \frac{1}{L_{\text{dc}} C_{\text{tot}}}, \quad \omega_4 = \frac{R_{\text{dc}}}{L_{\text{dc}}}$$

4.2. System representation

and taking into account (4.14), the transfer function of the system from ΔP_1 to ΔW is

$$G(s) = \frac{\Delta W(s)}{\Delta P_1(s)} = \left[\mathbf{C}_{\text{dc-link}} (s\mathbf{I} - \mathbf{A}_{\text{dc-link}})^{-1} \mathbf{B}_{\text{dc-link}} + \mathbf{D}_{\text{dc-link}} \right] \Rightarrow$$

$$G(s) = \frac{2C_{\text{tot}}^{-1} [s^2 + s(\omega_2 + \omega_4) + \omega_3 + \omega_2\omega_4]}{s^3 + s^2(\omega_1 + \omega_2 + \omega_4) + s[2\omega_3 + \omega_2\omega_4 + \omega_1(\omega_2 + \omega_4)] + 2\omega_3(\omega_1 + \omega_2)} \quad (4.16)$$

In a conventional sense, the flow of current \mathbf{i} across an impedance \mathbf{Z} causes a voltage drop $\mathbf{u} = \mathbf{Z} \cdot \mathbf{i}$. In a similar manner and observing (4.16), the flow of power $\Delta P_1(s)$ into the dc grid causes an "energy" change $\Delta W = G(s) \cdot \Delta P_1(s)$. Thereby, $G(s)$ is addressed to as the *input impedance* of the dc grid.

4.2.2 AC-side transfer function

This section concerns the ac-side dynamics of Station 1 in Fig. 4.2 and its interaction with the dc-transmission link. Assuming a lossless converter and power-invariant space-vector scaling [61] or p.u. quantities, the conservation of power on the dc- and ac-side of the converter implies

$$P_1 = v_{c1}^d i_{f1}^d + v_{c1}^q i_{f1}^q \quad (4.17)$$

which in terms of small deviations becomes

$$\Delta P_1 = v_{c1,0}^d \Delta i_{f1}^d + i_{f1,0}^d \Delta v_{c1}^d + v_{c1,0}^q \Delta i_{f1}^q + i_{f1,0}^q \Delta v_{c1}^q \quad (4.18)$$

As mentioned earlier, the ac grid at the PCC is assumed to be infinitely strong and is represented by a voltage source with a fixed frequency ω_{g1} and magnitude $v_{g1}^d + jv_{g1}^q$ on the converter dq -frame. Once the PLL has estimated the correct angle of its dq -frame, any changes in the system will not affect the measured angle and the dynamics of the PLL itself will have no influence on the system. Consequently, the q -component of the ac-grid voltage has become $v_{g1}^q = 0$, the d -component of the ac-grid voltage v_{g1}^d is constant over time. The ac-side dynamics are then the following, expressed on the converter dq -frame

$$\begin{aligned} v_{c1}^d &= v_{g1}^d - (R_{f1} + sL_{f1}) i_{f1}^d + \omega_{g1} L_{f1} i_{f1}^q \\ v_{c1}^q &= -(R_{f1} + sL_{f1}) i_{f1}^q - \omega_{g1} L_{f1} i_{f1}^d \end{aligned} \quad (4.19)$$

which can then be linearized in the following form

$$\begin{aligned} \Delta v_{c1}^d &= -(R_{f1} + sL_{f1}) \Delta i_{f1}^d + \omega_{g1} L_{f1} \Delta i_{f1}^q \\ \Delta v_{c1}^q &= -(R_{f1} + sL_{f1}) \Delta i_{f1}^q - \omega_{g1} L_{f1} \Delta i_{f1}^d \end{aligned} \quad (4.20)$$

The steady-state values $v_{c1,0}^d$ and $v_{c1,0}^q$ can be derived from (4.20) as

$$\begin{aligned} v_{c1,0}^d &= v_{g1,0}^d - R_{f1} i_{f1,0}^d + \omega_{g1} L_{f1} i_{f1,0}^q \\ v_{c1,0}^q &= -R_{f1} i_{f1,0}^q - \omega_{g1} L_{f1} i_{f1,0}^d \end{aligned} \quad (4.21)$$

Inserting (4.20) and (4.21) into (4.18), provides the following expression for ΔP_1

$$\begin{aligned} \Delta P_1 &= \left[-i_{f1,0}^d (2R_{f1} + sL_{f1}) + v_{g1,0}^d \right] \Delta i_{f1}^d + \left[-i_{f1,0}^q (2R_{f1} + sL_{f1}) \right] \Delta i_{f1}^q \Rightarrow \\ \Delta P_1 &= -i_{f1,0}^d L_{f1} (s + b_1^d) \Delta i_{f1}^d - i_{f1,0}^q L_{f1} (s + b_1^q) \Delta i_{f1}^q \end{aligned} \quad (4.22)$$

where

$$b_1^d = 2 \frac{R_{f1}}{L_{f1}} - \frac{v_{g1,0}^d}{L_{f1} i_{f1,0}^d}, \quad b_1^q = 2 \frac{R_{f1}}{L_{f1}} \quad (4.23)$$

For a current controller designed as in Section (2.4.1), with closed-loop dynamics of a low-pass filter with bandwidth a_{cc} and perfect cancellation of the cross-coupling term, the relation between dq current references and filter currents acquire the following linearized form

$$\Delta i_{f1}^d = \frac{a_{cc}}{s + a_{cc}} \Delta i_{f1}^{d*}, \quad \Delta i_{f1}^q = \frac{a_{cc}}{s + a_{cc}} \Delta i_{f1}^{q*} \quad (4.24)$$

It is assumed that i_{f1}^{q*} is constant and therefore $\Delta i_{f1}^{q*} = 0$. Thus, inserting (4.24) into (4.22) provides

$$\Delta P_1 = -a_{cc} i_{f1,0}^d L_{f1} \frac{s + b_1^d}{s + a_{cc}} \Delta i_{f1}^{d*} \quad (4.25)$$

The direct-voltage controller of the station is designed in the same way as in Section (2.4.3)

$$P_{in}^* = K_p (W^* - W) + P_f \quad (4.26)$$

where P_f is the filtered feedforward power

$$P_f = H(s) P_m \quad (4.27)$$

and

$$H(s) = \frac{a_f}{s + a_f} \quad (4.28)$$

is a low-pass filter of bandwidth a_f . The actual power P_{in} will follow its reference P_{in}^* with a time constant defined by the selected control parameters. This power is different from P_1 because of the reactor resistance R_{f1} and the associated power loss. Given the fact that the steady-state value of the feedforward term P_f is equal to P_1 , it is understood that there is a need for an integrator with a very low gain K_i to compensate for the small steady-state deviation between P_{in} and P_1 . For very low values of K_i , the integrator has negligible effect on the overall dynamics and can, at this point, be assumed to be zero [43].

The reference power P_{in}^* in terms of PCC properties is

$$P_{in}^* = v_{g1}^d i_{f1}^{d*} \quad (4.29)$$

which when inserted to (4.26) gives

$$v_{g1}^d i_{f1}^{d*} = K_p (W^* - W) + P_f \Rightarrow v_{g1,0}^d \Delta i_{f1}^{d*} = K_p (\Delta W^* - \Delta W) + \Delta P_f \Rightarrow$$

4.2. System representation

$$\Delta i_{f1}^{d*} = \frac{K_p (\Delta W^* - \Delta W) + \Delta P_f}{v_{g1,0}^d} \quad (4.30)$$

Relations (4.25) and (4.30) provide the final expression for the injected power to the dc-transmission link

$$\Delta P_1 = K(s) [K_p (\Delta W^* - \Delta W) + \Delta P_f] \quad (4.31)$$

with

$$K(s) = -\frac{a_{cc} i_{f1,0}^d L_{f1}}{v_{g1,0}^d} \frac{s + b_1^d}{s + a_{cc}} \quad (4.32)$$

Given relation (4.27), the filtered power ΔP_f can be expressed as

$$\Delta P_f = H(s) \Delta P_m \quad (4.33)$$

The challenge at this stage is to relate ΔP_m directly to ΔP_1 . In order to achieve this, it is necessary to resort back to the analysis of the dc-grid transfer function in Section (4.2.1) and its state-space description in (4.15).

Based on the arrangement of Fig. 4.2, as well as the fact that capacitors C_{conv} and C_{dc} share the same voltage at all times, the dc-side powers measured at different points of the transmission-link model are connected in the following way

$$\left. \begin{aligned} \frac{1}{2} C_{conv} \frac{dW}{dt} &= P_1 - P_m \\ \frac{1}{2} C_{dc} \frac{dW}{dt} &= P_m - v_{dc1} i_{dc} \end{aligned} \right\} \Rightarrow \frac{P_1 - P_m}{C_{conv}} = \frac{P_m - v_{dc1} i_{dc}}{C_{dc}} \Rightarrow$$

$$P_m = \frac{C_{dc}}{C_{conv} + C_{dc}} P_1 + \frac{C_{conv}}{C_{conv} + C_{dc}} v_{dc1} i_{dc} \Rightarrow$$

$$P_m = \frac{C_{dc}}{C_{tot}} P_1 + \frac{C_{conv}}{C_{tot}} v_{dc1} i_{dc} \quad (4.34)$$

Relation (4.34) can then be linearized into

$$P_m = \frac{C_{dc}}{C_{tot}} P_1 + \frac{C_{conv}}{C_{tot}} v_{dc1} i_{dc} \Rightarrow \Delta P_m = \frac{C_{dc}}{C_{tot}} \Delta P_1 + \frac{C_{conv}}{C_{tot}} v_{dc1,0} \Delta i_{dc} + \frac{C_{conv}}{C_{tot}} i_{dc,0} \Delta v_{dc1} \Rightarrow$$

$$\Delta P_m = \frac{C_{dc}}{C_{tot}} \Delta P_1 + \frac{C_{conv} v_{dc1,0}}{C_{tot}} \Delta i_{dc} + \frac{C_{conv} P_{1,0}}{C_{tot} v_{dc1,0}} \Delta v_{dc1} \quad (4.35)$$

At this point considering the same system as in Section (4.2.1) with the same single input ΔP_1 , but new output of ΔP_m as in (4.35), the new state-space representation becomes

$$\mathbf{A}_{dc} = \begin{bmatrix} -\frac{1}{C_{tot} R_{10}} & -\frac{1}{C_{tot}} & 0 \\ \frac{1}{L_{dc}} & -\frac{R_{dc}}{L_{dc}} & -\frac{1}{L_{dc}} \\ 0 & \frac{1}{C_{tot}} & -\frac{1}{C_{tot} R_{20}} \end{bmatrix} \quad (4.36)$$

$$\mathbf{B}_{dc} = \begin{bmatrix} \frac{1}{C_{tot} v_{dc1,0}} \\ 0 \\ 0 \end{bmatrix}, \quad \mathbf{C}_{dc} = \begin{bmatrix} \frac{C_{conv} P_{1,0}}{C_{tot} v_{dc1,0}} & \frac{C_{conv} v_{dc1,0}}{C_{tot}} & 0 \end{bmatrix}, \quad \mathbf{D}_{dc} = \frac{C_{dc}}{C_{tot}}$$

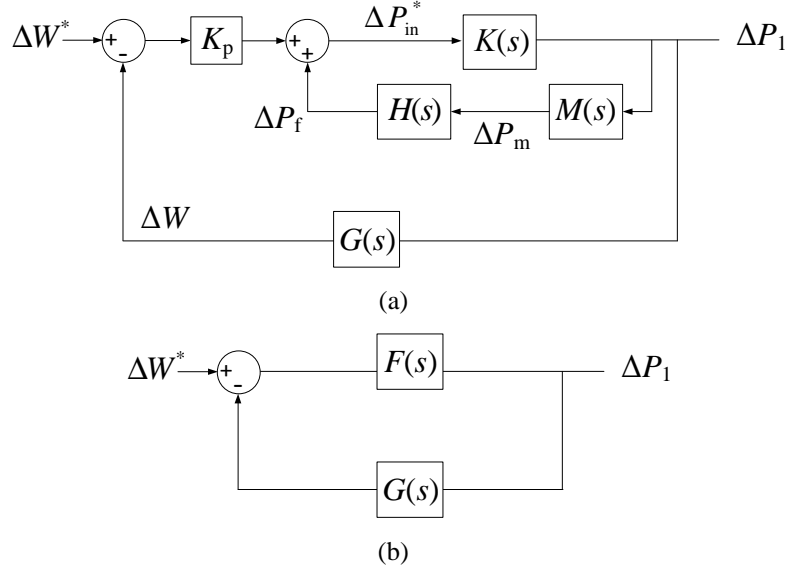


Fig. 4.4 SISO representation of two-terminal VSC-HVDC model: (a) detailed representation, (b) condensed representation.

with the only difference compared to (4.15), being found in matrices \mathbf{C}_{dc} and \mathbf{D}_{dc} . The transfer function from ΔP_1 to ΔP_m is now

$$M(s) = \frac{\Delta P_m(s)}{\Delta P_1(s)} = \left[\mathbf{C}_{dc} (s\mathbf{I} - \mathbf{A}_{dc})^{-1} \mathbf{B}_{dc} + \mathbf{D}_{dc} \right] \Rightarrow$$

$$M(s) = \frac{C_{conv}}{C_{tot}^2 v_{dc1,0}^2} \cdot \frac{C_{tot} v_{dc1,0}^2 (s + \omega_2) \omega_3 + P_{1,0} [s^2 + s(\omega_2 + \omega_4) + \omega_3 + \omega_2 \omega_4]}{s^3 + s^2(\omega_1 + \omega_2 + \omega_4) + s[2\omega_3 + \omega_2 \omega_4 + \omega_1(\omega_2 + \omega_4)] + 2\omega_3(\omega_1 + \omega_2)} + \frac{C_{dc}}{C_{tot}} \quad (4.37)$$

4.2.3 Closed-loop SISO feedback representation

Following the previous segmental investigation, the individual transfer functions can be combined in order to obtain a representation of the system's dynamics, relating the single input ΔW^* to the output ΔP_1 . The equations of interest are (4.16), (4.31), (4.32), (4.28) and (4.37) whose proper linking leads to the graphical representation of Fig. 4.4(a).

The feedback-loop transfer function $G(s)$ in Fig. 4.4(a) already complies with the SISO form of Fig. 4.1 but the path from the input to the output, appears more complicated. The latter can be merged into a single transfer function

$$F(s) = K_p \frac{K(s)}{1 - K(s)H(s)M(s)} \quad (4.38)$$

with the system taking the final desired form of Fig. 4.4(b). This form will be used in the later parts of this chapter.

4.3. Frequency-domain analysis: Passivity approach

It is interesting to observe that if the direct-voltage controller was only a basic PI-controller with transfer function $K_p + K_i/s$, the input-admittance transfer function would simply become

$$F(s) = \frac{K_p s + K_i}{s} \cdot K(s) \quad (4.39)$$

The dynamics of this expression are completely decoupled from those of the dc-transmission link. Conversely, the presence of the power feedforward term in the considered control introduces $M(s)$ into the final expression of $F(s)$ in (4.38), implying that the latter is now coupled to the dc-transmission system and inherits its dynamics.

From an electrical point of view, a voltage drop \mathbf{u} across an admittance \mathbf{Y} causes a current $\mathbf{i} = \mathbf{Y} \cdot \mathbf{u}$. In a similar manner and with a reference of Fig. 4.4(b), the appearance of an "energy" drop $e = \Delta W^* - \Delta W$ causes the converter to respond with a power flow $\Delta P_1 = F(s) \cdot e$. Thereby, $F(s)$ is addressed to as the *input admittance* of the VSC converter.

4.3 Frequency-domain analysis: Passivity approach

In this section the stability of a two-terminal VSC-HVDC, as shown in Fig. 4.2, is investigated using a frequency-domain approach. The investigation intends to utilize the passivity properties of the system and the Nyquist criterion. As such, a SISO representation of Fig. 4.4(b) is considered, where the transfer functions $F(s)$ and $G(s)$ must be stable. The investigation begins by considering a simple form of direct-voltage control. Thereby, a commonly used PI-controller is chosen in the beginning, with a later consideration for a proportional controller with power-feedforward.

4.3.1 DC-grid subsystem for passivity studies

The dc-grid transfer function $G(s)$ in (4.16) has three poles, one of which is real. As will be shown later in Section (6.3), this real pole is always positive for a non-zero power transfer, rendering $G(s)$ unstable and therefore non-passive. This implies that the analysis of the SISO system in terms of passivity cannot be performed. However, in a related analysis in [19], if

$$\frac{L_{dc}}{C_{tot}} \ll 2 \quad (4.40)$$

it is possible to approximate $G(s)$ with the transfer function $G'(s)$, where the real pole is fixed at zero

$$G'(s) = \frac{2C_{tot}^{-1} [s^2 + s(\omega_2 + \omega_4) + \omega_3 + \omega_2\omega_4]}{s(s^2 + \omega_4 s + 2\omega_3)} \quad (4.41)$$

Condition (4.40) is usually fulfilled in cable-type of lines, where the real pole is sufficiently close to zero due to the low inductance of the transmission link is, but not necessarily in case of overhead lines. This will be further investigated in Chapter 6.

As demonstrated in [19], the replacement of $G(s)$ with $G'(s)$ has practically negligible effects in the closed-loop poles of the SISO system and is therefore valid to be considered as the feedback transfer function. However, the main benefit of considering $G'(s)$ is that, unlike $G(s)$, it is stable. This is a precondition for the passivity analysis.

4.3.2 VSC subsystem

The input-admittance transfer function $F(s)$ is determined by the ac-side characteristics of the rectifier VSC Station 1 and its control. Following the analysis of Section (4.2.3), a PI-controller is at this stage chosen (instead of a proportional controller with power-feedforward) for the direct-voltage control. This is because, in order to perform a passivity analysis, transfer function $F(s)$ must be at least stable. Expression (4.39) corresponding to the use of a simple PI-controller is always stable, but not (4.38), which is related to the proportional controller with power-feedforward. For a selection of $K_p = a_d C_{\text{conv}}$ and $K_i = a_d^2 C_{\text{conv}}/2$ as in [14], the ideal closed-loop direct-voltage control of the rectifier (assuming no dc-transmission link), would have two real poles at $s = a_d$. As such, the input-admittance transfer function of the SISO system has the general form of (4.39), providing the final expression

$$F(s) = \frac{K_p s + K_i}{s} \cdot K(s) = -\frac{a_d a_{cc} i_{f1,0}^d L_{f1} C_{\text{conv}}}{v_{g1,0}^d} \frac{(s + a_d/2)}{s} \frac{(s + b_1^d)}{(s + a_{cc})} \quad (4.42)$$

As it can be observed, $F(s)$ is always stable. This, combined with the fact that $G'(s)$ is stable, indicates that a passivity approach of the system can be considered to investigate the stability of the closed-loop system.

4.3.3 Analysis

The complete VSC-HVDC link is here evaluated and for scaling purposes the system is examined in per-unit. The passivity properties of the system may alter according to the operational conditions and choice of control parameters and passive elements. Their values are the same as in Table 2.2, with nominal power transfer and direct voltage, with the difference that the bandwidth a_d of the closed-loop direct-voltage control is allowed to vary. A cable-type of the transmission line is chosen with physical characteristics provided in Table 2.1. The cable length is here set to 50 km.

The frequency response of $G'(s)$ is presented in Fig. 4.5. A resonance peak is observed at $\omega = 7.42$ pu, which is very close to the resonance frequency of the transmission link, having $\omega_{\text{res}} = 7.40$ pu, as defined by (3.17). It can also be seen that the phase angle of the transfer function is always between -90° and 90° and since it is also marginally stable, $G'(s)$ is passive for all frequencies. Therefore, with $F(s)$ being already stable, the passivity analysis dictates that if there is a chance of instability in the closed-loop SISO system then $F(s)$ will necessarily be non-passive.

The system is now tested for three different bandwidths of the close-loop direct-voltage control: (a) $a_d = 0.4$ pu, (b) $a_d = 1.4$ pu and (c) $a_d = 2.4$ pu. Figure 4.6 shows the real and imaginary

4.3. Frequency-domain analysis: Passivity approach

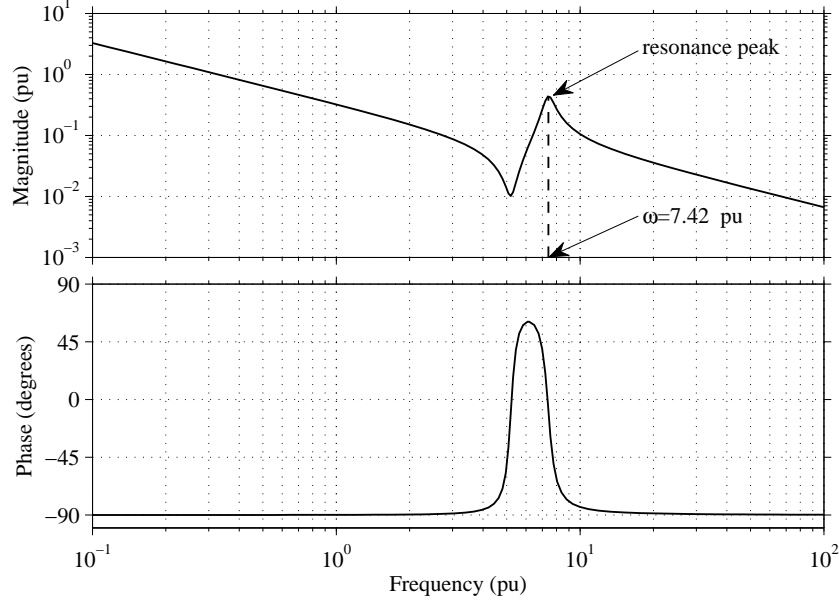


Fig. 4.5 Frequency response of $G'(s)$.

parts of $G'(j\omega)$ and $F(j\omega)$ for each of the cases. Observe that for the investigated cases, $\text{Re}[F]$ is negative over a large part of the frequency domain, indicating that $F(s)$ is non-passive and therefore provides a hint for possible instability. Observe that $F(s)$ is non-passive for any amount of positive power transfer.

In this case, the Nyquist criterion should be applied. For a certain frequency ω , the transfer functions $F(s)$ and $G'(j\omega)$ can be regarded in terms of their real and imaginary parts as

$$F(j\omega) = F_r(\omega) + jF_i(\omega) \quad (4.43)$$

$$G'(j\omega) = G'_r(\omega) + jG'_i(\omega) \quad (4.44)$$

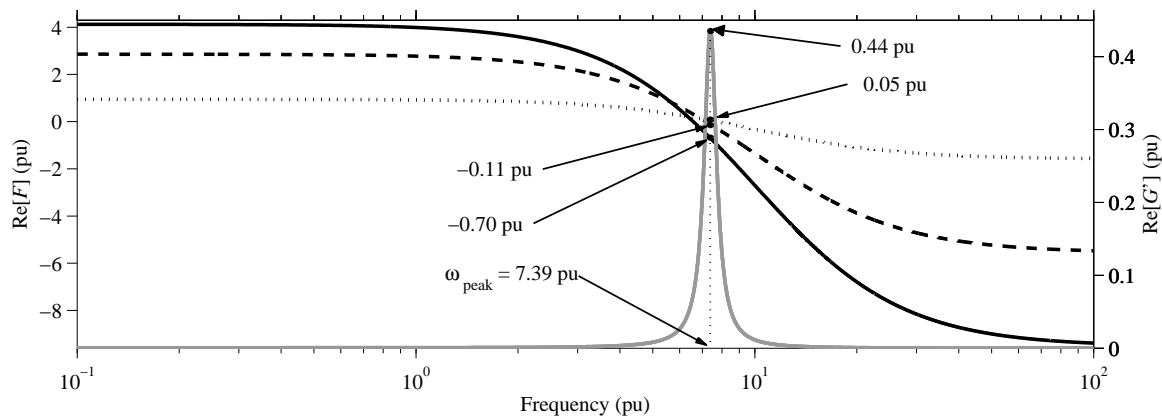
At a frequency ω_N the Nyquist curve $F(j\omega)G'(j\omega)$ crosses the real axis. There could be multiple such frequencies but if there is a poorly-damped potential resonance, then a ω_N will exist close to that resonant frequency with $F(j\omega_N)G'(j\omega_N)$ being close to the -1 value [62]. If the closed-loop SISO system is to remain stable, then

$$F(j\omega_N)G'(j\omega_N) > -1 \Rightarrow F_r(\omega_N)G'_r(\omega_N) - F_i(\omega_N)G'_i(\omega_N) > -1 \quad (4.45)$$

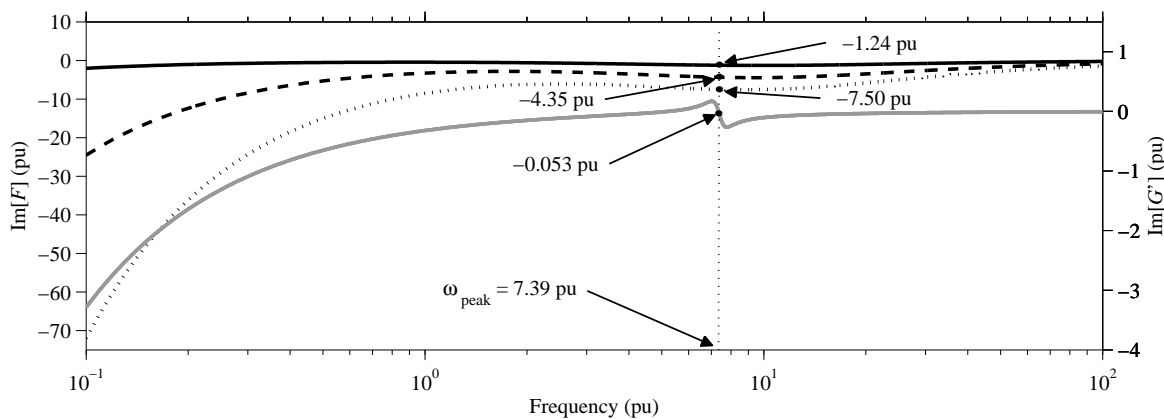
Such a resonant frequency ω_N is found to exist for each of the examined a_d cases, with it being always close to the $\omega_{\text{peak}} = 7.39$ pu of $\text{Re}[G']$, which is itself very close to the resonant frequency $\omega_{\text{res}} = 7.4$ pu of the dc-transmission link. As it can be observed in Fig. 4.6(b), the value of $\text{Im}[G']$ (equal to $G'_i(\omega)$) around ω_{peak} (and therefore ω_N as well) is very close to zero. A consequence of this is that the term $F_i(\omega_N)G'_i(\omega_N)$ in (4.45) becomes much smaller than $F_r(\omega_N)G'_r(\omega_N)$ and can thereby be neglected. Expression (4.45) can now be approximated by

$$F_r(\omega_N)G'_r(\omega_N) > -1 \quad (4.46)$$

Chapter 4. Stability in two-terminal VSC-HVDC systems: frequency-domain analysis



(a) Real parts of $F(j\omega)$ and $G'(j\omega)$.



(b) Imaginary parts of $F(j\omega)$ and $G'(j\omega)$.

Fig. 4.6 Real and imaginary parts of $F(j\omega)$ and $G'(j\omega)$. Solid gray: G' . Dotted: F for $a_d = 0.4$ pu. Dashed: F for $a_d = 1.4$ pu. Solid: F for $a_d = 2.4$ pu.

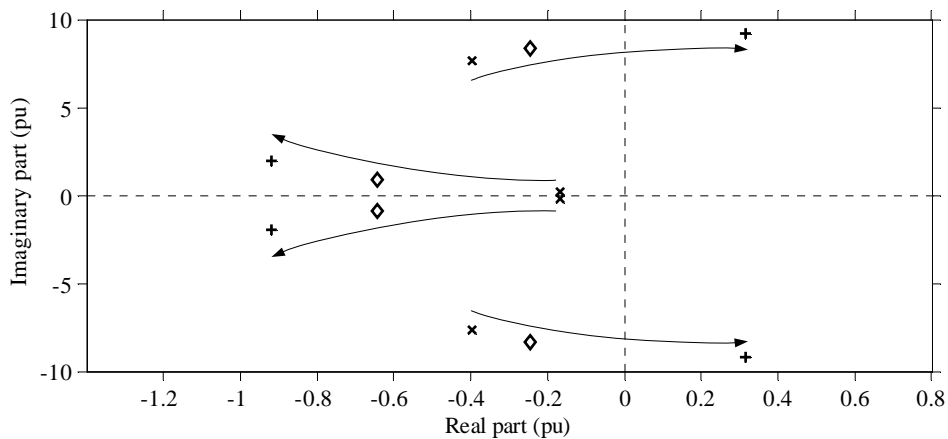


Fig. 4.7 Pole movement of the closed-loop SISO system for $a_d = 0.4$ pu (\times), $a_d = 1.4$ pu (\diamond), $a_d = 2.4$ pu ($+$). The fifth pole associated with the current-controller bandwidth a_{cc} is far to the left and is not shown here.

4.4. Frequency-domain analysis: Net-damping approach

and since ω_N is close to ω_{peak} , (4.46) becomes

$$F_r(\omega_{\text{peak}}) G_r'(\omega_{\text{peak}}) > -1 \quad (4.47)$$

Since $G_r'(\omega_{\text{peak}}) = 0.44$ pu, (4.47) provides the information that for an increasingly negative value of $F_r(\omega_{\text{peak}})$, the value of $F_r(\omega_{\text{peak}}) G_r'(\omega_{\text{peak}})$ decreases with the possibility of surpassing -1 and the closed-loop system becoming unstable. This behavior is observed in Fig. 4.6(a) where for an increasing a_d , the value of $F_r(\omega_{\text{peak}})$ is initially positive but gradually turns negative and keeps decreasing. This indicates that the increase of a_d decreases the damping of the resonant poles of the system and, eventually, leads to the instability of the system.

This can be visually demonstrated in Fig. 4.7 where the closed-loop poles of the system are plotted for the three different cases of a_d . Indeed, an increase of a_d causes the poorly-damped resonant poles of the system, with a natural frequency close to ω_{peak} , to become increasingly under-damped until they become unstable for $a_d = 2.4$ pu.

4.3.4 Altered system configuration

At this stage, the same dc-transmission link as before is considered but the direct-voltage control is changed to a proportional controller with power-feedforward. This means that the input-admittance transfer function $F(s)$ is the one described by (4.38). As mentioned in Section (4.2.3), the transfer function $H(s)$, which exists within the expression of $F(s)$, inherits the dynamics of the dc-transmission system and is unstable. Furthermore, the fact that $H(s)$ is located on a positive feedback loop that forms the final $F(s)$, as seen in Fig. 4.4(a), causes the complete $F(s)$ function to be permanently unstable. This means that the passivity approach cannot be used for the frequency analysis of the closed-loop stability.

One natural way to still use the passivity approach is to approximate $G(s)$ with $G'(s)$ when deriving the feedforward term for $F(s)$. However, as it will be shown in Chapter 5 and 6, this approximation does not always hold. For this reason, an alternative frequency-domain method to assess the system stability will be described in the following section.

4.4 Frequency-domain analysis: Net-damping approach

The net-damping approach in evaluating the stability of a SISO system has no regards on the passivity of its subsystems $F(s)$ and $G(s)$. Additionally, it was shown that when possible, the passivity approach along with the Nyquist curve can provide information on the risk of stability but not strict information on the stability status of a system. This section demonstrates applications of the net-damping criterion in a two-terminal VSC-HVDC system. In all cases, the direct-voltage controller features the power-feedforward term.

4.4.1 Open-loop resonances

The system under investigation in this part is identical to the two-terminal VSC-HVDC model whose performance was examined in Section (3.3.2). That system featured long overhead dc-transmission lines and the transferred power was ramped up in stages, from 0 MW (0 pu) to 500 MW (0.5 pu) and finally to 1000 MW (1 pu). While the model appeared to be stable in the beginning, as shown in Fig. 3.11, when the power reached 900 MW (0.9 pu), it became unstable with a resonance of 199.4 Hz. Once the power started decreasing until 500 MW, the stability was restored.

The SISO representation of the system considers the input-admittance transfer function $F(s)$ and the feedback transfer function $G(s)$ as defined in (4.38) and (4.16), respectively. The investigation starts by locating potential open-loop resonances of $|F(j\omega)|$ and $|G(j\omega)|$ ¹. The frequency domain plots of those transfer functions are shown in Fig. 4.8(a) and Fig. 4.8(b)), respectively, for the three different power transfers of interest; 0 pu, 0.5 pu and 0.9 pu. Observing $|G(j\omega)|$, it is immediately apparent that there is always a single resonance at a frequency that is almost independent on the transmitted power and is very close to the resonant frequency of the dc grid, defined in (3.17). On the other hand, $|F(j\omega)|$ seems to exhibit no resonances for powers of 0 pu and 0.5 pu, but does have one for a power of 0.9 pu with a frequency of 0.72 pu. Table 4.1 displays the characteristic frequency of these resonances.

The value of the damping $D_F(\omega)$ at the point of all the observed resonances is positive. Thereby, the positive-net-damping criterion of (4.5) will be evaluated. As it can be seen in Table 4.1, the total damping $D(\omega)$ is always positive at the open-loop resonant frequencies for powers of 0 pu and 0.5 pu. This means that the system should be stable, as demonstrated through the time-domain simulation of Fig. 3.11. However, once the system has a transferred power of 0.9 pu, $|F(j\omega)|$ develops a resonance at 0.72 pu as mentioned before, where $D(\omega)$ is negative with a value of -0.32 pu. This indicates an unstable system, confirming the unstable conditions displayed in Fig. 3.11.

This behavior can be observed in terms of the pole movement of the system for the different power transfers, as displayed in Fig. 4.9. The poles are calculated for the closed-loop transfer function $F(s) / (1 + F(s)G(s))$. As demonstrated, the system exhibits a pair of poorly-damped complex conjugate poles which are of concern due to their proximity to the imaginary axis. For a power transfer of 0 pu and 0.5 pu, these poles are stable. However, when the power increases to 0.9 pu, the already poorly-damped poles become unstable with a predicted resonant frequency of 0.623 pu, or 195.7 Hz, which is very close to the 199.4 Hz oscillation observed in the time-domain simulation.

¹ $F(s)$ and $G(s)$ are both unstable. An attempt to locate their resonant points by plotting the bode plot in a way that a sinusoidal input signal is provided and the amplitude and phase of the output signal are measured, is not useful as the response of such systems for any input would be a signal that reaches infinity. However, plotting $|F(j\omega)|$ and $|G(j\omega)|$ still allows the identification of the local peaks that serve as the open-loop resonances and can be further used in the net-damping analysis.

4.4. Frequency-domain analysis: Net-damping approach

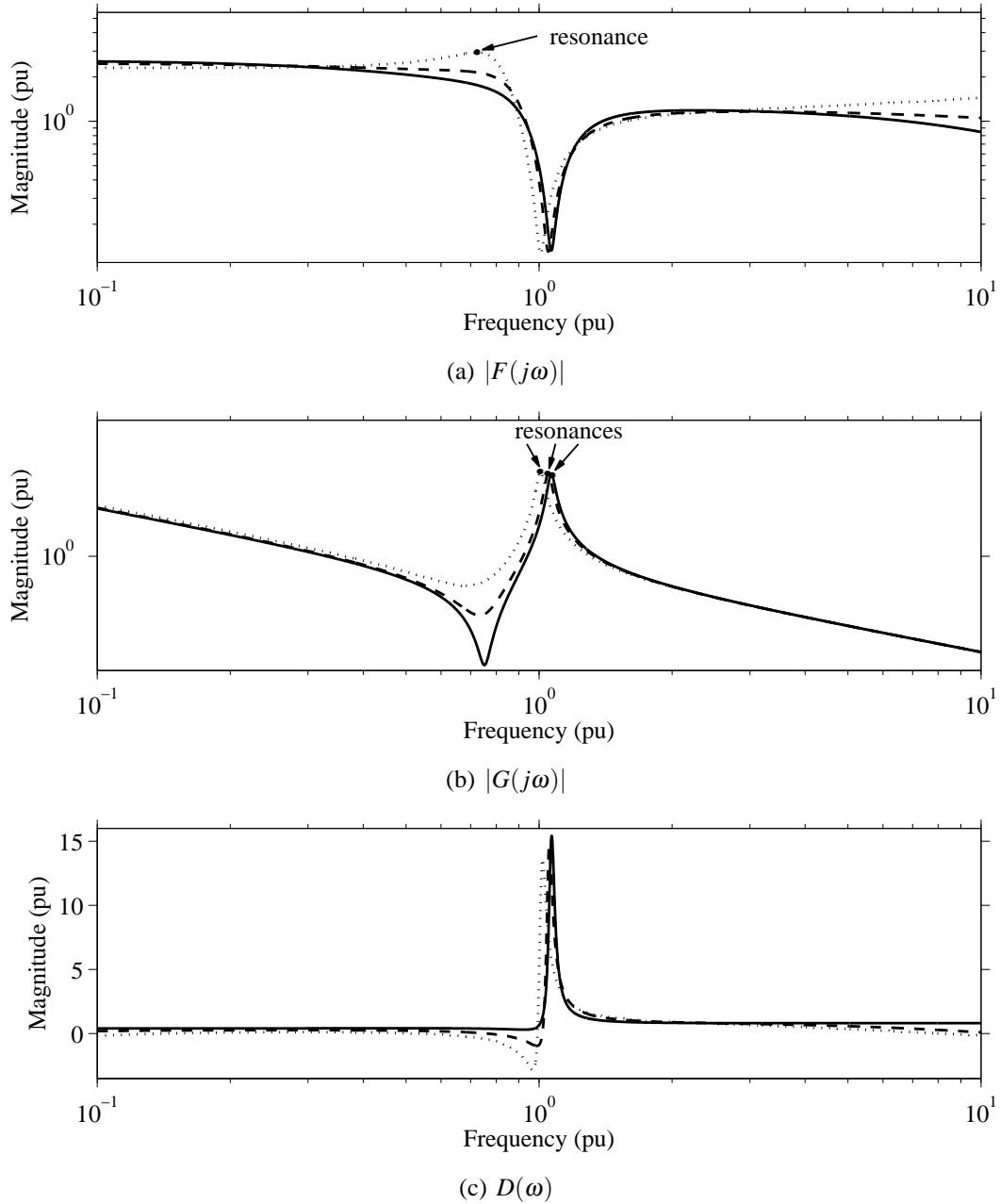


Fig. 4.8 Frequency analysis of subsystems and total damping for transferred power equal to 0 pu (solid), 0.5 pu (dashed) and 0.9 pu (dotted).

TABLE 4.1. LOCATION OF OPEN-LOOP RESONANCES AND TOTAL DAMPING

Power (pu)	$ F(j\omega) $ resonant frequency (pu)	$ G(j\omega) $ resonant frequency (pu)	$D(\omega)$ at $ F(j\omega) $ resonance (pu)	$D(\omega)$ at $ G(j\omega) $ resonance (pu)
0	-	1.07	-	15.3
0.5	-	1.05	-	13.46
0.9	0.72	1.01	-0.32	10.48

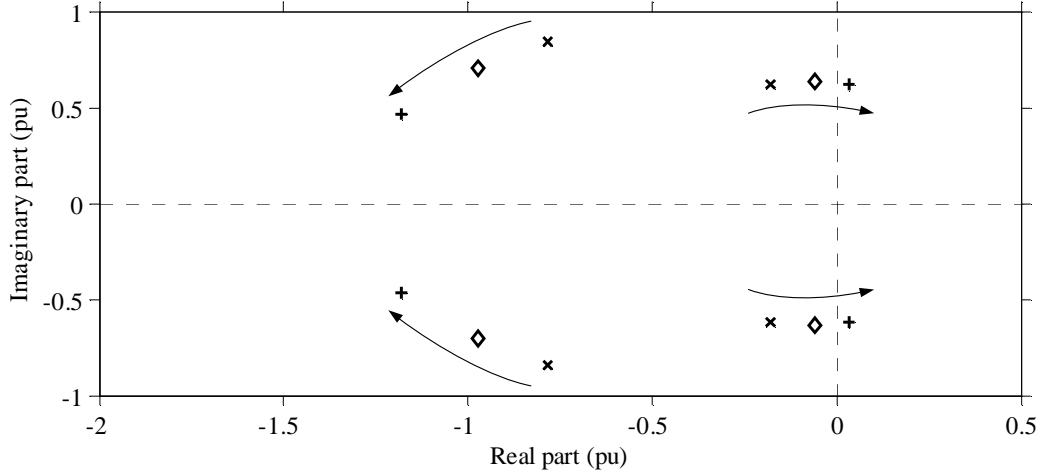


Fig. 4.9 Pole movement of the closed-loop SISO system for transferred power equal to 0 pu (\times), 0.5 pu (\diamond) and 0.9 pu ($+$). The fifth pole associated with the current-controller bandwidth a_{cc} is far to the left and is not shown here.

4.4.2 Non-apparent cases

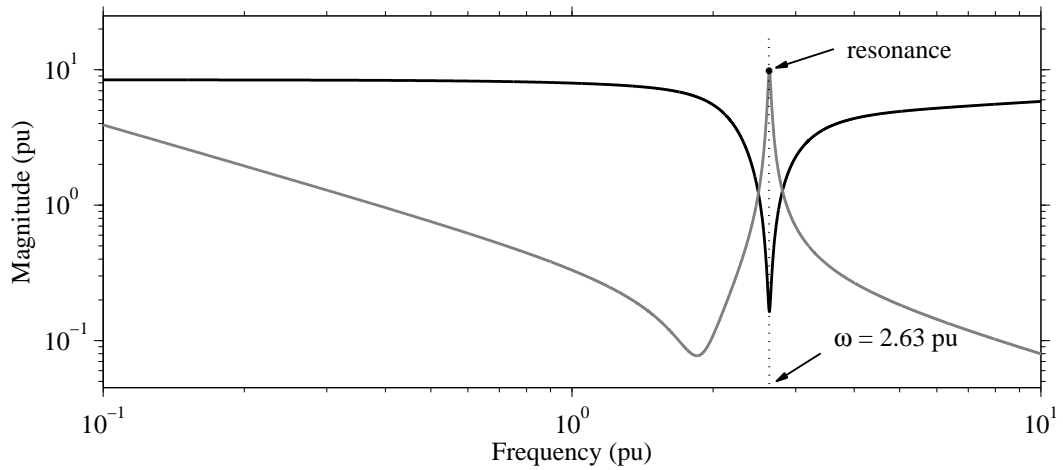
In the vast majority of the examined cases, a straightforward commenting for the stability of the system could be provided by focusing only on the open-loop resonances, as in Section (4.4.1). However there are some rare and unusual scenarios where this approach could not give an explanation for the instability of the system. One of these cases is investigated here. The model used is the same as in Section (4.4.1) with the differences being

1. the overhead line length is reduced to 50 km.
2. the power transfer is set to 1 pu.
3. the closed-loop bandwidths a_d and a_f are both increased from 1 pu to 3.5 pu.

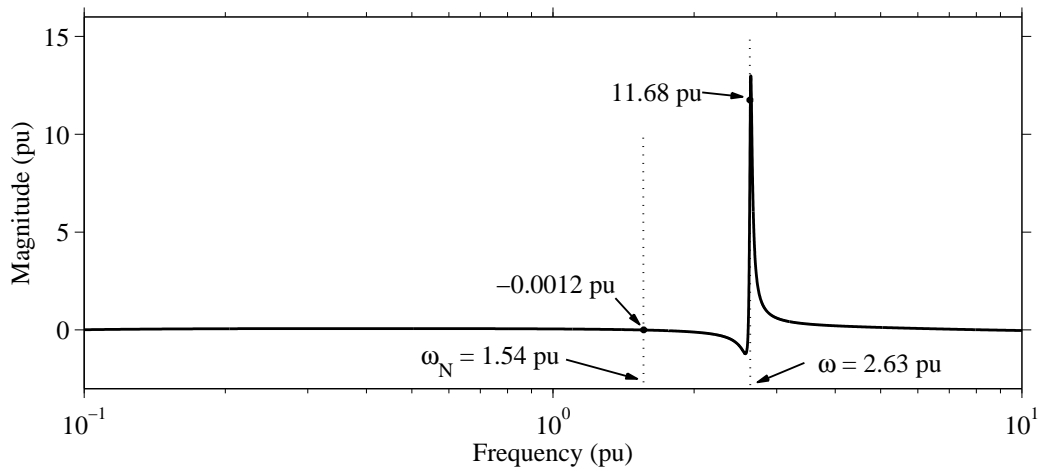
Under these conditions, the closed-loop system is unstable with a pair of unstable complex conjugate poles at 0.0044 ± 1.541 (pu). The frequency domain results of $|F(j\omega)|$ and $|G(j\omega)|$ are presented in Fig. 4.10(a); as it can be observed, there is only one open-loop resonance which is found on $|G(j\omega)|$ at $\omega = 2.63$ pu; $|F(j\omega)|$ appears to have no resonances. At that frequency, damping $D_F(\omega)$ is positive, meaning that the total damping $D(\omega)$ should be positive as well. Indeed, measuring the latter at the resonant frequency gives a positive value of $D(\omega) = 11.68$ pu (as seen in Fig. 4.10(b)), suggesting that the system should be stable. This creates a controversy since the system is already known to be unstable.

It should be reminded here that, as mentioned in Section (4.1.2), the net-damping criterion should be evaluated not only for the open-loop resonances, but for low frequencies as well where the loop gain exceeds unity. Following this statement, the Nyquist curve of the system showed that the $F(j\omega)G(j\omega)$ curve crosses the real axis with a value of -1.02 pu (enclosing point -1 and causing instability) at a frequency $\omega_N = 1.54$ pu. This frequency is below the open-loop

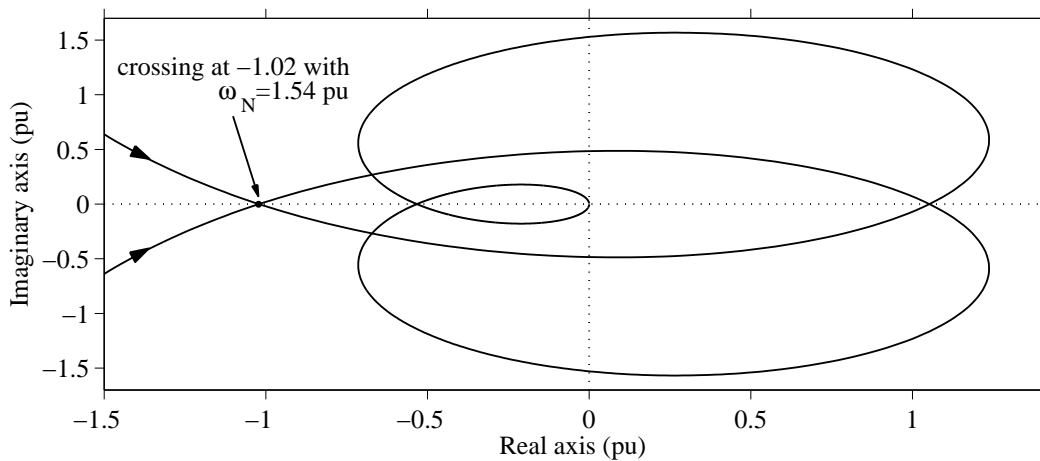
4.4. Frequency-domain analysis: Net-damping approach



(a) $|F(j\omega)|$ (black curve) and $|G(j\omega)|$ (gray curve).



(b) $D(\omega)$



(c) Nyquist curve of $F(j\omega)G(j\omega)$.

Fig. 4.10 Frequency analysis of subsystems, total damping and Nyquist curve of the system.

resonance of 2.63 pu. At this frequency, $D_F(\omega)$ is positive and the total damping $D(\omega)$ is equal to -0.0012 pu, indicating that there is instability, even though barely. As mentioned in [24], negative total damping at low frequencies is a strong indication of instability, even though the open-loop resonances may have positive damping. This has been demonstrated here, proving that the net-damping criterion still provides an answer in the rare occasions when the system is unstable, despite a good damping of the apparent open-loop resonances.

4.5 Correlation between net-damping and damping factor

In the previous section, it was shown how the net-damping criterion can provide direct information on whether a SISO system is stable or unstable. However there has been no information relating the criterion to poorly-damped or near-instability conditions.

4.5.1 Damping in a multi-pole system

As mentioned in Section (3.1), the damping of a system can be strictly defined only for 2nd order systems as the one described in (3.1). When it comes to multi-pole systems it is not possible to provide a similarly strict definition of the system's damping. A step-wise excitation of the system excites all of its eigenmodes (given the fact the unit step contains the full frequency spectrum) and the total system response consists of their superposition.

However, the behavior of a multi-pole system is normally dominated by its dominant poles (if these exist), which dictate the main properties of its response to a perturbation. Furthermore, poles with very low damping have, by definition, a very small absolute real part, becoming potentially dominant as they find themselves very close to the imaginary axis. In such cases, the final response of the system will be mostly dictated by those poorly-damped poles and it is here suggested, in a non-strict manner, that their damping factor can be regarded as the damping of the complete system.

4.5.2 Net-damping in poorly-damped configurations

Typically, the encirclement by the Nyquist plot of -1 occurs at low frequencies and in the neighborhood of resonances [62]. These resonances are usually identified with poorly-damped poles that move towards the RHP of the complex plane due to a change of a critical parameter (e.g. transferred power). When the system is on the verge of instability, the Nyquist curve intersects with the point -1. This occurs at a frequency ω_{crit} with the corresponding closed-loop system having either a real pole at the origin of the s -plane or a pair of marginally-stable complex-conjugate poles with a damped natural frequency $\omega_d = \omega_{\text{crit}}$. If these poles have not yet become unstable but are close enough to the imaginary axis, the Nyquist curve will cross the real axis on the right of -1 but in close proximity to it. This occurs at a frequency ω_N that is closely related to the damped natural frequency of the related poorly-damped poles.

4.5. Correlation between net-damping and damping factor

If the system is marginally stable, its net-damping at the frequency $\omega_N = \omega_{\text{crit}} = \omega_d$ is equal to zero

$$D(\omega_N) = D(\omega_{\text{crit}}) = D_F(\omega_{\text{crit}}) + D_G(\omega_{\text{crit}}) = 0 \quad (4.48)$$

Based on the previous analysis, it is here suggested that it is possible to correlate the level of net damping of a system measured at ω_N , with the existence of poorly-damped poles that are close to instability. The closer these poles approach the imaginary axis, the more the net damping $D(\omega_N)$ should approach zero until the poles become marginally stable and $D(\omega_N) = 0$. The value that quantifies the level of damping for these poles is their damping factor. The closer the latter is to zero, the less damped the poles and the system is closer to instability.

The objective of this analysis, is to provide a way though solely a frequency analysis of the system to determine whether there are poorly-damped poles critically close to the imaginary axis, without actually finding the poles of the system and the frequency characteristics of the poorly-damped poles. For this reason, four different scenarios are examined where the two-terminal VSC-HVDC system appears to have poorly-damped poles whose damping decreases with the change of a system parameter or operational condition, until they almost become marginally stable. In all cases, the damping of these poles is plotted in conjunction with the measurement of the net damping at the frequency ω_N where the Nyquist curve crosses the real axis closest to -1. As for the previous sections, the direct-voltage controller is at all times considered to feature the power-feedforward term.

The four different cases use the basic values as defined in Table 2.2 with the custom differences being identified in the following way

- **Case 1:** The system features overhead dc-transmission lines with their properties defined in Table 2.1 and their length is varied from 50-230 km.
- **Case 2:** The system features overhead dc-transmission lines and the controller bandwidths a_d and a_f are equal and varied from 200-630 rad/s.
- **Case 3:** The system features overhead dc-transmission lines of 230 km in length and the transferred power at the inverter Station 2 is varied from 0-1000 MW.
- **Case 4:** The system features cable dc-transmission lines with their properties defined in Table 2.1 and their length is varied from 26-43 km.

Each of the graphs in Fig. 4.11 shows the pole movement of the system for an increasing trend of the chosen variable, with the concerned poles being encircled. In the first three cases, the damping $D_F(\omega_N)$ of the VSC input admittance is positive at ω_N and therefore for the system to be stable, the net-damping should be positive. This is confirmed in Figures 4.11(a)-4.11(c) where the systems are already known to be stable and the measured net damping is indeed

Chapter 4. Stability in two-terminal VSC-HVDC systems: frequency-domain analysis

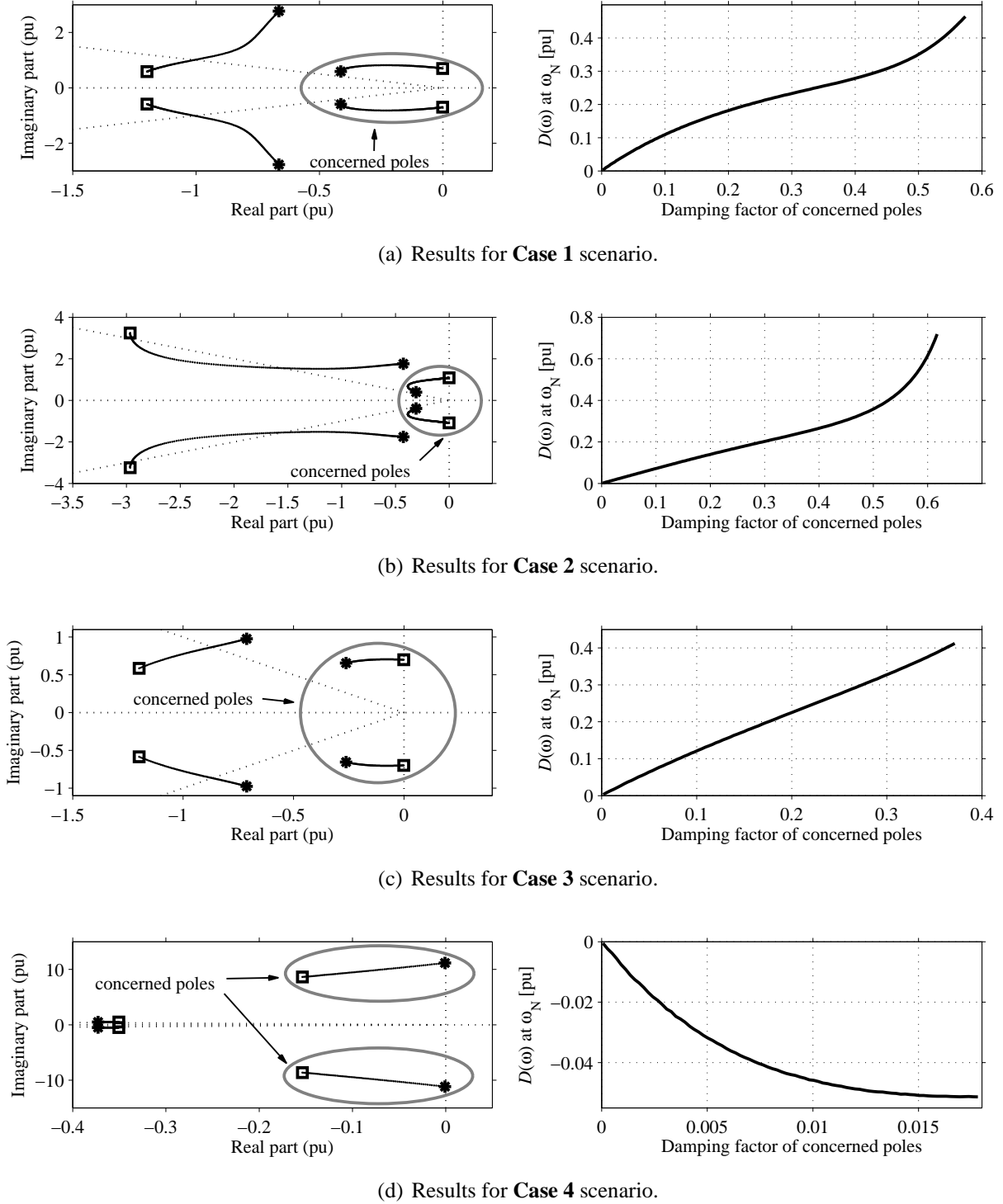


Fig. 4.11 Frequency analysis of poorly-damped systems. Four scenarios are examined with a different variable of the system changing in each of them. In the pole movement, "*" corresponds to the starting value and "□" to the final value of the variable. The fifth pole associated with the current-controller bandwidth a_{cc} is far to the left and is not shown here.

4.6. Stability improvement

positive. On the contrary, in Case 4 the damping $D_F(\omega_N)$ is negative and according to (4.8), the net damping should be negative to ensure stability. This is verified in Fig. 4.11(d) where the stable system exhibits negative net damping at ω_N .

At this stage it is interesting to notice that for all the investigated scenarios there is a consistency in a sense that there is a monotonous relationship between the net damping of the system and the damping factor of the poorly-damped poles, provided that the latter are sufficiently close to the imaginary axis. The pattern that is exhibited in the right graphs of Fig. 4.11 dictates that a net damping value $|D(\omega_N)|$ that is moving consistently towards zero, implies the existence of poorly-damped poles whose damping factor decreases consistently, until they become marginally stable. In this case, the system would be on the verge of stability. In fact, for poorly-damped poles which are quite close to the imaginary axis, the relation between $|D(\omega_N)|$ and damping factor becomes almost linear. This provides the information that a certain rate of change in the net damping implies a similar rate of change in the damping factor of the concerned complex poles.

It is important to notice that the previous analysis reaches conclusions regarding

1. the stability of the system
2. the existence of poorly-damped poles
3. the progression of the damping factor of the poorly-damped poles, for a change of a critical variable

by only using information from the frequency analysis of the system, without explicitly solving the characteristic polynomial to identify specific poles and define which of them are possibly poorly damped. Another comment on the results is that a relatively large absolute value of the net-damping measured at the frequency ω_N , suggests that even if there are poorly-damped poles, they are sufficiently far away from the imaginary axis and the risk of instability is minimized.

4.6 Stability improvement

At this stage, an intervention is made to the control of the rectifier station by adding a filtering stage in an attempt to improve the closed-loop stability. The effects of this action are demonstrated and explained from a net-damping point of view, showing how each subsystem is individually affected and finally contributes to the overall stability improvement.

4.6.1 Notch filter in the control structure

A notch filter is essentially a 2nd order band-stop filter, centered at a selected frequency and having a dc-gain equal to unity. It is defined as

$$H_{\text{notch}}(s) = \frac{s^2 + 2\xi_1 \omega_n s + \omega_n^2}{s^2 + 2\xi_2 \omega_n s + \omega_n^2} \quad (4.49)$$

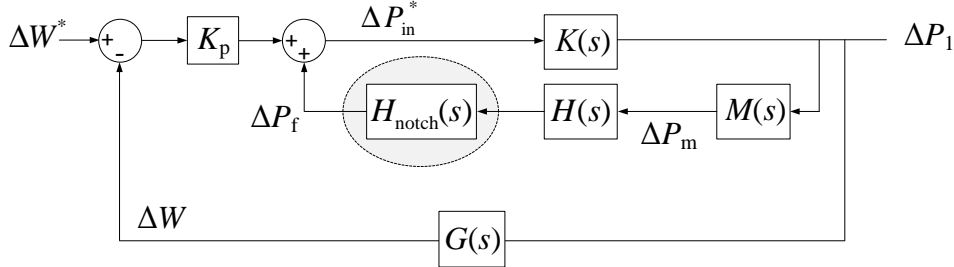


Fig. 4.12 SISO representation of the two-terminal VSC-HVDC model with a notch filter on the power-feedforward term.

where the three positive and adjustable parameters are ξ_1 , ξ_2 and ω_n . A mitigating behavior of the filter requires $\xi_1 < \xi_2$. The ratio of ξ_2/ξ_1 determines the depth of the notch centered at the selected frequency ω_n , where the larger the ratio, the deeper the notch. Additionally, the absolute values of ξ_1 , ξ_2 determine the Q -factor of the filter. The higher the Q , the narrower and "sharper" the notch is.

In the direct-voltage control structure of the rectifier, if there is a poorly damped resonance on the dc-side, the measured power P_m will contain an oscillation at the resonant frequency. This signal will pass through the power-feedforward term into the control process and affect the generated power reference signal. If this frequency appears in the frequency range where the direct-voltage controller is active, it is possible to mitigate it by introducing a notch filter centered at the resonant frequency. The ideal location is to add it in series with the pre-existing low-pass filter of the power-feedforward control branch. Considering the earlier control version shown in Fig. 4.4(a), the addition of the notch filter transforms the control path as in Fig. 4.12.

Under this modification, the new input admittance transfer function of the VSC rectifier station becomes

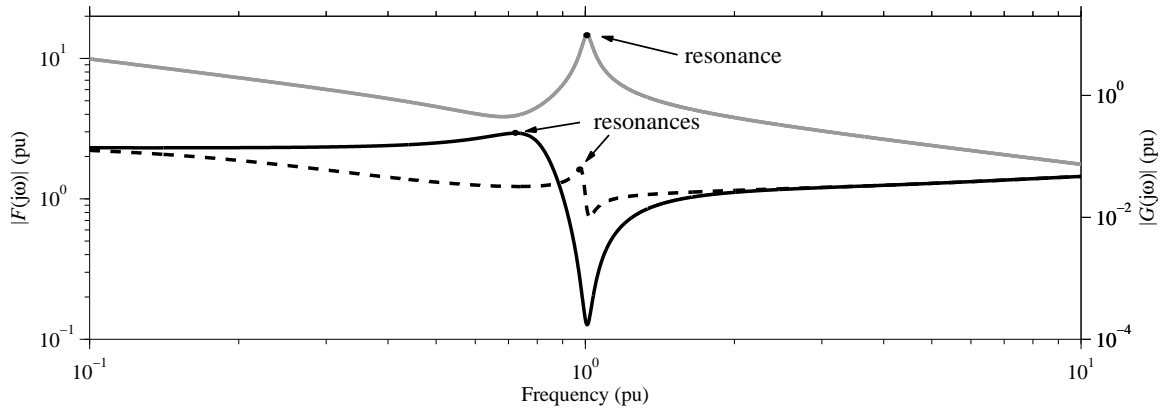
$$F(s) = K_p \frac{K(s)}{1 - K(s)H_{\text{notch}}(s)H(s)M(s)} \quad (4.50)$$

4.6.2 Damping effect of the notch filter

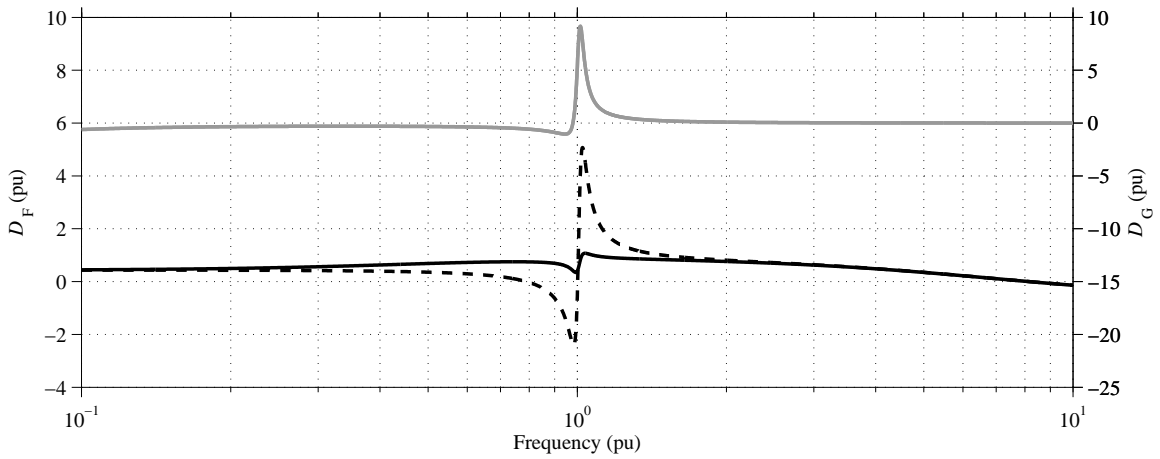
The effectiveness of the notch filter in enhancing the stability of the system is here demonstrated by using the examples described in Section (3.3.2) and in Section (4.4.1). The considered two-terminal VSC-HVDC link, featuring overhead dc-lines of 300 km in length, is found to be unstable for a power transfer of 0.9 pu. The poles of this configuration can be observed in Fig. 4.9 (indicated with "+") and it is obvious that there is a pair of unstable complex conjugate poles with a resonant frequency of 0.623 pu. The bandwidth of the direct-voltage controller is 0.955 pu. Therefore, the observed resonant frequency is within the limits of the controller's action and as stated earlier, the addition of a notch filter could offer some improvement.

It is here assumed that the properties of the system and the dc lines are not precisely known (as in reality) and the resonant frequency can not be calculated exactly at 0.623 pu. However, for a fair deviation of the considered system's parameters from the actual ones, the resonant frequency is not expected to deviate significantly. A certain experimental convention is thus considered.

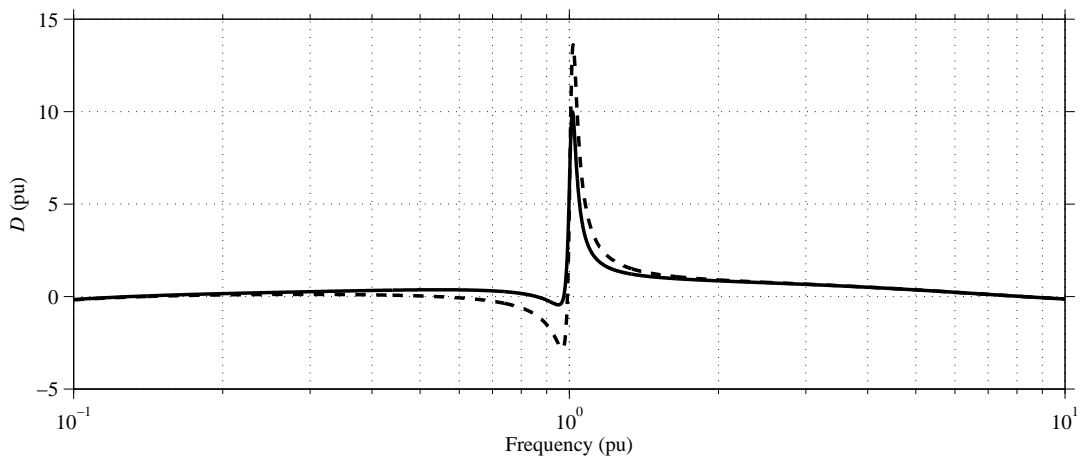
4.6. Stability improvement



(a) Solid black: $|F(j\omega)|$ with notch filter. Dashed black: $|F(j\omega)|$ without notch filter. Solid gray: $|G(j\omega)|$.



(b) Solid black: $D_F(\omega)$ with notch filter. Dashed black: $D_F(\omega)$ without notch filter. Solid gray: $D_G(\omega)$.



(c) Solid: $D(\omega)$ with notch filter. Dashed: $D(\omega)$ without notch filter.

Fig. 4.13 Frequency analysis of the system in the presence or without a notch filter.

TABLE 4.2. DAMPING ANALYSIS IN SYSTEM AFFECTED BY THE NOTCH FILTER

	Without notch filter	With notch filter
$ F(j\omega) $ resonant frequency (pu)	0.72	0.98
$ G(j\omega) $ resonant frequency (pu)	1.01	1.01
$D_F(\omega)$ at $ F(j\omega) $ resonance (pu)	0.15	0.44
$D_F(\omega)$ at $ G(j\omega) $ resonance (pu)	2.15	0.60
$D_G(\omega)$ at $ F(j\omega) $ resonance (pu)	-0.47	-0.36
$D_G(\omega)$ at $ G(j\omega) $ resonance (pu)	8.33	8.33
$D(\omega)$ at $ F(j\omega) $ resonance (pu)	-0.32	0.09
$D(\omega)$ at $ G(j\omega) $ resonance (pu)	10.48	8.93

Since the expected resonance is not too far from the bandwidth a_d of the direct-voltage control (at least the same order of magnitude), the notch filter is tuned to have a center frequency ω_n equal to a_d . The ξ_1 and ξ_2 parameters are also chosen so that the depth of the filter's notch is -20 dB and the Q -factor is not too high, so that relatively neighboring frequencies to ω_n can be sufficiently attenuated (including the resonant frequency of 0.623 pu).

It should also be mentioned that for too deep notches and frequencies close to ω_n , the phase of $H_{\text{notch}}(j\omega)$ starts reaching values close to -90° and 90° , instead of remaining close to 0° , as is the case for smaller notch depths. This is not desirable as signals could be introduced to the control with a severe distortion of their phase, deteriorating the closed-loop stability.

Figure 4.13 presents a frequency analysis of the system with and without a notch filter included. Specifically, in Fig. 4.13(a) it is possible to observe the $|F(j\omega)|$ and $|G(j\omega)|$ curves where, as expected, there is a single curve for the grid impedance since it is not affected by the presence of the notch filter. This also means that the damping $D_G(\omega)$ of $G(j\omega)$ in Fig. 4.13(b), as well as the open-loop resonance of the dc grid at a frequency of 1.01 pu, remains unaffected. Focusing on $|F(j\omega)|$, it is possible to notice that the addition of the notch filter has caused the open-loop resonance to move from 0.72 pu to 0.98 pu in frequency. The resonance spine has become sharper but the absolute value of $|F(j\omega)|$ at that frequency has decreased, indicating a smaller intensity in the related time domain oscillations.

The value of $D_F(\omega)$ at all open-loop resonances is always positive, as seen in Table 4.2. This means that to achieve stability, the net-damping $D(\omega)$ at those frequencies should be positive with a higher value implying an improved damping factor on the poorly-damped poles. As observed in Section (4.4.1) and repeated in Table 4.2, the system without a notch filter has a negative net-damping at the VSC input-admittance resonance, making the system unstable.

Since $D(\omega) = D_F(\omega) + D_G(\omega)$ and the $D_G(\omega)$ does not change, an improvement of stability by introducing the notch filter should translate into an upwards movement of the $D_F(\omega)$. An increase in the value of $D_F(\omega)$ in the open-loop resonant frequencies would increase the total $D(\omega)$ there, making it positive; thus ensuring stability. This can indeed be displayed in Fig. 4.13(b) where the introduction of the notch filter has caused $D_F(\omega)$ to raise in general and in fact be constantly positive in a wide spectrum around the critical resonant frequencies. As a result, the complete $D(\omega)$ curve has been raised as well in Fig. 4.13(c), in the same spectrum of frequencies with only a small negative notch relatively close to the input admittance resonance.

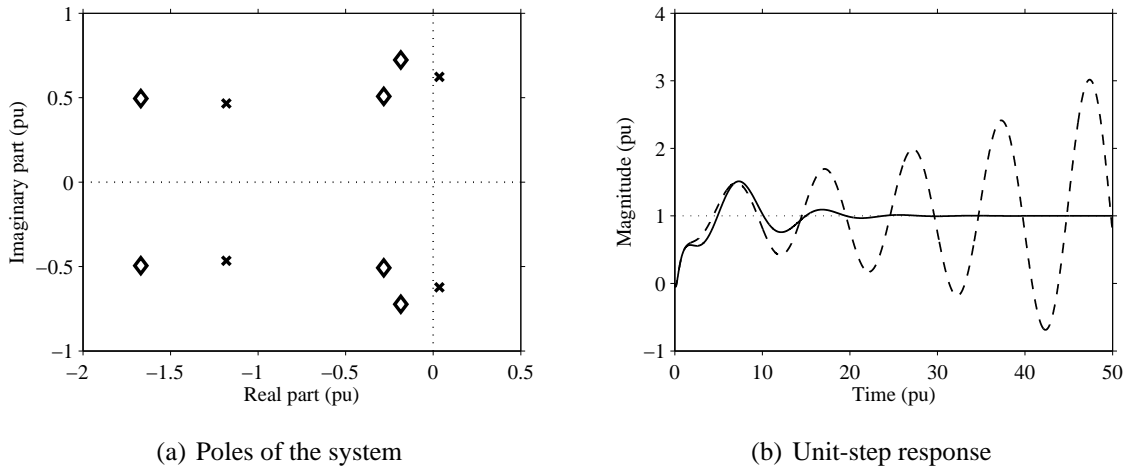


Fig. 4.14 Stability effect of notch filtering. (a) Pole placement for the system with (\diamond) and without (\times) a notch filter. An additional pole associated with the current-controller bandwidth a_{cc} is far to the left and is not shown here. (b) Unit-step response of the system with (solid line) and without (dashed line) a notch filter.

From a pole movement perspective, as depicted in Fig. 4.14(a), the addition of the notch filter has managed to

1. increased the damping of the already well-damped complex poles on the left side of the plot
2. stabilize the previously unstable complex poles
3. introduce a new pair of complex poles close to the now stabilized poles, but with much better damping than them, without significantly affecting final response of the system

Finally, from a time domain investigation of the system in Fig. 4.14(b), it is observed that the initial stages of the unit-step response of the system is only slightly slower when a notch filter is used. This is attributed to the newly introduced complex pole pair, whose relatively small real part implies a contribution with slow dynamics. However, the major comment is that the system is now stable with a quick damping of the oscillation which has been excited, only after approximately 2 periods.

A conventional pole movement approach cannot directly explain the improvement in the stability of the system with the introduction of the notch filter, but merely depict the updated pole location. Nevertheless, the net damping approach clearly offers an explanation the phenomenon. While the grid impedance and its damping remained unaltered, the notch filter incurred an increase solely in the damping of the VSC input admittance causing the total damping $D(\omega)$ of the system to be high enough and positive at all of the open-loop resonances, thereby stabilizing it. Concluding, any intervention, either in the dc-transmission system or the control of the rectifier station (or both), that can increase $D(\omega)$ in the critical resonant points will provide better damping characteristics for the overall system and possibly stabilize an otherwise unstable configuration.

4.7 Summary

In this chapter, the dynamics of the generic two-terminal VSC-HVDC system has been studied, using a frequency domain approach. To assist this type of analysis, the system was modeled as a SISO feedback system. This comprised of two subsystems:

1. An input-admittance transfer function $F(s)$, describing the way the direct-voltage controlled VSC subsystem reacts to a given change of direct voltage at its terminals, by injecting a controlled amount of active power to the dc grid.
2. A feedback transfer function $G(s)$, describing the way the passive dc-grid subsystem reacts to an injection of power from the direct-voltage controlled VSC, by altering the voltage at the dc-side capacitor of the latter.

Initially, the passivity approach is utilized. If both subsystems are passive, the SISO is stable as well but at least one non-passive subsystem serves as an indication that the system could be unstable. The dc-grid transfer function $G(s)$ is naturally unstable but for low values of transmission line inductance (cable-type of line), it can be approximated by the marginally stable $G'(s)$, which is also passive. The latter means that it cannot be the source of instability in the system. If $F(s)$ is stable, the closed-loop SISO system stability can then be assessed by the passivity properties of $F(s)$. For this reason, a conventional PI voltage control structure without power-feedforward is chosen, rendering $F(s)$ stable. It was shown that high values in the bandwidth a_d rendered $F(s)$ non-passive and the SISO was indeed unstable. This demonstrated the usefulness of the passivity approach on providing a good indication on the closed-loop stability in the frequency domain.

However, for other types of direct-voltage controllers or different types of transmission lines e.g. overhead lines, $F(s)$ can be unstable and $G(s)$ may no longer be approximated by a marginally stable $G'(s)$. Hence, the passivity approach cannot be used. The net-damping criterion was thus considered, because it does not require passive or even stable subsystem transfer functions to provide answers regarding the stability of the closed-loop SISO system. In systems with a direct-voltage controller with power-feedforward and overhead lines in the dc grid, the net-damping criterion demonstrated very accurate predictions on the closed-loop stability and a relation was derived, correlating the absolute net-damping value and the actual damping factor of the poorly-damped poles of the system. Finally, the stabilizing effect of adding a notch filter in the direct-voltage controller of an unstable system was observed and assessed through a net-damping approach.

Having utilized a frequency domain approach in the analysis of the closed-loop stability of the two-terminal VSC-HVDC system, the following chapter has the same goal but attempts to analytically describe the poles of a simplified version of the same system. In this way, it is desired to derive closed-form expressions, containing all the physical and control parameters of the system, thereby providing immediate information on the real and imaginary part of the system's poles and thereby, the closed-loop stability and damping.

Chapter 5

Stability in two-terminal VSC-HVDC systems: analytical approach

A numerical approach and thereby pole movement of the system's eigenvalues is a very powerful tool to investigate the stability of a system and the impact of different variables (either system or control variables) on the system performance. However, one flaw in this kind of approach is that it does not provide a proper understanding of the impact of each parameter on the system stability. This is where the major advantage of an analytical over the classical numerical approach lies; by using an analytical method, the eigenvalues of the system can be expressed in symbolic form and this provides important assistance in getting a deeper understanding on how each single parameter impacts the stability and, more in general, the pole movement. Furthermore, with the analytical approach it is possible to understand how a certain parameter contributes to the placement of a pole and can therefore be utilized in understanding how a system can be simplified for easier further analysis.

This chapter focuses on the derivation of closed-form analytical expressions for the description of a system's eigenvalues in terms of their real and imaginary part. The objective is to provide a tool in thoroughly understanding the dynamics of the system, while at the same time maintaining a desired level of accuracy on predicting the approximate location of the poles. One method to achieve this is the existing *LR* iterative algorithm, an overview of which is given here. Additionally, a new method for the analytical derivation of eigenvalues, addressed to as the *Similarity Transformation Matrix* (SMT), is proposed and its concept and applicability are analyzed. Since both of the examined methods utilize the state-space representation of a system, the chapter concludes with the derivation of the state-space models of two systems whose eigenvalues are desired to be analytically described: (a) a two-terminal VSC-HVDC system and (b) the dc-transmission link that connects the two VSC stations of the former.

5.1 Analytical investigation of dynamic stability

As observed earlier, a dynamic system may become poorly damped or even unstable under certain conditions. A deeper knowledge of how a specific parameter (or group of parameters)

appears in the eigenvalue expressions of a system, is of importance in understanding the mechanisms that govern the stability of the latter and can be further used as a tool for its proper design. Considering VSC-HVDC applications, poorly-damped resonances between the converter stations and the transmission system can appear both in point-to-point and multiterminal configurations. An analytical description of the system poles, in terms of damping and characteristic frequency, can provide useful information on the way the control parameters, amount of power transfer, direct-voltage level or values of passive elements can contribute to conditions of poor-dynamic performance. The derivation of analytical expressions can therefore be used to predict and correct the behavior of a system of future consideration or modify an existing VSC-HVDC installation to improve its dynamic properties. However, a great obstacle is that the analytical description of the eigenvalues of a high-order system is challenging and in many cases impossible. Although the eigenvalues of polynomials with a degree up to the 4th can be found analytically, the resulting expressions are usually very complex and uninterpretable if the degree is greater than two. Modeling a VSC-HVDC connection maintaining a good level of complexity, can lead to a system whose order can easily surpass the 10th order. However, under valid approximations, the description of a two-terminal VSC-HVDC connection can be reduced to a 4th-order system. Any further attempt to reduce the system's order would imply the sacrifice of fundamental control components or critical passive elements that define the dynamic response of the system. Other approaches, as the ones described in the previous chapter, must be considered if a more detailed model of the system is needed.

5.1.1 Cubic equation

If it is possible to represent a system by a third order characteristic polynomial, there is an analytical way to derive the symbolic eigenvalues. The general form of the cubic equation is

$$ax^3 + bx^2 + cx + d = 0 \quad (5.1)$$

with $a \neq 0$. The coefficients a, b, c and d can belong to any field but most practical cases consider them to be real (as will be the case below). Every cubic equation with real coefficients will have at least one real solution x_1 , with x_2 and x_3 being either both real or a complex-conjugate pair.

The general formula for the analytical derivation of the equation's roots is, as in [63],

$$x_k = -\frac{1}{3a} \left(b + u_k C + \frac{\Delta_0}{u_k C} \right), \quad k \in \{1, 2, 3\} \quad (5.2)$$

5.1. Analytical investigation of dynamic stability

where

$$u_1 = 1, \quad u_2 = \frac{-1+i\sqrt{3}}{2}, \quad u_3 = \frac{-1-i\sqrt{3}}{2}$$

$$C = \sqrt[3]{\frac{\Delta_1 + \sqrt{\Delta_1^2 - 4\Delta_0^3}}{2}}$$

$$\Delta_1 = b^2 - 3ac$$

$$\Delta_2 = 2b^3 - 9abc + 27a^2d$$

Even though (5.2) does not appear complicated, the existence of the root $\sqrt[3]{}$ within it is very problematic if there is a complex-conjugate pair of solutions, whose real and imaginary parts are desired to be treated separately. It is possible to derive such expressions for complex roots of the equation, as in [64], but they always include complex cosines and arc-cosines. This is not practical when it comes to presenting a direct relation between a coefficient of the cubic equation and the final roots. Nevertheless, complex systems can rarely be approximated by a third-order characteristic polynomial, rendering the value of (5.2) even more questionable.

5.1.2 Quartic equation

As mentioned earlier and will be shown later, a two-terminal VSC-HVDC system can be represented, at least in general terms, by a 4th-order model, whose analytically derived eigenvalues can theoretically be found. As with the cubic equation in the previous section, the general form of the quartic equation is

$$ax^4 + bx^3 + cx^2 + dx + e = 0 \quad (5.3)$$

Every quartic equation with real coefficients will have: a) four real roots, b) two real roots and a complex-conjugate root pair or, c) two complex-conjugate root pairs. The general formula for the analytical derivation of the equation's roots is, as in [65],

$$\begin{aligned} x_{1,2} &= -\frac{b}{4a} - S \pm \frac{1}{2} \sqrt{-4S^2 - 2p + \frac{q}{S}} \\ x_{3,4} &= -\frac{b}{4a} + S \pm \frac{1}{2} \sqrt{-4S^2 - 2p - \frac{q}{S}} \end{aligned} \quad (5.4)$$

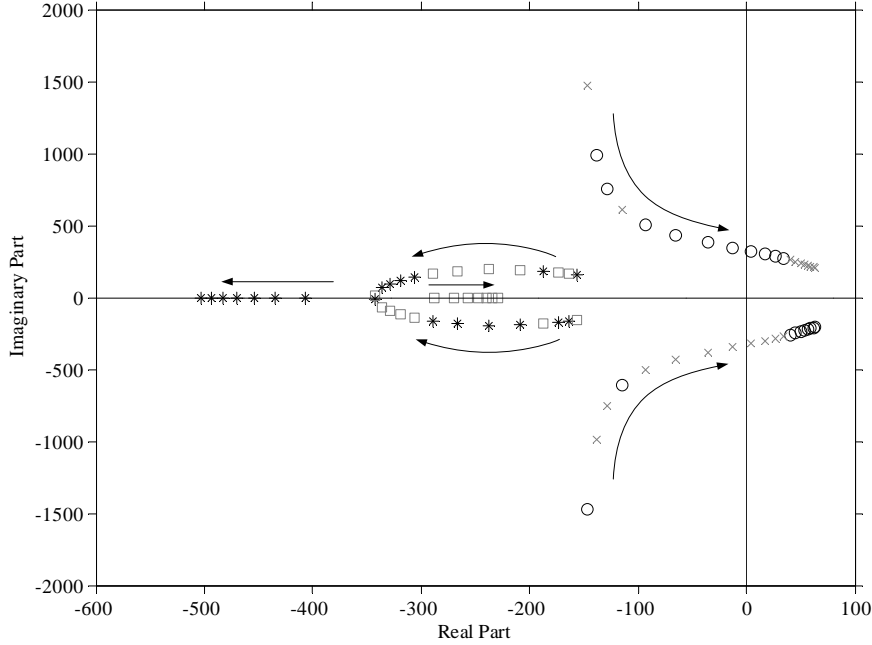


Fig. 5.1 Roots of a 4th order characteristic polynomial of a simplified VSC-HVDC system; x_1 (gray cross), x_2 (black circle), x_3 (gray square) and x_4 (black asterisk)

where

$$p = \frac{8ac-3b^2}{8a^2}, \quad q = \frac{b^3-4abc+8a^2d}{8a^3}$$

$$S = \frac{1}{2} \sqrt{-\frac{2}{3}p + \frac{1}{3a} \left(Q + \frac{\Delta_0}{Q} \right)}$$

$$Q = \sqrt[3]{\frac{\Delta_1 + \sqrt{\Delta_1^2 - 4\Delta_0^3}}{2}}$$

$$\Delta_0 = c^2 - 3bd + 12ae$$

$$\Delta_1 = 2c^3 - 9bcd + 27b^2e + 27ad^2 - 72ace$$

The full expansion of (5.4) is too large to be presented here, implying that the practical value of such expressions is doubtful. Just as in the roots of the cubic equation, the existence of the root $\sqrt[3]{\quad}$ within the quadratic solutions is very problematic if there is a complex-conjugate pair of solutions, whose real and imaginary parts are desired to be explicit in form. Another problem is related to the consistency of the solutions in (5.4). Unfortunately, each of the x_1 , x_2 , x_3 and x_4 expressions cannot consistently describe a selected root of the system while performing a variation of the system's coefficients. This can be viewed in Fig. 5.1 where the roots of the 4th order characteristic polynomial of a simplified VSC-HVDC system are plotted using (5.4). The cable length of this system is varied from 20-400 km in steps of 20 km, causing a movement of the eigenvalues along the arrow-paths indicated in the figure. The system has a pair of poles which retains a complex-conjugate form for the whole cable-length variation, as well as two

other poles that start as a complex-conjugate pair and then splits into 2 real poles. Each of x_1 , x_2 , x_3 and x_4 is plotted with a distinctive marker.

As one can see, the root expressions are not consistent, with all x_1 , x_2 , x_3 and x_4 failing to track their dedicated pole. This means that even if the expressions in (5.4) present a simple form, they are not useful in describing specific poles.

5.1.3 Alternative solutions

Even if it is theoretically possible to derive the analytical poles of a 3rd and 4th order system, it was shown that there are practical obstacles that prevent it from taking place if the exact solutions are to be described. A solution to this problem is to develop approximating methods that can provide such analytical descriptions for equivalent models having poles that are sufficiently close to those of the initial systems.

In [28, 29, 66], the approximate solutions of the generalized eigenvalue problem $\det(s\mathbf{B} - \mathbf{A})=0$ are sought, where the matrix pencil (\mathbf{A}, \mathbf{B}) is computed by the semistate equations of an electronic circuit. The solutions are found by an extensive elimination of those entries in \mathbf{A} and \mathbf{B} that are insignificant to the computation of a selected eigenvalue, until the characteristic polynomial of the system becomes 1st or 2nd order. This method has been developed into the commercial tool "Analog Insydes" as a Mathematica[®] application package for modeling, analysis and design of analogue electronic circuits. However, this process may not always be successful and could lead to a significant loss of information. Following a different approach, the poles of an analogue circuit are calculated through the time constant matrix of the system in [30]. However, only the first two dominant poles are computed and any other pole requires major simplification of the system. In [31–33, 67], the *LR* iterative method is used to calculate the symbolic poles and zeros of analogue electronic circuits, based on their state matrix. This involves intricate computations which may quickly exceed the computational capabilities of a typical computer [32]. Subsequently, the state matrix should not exceed 6×6 in size while there should be no more than four symbolic variables. Nevertheless, numerous simplifications are still required to produce compact final expressions. Despite these problems, the *LR* method appears to be the most adequate candidate among the mentioned methods, in attempting to analytically describe a relatively high-order system.

5.2 Approximating methods

In this section, two major approximating methods are presented, in an effort to establish a foundation for the analytical investigation of the eigenvalues of a VSC-HVDC system. The *LR* method is described in detail with special mention to its potential in symbolic approximation of eigenvalues, along with its advantages and disadvantages. The other method is a newly proposed algorithm which tries to achieve the same goal of analytically describing the eigenvalues of a dynamic system, but in a non-iterative way.

In this thesis it is desired to mainly investigate the dynamics of a two-terminal VSC-HVDC system. As will be shown later in Section (5.3.3), such a system can be sufficiently simplified to a 4th order state-space representation. Given the task of extracting symbolic eigenvalues, a similarity transformation is supposed to be applied to the system's state matrix. As such, matrix \mathbf{N} is equated to the latter and will be 4×4 in size. The system is dynamically described by four eigenvalues. Without replacing numerical values to the symbolic entries of the matrix, it is not possible to have an initial idea on the nature of these eigenvalues. There are three possible cases:

1. All eigenvalues are real
2. There are two complex-conjugate eigenvalue pairs
3. There is one complex-conjugate eigenvalue pair and two real eigenvalues

Even if the nature of the eigenvalues was known for a certain choice of numerical values for the variables of matrix \mathbf{N} , a slightly different choice of values might totally change the nature of the eigenvalues. This is of great concern if it is desired to obtain analytical solutions for the eigenvalues and observe the results while sweeping the values of certain variables within a wide interval. In this case, the obtained solutions may prove inconsistent.

To overcome this problem, it is assumed that the nature of the eigenvalues is unknown. However, as mentioned earlier, a 2×2 sub-matrix along the diagonal of a quasi-triangular matrix hints the existence of two eigenvalues which can be either a complex-conjugate eigenvalue pair or two real eigenvalues. Therefore, all three of the previous cases can be covered if $\tilde{\mathbf{N}}$ is quasi-triangular with two blocks of 2×2 sub-matrices along its diagonal while one of the remaining 2×2 blocks is filled with zeros, depending on whether $\tilde{\mathbf{N}}$ is upper or lower triangular. For the lower triangular case, $\tilde{\mathbf{N}}$ has the following form

$$\tilde{\mathbf{N}} = \begin{bmatrix} \boxed{\begin{matrix} a_{1,1} & a_{2,1} \\ a_{2,1} & a_{2,2} \end{matrix}} & \begin{matrix} 0 & 0 \\ 0 & 0 \end{matrix} \\ \begin{matrix} a_{3,1} & a_{3,2} \\ a_{4,1} & a_{4,2} \end{matrix} & \boxed{\begin{matrix} a_{3,3} & a_{3,4} \\ a_{4,3} & a_{4,4} \end{matrix}} \end{bmatrix} \quad (5.10)$$

where each of the 2×2 enclosed sub-matrices is related to two eigenvalues. The block diagonal matrix $\tilde{\mathbf{N}}$ will have at least one zero non-diagonal block matrix, which implies that at least four elements of $\tilde{\mathbf{N}}$ should be equal to zero; this leads to four equations to be solved.

A 4×4 similarity transformation matrix \mathbf{P} is used to perform the similarity transformation of \mathbf{N} . Its general form is

$$\mathbf{P} = \begin{bmatrix} x_{11} & x_{12} & x_{13} & x_{14} \\ x_{21} & x_{22} & x_{23} & x_{24} \\ x_{31} & x_{32} & x_{33} & x_{34} \\ x_{41} & x_{42} & x_{43} & x_{44} \end{bmatrix} \quad (5.11)$$

Performing the similarity transformation of \mathbf{N} based on \mathbf{P} gives

$$\tilde{\mathbf{N}} = \mathbf{P}^{-1} \mathbf{N} \mathbf{P} = \begin{bmatrix} x_{11} & x_{12} & x_{13} & x_{14} \\ x_{21} & x_{22} & x_{23} & x_{24} \\ x_{31} & x_{32} & x_{33} & x_{34} \\ x_{41} & x_{42} & x_{43} & x_{44} \end{bmatrix}^{-1} \cdot \mathbf{N} \cdot \begin{bmatrix} x_{11} & x_{12} & x_{13} & x_{14} \\ x_{21} & x_{22} & x_{23} & x_{24} \\ x_{31} & x_{32} & x_{33} & x_{34} \\ x_{41} & x_{42} & x_{43} & x_{44} \end{bmatrix} \Rightarrow$$

5.2. Approximating methods

$$\tilde{\mathbf{N}} = \begin{bmatrix} y_{11} & y_{12} & y_{13} & y_{14} \\ y_{21} & y_{22} & y_{23} & y_{24} \\ y_{31} & y_{32} & y_{33} & y_{34} \\ y_{41} & y_{42} & y_{43} & y_{44} \end{bmatrix} = \begin{bmatrix} \mathbf{Y}_{11} & \mathbf{Y}_{12} \\ \mathbf{Y}_{21} & \mathbf{Y}_{22} \end{bmatrix} \quad (5.12)$$

The form of matrix $\tilde{\mathbf{N}}$ must comply with (5.10), therefore it is required that

$$\mathbf{Y}_{12} = 0 \Rightarrow \begin{bmatrix} y_{13} & y_{14} \\ y_{23} & y_{24} \end{bmatrix} = 0 \Rightarrow \begin{cases} y_{13} = 0 \\ y_{14} = 0 \\ y_{23} = 0 \\ y_{24} = 0 \end{cases} \quad (5.13)$$

Equation (5.13) dictates that the definition of an appropriate transformation matrix \mathbf{P} requires the solution of four equations. However, each of y_{13} , y_{14} , y_{23} and y_{24} is a non-linear function of all elements of \mathbf{P} which renders the solution of (5.13) very cumbersome. Additionally, if all sixteen elements of \mathbf{P} are expected to be defined symbolically, a solution is theoretically not possible to be reached since there are four equations to be solved with sixteen unknown variables to be defined. If a solution is expected to be found, only four entries of \mathbf{P} are considered to be symbolic variables while the rest must be replaced with numerical values. The more zero entries matrix \mathbf{P} has, the easier the task of solving (5.13) becomes.

Even limiting the symbolic entries of \mathbf{P} to only four, does guarantee the solution of (5.13) by default. A random choice of the four necessary elements of \mathbf{P} will most likely lead to a large expression of \mathbf{P}^{-1} which, in turn, shall lead to very complex expressions of y_{13} , y_{14} , y_{23} and y_{24} . Consequently, it is important to ensure such a choice of elements in \mathbf{P} that \mathbf{P}^{-1} will have a simple form.

By definition, the inverse of matrix \mathbf{P} is

$$\mathbf{P}^{-1} = \frac{1}{\det(\mathbf{P})} \text{adj}(\mathbf{P}) \quad (5.14)$$

A first step of simplification is to choose such a \mathbf{P} that $\det(\mathbf{P})$ is as simple as possible. The best choice is to consider a triangular \mathbf{P} with all the elements across its diagonal being equal to 1. In this case, $\det(\mathbf{P})=1$. This leads to the expression

$$\mathbf{P} = \begin{bmatrix} 1 & x_{12} & x_{13} & x_{14} \\ 0 & 1 & x_{23} & x_{24} \\ 0 & 0 & 1 & x_{34} \\ 0 & 0 & 0 & 1 \end{bmatrix} \quad (5.15)$$

As stated earlier, only four of the variable entries in (5.15) can be kept in symbolic form. Choosing to equate terms x_{12} and x_{34} to 0, the final form of \mathbf{P} and corresponding \mathbf{P}^{-1} are

$$\mathbf{P} = \begin{bmatrix} 1 & 0 & x_{13} & x_{14} \\ 0 & 1 & x_{23} & x_{24} \\ 0 & 0 & 1 & 0 \\ 0 & 0 & 0 & 1 \end{bmatrix} = \begin{bmatrix} \mathbf{I} & \mathbf{X} \\ \mathbf{0} & \mathbf{I} \end{bmatrix} \quad (5.16)$$

$$\mathbf{P}^{-1} = \begin{bmatrix} 1 & 0 & -x_{13} & -x_{14} \\ 0 & 1 & -x_{23} & -x_{24} \\ 0 & 0 & 1 & 0 \\ 0 & 0 & 0 & 1 \end{bmatrix} = \begin{bmatrix} \mathbf{I} & -\mathbf{X} \\ \mathbf{0} & \mathbf{I} \end{bmatrix} \quad (5.17)$$

This choice has given \mathbf{P} and \mathbf{P}^{-1} a convenient form, where the remaining four unknown entries are clustered in a 2×2 block sub-matrix. This will ease further steps of the analysis. The similarity transformation of \mathbf{N} can now be performed, utilizing (5.15) and (5.16)

$$\begin{aligned} \tilde{\mathbf{N}} &= \mathbf{P}^{-1}\mathbf{N}\mathbf{P} = \begin{bmatrix} \mathbf{I} & -\mathbf{X} \\ \mathbf{0} & \mathbf{I} \end{bmatrix} \cdot \begin{bmatrix} \mathbf{N}_{11} & \mathbf{N}_{12} \\ \mathbf{N}_{21} & \mathbf{N}_{22} \end{bmatrix} \cdot \begin{bmatrix} \mathbf{I} & \mathbf{X} \\ \mathbf{0} & \mathbf{I} \end{bmatrix} \Rightarrow \\ \tilde{\mathbf{N}} &= \begin{bmatrix} \mathbf{N}_{11} - \mathbf{X}\mathbf{N}_{21} & \mathbf{N}_{11}\mathbf{X} - \mathbf{X}\mathbf{N}_{21}\mathbf{X} + \mathbf{N}_{12} - \mathbf{X}\mathbf{N}_{22} \\ \mathbf{N}_{21} & \mathbf{N}_{21}\mathbf{X} + \mathbf{N}_{22} \end{bmatrix} = \begin{bmatrix} \mathbf{Y}_{11} & \mathbf{Y}_{12} \\ \mathbf{Y}_{21} & \mathbf{Y}_{22} \end{bmatrix} \end{aligned} \quad (5.18)$$

The condition expressed by (5.13) needs to be fulfilled, thus the 2×2 sub-matrix \mathbf{Y}_{12} must suffice the following

$$\mathbf{N}_{11}\mathbf{X} - \mathbf{X}\mathbf{N}_{21}\mathbf{X} + \mathbf{N}_{12} - \mathbf{X}\mathbf{N}_{22} = \begin{bmatrix} y_{13} & y_{14} \\ y_{23} & y_{24} \end{bmatrix} = \mathbf{0} \quad (5.19)$$

If (5.19) can be solved, resulting in an analytical definition of the entries x_{13} , x_{14} , x_{23} and x_{24} , the eigenvalues of the system can be determined by the following 2×2 block matrices of (5.18)

$$\mathbf{Y}_{11} = \mathbf{N}_{11} - \mathbf{X}\mathbf{N}_{21} \quad (5.20)$$

$$\mathbf{Y}_{22} = \mathbf{N}_{21}\mathbf{X} + \mathbf{N}_{22} \quad (5.21)$$

Each of \mathbf{Y}_{11} and \mathbf{Y}_{22} will provide two eigenvalues in the general form of (5.7). Provided that x_{13} , x_{14} , x_{23} and x_{24} have been defined analytically and matrix \mathbf{N} is maintained in symbolic form, the previous eigenvalues will be completely analytical expressions.

It is important to notice that the closed form solution of (5.19) cannot be guaranteed and even if it is possible to be defined, the derived expressions can be so large that offer no practical advantage in trying to describe the system's eigenvalues symbolically. It is possible however to apply simplifications which allow the approximate solution of (5.19). In this case, variables x_{13} , x_{14} , x_{23} and x_{24} are still derived in analytical form but are not completely accurate, compared to the solution provided by a numerical solution of (5.19) when all variables are replaced with numerical values. The amount of deviation between the corresponding approximate symbolic matrix \mathbf{P} and its accurate numerical counterpart defines the accuracy of the analytical model.

5.2.2 The LR algorithm

The *LR* algorithm belongs to an extended family of related algorithms, called "Algorithms of decomposition type" [69], that calculate eigenvalues and eigenvectors of matrices. The two best known members of this family are the *LR* and *QR* algorithms [70]. Other related, but less used,

algorithms in the same family are the *SR* algorithm [71] and the *HR* algorithm [72]. The authors in [69] develop a general convergence theory for the previous algorithms of decomposition type, while an effort to answer to the question of how such algorithms can be implemented in practical problems is performed in [73].

The common principle in the attempt of all these algorithms to calculate the eigenvalues of a matrix \mathbf{A} , is the use of an iterative action which bears the following generic characteristics

1. In iteration m , a matrix \mathbf{A}_m whose eigenvalues are expected to be calculated, is provided as an input to the algorithm.
2. Matrix \mathbf{A}_m is decomposed into a number of matrices of special form.
3. These matrices are used to construct a matrix \mathbf{A}_{m+1} which is *similar* to \mathbf{A}_m , thus having the same eigenvalues.
4. The matrices produced by the decomposition of \mathbf{A}_m , are appropriately created such that \mathbf{A}_{m+1} approaches in form a triangular or quasi-triangular matrix as in (5.6) i.e. the numerical value of the elements of its upper or lower triangular approach zero.
5. Matrix \mathbf{A}_{m+1} serves as the input of iteration $m + 1$.
6. The iterations are terminated when the form of the final matrix output \mathbf{A}_m is sufficiently close to a triangular or quasi-triangular form. The approximate eigenvalues can then be extracted from the diagonal elements of \mathbf{A}_m .
7. Matrix \mathbf{A} is the input to the first iteration of the algorithm.

QR algorithm

The *QR* algorithm is currently the most popular method for calculating the eigenvalues of a matrix [74]. A descendant of Rutishauser's *LR* algorithm [75, 76], it was developed independently by Francis [77, 78] and Kublanovskaya [79]. The fundamental idea in the iterative process of this algorithm is to perform a *QR decomposition* in each iteration i.e. decompose a matrix of interest by equalizing it to a product of an orthogonal matrix and an upper triangular matrix.

In principle, let \mathbf{A} be the real matrix whose eigenvalues are to be computed and define $\mathbf{A}_1 = \mathbf{A}$. At the m^{th} iteration (starting with $m=1$), the *QR* decomposition $\mathbf{A}_m = \mathbf{Q}_m \mathbf{R}_m$ is computed where \mathbf{Q}_m is an orthogonal matrix (i.e., $\mathbf{Q}^T = \mathbf{Q}^{-1}$) and \mathbf{R}_m is an upper triangular matrix. The matrices \mathbf{Q}_m and \mathbf{R}_m are then used to construct the matrix $\mathbf{A}_{m+1} = \mathbf{R}_m \mathbf{Q}_m$, used as input in the following iteration. Note that

$$\mathbf{A}_{m+1} = \mathbf{R}_m \mathbf{Q}_m = \mathbf{Q}_m^{-1} \mathbf{Q}_m \mathbf{R}_m \mathbf{Q}_m = \mathbf{Q}_m^{-1} \mathbf{A}_m \mathbf{Q}_m$$

which is a similarity transformation, proving that all the \mathbf{A}_m matrices are *similar* and have the same eigenvalues. Under certain conditions [80], the matrices \mathbf{A}_m gradually converge to a triangular type of matrix, allowing the extraction of the eigenvalues from the diagonal elements.

Even though the *QR* algorithm converges in much fewer iterations than the *LR* algorithm, matrices \mathbf{Q}_m and \mathbf{R}_m can be very intricate in form, starting with the very first iteration. As a result, the *QR* algorithm is not deemed the best approach for symbolic calculations but is still the best solution for the numerical calculation of the eigenvalues of a matrix.

LR algorithm

The *LR* algorithm is a major representative of the "Algorithms of decomposition type" and was first introduced by Rutishauser [75] [76]. The main idea behind it is the application of a form of the *LU decomposition* of a matrix during each iteration of the algorithm. In numerical analysis, LU decomposition (where "LU" stands for "Lower Upper") factorizes a matrix as the product of a lower triangular matrix and an upper triangular matrix. The LU decomposition can be regarded as the matrix form of Gaussian elimination.

The algorithm follows the typical iterative steps described earlier. Let an $n \times n$ non-singular matrix \mathbf{A} be the subject of investigation. This matrix will serve as the initial input to the algorithm. In the m^{th} repetition of the algorithm, matrix \mathbf{A}_m (calculated in the previous iteration and is the input of the current iteration) is factorized to a lower triangular matrix and an upper triangular matrix as below

$$\mathbf{A}_m = \begin{bmatrix} a_{1,1} & & \cdots & & a_{1,n} \\ & a_{2,2} & & & \\ & & \ddots & & \\ \vdots & & & a_{k,k} & \vdots \\ & & & & \ddots \\ & & & & & a_{n-1,n-1} \\ a_{n,1} & & \cdots & & & a_{n,n} \end{bmatrix} = \mathbf{L}_m \cdot \mathbf{U}_m \quad (5.22)$$

$$\mathbf{L}_m = \begin{bmatrix} 1 & & & & & \\ & 1 & & & & \mathbf{0} \\ & & \ddots & & & \\ & & & 1 & & \\ & & & & \ddots & \\ \mathbf{l}_{i,j} & & & & & 1 \\ & & & & & & 1 \end{bmatrix} \quad (5.23)$$

$$\mathbf{U}_m = \begin{bmatrix} u_{1,1} & & & & & \\ & u_{2,2} & & & & \mathbf{u}_{i,j} \\ & & \ddots & & & \\ & & & u_{k,k} & & \\ & & & & \ddots & \\ \mathbf{0} & & & & & u_{n-1,n-1} \\ & & & & & & u_{n,n} \end{bmatrix} \quad (5.24)$$

5.2. Approximating methods

Notice that \mathbf{L}_m in (5.23) is not just a lower triangular matrix but has a unitary diagonal. The formulation of the \mathbf{L}_m and \mathbf{U}_m matrix in each iteration is performed via the following algorithm

$$\begin{aligned}
 & \text{Initialization } \left\{ \begin{array}{l} \mathbf{L}_m = \text{Identity matrix of size } n \\ \mathbf{U}_m = \mathbf{A}_m \end{array} \right\} \\
 & \text{for } (i = 1, i \leq n - 1, i = i + 1) \\
 & \quad \text{for } (j = i + 1, j \leq n, j = j + 1) \\
 & \quad \left\{ \begin{array}{l} (\text{Row } j \text{ of } \mathbf{U}_m) = (\text{Row } j \text{ of } \mathbf{U}_m) - \frac{u_{j,i}}{u_{i,i}} \cdot (\text{Row } i \text{ of } \mathbf{U}_m) \\ l_{j,i} = \frac{u_{j,i}}{u_{i,i}} \end{array} \right. \quad (5.25) \\
 & \quad \left. \right\} \\
 & \quad \text{end} \\
 & \text{end}
 \end{aligned}$$

As described above, during the formulation of \mathbf{L}_m and \mathbf{U}_m , a division by the elements $u_{i,i}$ is performed. This could cause problems if any $u_{i,i}$ is equal to zero (something not uncommon in sparse matrices). In order to avoid this issue, a partial pivoting of matrix \mathbf{A}_m must be performed in principle, ensuring that the elements in the diagonal of the initial \mathbf{U}_m are non-zero. However, a zero element in the diagonal does not automatically imply a singularity. As shown in (5.25), a row of \mathbf{U}_m will appropriately update its successive row, altering its values and possibly turn a zero diagonal entry into a non-zero entity; thus eliminating the problem. In practice, pivoting matrix \mathbf{A} so that $a_{1,1} \neq 0$ is sufficient to avoid subsequent singularities.

Following the previous decomposition, a new matrix \mathbf{A}_{m+1} is constructed such that

$$\mathbf{A}_{m+1} = \mathbf{U}_m \cdot \mathbf{L}_m = \begin{bmatrix} b_{1,1} & & \cdots & & b_{1,n} \\ & b_{2,2} & & & \\ & & \ddots & & \\ \vdots & & & b_{k,k} & \vdots \\ & & & & \ddots \\ & & & & & b_{n-1,n-1} \\ b_{n,1} & & \cdots & & & b_{n,n} \end{bmatrix} \quad (5.26)$$

This new matrix bears the feature of

$$\mathbf{A}_{m+1} = \mathbf{U}_m \mathbf{L}_m = \mathbf{L}_m^{-1} \mathbf{L}_m \mathbf{U}_m \mathbf{L}_m = \mathbf{L}_m^{-1} \mathbf{A}_m \mathbf{L}_m$$

which is a similarity transformation, proving that all the \mathbf{A}_m matrices are *similar* and have the same eigenvalues. Therefore, in the end of every iteration, all resulting matrices \mathbf{A}_{m+1} retain the same eigenvalues as the original matrix \mathbf{A} . The result of performing the action described in (5.26) is that when \mathbf{A}_{m+1} is compared to \mathbf{A}_m , the elements in the lower triangular portion of \mathbf{A}_{m+1} have smaller values than the same elements in \mathbf{A}_m . The rest of the entries of \mathbf{A}_{m+1} have also been altered during the transformation in (5.26) but this has had no effect on the eigenvalues which are the same as those of \mathbf{A}_m .

eigenvalues, there will be y 2×2 sub-matrices along the diagonal of \mathbf{A}_{v+1} , with all remaining elements below its diagonal and outside the boundaries of these 2×2 sub-matrices, being close to zero in value.

The advantage of the *LR* algorithm is that it only uses the actions and symbols "+", "-", "*", and "/" (as well as " $\sqrt{}$ " for complex eigenvalues) compared to the QR algorithm which due to the orthogonal transformations uses more complicated expressions.

Convergence and computational issues of the LR algorithm

As an iterative process, there should be a criterion according to which the iterations can be interrupted. This criterion is the proximity in value, between the final approximated eigenvalues and their exact counterparts, based on a predetermined threshold error ε . The convergence and stability of the *LR* algorithm is investigated in [81–83] as well as in other sources in the literature and depends on several factors with the most important being the following

1. The sparseness of matrix \mathbf{A} . An abundance of zero elements in the matrix at the beginning of the iterations greatly reduces the amount of iterations to achieve sufficiently approximated eigenvalues
2. The proximity of the eigenvalues. Clustered eigenvalues result in a slower convergence.
3. The arrangement of the elements in \mathbf{A} . The authors in [31, 32, 67] suggest that a preliminary ordering of \mathbf{A} satisfying $|a_{1,1}| \geq |a_{2,2}| \geq \dots \geq |a_{n,n}|$ can reduce the computational complexity. This ordering can be achieved by changing simultaneously a pair of rows between them and the same pair of columns between them. Such an action does not alter the eigenvalues of the matrix. This practice is however contested in [33] where the authors claim that a re-ordering of the diagonal elements of \mathbf{A} in decreasing order can lead to supplementary iterations.
4. The threshold error ε . The choice of a very small error ε can lead to an increased number of iterations.
5. The order n of the system does not seem to affect the convergence speed of the algorithm but significantly increasing the complexity of the entries of matrices \mathbf{A}_{m+1} .

The implementation of the *LR* algorithm with a numerical input matrix \mathbf{A} should not normally cause computational time issues, even for large matrices. However, when symbols are introduced in the entries of \mathbf{A} , and especially when \mathbf{A} is fully symbolic, the computational capabilities of a modern computer can be quickly overwhelmed. Even for small symbolic matrices (e.g. 6×6), achieving convergence may be impossible. It is therefore necessary to implement techniques that can reduce the computational effort, if possible, and lead the algorithm into a quicker convergence.

An important information is the fact that different eigenvalues converge at different speeds. It can be common that an eigenvalue converges after only a limited number of iterations while another needs considerably more (even orders of magnitude) further iterations to achieve that. This

can cause problems because every additional iteration of the algorithm significantly increases the size of the entries of \mathbf{A}_{m+1} . If the algorithm manages to converge, the final expressions of the eigenvalues could be prohibitively large to be of any practical use. In this case, a technique is used such that, every time a diagonal element $b_{k,k}$ of \mathbf{A}_{m+1} converges to a real eigenvalue of \mathbf{A} , a new matrix $\bar{\mathbf{A}}_{m+1}$ will be used instead, in the subsequent iteration. $\bar{\mathbf{A}}_{m+1}$ is equal to the version of \mathbf{A}_{m+1} with the k^{th} row and k^{th} column removed as in (5.30), reducing the size of the matrix to $(n-1) \times (n-1)$.

$$\mathbf{A}_{m+1} = \begin{bmatrix} b_{1,1} & \cdots & \boxed{b_{1,k}} & \cdots & b_{1,n} \\ \vdots & b_{2,2} & \vdots & & \vdots \\ & & \ddots & & \\ b_{k,1} & \cdots & b_{k,k-1} & \boxed{b_{k,k}} & b_{k,k+1} & \cdots & b_{k,n} \\ & & \ddots & b_{k+1,k} & \ddots & & \\ \vdots & & & \vdots & & & \\ b_{n,1} & \cdots & & b_{n,k} & & b_{n-1,n-1} & \vdots \\ & & & & & \cdots & b_{n,n} \end{bmatrix} \quad (5.30)$$

Similarly, if a 2×2 block matrix $\begin{bmatrix} b_{k,k} & b_{k,k+1} \\ b_{k+1,k} & b_{k+1,k+1} \end{bmatrix}$ on the diagonal of \mathbf{A}_{m+1} has eigenvalues which converge to a complex-conjugate eigenvalue pair of \mathbf{A} , then \mathbf{A}_{m+1} will be replaced by $\bar{\mathbf{A}}_{m+1}$. The latter is equal to \mathbf{A}_{m+1} whose k and $k+1$ rows and columns have been removed as in (5.31), reducing the size of the matrix to $(n-2) \times (n-2)$.

$$\mathbf{A}_{m+1} = \begin{bmatrix} b_{1,1} & \cdots & \boxed{b_{1,k} \quad b_{1,k+1}} & \cdots & b_{1,n} \\ \vdots & & \vdots & & \vdots \\ & & \ddots & & \\ b_{k,1} & \cdots & b_{k,k-1} & \boxed{b_{k,k} \quad b_{k,k+1}} & b_{k,k+2} & \cdots & b_{k,n} \\ b_{k+1,1} & \cdots & b_{k+1,k-1} & \boxed{b_{k+1,k} \quad b_{k+1,k+1}} & b_{k+1,k+2} & \cdots & b_{k+1,n} \\ & & \ddots & b_{k+2,k} \quad b_{k+2,k+1} & \ddots & & \\ \vdots & & & \vdots & & & \\ b_{n,1} & \cdots & & b_{n,k} \quad b_{n,k+1} & & \cdots & b_{n,n} \end{bmatrix} \quad (5.31)$$

Nevertheless, the expressions $b_{k,k}$ (for the real eigenvalue case) or $\text{eig} \left(\begin{bmatrix} b_{k,k} & b_{k,k+1} \\ b_{k+1,k} & b_{k+1,k+1} \end{bmatrix} \right)$ (for the complex-conjugate eigenvalue pair case), are now reserved as the approximations of their respective eigenvalues while the algorithm continues iterating using the $\bar{\mathbf{A}}_{m+1}$ matrix.

Another technique to reduce the computational cost and the size of the final expressions of the approximated eigenvalues is the elimination of terms within the matrices during every iteration. There is a possibility that certain terms in some entries (or even complete entries) of matrices \mathbf{A} , \mathbf{A}_m , \mathbf{L}_m and \mathbf{U}_m may have insignificant effect on the final convergence of the eigenvalues and can thus be replaced by zero. This has to be checked at every iteration by replacing all symbols with their numerical values, apart from the selected term which is set to 0, and executing an

5.3. State-space modeling of systems under investigation

intermediate numerical *LR* algorithm [31]. If the algorithm converges, then the selected term can be eliminated and the symbolic execution of the *LR* can resume. It is possible that only certain eigenvalues of \mathbf{A} are desired to be approximated. In this case the previous method can be applied with regard to only those selected eigenvalues.

A final technique is derived from experimental results. It is possible that in the case of complex-conjugate eigenvalues, either the real or the imaginary part of the approximated eigenvalue expressions seem to converge at a different speed. The final expression of these eigenvalues can then be formed by the combination of the real and imaginary part expressions at the iteration where each of them converged. This does not affect the overall speed of the algorithm but can reduce the size of the final approximated eigenvalues.

5.3 State-space modeling of systems under investigation

In a two-terminal VSC-HVDC link, at least one of the converter stations controls the direct voltage, while the other station has the duty to control the active power. Consequently, the active power is automatically balanced between the two converter stations. This balancing is achieved by the action of the local control system of the direct-voltage controlled converter, trying to stabilize the naturally unstable dc-transmission link. The properties of the latter affect the design of the control. As described in [14], the RHP pole of a process, described by the transfer function $G_d(s)$, imposes a fundamental lower limit on the speed of response of the controller. The closed-loop system of the direct-voltage control has to achieve a bandwidth that is higher than the location of the RHP pole of $G_d(s)$ to stabilize the process. It is thus useful to know in depth the dynamics of the dc-transmission link and then proceed into describing the dynamics of the complete VSC-HVDC link.

5.3.1 Investigated system

The system under consideration is a two-terminal symmetrical monopole VSC-HVDC link, as in Fig. 5.2. This is practically identical to the model examined in Section (4.2) and shown in Fig. 4.2(b). The connection is comprised of two VSC stations, as well as ac- and dc-side components. Assuming a strong ac grid, the arrangement consisting of the ac grid, the transformer

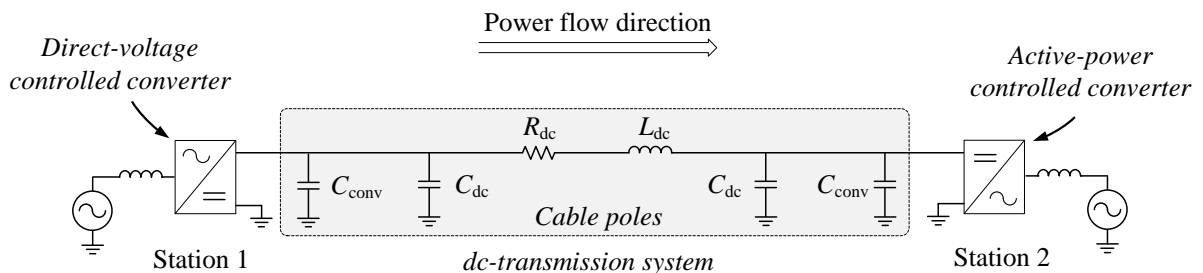


Fig. 5.2 Model of a the two-terminal VSC-HVDC system investigated in this chapter.

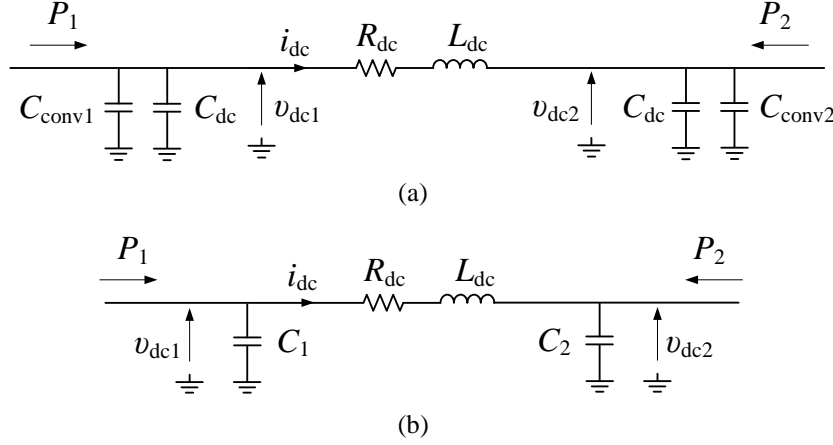


Fig. 5.3 (a) Detailed dc-transmission link description, (b) dc-transmission link description with lumped capacitances.

and the ac-harmonic filters is represented by a voltage source. Furthermore, the phase reactor is assumed to be lossless and is represented by a single inductor.

Regarding the dynamic description of the system, the closed-loop response of the current control is typically much faster (at least an order of magnitude) than the closed-loop response of the outer (direct-voltage and active-power) controllers [52]. Therefore, a valid simplification is to consider an infinitely fast current control, causing the ac side dynamics to be effectively ignored.

5.3.2 DC-link transmission model

The process of expressing the dynamics of the dc-system is almost identical with the process followed in Section (4.2.1), but with a number of customizations and nomenclature changes to accommodate a more generic approach to the investigation. The passive elements comprising the dc-link transmission system can be seen in Fig. 5.2, as the objects within the gray area. The figure shows that both stations have dc-link capacitors with the same value C_{conv} . A more general approach of the system can be considered here where the two capacitors are not identical, with one having a generic capacitance of C_{conv1} and the other having C_{conv2} , respectively. This convention is followed only in this section and the resulting generic dc-transmission link can be seen in Fig. 5.3(a).

Capacitors C_{conv1} and its adjacent C_{dc} are connected in parallel. The two pairs can be replaced by the equivalent lumped capacitors $C_1 = C_{conv1} + C_{dc}$ and $C_2 = C_{conv2} + C_{dc}$, as shown in Fig. 5.3(b). Considering power P_1 being injected from the left side of the dc-link transmission and power P_2 from the right side (representing the instantaneous powers from Converter 1 and Converter 2), the system is linearized as

$$C_1 \frac{dv_{dc1}}{dt} = \frac{P_1}{v_{dc1}} - i_{dc} \Rightarrow$$

5.3. State-space modeling of systems under investigation

$$\frac{d\Delta v_{dc1}}{dt} = \frac{1}{C_1 v_{dc1,0}} \Delta P_1 - \frac{P_{1,0}}{C_1 v_{dc1,0}^2} \Delta v_{dc1} - \frac{1}{C_1} \Delta i_{dc} \quad (5.32)$$

representing the dynamics of voltage v_{dc1} across the capacitor C_1 and

$$C_2 \frac{dv_{dc2}}{dt} = i_{dc} + \frac{P_2}{v_{dc2}} \Rightarrow$$

$$\frac{d\Delta v_{dc2}}{dt} = \frac{1}{C_2} \Delta i_{dc} + \frac{1}{C_2 v_{dc2,0}} \Delta P_2 - \frac{P_{2,0}}{C_2 v_{dc2,0}^2} \Delta v_{dc2} \quad (5.33)$$

representing the dynamics of voltage v_{dc2} across the capacitor C_2 and finally

$$L_{dc} \frac{di_{dc}}{dt} = -R_{dc} i_{dc} - v_{dc2} + v_{dc1} \Rightarrow$$

$$\frac{d\Delta i_{dc}}{dt} = \frac{1}{L_{dc}} \Delta v_{dc1} - \frac{R_{dc}}{L_{dc}} \Delta i_{dc} - \frac{1}{L_{dc}} \Delta v_{dc2} \quad (5.34)$$

representing the dynamics of the current i_{dc} , flowing across the cable resistance R_{dc} and the cable inductance L_{dc} .

The state-space model of the considered dc-transmission system is created by considering (5.32), (5.33) and (5.34). The states of the system are $x_1 = \Delta v_{dc1}$, $x_2 = \Delta i_{dc}$ and $x_3 = \Delta v_{dc2}$. The inputs are $u_1 = \Delta P_1$ and $u_2 = \Delta P_2$, while $y_1 = \Delta v_{dc1}$ and $y_2 = \Delta v_{dc2}$ serve as the output of the system. The resulting state-space model is

$$\mathbf{A}_{dc-link} = \begin{bmatrix} -\frac{P_{1,0}}{C_1 v_{dc1,0}^2} & -\frac{1}{C_1} & 0 \\ \frac{1}{L_{dc}} & -\frac{R_{dc}}{L_{dc}} & -\frac{1}{L_{dc}} \\ 0 & \frac{1}{C_2} & -\frac{P_{2,0}}{C_2 v_{dc2,0}^2} \end{bmatrix}$$

$$\mathbf{B}_{dc-link} = \begin{bmatrix} \frac{1}{C_1 v_{dc1,0}} & 0 \\ 0 & 0 \\ 0 & \frac{1}{C_2 v_{dc2,0}} \end{bmatrix} \quad (5.35)$$

$$\mathbf{C}_{dc-link} = \begin{bmatrix} 1 & 0 & 0 \\ 0 & 0 & 1 \end{bmatrix}, \quad \mathbf{D}_{dc-link} = \begin{bmatrix} 0 & 0 \\ 0 & 0 \end{bmatrix}$$

5.3.3 Two-terminal VSC-HVDC model

This section regards the two-terminal VSC-HVDC system of Section (5.3.1) as a complete entity, with the aim of merging the dynamics of the control systems and the dc-link transmission into a common state-space model. This model will effectively describe the interaction between the physical system and the controller structures.

Direct-Voltage Control

The portion of the complete model that describes the dynamics of the direct-voltage controller is presented in Fig. 5.4. A difference in the treatment of the direct-voltage controller compared to the design approach of Chapter 2 is the fact that the dynamics of the converter capacitor C_{conv} cannot be considered separately from the capacitor C_{dc} of the equivalent dc-link Π -model. The dynamics of the two capacitors are restricted by their common voltage v_{dc1} . The combined energy stored in these dc-capacitors is $(C_{\text{conv}} + C_{\text{dc}})v_{\text{dc1}}^2/2$, with the value $W = v_{\text{dc1}}^2$ being proportional to this energy. The dynamics of the combined capacitors become

$$\frac{1}{2}(C_{\text{conv}} + C_{\text{dc}})\frac{dW}{dt} = P_{\text{in}} - P_{\text{line}} \xrightarrow{\mathcal{L}\{\cdot\}} W = \frac{2}{s(C_{\text{conv}} + C_{\text{dc}})}(P_{\text{in}} - P_{\text{line}}) \quad (5.36)$$

with P_{in} and P_{line} the active power drawn from the ac side and the propagated dc power beyond the capacitor C_{dc} of the dc-link Π -model, respectively.

The direct-voltage controller used here is the same as described in Section (2.4.3), featuring a power-feedforward term. Assuming no losses on the phase reactor, the converter and the dc-side capacitors, the controller integral gain K_i can be equalized to zero. Thus, as earlier described, the expression of the direct-voltage controller can then be written as

$$\begin{aligned} P_{\text{in}}^* &= F(s)(W^* - W) + P_{\text{f}} = K_{\text{p}}(W^* - W) + P_{\text{f}} \Rightarrow \\ P_{\text{in}}^* &= K_{\text{p}}(W^* - W) + H(s)P_{\text{m}} \end{aligned} \quad (5.37)$$

The transmitted dc-side power is measured after the converter capacitor C_{conv} , as also shown in [43]. This corresponds to power P_{m} in Fig. 5.4(a). Power P_{line} is not a measurable quantity because it exists only in the equivalent dc-link Π -model. Therefore, P_{f} is equal to the filtered value of P_{m} , by means of a first-order low-pass filter with a transfer function $H(s) = a_{\text{f}}/(s + a_{\text{f}})$, where a_{f} is the bandwidth of the filter.

Assuming perfect knowledge of the grid-voltage angle and an infinitely fast current-control loop, the requested active power P_{in}^* can be immediately applied, thus $P_{\text{in}} = P_{\text{in}}^*$. Substituting (5.36) to (5.37) gives

$$W = \frac{2K_{\text{p}}}{2K_{\text{p}} + s(C_{\text{conv}} + C_{\text{dc}})}W^* + \frac{2H(s)}{2K_{\text{p}} + s(C_{\text{conv}} + C_{\text{dc}})}P_{\text{m}} - \frac{2}{2K_{\text{p}} + s(C_{\text{conv}} + C_{\text{dc}})}P_{\text{line}} \Rightarrow$$

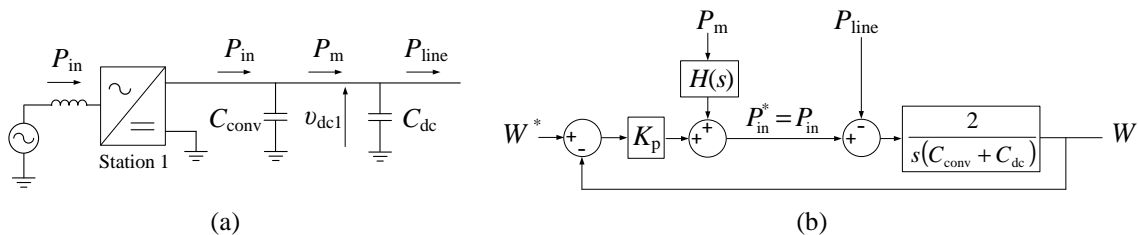


Fig. 5.4 (a) VSC rectifier (b) Closed-loop rectifier control process.

5.3. State-space modeling of systems under investigation

$$W = G_{cp} \cdot W^* + Y_{cp1} \cdot P_m - Y_{cp2} \cdot P_{line} \quad (5.38)$$

where G_{cp} is the closed-loop transfer function of the voltage controller for $P_{dc}=0$. If the combined value of $(C_{conv} + C_{dc})$ is known, then as suggested in [52], the proportional gain is selected as $K_p = a_d(C_{conv} + C_{dc})/2$. Considering the previous, G_{cp} is now equal to $a_d/(s + a_d)$ which is a first-order low pass filter with bandwidth a_d . However, C_{dc} is not easily measured, or even the equivalent Π -model is not exactly valid in reality. As a result, the only available value is C_{conv} which can be measured on the real dc-side capacitors of the VSC station. Therefore, the proportional gain is selected as $K_p = a_d C_{conv}/2$.

Based on the arrangement of Fig. 5.4, as well as relation (4.34), powers P_{in} , P_m and P_{line} are connected in the following way

$$P_m = \frac{C_{dc}}{C_{tot}} P_{in} + \frac{C_{conv}}{C_{tot}} P_{line} \quad (5.39)$$

where C_{tot} is equal to the added capacitances $C_{conv} + C_{dc}$.

Using (5.37) and (5.39), and considering that W^* is equal to $(v_{dc}^*)^2$ (where v_{dc}^* is the corresponding voltage reference for v_{dc1}), the dynamics of the power-feedforward term become

$$\begin{aligned} P_f &= H(s) P_m = \frac{a_f}{s+a_f} P_m \Rightarrow sP_f = -a_f P_f + a_f P_m \xrightarrow{\mathcal{L}^{-1}\{\cdot\}} \\ \frac{dP_f}{dt} &= -a_f P_f + a_f P_m \Rightarrow \frac{dP_f}{dt} = -a_f P_f + a_f \frac{C_{dc}}{C_{tot}} P_{in} + a_f \frac{C_{conv}}{C_{tot}} P_{line} \Rightarrow \\ \frac{dP_f}{dt} &= -a_f P_f + a_f \frac{C_{dc}}{C_{tot}} [K_p (W^* - W) + P_f] + a_f \frac{C_{conv}}{C_{tot}} v_{dc1} i_{dc} \Rightarrow \\ \frac{dP_f}{dt} &= -a_f P_f + a_f \frac{C_{dc}}{C_{tot}} [K_p ((v_{dc}^*)^2 - v_{dc1}^2) + P_f] + a_f \frac{C_{conv}}{C_{tot}} v_{dc1} i_{dc} \Rightarrow \\ \frac{dP_f}{dt} &= -a_f \left(1 - \frac{C_{dc}}{C_{tot}}\right) P_f + a_f \frac{C_{dc}}{C_{tot}} K_p (v_{dc}^*)^2 - a_f \frac{C_{dc}}{C_{tot}} K_p v_{dc1}^2 + a_f \frac{C_{conv}}{C_{tot}} v_{dc1} i_{dc} \Rightarrow \end{aligned}$$

$$\begin{aligned} \frac{d\Delta P_f}{dt} &= -a_f \frac{C_{conv}}{C_{tot}} \Delta P_f + a_f \frac{C_{dc}}{C_{tot}} a_d C_{conv} v_{dc1,0} \Delta v_{dc}^* - a_f \frac{C_{dc}}{C_{tot}} a_d C_{conv} v_{dc1,0} \Delta v_{dc1} + a_f \frac{C_{conv}}{C_{tot}} v_{dc1,0} \Delta i_{dc} + a_f \frac{C_{conv}}{C_{tot}} i_{dc,0} \Delta v_{dc1} \Rightarrow \\ \frac{d\Delta P_f}{dt} &= -a_f \frac{C_{conv}}{C_{tot}} \Delta P_f - a_f \frac{a_d C_{dc} C_{conv} v_{dc1,0} - C_{conv} i_{dc,0}}{C_{tot}} \Delta v_{dc1} + a_f \frac{C_{conv} v_{dc1,0}}{C_{tot}} \Delta i_{dc} + a_f a_d \frac{C_{dc} C_{conv} v_{dc1,0}}{C_{tot}} \Delta v_{dc}^* \quad (5.40) \end{aligned}$$

Furthermore, the dynamics of the dc-voltage capacitor at the terminals of the voltage controlled station become

$$\begin{aligned}
 \frac{1}{2}C_{\text{tot}} \frac{dW}{dt} &= P_{\text{in}} - P_{\text{line}} = P_{\text{in}}^* - P_{\text{line}} \Rightarrow \\
 \frac{1}{2}C_{\text{tot}} \frac{dW}{dt} &= K_p (W^* - W) + P_f - P_{\text{line}} \Rightarrow \\
 \frac{1}{2}C_{\text{tot}} \frac{dW}{dt} &= K_p \left[(v_{\text{dc}}^*)^2 - v_{\text{dc}1}^2 \right] + P_f - v_{\text{dc}1} i_{\text{dc}} \Rightarrow \\
 \frac{dv_{\text{dc}1}^2}{dt} &= \frac{a_d C_{\text{conv}}}{C_{\text{tot}}} (v_{\text{dc}}^*)^2 - \frac{a_d C_{\text{conv}}}{C_{\text{tot}}} v_{\text{dc}1}^2 + \frac{2}{C_{\text{tot}}} P_f - \frac{2}{C_{\text{tot}}} v_{\text{dc}1} i_{\text{dc}} \Rightarrow \\
 \frac{d\Delta v_{\text{dc}1}}{dt} &= \frac{a_d C_{\text{conv}}}{2C_{\text{tot}} v_{\text{dc}1,0}} \Delta (v_{\text{dc}}^*)^2 - \frac{a_d C_{\text{conv}}}{C_{\text{tot}}} \Delta v_{\text{dc}1} + \frac{1}{C_{\text{tot}} v_{\text{dc}1,0}} \Delta P_f - \frac{1}{C_{\text{tot}}} \Delta i_{\text{dc}} - \frac{i_{\text{dc},0}}{C_{\text{tot}} v_{\text{dc}1,0}} \Delta v_{\text{dc}1} \Rightarrow \\
 \frac{d\Delta v_{\text{dc}1}}{dt} &= \frac{a_d C_{\text{conv}}}{C_{\text{tot}}} \Delta v_{\text{dc}}^* - \left(\frac{a_d C_{\text{conv}}}{C_{\text{tot}}} + \frac{i_{\text{dc},0}}{C_{\text{tot}} v_{\text{dc}1,0}} \right) \Delta v_{\text{dc}1} + \frac{1}{C_{\text{tot}} v_{\text{dc}1,0}} \Delta P_f - \frac{1}{C_{\text{tot}}} \Delta i_{\text{dc}} \quad (5.41)
 \end{aligned}$$

Modeling of the dc system

Figure 5.5 shows the related dc system and VSC Station 2. From a general perspective and assuming that the dynamics of the current control of Station 2 were not neglected, the dynamics of the active-power transfer in Station 2 are independent from the dynamics of the direct-voltage control and the dc circuit. This happens because, with regards to this station

1. the current controller beneath the active-power controller does not use any properties or measured signals from the dc-side to impose the current i_f^d that tries to follow the current reference $i_f^{d,*}$.
2. The PCC voltage for the considered strong grid is considered constant. Even if a weak grid is considered, the change of the PCC voltage is related to the ac side physical properties and the current flow caused by the current controller. Therefore, the PCC voltage dynamics are not related to the dc-side.
3. The active-power controller uses a feedback of P_{out} to produce a current reference $i_f^{d,*}$. However P_{out} is the product of i_f^d and v_g^d . As referred above, neither of these are related to the properties on the dc-side of Station 2.

Therefore, the flow of P_{out} is related only to properties of the active-power controller, the current controller and the associated ac-grid structure. Additionally, assuming linear operation of the VSC, the current controller's operation is not affected by the level of $v_{\text{dc},2}$. Therefore, the active-power controlled VSC acts as an ideal power source, transferring power P_{out} between its dc and ac side, with P_{out} seen as an externally provided input by the rest of the system.

The dc-cable dynamics are provided as

5.3. State-space modeling of systems under investigation

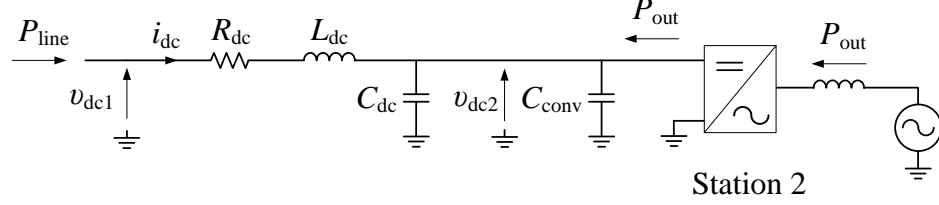


Fig. 5.5 DC cable and inverter station of the VSC-HVDC link.

$$L_{dc} \frac{di_{dc}}{dt} = -R_{dc}i_{dc} - v_{dc2} + v_{dc1} \Rightarrow$$

$$\frac{d\Delta i_{dc}}{dt} = \frac{1}{L_{dc}}\Delta v_{dc1} - \frac{R_{dc}}{L_{dc}}\Delta i_{dc} - \frac{1}{L_{dc}}\Delta v_{dc2} \quad (5.42)$$

while the dynamics of the dc capacitor located at the terminals of the power controlled station will be

$$(C_{conv} + C_{dc}) \frac{dv_{dc2}}{dt} = i_{dc} + \frac{P_{out}}{v_{dc2}} \Rightarrow$$

$$C_{tot} \frac{d\Delta v_{dc2}}{dt} = \Delta i_{dc} - \frac{P_{2,0}}{v_{dc2,0}^2} \Delta v_{dc2} + \frac{1}{v_{dc2,0}} \Delta P_{out} \Rightarrow$$

$$\frac{d\Delta v_{dc2}}{dt} = \frac{1}{C_{tot}} \Delta i_{dc} - \frac{P_{2,0}}{C_{tot} v_{dc2,0}^2} \Delta v_{dc2} + \frac{1}{C_{tot} v_{dc2,0}} \Delta P_{out} \quad (5.43)$$

where $P_{2,0}$ is the steady-state value of P_{out} .

State-space representation

The state space model of the considered two-terminal VSC-HVDC is created by considering (5.40)-(5.43). The states of the system are $x_1 = \Delta P_f$, $x_2 = \Delta v_{dc1}$, $x_3 = \Delta i_{dc}$ and $x_4 = \Delta v_{dc2}$. The inputs are $u_1 = v_{dc}^*$ and $u_2 = \Delta P_{out}$, while $y_1 = v_{dc1}$ and $y_2 = \Delta P_{in}$ serve as the outputs of the system. The output ΔP_{in} is derived using (5.37) and the earlier assumption that $P_{in} = P_{in}^*$ as follows

$$P_{in} = K_p (W^* - W) + P_f \Rightarrow P_{in} = \frac{a_d C_{conv}}{2} \left[(v_{dc}^*)^2 - v_{dc1}^2 \right] + P_f \Rightarrow$$

$$\Delta P_{in} = \frac{a_d C_{conv}}{2} \left[2v_{dc1,0} \Delta v_{dc}^* - 2v_{dc1,0} \Delta v_{dc1} \right] + \Delta P_f \Rightarrow$$

$$\Delta P_{in} = a_d C_{conv} v_{dc1,0} \Delta v_{dc}^* - a_d C_{conv} v_{dc1,0} \Delta v_{dc1} + \Delta P_f \quad (5.44)$$

Regarding the steady-state of the system, the steady-state value of P_{in} is $P_{1,0}$. As a result, $i_{dc,0}$ can be expressed as $i_{dc,0} = P_{1,0} / v_{dc1,0}^2 = -P_{2,0} / v_{dc2,0}^2$. Under these conditions, the state-space model of the system becomes

$$\begin{aligned}
 \mathbf{A}_{\text{HVDC}} &= \begin{bmatrix} -a_f \frac{C_{\text{conv}}}{C_{\text{tot}}} & a_f \left(-\frac{a_d C_{\text{conv}} C_{\text{dc}} v_{\text{dc}1,0}}{C_{\text{tot}}} - \frac{C_{\text{conv}} P_{2,0}}{C_{\text{tot}} v_{\text{dc}2,0}} \right) & a_f \frac{C_{\text{conv}} v_{\text{dc}1,0}}{C_{\text{tot}}} & 0 \\ \frac{1}{C_{\text{tot}} v_{\text{dc}1,0}} & -\frac{a_d C_{\text{conv}}}{C_{\text{tot}}} - \frac{P_{1,0}}{C_{\text{tot}} v_{\text{dc}1,0}^2} & -\frac{1}{C_{\text{tot}}} & 0 \\ 0 & \frac{1}{L_{\text{dc}}} & -\frac{R_{\text{dc}}}{L_{\text{dc}}} & -\frac{1}{L_{\text{dc}}} \\ 0 & 0 & \frac{1}{C_{\text{tot}}} & -\frac{1}{C_{\text{tot}} v_{\text{dc}2,0}^2} \end{bmatrix} \\
 \mathbf{B}_{\text{HVDC}} &= \begin{bmatrix} a_f a_d \frac{C_{\text{dc}} C_{\text{conv}} v_{\text{dc}1,0}}{C_{\text{tot}}} & 0 \\ \frac{a_d C_{\text{conv}}}{C_{\text{tot}}} & 0 \\ 0 & 0 \\ 0 & \frac{1}{C_{\text{tot}} v_{\text{dc}2,0}} \end{bmatrix} \\
 \mathbf{C}_{\text{HVDC}} &= \begin{bmatrix} 0 & 1 & 0 & 0 \\ 1 & -a_d C_{\text{conv}} v_{\text{dc}1,0} & 0 & 0 \end{bmatrix}, \quad \mathbf{D}_{\text{HVDC}} = \begin{bmatrix} 0 & 0 \\ a_d C_{\text{conv}} v_{\text{dc}1,0} & 0 \end{bmatrix}
 \end{aligned} \tag{5.45}$$

5.3.4 Validity of VSC-HVDC model simplifications

The purpose of deriving the simplified state-space model of a two-terminal VSC-HVDC model in Section (5.3.3), is to sufficiently approximate an original high-order system with a much simpler and lower-order model. The eigenvalues of the latter will be approximated by the analytical methods described earlier. It is thus important to ensure that the derived expression (5.45) of the linearized simplified model, represents to a fairly good degree the equivalent complete high-order system, with small loss in accuracy.

Modeling of systems

The first step in the verification process is to describe the full model which will later be simplified. This model appears in Fig. 5.6(a) and is in essence the same as Fig. 5.2. Both converters feature a current controller as described in Section (2.4.1) with a closed-loop bandwidth a_{cc} .

The direct-voltage controlled station features a controller identical to the one described in Section (2.4.3), which is exactly the same as in (5.37). Given a reference W^* , this controller produces a reference P_{in}^* which when divided by the modulus of the ac grid voltage E_{d1} , will provide the reference i_d^* of the current controller. The current controller of the direct-voltage controlled station will then impose a current i_d across the inductance L_{c1} , causing the flow of power P_{in} . The active power controller of Station 2 is a PI-based controller as described in Section (2.4.4).

Taking into consideration the simplifications mentioned in the previous section, the previous model can be simplified into the one shown in Fig. 5.6(b). As such, the strong grid and an infinitely fast current controller causes the dynamics of the dynamics related to the ac sides and current controllers to be effectively ignored. Having infinitely fast current controllers means that P_{in}^* and P_{out}^* from the direct-voltage and active power controllers can be imposed instantaneously as P_{in} and P_{out} , respectively. The two stations can then be replaced with power sources which

5.3. State-space modeling of systems under investigation

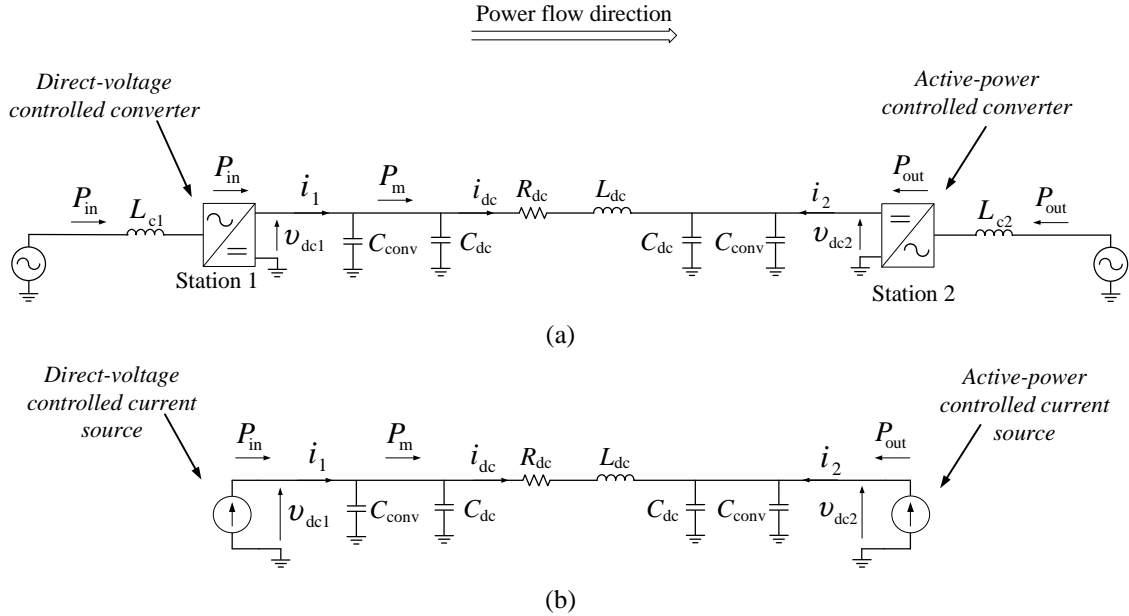


Fig. 5.6 (a) Complete model of a two-terminal VSC-HVDC link, (b) Simplified current-source based model of a two-terminal VSC-HVDC link

cause the flow of powers P_{in} and P_{out} , respectively. This can be represented electrically with current sources that provide dc currents $i_1 = P_{in}/v_{dc1}$ and $i_2 = P_{out}/v_{dc2}$.

The procedure described in Section (5.3.3) is effectively an investigation of the dynamic properties of the simplified model in Fig. 5.6(b). This model is non-linear and was thus linearized to provide the expressions (5.45). A difference between the two is that the dynamics associated with the active power controller have not been considered in the linearized model because, as claimed in Section (5.3.3), they can be treated separately from the dynamics of the rest of the circuit (which are of specific interest) and P_{out} can act as an external input to the system. This will be verified in the following comparative simulations.

Comparative simulations

The three different models described earlier are here compared under the same conditions and scenarios. This will clarify whether the simplified models (and especially the linearized model) sufficiently approximate the initial detailed model, in terms of dynamic response. If the approximation is acceptable, the linearized model can be used further on for the analytical identification of the system's eigenvalues.

The complete two-terminal VSC-HVDC model shown in Fig. 5.6(a), as well as its simplified current-source based equivalent of Fig. 5.6(b) are simulated in PSCAD, while the linearized model of (5.45) is applied in Simulink. It should be noted that the first two models feature a fully functional active-power controller, in contrast with the linearized model. All of the models are then operating using the values of Table 5.1. The dc-transmission system comprises of cables-type of lines. The direct-voltage controllers attempt to regulate the voltage v_{dc1} (via its

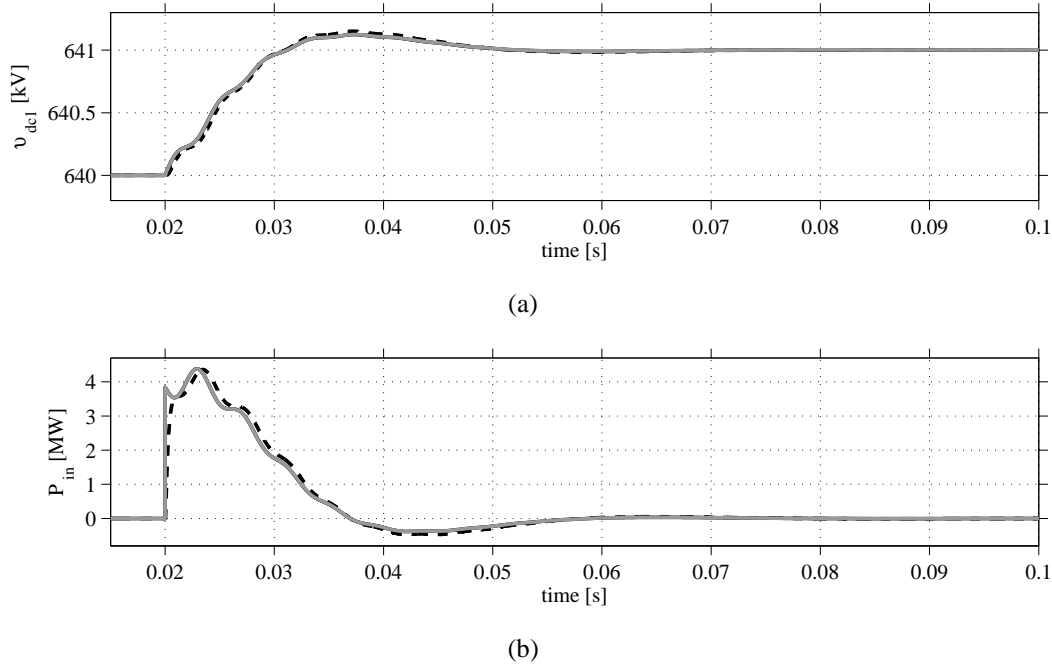


Fig. 5.7 Response of v_{dc1} and P_{in} after a direct-voltage reference step of 1 kV, for zero steady-state power transfer. Complete model (dashed black), simplified current-source based model (solid black), linearized model (solid gray).

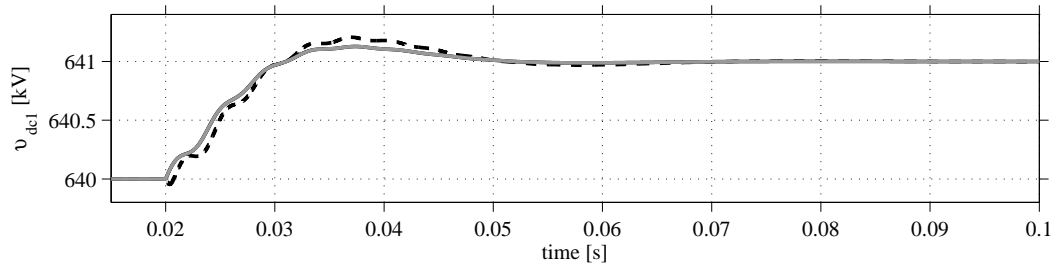
equivalent energy W) so that $v_{dc1} = v_{dc}^* = V_{dc,b}$. Furthermore, two different steady-state power transfer scenarios are investigated; $P_{out} = 0$ MW and $P_{out} = P_b = 1000$ MW. In any case, the systems will react to a direct-voltage reference step of 1 kV at $t = 0.02$ s.

Figure 5.7 present the reaction of all three models for a zero steady-state power transfer. The response of the linearized model is practically indistinguishable from the simplified model, regarding both v_{dc1} and P_{in} . It can also be observed that both of these models approximate very sufficiently the behavior of the complete model, with minimal loss of accuracy. The voltage-step scenario is then repeated for $P_{out} = 1000$ MW, with results presented in Fig. 5.8. Both of the simplified and the linearized models approximate the complete model sufficiently well, regarding both v_{dc1} and P_{in} .

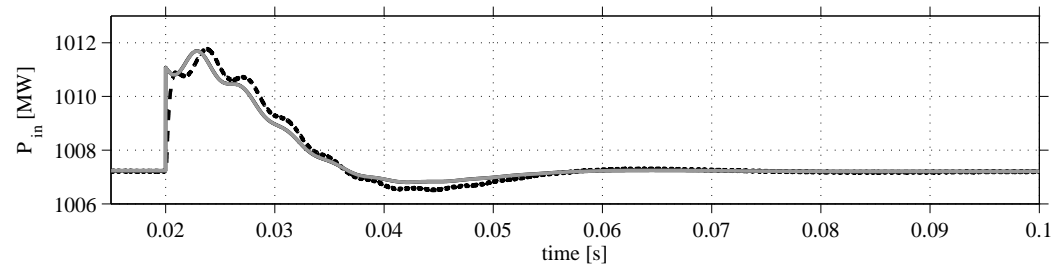
TABLE 5.1. RATED VALUES OF THE MODELED VSC-HVDC LINK

P_b	rated active power	1000 MW
$V_{dc,b}$	rated direct voltage	640 kV
C_{conv}	shunt converter capacitor	20 μ F
a_d	bandwidth of the closed-loop direct-voltage control	300 rad/s
a_f	bandwidth of the power-feedforward filter	300 rad/s
a_{cc}	bandwidth of the closed-loop current control	3000 rad/s
L_c	phase reactor inductance	50.0 mH
$length$	cable line length	100 km

5.3. State-space modeling of systems under investigation

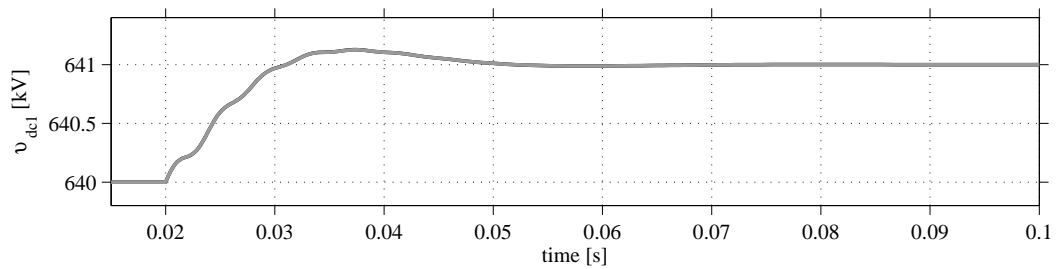


(a)

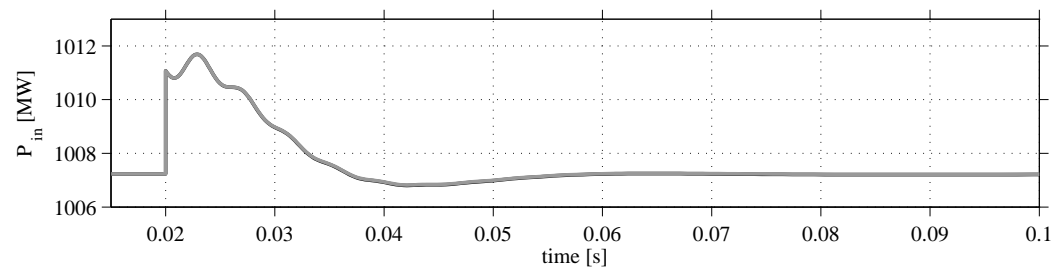


(b)

Fig. 5.8 Response of v_{dc1} and P_{in} after a direct-voltage reference step of 1 kV, for 1000 MW steady-state power transfer. Complete model (dashed black), simplified current-source based model (solid black), linearized model (solid gray).



(a)



(b)

Fig. 5.9 Response of v_{dc1} and P_{in} after a direct-voltage reference step of 1 kV, for 1000 MW steady-state power transfer. Linearized model (solid black), linearized model with modified linearization points (solid gray).

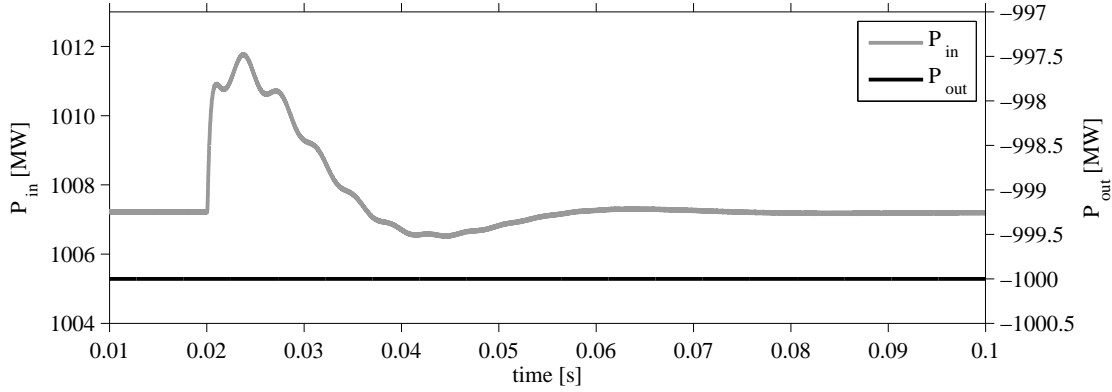


Fig. 5.10 Response of P_{in} and P_{out} of the complete model after a direct-voltage reference step of 1 kV at $t=0.02$ s, for 1000 MW steady-state power transfer.

The behavior of the linearized model theoretically relies heavily on the initial conditions $P_{1,0}$, $P_{2,0}$, $v_{dc2,0}$ and $v_{dc1,0}$. However, given that the losses on the transmission link are usually a small fraction of the transmitted power, the difference between $P_{1,0}$ and $P_{2,0}$, as well as between $v_{dc2,0}$ and $v_{dc1,0}$, is usually small. An approach that could simplify the description of the linearized model and contribute to a more compact analytical description of its eigenvalues, is to consider the approximation $P_{1,0} = P_{2,0}$, which is equal to the desired steady-state of P_{out} , and at the same time $v_{dc2,0} = v_{dc1,0} = V_{dc,b}$. Under this simplification, the response of the modified linearized model, in comparison with the complete and simplified models, is plotted in Fig. 5.9. This figure clearly shows that the linearized model behaves practically identically to the simplified one, with the same dynamics and steady-state response. Finally, both of them have very close dynamics and behavior as the complete model, with only a slight overestimation of the damping properties of the systems poles. Judging by these results, the latest simplification of the linearization points is always considered in all the analysis that follows.

A final remark regards the earlier consideration that P_{out} is treated as an external input by the rest of the system, with dynamics that are unrelated to those of the direct-voltage controller and dc-transmission link. Figure 5.10 shows the behavior of the complete HVDC model, with the active-power controller operating (thus P_{out} could vary if the power feedback of the controller was disturbed). The direct-voltage reference step at $t = 0.02$ s has, as expected, effect on P_{in} but no effect at all on P_{out} . This proves that the dynamics leading to the creation of P_{out} are totally isolated from the dc-dynamics of the system. As a result, P_{out} can indeed be treated as an input to (5.45) and Station 2 can be, indeed, regarded as a power source of P_{out} .

Concluding, the assumptions taken to simplify the original two-terminal VSC-HVDC model leading to the final linearized expression of (5.45), were proved to be effective. This means that the linearized model can be safely considered as representative of the original complete system, in terms of dynamics, and will thus form the basis for the upcoming analytical investigation of the system's eigenvalues.

5.4 Summary

This section highlighted the value of an analytical approach in the analysis of dynamic systems, with emphasis given on two-terminal VSC-HVDC transmission systems. Initially, the problems encountered in a conventional approach to the analytical solution of a higher than 2nd order characteristic polynomial were discussed. As part of alternative processes to solve these problems, the *SMT* method was introduced as a powerful tool to derive the analytical eigenvalues of a 4th order system. Its concept and algorithmic process were thoroughly presented, followed by an overview of the already established *LR* method, whose value in the field of analytical eigenvalue derivation has been proven.

In order to demonstrate the effectiveness and compare these two methods, an advanced two-terminal VSC-HVDC system was sufficiently approximated by a simplified 4th order state-space model that is suitable for use by both methods, without compromising a lot of the accuracy in the dynamic description of the original system. Furthermore, the dc-transmission link connecting the two VSC stations contains vital information for the design of the system's direct voltage controller. Given the subsequent interest in the description of its poles, the state-space model of a generic dc-transmission link is developed.

The following chapter considers the application of the *SMT* and *LR* methods to the earlier described models, with the objective of extracting useful and compact analytical expressions of their eigenvalues.

Chapter 5. Stability in two-terminal VSC-HVDC systems: analytical approach

Chapter 6

Applications of the analytical approach

The previous chapter focused on the establishment of the proposed *SMT* analytical method, the presentation of the iterative *LR* method, as well as the formulation of the state-space representations for a 3rd order dc-transmission link model and a 4th order two-terminal VSC-HVDC model. In this chapter, the previously described methods are applied on the latter model, in an attempt to derive the analytical expressions of its eigenvalues. Additionally, the *LR* method is used to estimate the analytical eigenvalue expressions of the dc-transmission link model, being more suitable than the *SMT* method in performing this task. The models are transformed into a suitable form for use by each of the methods and the accuracy of the analytically derived expressions is assessed by comparing their values to those of the numerically derived eigenvalues, for a wide range of parameter variation.

6.1 Application of Similarity Matrix Transformation

In this section, the *SMT* method is applied in an effort to demonstrate its potential in determining the analytical eigenvalue expressions of a two-terminal VSC-HVDC connection. The simplified 4th order model described in section Section (5.3.3) is selected as the object of the investigation.

The *SMT* method utilizes the state matrix of a linear or linearized dynamic system. As such, a 4×4 state-matrix \mathbf{A}_s is set equal to the state matrix provided in Section (5.45), containing all the necessary information for the estimation of the system's eigenvalues.

$$\mathbf{A}_s = \begin{bmatrix} -a_f \frac{C_{\text{conv}}}{C_{\text{tot}}} & a_f \left(-\frac{a_d C_{\text{conv}} C_{\text{dc}} v_{\text{dc}1,0}}{C_{\text{tot}}} - \frac{C_{\text{conv}} P_{2,0}}{C_{\text{tot}} v_{\text{dc}2,0}} \right) & a_f \frac{C_{\text{conv}} v_{\text{dc}1,0}}{C_{\text{tot}}} & 0 \\ \frac{1}{C_{\text{tot}} v_{\text{dc}1,0}} & -\frac{a_d C_{\text{conv}}}{C_{\text{tot}}} - \frac{P_{1,0}}{C_{\text{tot}} v_{\text{dc}1,0}^2} & -\frac{1}{C_{\text{tot}}} & 0 \\ 0 & \frac{1}{L_{\text{dc}}} & -\frac{R_{\text{dc}}}{L_{\text{dc}}} & -\frac{1}{L_{\text{dc}}} \\ 0 & 0 & \frac{1}{C_{\text{tot}}} & -\frac{1}{C_{\text{tot}} v_{\text{dc}2,0}^2} \end{bmatrix} \quad (6.1)$$

In order to proceed further, an appropriate similarity transformation matrix \mathbf{P} needs to be defined, which will transform \mathbf{A}_s into a similar 4×4 matrix $\tilde{\mathbf{A}}$ whose form is a lower quasi-triangular block matrix as in (5.10). Given the description of the suggested method presented in

Chapter 6. Applications of the analytical approach

Section (5.2.1), if a 4th order system is considered, the optimum choice of a similarity transformation matrix should have the form of (5.16). Reaching a final expression for the 4 eigenvalues of the system requires a number of simplifications to be performed. The validity of these simplifications is greatly dependent on the numerical values of the system's unknown parameters and their range of variation. Specific symbolic terms in intermediate stages of the analysis may have negligible impact on the final results, when replaced with their numerical values and can thus be neglected. This approach will simplify further steps in the analysis and will allow final closed formed expressions to be derived.

6.1.1 Parameter values

The state matrix \mathbf{A}_s described in (6.1) contains ten unknowns, i.e. four steady-state values $P_{1,0}$, $P_{2,0}$, $v_{1,0}$ and $v_{dc1,0}$; four dc-circuit parameters R_{dc} , L_{dc} , C_{dc} and C_{conv} ; two controller design parameters a_d and a_f . The rated parameters of the VSC-HVDC link are presented in Table 5.1.

In steady-state, the voltage controller stabilizes v_{dc1} so that its reference value is $V_{dc,b}$, thus $v_{dc1,0} = V_{dc,b}$. The steady-state power transfer with a direction from the power controlled station to its ac grid is represented by $P_{out,0}$ and is considered to be equal to the rated active power, $P_{out,0} = P_b$. Therefore the steady-state value of P_2 is $P_{2,0} = -P_{out,0}$. For a negative power transfer P_2 (exported from the power controlled station to its ac grid), voltage v_{dc2} will have a value slightly lower than v_{dc1} . However, in steady-state the difference between the two voltages is only dependent on the cable resistance and is therefore extremely small (no more than 0.5% at maximum power transfer). As a result, it is valid to consider $v_{dc2,0} = v_{dc1,0}$, without the loss of significant accuracy in terms of system dynamics. Considering low losses on the resistance R_{dc} leads to a further simplification of $|P_{1,0}| = |P_{2,0}|$; thus $P_{1,0} = P_{out,0}$. Matrix \mathbf{A}_s now takes the form

$$\mathbf{A}_s = \begin{bmatrix} -a_f \frac{C_{conv}}{C_{tot}} & a_f \left(-\frac{a_d C_{conv} C_{dc} v_{dc1,0}}{C_{tot}} + \frac{C_{conv} P_{out,0}}{C_{tot} v_{dc1,0}} \right) & a_f \frac{C_{conv} v_{dc1,0}}{C_{tot}} & 0 \\ \frac{1}{C_{tot} v_{dc1,0}} & -\frac{a_d C_{conv}}{C_{tot}} - \frac{P_{out,0}}{C_{tot} v_{dc1,0}^2} & -\frac{1}{C_{tot}} & 0 \\ 0 & \frac{1}{L_{dc}} & -\frac{R_{dc}}{L_{dc}} & -\frac{1}{L_{dc}} \\ 0 & 0 & \frac{1}{C_{tot}} & \frac{P_{out,0}}{C_{tot} v_{dc1,0}^2} \end{bmatrix} \quad (6.2)$$

6.1.2 Matrix simplification

Before performing the formal similarity transformation of matrix \mathbf{A}_s , it is possible to re-model its entries in an appropriate way, for easier further calculations. Having entries that are simple in form and possibly appear multiple times within the matrix that will be subjected to similarity transformation, is desirable because they ease the task of reaching compact final expressions for the eigenvalues.

By definition, a *similar* matrix has the same eigenvalues as the original matrix to which it is *similar*. Consequently, \mathbf{A}_s may be subjected to an abstract number of consecutive similarity transformations, with the resulting matrix still maintaining the same eigenvalues as \mathbf{A}_s . An

6.1. Application of Similarity Matrix Transformation

initial objective is therefore to find a similar matrix of \mathbf{A}_s which will have simplified entries. A corresponding similarity transformation matrix \mathbf{M} must be defined to achieve this. The form of \mathbf{M} is chosen as

$$\mathbf{M} = \begin{bmatrix} m_{11} & 0 & 0 & 0 \\ 0 & m_{22} & 0 & 0 \\ 0 & 0 & m_{33} & 0 \\ 0 & 0 & 0 & m_{44} \end{bmatrix} \quad (6.3)$$

Using \mathbf{M} to perform a similarity transformation of matrix \mathbf{A}_s produces a similar matrix \mathbf{A}_0 as

$$\mathbf{A}_0 = \mathbf{M}^{-1} \mathbf{A}_s \mathbf{M} = \begin{bmatrix} \frac{1}{m_1} & 0 & 0 & 0 \\ 0 & \frac{1}{m_2} & 0 & 0 \\ 0 & 0 & \frac{1}{m_3} & 0 \\ 0 & 0 & 0 & \frac{1}{m_4} \end{bmatrix} \cdot \begin{bmatrix} a_{11} & a_{12} & a_{13} & a_{14} \\ a_{21} & a_{22} & a_{23} & a_{24} \\ a_{31} & a_{32} & a_{33} & a_{34} \\ a_{41} & a_{42} & a_{43} & a_{44} \end{bmatrix} \cdot \begin{bmatrix} m_1 & 0 & 0 & 0 \\ 0 & m_2 & 0 & 0 \\ 0 & 0 & m_3 & 0 \\ 0 & 0 & 0 & m_4 \end{bmatrix} \Rightarrow$$

$$\mathbf{A}_0 = \begin{bmatrix} a_{11} & \frac{m_2}{m_1} a_{12} & \frac{m_3}{m_1} a_{13} & \frac{m_4}{m_1} a_{14} \\ \frac{m_1}{m_2} a_{21} & a_{22} & \frac{m_3}{m_2} a_{23} & \frac{m_4}{m_2} a_{24} \\ \frac{m_1}{m_3} a_{31} & \frac{m_2}{m_3} a_{32} & a_{33} & \frac{m_4}{m_3} a_{34} \\ \frac{m_1}{m_4} a_{41} & \frac{m_2}{m_4} a_{42} & \frac{m_3}{m_4} a_{43} & a_{44} \end{bmatrix} \quad (6.4)$$

The choice of m_1, m_2, m_3 and m_4 for optimum simplification of the entries of \mathbf{A}_0 is such that \mathbf{M} becomes

$$\mathbf{M} = \begin{bmatrix} v_{dc1,0} & 0 & 0 & 0 \\ 0 & 1 & 0 & 0 \\ 0 & 0 & 1 & 0 \\ 0 & 0 & 0 & 1 \end{bmatrix} \quad (6.5)$$

with the resulting \mathbf{A}_0 matrix becoming

$$\mathbf{A}_0 = \mathbf{M}^{-1} \mathbf{A}_s \mathbf{M} = \begin{bmatrix} -a_f \frac{C_{conv}}{C_{tot}} & a_f \left(-\frac{a_d C_{conv} C_{dc}}{C_{tot}} + \frac{C_{conv} P_{out,0}}{C_{tot} v_{dc1,0}^2} \right) & a_f \frac{C_{conv}}{C_{tot}} & 0 \\ \frac{1}{C_{tot}} & -\frac{a_d C_{conv}}{C_{tot}} - \frac{P_{out,0}}{C_{tot} v_{dc1,0}^2} & -\frac{1}{C_{tot}} & 0 \\ 0 & \frac{1}{L_{dc}} & -\frac{R_{dc}}{L_{dc}} & -\frac{1}{L_{dc}} \\ 0 & 0 & \frac{1}{C_{tot}} & \frac{P_{out,0}}{C_{tot} v_{dc1,0}^2} \end{bmatrix} \quad (6.6)$$

The immediate benefit of using (6.5) is the fact that $v_{dc1,0}$ has been eliminated from the matrix elements $A_{s,21}$ and $A_{s,13}$ in (6.2) if they are compared with the corresponding elements $A_{0,21}$ and $A_{0,13}$ in (6.6). This not only simplified some of the original entries but allowed them to now appear multiple times in the same matrix. Aiming at reducing the visual complexity, \mathbf{A}_0 is re-written as

$$\mathbf{A}_0 = \begin{bmatrix} -a & b & a & 0 \\ c & -d & -c & 0 \\ 0 & e & -R \cdot e & -e \\ 0 & 0 & c & f \end{bmatrix} = \begin{bmatrix} \mathbf{A}_{11} & \mathbf{A}_{12} \\ \mathbf{A}_{21} & \mathbf{A}_{22} \end{bmatrix} \quad (6.7)$$

Substituting the nominal values of Table 5.1, the previous matrix elements become $R = 2.92$, $a = 223.26$, $b = 0.0846$, $c = 37209.3$, $d = 314.1$, $e = 31.65$ and $f = 90.84$. In terms of magnitude comparison, the former translates into $c \gg a, d, e, f \gg b, R$. This relation is critical for simplification steps that will follow.

6.1.3 Similarity transformation

At this stage, matrix \mathbf{A}_0 is subjected to a similarity transformation that will produce a *similar* matrix $\tilde{\mathbf{A}}$, in the form of (5.10). A similarity matrix \mathbf{P} identical to the one in (5.16) is thus used, giving

$$\begin{aligned} \tilde{\mathbf{A}} &= \mathbf{P}^{-1} \mathbf{A}_0 \mathbf{P} = \begin{bmatrix} \mathbf{I} & -\mathbf{X} \\ \mathbf{0} & \mathbf{I} \end{bmatrix} \cdot \begin{bmatrix} \mathbf{A}_{11} & \mathbf{A}_{12} \\ \mathbf{A}_{21} & \mathbf{A}_{22} \end{bmatrix} \cdot \begin{bmatrix} \mathbf{I} & \mathbf{X} \\ \mathbf{0} & \mathbf{I} \end{bmatrix} \Rightarrow \\ \tilde{\mathbf{A}} &= \begin{bmatrix} \mathbf{A}_{11} - \mathbf{X}\mathbf{A}_{21} & \mathbf{A}_{11}\mathbf{X} - \mathbf{X}\mathbf{A}_{21}\mathbf{X} + \mathbf{A}_{12} - \mathbf{X}\mathbf{A}_{22} \\ \mathbf{A}_{21} & \mathbf{A}_{21}\mathbf{X} + \mathbf{A}_{22} \end{bmatrix} = \begin{bmatrix} \mathbf{Y}_{11} & \mathbf{Y}_{12} \\ \mathbf{Y}_{21} & \mathbf{Y}_{22} \end{bmatrix} \end{aligned} \quad (6.8)$$

As mentioned earlier in the method description in Section (5.2.1), the condition that needs to be fulfilled in order to give $\tilde{\mathbf{A}}$ a quasi-lower triangular form is that the upper right 2×2 block matrix \mathbf{Y}_{12} in (6.8) is a zero matrix:

$$\mathbf{Y}_{12} = \mathbf{A}_{11}\mathbf{X} - \mathbf{X}\mathbf{A}_{21}\mathbf{X} + \mathbf{A}_{12} - \mathbf{X}\mathbf{A}_{22} = \begin{bmatrix} y_{13} & y_{14} \\ y_{23} & y_{24} \end{bmatrix} = \mathbf{0} \quad (6.9)$$

which when broken down to its 4 individual elements, provides the following relations that must be fulfilled at the same time

$$y_{11} = a - a \cdot x_{11} + e \cdot R \cdot x_{11} - c \cdot x_{12} + (b - e \cdot x_{11})x_{21} = 0 \quad (6.10)$$

$$y_{12} = e \cdot x_{11} - a \cdot x_{12} - f \cdot x_{12} + (b - e \cdot x_{11})x_{22} = 0 \quad (6.11)$$

$$y_{21} = -c + c \cdot x_{11} + e \cdot R \cdot x_{21} - (d + e \cdot x_{21})x_{21} - c \cdot x_{22} = 0 \quad (6.12)$$

$$y_{22} = c \cdot x_{12} + e \cdot x_{21} - f \cdot x_{22} - (d + e \cdot x_{21})x_{22} = 0 \quad (6.13)$$

Extraction of expressions

Directly solving the non-linear equations (6.10)-(6.13) leads to large symbolic expressions of no practical use. Furthermore, when the values of the different unknowns are replaced and a certain parameter is swept, the pole movement is not continuous, leading to an undesirable type of closed form solution similar to what a numerical solver would derive for a 4th order system, as demonstrated earlier in Chapter 5. Reaching compact expressions that describe the poles of the system, requires further simplifications to be applied. In order to achieve this, it is necessary to observe the numerical behavior of the transformation matrix entries for different parameter sweeps. The numerical study of x_{11} , x_{12} , x_{21} and x_{22} is given in Fig. 6.1.

The solutions of x_{11} , x_{12} , x_{21} and x_{22} are calculated by fixing three out of the four parameters $a_d=300$ rad/s, $a_f=300$ rad/s, $length=100$ km and $P_{out}=1000$ MW, and studying the transformation

6.1. Application of Similarity Matrix Transformation

matrix variables with respect to the remaining parameter. Parameters a_d and a_f are each swept from 10-1000 [rad/s], the cable length is varied from 10-1000 [km] and the power transfer P_{out} can vary from 10-1000 [MW]. Consequently, the graphs can have a common horizontal axis in the range of 10-1000 units.

Figure 6.1 shows that for a wide variation of all the parameters under consideration, x_{11} has a value between -1.5 and 0.25, x_{22} is negative with an absolute value between 0.9 and 1.5, x_{12} takes very small positive values below 0.02, while x_{21} is negative and exhibits large variations for the different system parameters. It is interesting to notice that sweeping a_d and a_f results in the same graph pattern for both cases of x_{21} and x_{22} .

Relations (6.10) and (6.11) can be expressed as

$$\begin{aligned} \begin{bmatrix} x_{11} \\ x_{12} \end{bmatrix} &= \begin{bmatrix} a - eR + ex_{21} & c \\ -e + ex_{22} & a + f \end{bmatrix}^{-1} \cdot \begin{bmatrix} a + bx_{21} \\ bx_{22} \end{bmatrix} \Rightarrow \\ \begin{bmatrix} x_{11} \\ x_{12} \end{bmatrix} &= \begin{bmatrix} \frac{a^2 + af + abx_{21} + bfx_{21} - bcx_{22}}{a^2 + a[f + e(-R + x_{21})] + e[c + f(-R + x_{21}) - cx_{22}]} \\ \frac{a(e + bx_{22} - ex_{22}) + be(x_{21} - Rx_{22})}{a^2 + a[f + e(-R + x_{21})] + e[c + f(-R + x_{21}) - cx_{22}]} \end{bmatrix} \Rightarrow \\ \begin{bmatrix} x_{11} \\ x_{12} \end{bmatrix} &\cong \begin{bmatrix} \frac{a^2 + af - bcx_{22}}{a^2 + ec(1 - x_{22})} \\ \frac{ae(1 - x_{22})}{a^2 + ec(1 - x_{22})} \end{bmatrix} \end{aligned} \quad (6.14)$$

The last approximation is based on the fact that $c \gg a, d, e, f \gg b, R$ and that the value of x_{21} is much smaller than a . Since c is much larger than the other parameters a, b, d, e, f and R , the term $\Phi = eRx_{21} - (d + ex_{21})x_{21}$ in (6.12) is negligible if $|x_{21}|$ is small enough. Consequently (6.12) becomes

$$\begin{aligned} -c + cx_{11} + \Phi - cx_{11} = 0 \Rightarrow -1 + x_{11} + \frac{\Phi}{c} - x_{22} = 0 \Rightarrow -1 + x_{11} - x_{22} \approx 0 \Rightarrow \\ x_{22} \approx x_{11} - 1 \end{aligned} \quad (6.15)$$

An early positive assessment on the validity of (6.15) can be made by observing the graphs of x_{11} and x_{22} in Fig. 6.1, for the sweeping of the same parameter. Combining (6.14) and (6.15) provides the approximate solution for x_{11} as

$$x_{11} \approx 1 + \frac{b}{2e} + \frac{a^2}{2ce} - \frac{\sqrt{a^4 + 2a^2bc + b^2c^2 + 4c^2e^2 - 4acef}}{2ce} \quad (6.16)$$

which can be further simplified to

$$x_{11} \approx 1 + \frac{b}{2e} + \frac{a^2}{2ce} - \frac{\sqrt{a^4 + 2a^2bc + 4c^2e^2 - 4acef}}{2ce} \quad (6.17)$$

Finally, utilizing (6.13), (6.14), (6.15) and (6.17) provides the approximate solutions for x_{12} , x_{21} and x_{22} as follows

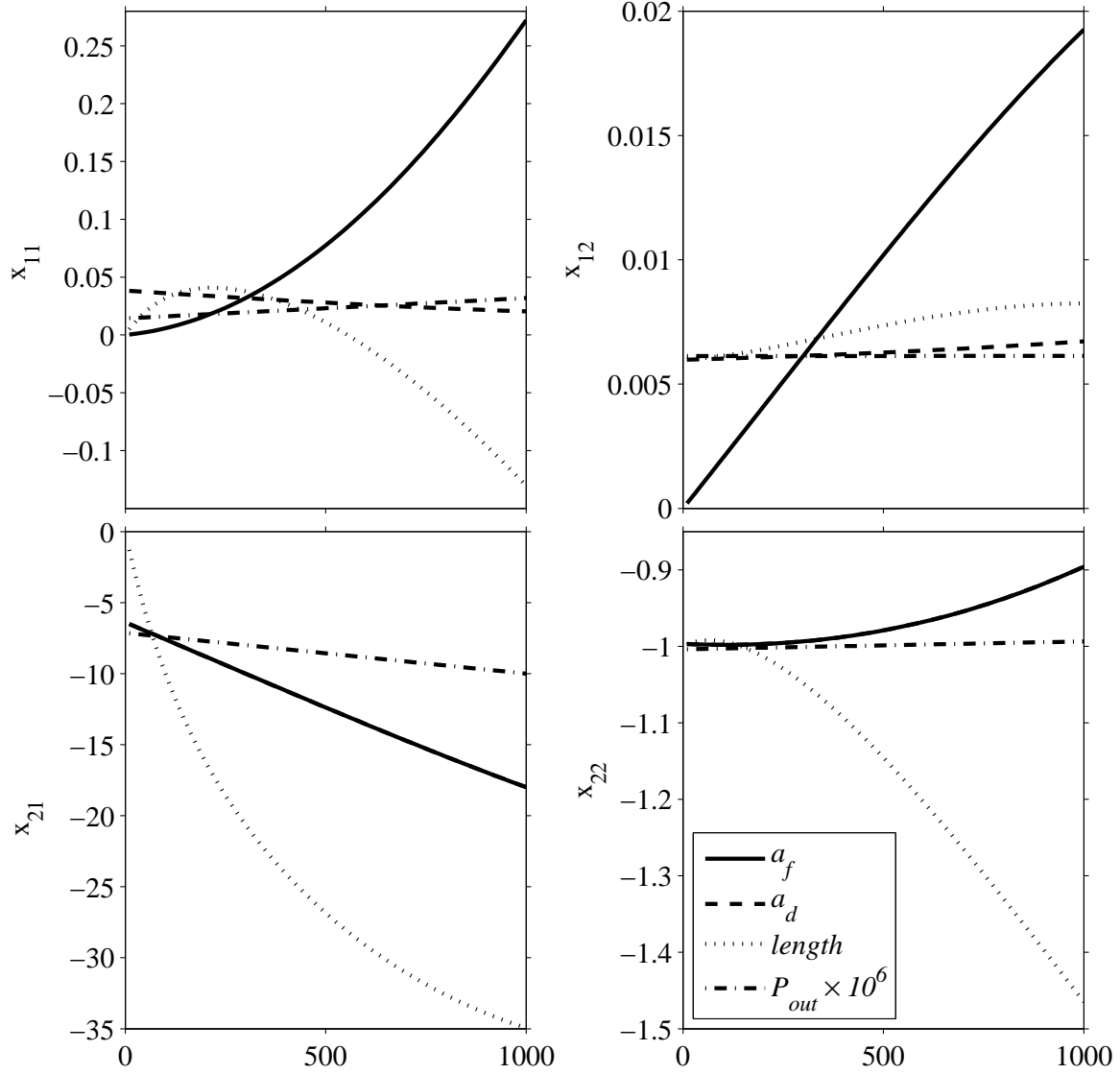


Fig. 6.1 Numerical study of x_{11} , x_{12} , x_{21} and x_{22} for sweeping parameters a_f , a_d , cable length and P_{out} .

$$x_{12} \approx -\frac{a \left(a^2 + bc - 2ce - \sqrt{a^4 + 2a^2bc + 4c^2e^2 - 4acef} \right)}{c \left(a^2 - bc + 2ce + \sqrt{a^4 + 2a^2bc + 4c^2e^2 - 4acef} \right)} \quad (6.18)$$

$$x_{22} \approx \frac{b}{2e} + \frac{a^2}{2ce} - \frac{\sqrt{a^4 + 2a^2bc + 4c^2e^2 - 4acef}}{2ce} \quad (6.19)$$

$$x_{21} = \frac{cx_{12} - (d + f)x_{22}}{e(x_{22} - 1)} \quad (6.20)$$

6.1. Application of Similarity Matrix Transformation

Eigenvalue analysis

After the proper selection of the entries of transformation matrix \mathbf{P} , the eigenvalues of the original state matrix \mathbf{A}_s are determined by the following 2×2 block matrices of $\tilde{\mathbf{A}}$ in (6.8)

$$\tilde{\mathbf{A}}_1 = \mathbf{A}_{11} - \mathbf{X}\mathbf{A}_{21} = \begin{bmatrix} -a & b - e \cdot x_{11} \\ c & -d - e \cdot x_{21} \end{bmatrix} \quad (6.21)$$

$$\tilde{\mathbf{A}}_2 = \mathbf{A}_{21}\mathbf{X} + \mathbf{A}_{22} = \begin{bmatrix} -e \cdot R + e \cdot x_{21} & -e + e \cdot x_{22} \\ c & f \end{bmatrix} \quad (6.22)$$

Simulations considering a wide variation of the unknown parameters of the system, show that $\tilde{\mathbf{A}}_2$ almost always provides the solution for a poorly damped complex-conjugate pole pair whose frequency is closely associated with the resonant frequency of the R-L-C dc-circuit of the system, comprising of the dc-cables and the capacitors of the stations. Further in the analysis, these poles will be referred to as "*Poorly-damped poles*". Taking into account relations (5.7)-(5.9) and (6.21), the analytical expression for the stated complex-conjugate eigenvalue pair will be

$$\lambda_{1,2} = \frac{f - eR + ex_{21}}{2} \pm j \frac{\sqrt{|(f + eR - ex_{21})^2 + 4ce(x_{22} - 1)|}}{2} \quad (6.23)$$

$\tilde{\mathbf{A}}_1$ will then provide the other two poles of the system, which according to the different choice of parameters are either a well-damped (compared to the previous pole pair) complex-conjugate pole pair or two real poles. Both of these forms are expressed by (6.24), where the sign of the expression under the square root defines the complex or real form of the solution.

$$\lambda_{3,4} = \frac{-a - d - ex_{21}}{2} \pm \frac{\sqrt{(a + d + ex_{21})^2 - 4(-bc + ad + cex_{11} + aex_{21})}}{2} \quad (6.24)$$

Further in the analysis, these poles will be referred to as "*Well-damped poles*".

6.1.4 Results

In this section, the exact eigenvalues of the two-terminal VSC-HVDC system, found by numerically extracting them from \mathbf{A}_s , are compared to the analytical eigenvalues expressed by (6.23) and (6.24). Different scenarios are investigated where the values of all the system's parameters and steady-state entries are set to be constantly equal to the values of Table 5.1, with the exception of a parameter that is allowed to vary. The interest in doing so is to observe the accuracy of the analytical expressions compared to the exact eigenvalues, for different values of the selected parameter. It should be further noted that the values of Table 5.1 are considered typical for actual installations, based on the references provided in Chapter 2 and any variations around them define deviations from the norm. Five scenarios are considered

1. Variation of a_f between 10-600 rad/s

Chapter 6. Applications of the analytical approach

2. Variation of a_d between 10-600 rad/s
3. Variation of $a_d = a_f$ between 10-600 rad/s
4. Variation of the cable length between 20-600 km
5. Variation of $P_{out,0}$ within the interval 0-1000 MW

Each scenario is assessed based on a common figure pattern. Initially, the movement of the exact and approximated poles of the system for the variation of the desired parameter (or parameters) is presented. All poles, both the *Poorly-damped poles* and *Well-damped poles* are originally presented in a common graph, highlighting their relative location in the complex plain. Given the fact that the *Poorly-damped poles* typically have much higher characteristic frequency than the *Well-damped poles* (approximately 1 order of magnitude larger), the depiction of all the poles in the same graph could obscure the differences between the exact and approximated poles, especially if the level of approximation is very high. A closer view of each of the two type of poles is thus provided, ensuring a better visual inspection of the fine differences between the exact and approximate solutions.

A separate figure shows the nominal algebraic magnitude error $\epsilon_{N,nom}$ for each of the poorly and well-damped conjugate pole pairs that normally appear. Let \mathbf{p} represent a nominal set (design point) of the n unknown parameters that describe a given condition of the system ($\mathbf{p} \subset \mathbb{R}^n$), $g(\mathbf{p})$ the expression for the exact solution of a pole at \mathbf{p} and $h(\mathbf{p})$ the approximation of $g(\mathbf{p})$. Then the nominal algebraic magnitude error $\epsilon_{N,nom}$ of this pole is here defined as

$$\epsilon_{N,nom} = \frac{\|g(\mathbf{p}) - h(\mathbf{p})\|}{\|g(\mathbf{p})\|} \quad (6.25)$$

This expression considers not only the magnitude difference between the exact and approximated pole solutions, but also their angle differences.

It was observed that in some cases, while varying the selected system parameter, two poles constituting a well-damped pole pair would eventually become real poles of unequal magnitudes. Furthermore, this did not occur for the same values of the selected parameter in the exact and approximated systems. This causes complications since the comparison between a pole pair and two distinct real poles does not provide useful information. For this reason, the pole magnitude error of the well-damped pole pair is shown only when both the exact and approximated expressions are complex-conjugate in form.

Since the poorly-damped poles are of greater importance for the investigation of a system's stability than the well-damped poles, more information are presented for the former. Thus, a separate figure is used to present the error of the poorly damped pole pair approximation, split into real part error $\epsilon_{N,real}$ and imaginary part error $\epsilon_{N,imag}$ and defined as

$$\epsilon_{N,real} = \left| \frac{\text{Re}[g(\mathbf{p})] - \text{Re}[h(\mathbf{p})]}{\text{Re}[g(\mathbf{p})]} \right| \quad (6.26)$$

$$\epsilon_{N,imag} = \left| \frac{\text{Im}[g(\mathbf{p})] - \text{Im}[h(\mathbf{p})]}{\text{Im}[g(\mathbf{p})]} \right| \quad (6.27)$$

6.1. Application of Similarity Matrix Transformation

At this point it should be mentioned that expressions (6.25)-(6.27) may take large values if the location of $g(\mathbf{p})$ is quite close to the origin of the axes of the complex plain, even if the absolute error difference is not large. The fact that $g(\mathbf{p})$ is in the denominator of the previous expressions implies that the division with a small value could lead to large errors $\epsilon_{N,\text{nom}}$, $\epsilon_{N,\text{real}}$ and $\epsilon_{N,\text{imag}}$, which may not reflect fairly the quality of the approximation.

Variation of a_f

The bandwidth a_f is usually chosen to be close or equal to the direct-voltage closed-loop bandwidth a_d [43]. The current scenario examines the impact of a varied difference between the two bandwidths, while keeping a_d constant. Fig. 6.2 presents the results of the parametric sweep of a_f . The poorly-damped poles appear to be stiff in terms of frequency variation, as observed by the related $\epsilon_{N,\text{imag}}$ error which does not exceed 2.2%. The well-damped poles start as two real poles and at around $a_f=35$ rad/s, split into two complex-conjugate poles with increasing frequency and almost constant damping. In the same figure, the approximated poles clearly follow closely the exact values, both of poorly- and well-damped poles. Errors $\epsilon_{N,\text{nom}}$ and $\epsilon_{N,\text{imag}}$ of the poorly-damped poles increase almost linearly for an increase of a_f but remain below 1.82% and 1.7% respectively. Error $\epsilon_{N,\text{real}}$ of the poorly-damped poles follows the same increasing trend and is limited to 4.97% for the maximum value of a_f .

The match of exact and approximate values is quite close for the well-damped poles with their error $\epsilon_{N,\text{nom}}$ starting at around 3.6% for $a_f=35$ rad/s, then quickly dropping below 0.77% and gradually increasing up to 4.48%. The initial relatively high error followed by a rapid decrease happens because in that region, the absolute value of the exact pole is relatively small and as explained earlier, its use in the division within $\epsilon_{N,\text{nom}}$ leads to a numerically high error as a percentage which is not representative of the overall sufficient approximation. Observe however, that this error is fairly small.

Variation of a_d

This scenario examines the impact of a varied difference between the two bandwidths a_d and a_f , while keeping the main bandwidth of the direct-voltage controller a_d constant. In Fig. 6.3, the movement and relative position of the poles for a variation of a_d is very similar to the one observed earlier in Fig. 6.2 for a variation of a_f . Once again, the approximated poles follow closely the numerical values and movement trend of the exact poles for the whole variation region of a_d , both for poorly- and well-damped poles. Errors $\epsilon_{N,\text{nom}}$ and $\epsilon_{N,\text{imag}}$ of the poorly-damped poles are constantly below 1% while the corresponding error $\epsilon_{N,\text{real}}$ has a peak value of 2.2% around $a_d=442$ rad/s.

The error $\epsilon_{N,\text{nom}}$ of the well-damped poles starts just below 6.5% for $a_d=36$ rad/s, but quickly drops and stabilizes below 2.8% throughout the range of [42-600] rad/s. Similarly as in the previous simulation scenario, the proximity of the accurate pole to the origin of the axes for small values of a_d , causes $\epsilon_{N,\text{nom}}$ to be relatively high in that region.

Concurrent variation of a_d and a_f

As mentioned earlier, the bandwidth a_f of the power-feedforward filter and the bandwidth a_d of the direct-voltage controller are normally chosen to be approximately or even precisely the same in value. This scenario examines the case where $a_d=a_f$ and vary from 10-600 rad/s. As observed in Fig. 6.4, increasing the value of parameters $a_d=a_f$ causes the real part of both pole pairs to drastically reduce. The poorly-damped poles maintain their characteristic frequency quite close to 1500 rad/s all the time, while the well-damped poles seems to feature a virtually constant damping throughout the sweeping range of $a_d=a_f$.

The approximation achieved in Fig. 6.4 is exceptionally well for all the values of the swept bandwidths. Regarding the poorly-damped poles, their error $\epsilon_{N,\text{imag}}$ has a peak value of 0.74% at $a_d=a_f=505$ rad/s, $\epsilon_{N,\text{nom}}$ is constantly increasing from 0.2% until 1.44% in the available region of bandwidth variation while error $\epsilon_{N,\text{real}}$ follows the same pattern of constantly increasing value from 0.38-6.82% in the same region. The error $\epsilon_{N,\text{nom}}$ of the well-damped poles starts just below 3.54% for $a_d=10$ rad/s, but quickly drops and then keeps increasing to a maximum value of 5.97% at the maximum value of $a_d=a_f=600$ rad/s.

Variation of cable length

The analysis of the results shown in Fig. 6.5 show that the approximated eigenvalues follow the movement trend of the exact eigenvalues, for both pole pairs, but the relative errors are a bit higher compared to the previous scenarios, especially when the cable length is at its maximum value. A general comment is that for increasing cable length, the real part of both poorly- and well-damped poles increases algebraically while the imaginary part of both pole pairs decreases. The rate of imaginary part decrease is large in the case of the poorly-damped poles, hinting a close relation between the frequency of this pole pair and the physical properties of the dc-cables, unlike the other pole pair whose rate of imaginary part (i.e. frequency) decrease is much more limited.

All the measured errors of the poles have a constantly increasing trend for an increase of the cable length. Regarding the poorly-damped poles, errors $\epsilon_{N,\text{nom}}$, $\epsilon_{N,\text{real}}$ and $\epsilon_{N,\text{imag}}$ reach a peak value of 4.67%, 8.84% and 4.27% respectively for a cable length of 600 km, while the error $\epsilon_{N,\text{nom}}$ of the well-damped poles has a peak of 8.72% at the same cable length.

In order to relate the range of length variation used in this section with actual values, it can be mentioned that typical transmission-lengths for VSC-HVDC systems of existing and planned sites are in the range of 100 up to 400 km [3, 84], with the notable exception of Caprivi-link that measures 950 km [85].

Variation of transferred power

The results for varying transfer power in Fig. 6.6 show a good approximation of the exact poles. It is interesting to notice that the pole movement for the entire power variation interval is quite minimal, implying a poor correlation between transferred power and system eigenvalue, for the

6.1. Application of Similarity Matrix Transformation

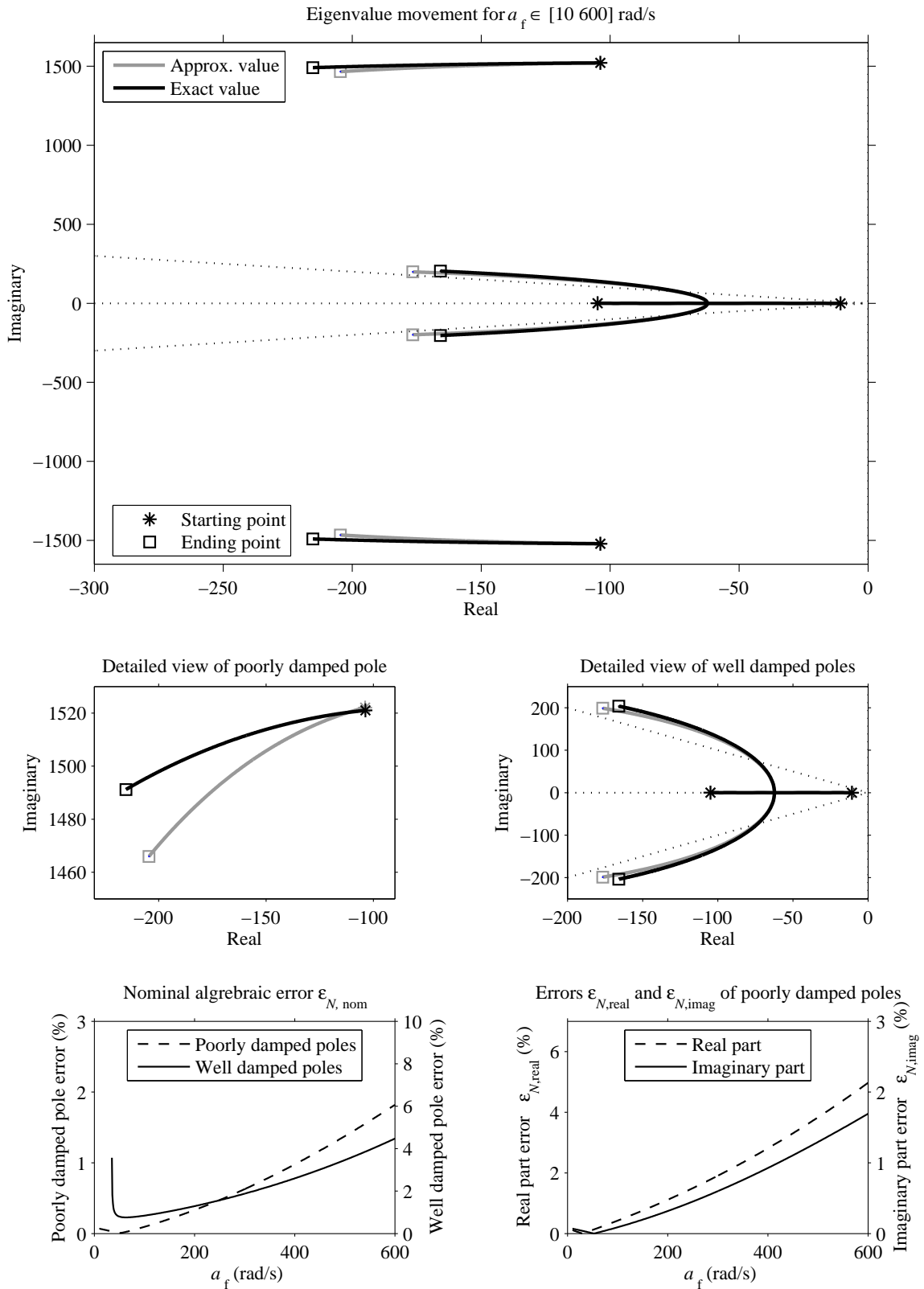


Fig. 6.2 Pole movement and approximation error studies on scenario #1 where a_f is varied.

Chapter 6. Applications of the analytical approach

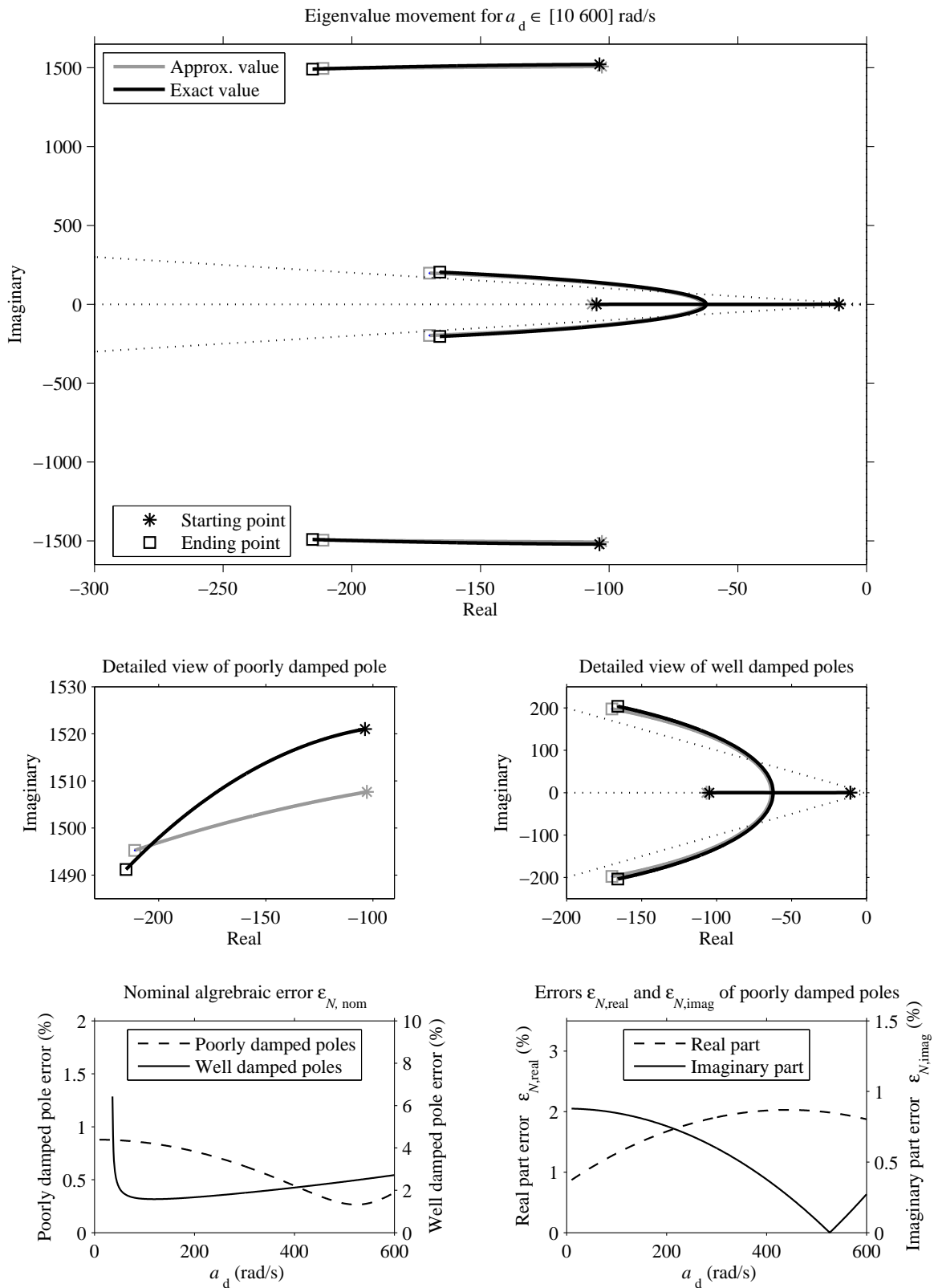


Fig. 6.3 Pole movement and approximation error studies on scenario #2 where a_d is varied.

6.1. Application of Similarity Matrix Transformation

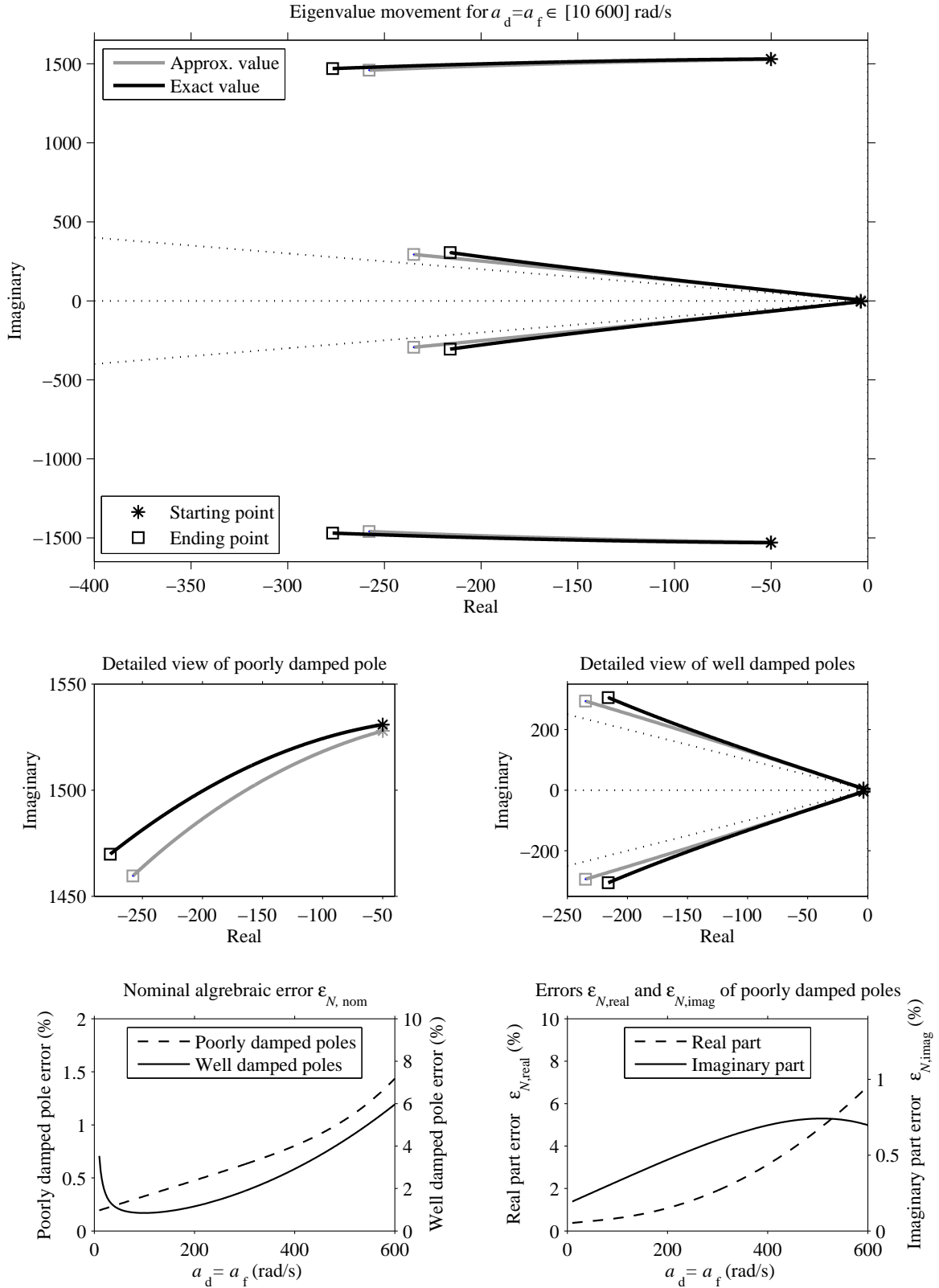


Fig. 6.4 Pole movement and approximation error studies on scenario #3 where a_d and a_f vary.

Chapter 6. Applications of the analytical approach

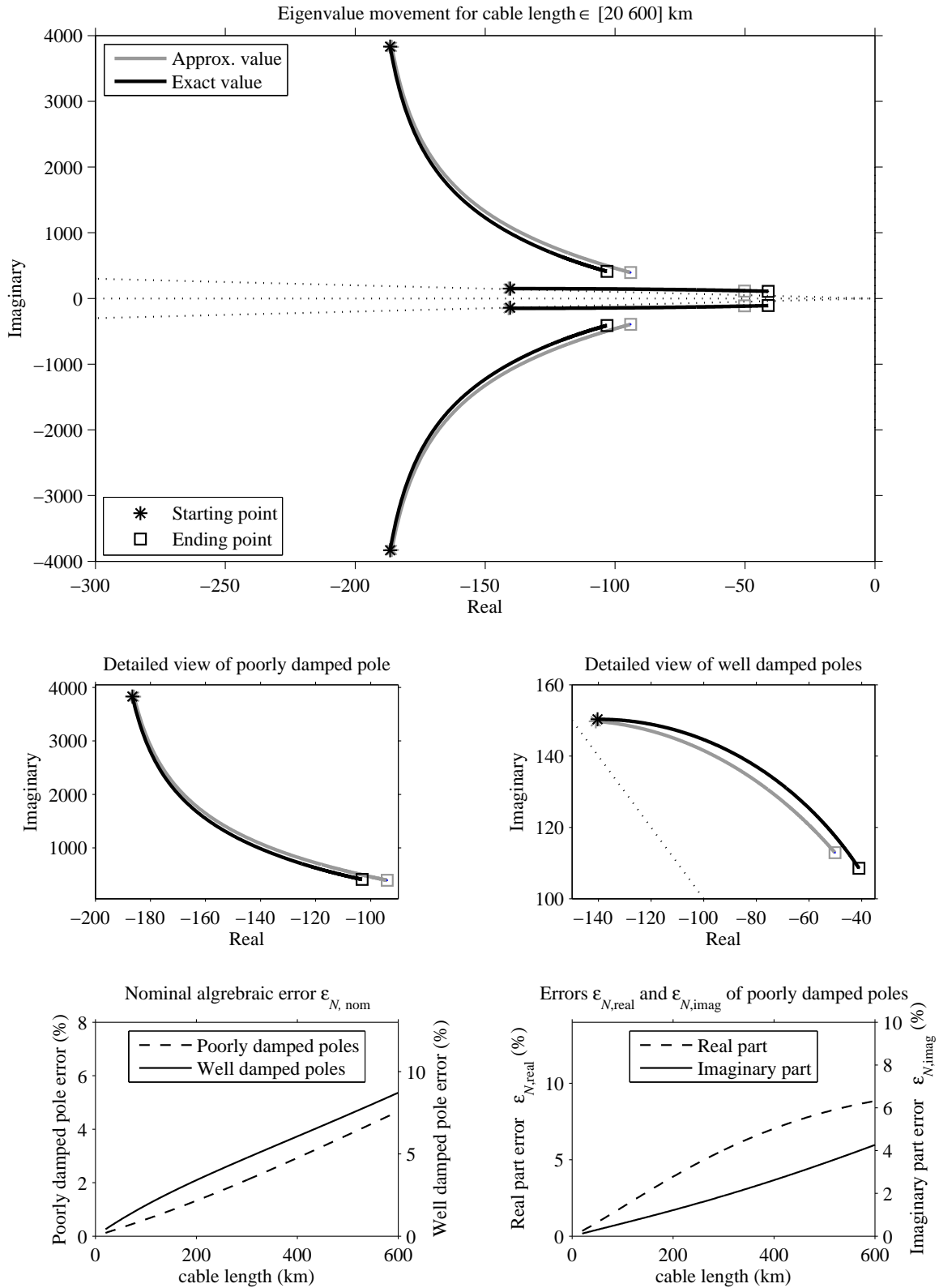


Fig. 6.5 Pole movement and approximation error studies on scenario #4 where the cable length is varied.

6.1. Application of Similarity Matrix Transformation

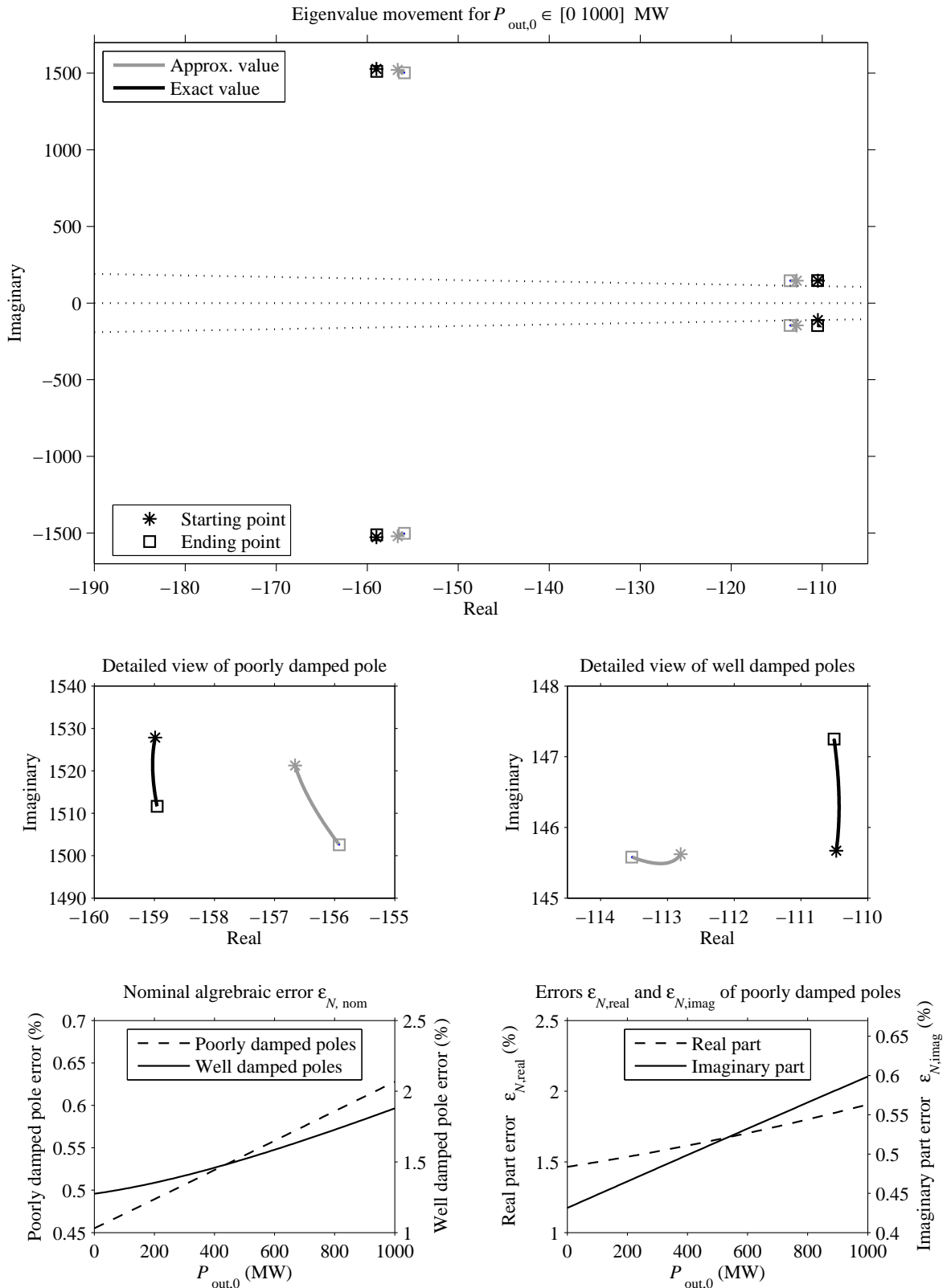


Fig. 6.6 Pole movement and approximation error studies on scenario #5 where $P_{out,0}$ is varied.

selected properties of the given HVDC. Just as in the cable length variation scenario, all the measured errors of the poles have a constantly increasing trend for an increase of the cable length. Regarding the poorly-damped poles, errors $\varepsilon_{N,\text{nom}}$, $\varepsilon_{N,\text{real}}$ and $\varepsilon_{N,\text{imag}}$ reach a peak value of 0.63%, 1.91% and 0.60% respectively for a maximum power transfer of 1000 MW, while the error $\varepsilon_{N,\text{nom}}$ of the well-damped poles has a peak of 1.88% at the same power transfer level.

6.2 Application of the LR algorithm to a VSC-HVDC system

In this section, the *LR* algorithm is applied to a two-terminal VSC-HVDC connection. The objective is to demonstrate the potential of this method in analytically determining the eigenvalues of this system, investigate the complexities involved as well as the advantages, disadvantages and limitations of the *LR* method compared to the earlier suggested *SMT* technique. In an attempt to perform a comparison with the *SMT* technique, the simplified 4th order model described in Section (5.3.3) is again selected here as the object of the investigation. The state matrix of the complete model in (6.1) was further simplified to the one in (6.2). The refined version of the latter is provided in (6.6), whose visually simplified version is given in (6.7) and repeated below.

$$\mathbf{A}_1 = \begin{bmatrix} -a & b & a & 0 \\ c & -d & -c & 0 \\ 0 & e & -R \cdot e & -e \\ 0 & 0 & c & f \end{bmatrix}$$

The nominal values of the VSC-HVDC link are the same as in Table 5.1 and the LR algorithm will investigate the eigenvalue movement of \mathbf{A}_1 for a perturbation of the system's values around the nominal quantities. As described in Section (5.3.3), the convergence of the algorithm is assisted if the diagonal elements are rearranged in a descending order, as far as their absolute values are concerned. For the nominal values of Table 5.1, it is observed that $|-d| > |-a| > |-R \cdot e| > |f|$. Matrix \mathbf{A}_1 is thus pivoted to the expression (6.28), having its diagonal elements in descending order.

$$\mathbf{A}_1 = \begin{bmatrix} -d & c & -c & 0 \\ b & -a & -a & 0 \\ 0 & e & -R \cdot e & -e \\ 0 & 0 & c & f \end{bmatrix} \quad (6.28)$$

The authors in [31–33], have used the *LR* method in sparse state matrices of analogue electronic circuits using at most four symbolic variables. Matrix \mathbf{A}_1 is however not sparse and it is desired to acquire eigenvalue expressions which reflect the effect of all the parameters of the system. As such, the entries of (6.28) are going to be treated fully symbolically, as well as the variables each of these entries represent.

6.2.1 General expression of eigenvalues

Using the steps described in Section (5.2.2), a similar matrix \mathbf{A}_{m+1} is produced at the end of the m^{th} iteration of the algorithm, whose general form is given in (5.26). Given the characteristic form of the initial matrix \mathbf{A}_1 in (6.28), matrix \mathbf{A}_{m+1} is observed to have the following form

$$\mathbf{A}_{m+1} = \left[\begin{array}{cc|cc} b_{11} & b_{12} & -c & 0 \\ b_{21} & b_{22} & b_{23} & 0 \\ \hline b_{31} & b_{32} & b_{33} & -e \\ 0 & 0 & b_{43} & b_{44} \end{array} \right] = \left[\begin{array}{cc} \mathbf{A}_{11} & \mathbf{A}_{12} \\ \mathbf{A}_{21} & \mathbf{A}_{22} \end{array} \right] \quad (6.29)$$

where the elements $b_{i,j}$ are different in every iteration. Just as in the case of the *SMT*, the four approximated eigenvalues of \mathbf{A}_1 are found from the diagonal block matrices \mathbf{A}_{11} and \mathbf{A}_{22} in (6.29). Matrix \mathbf{A}_{11} provides two eigenvalues $\lambda_{1,2}$ as below

$$\lambda_{1,2} = \underbrace{\frac{b_{1,1} + b_{2,2}}{2}}_{\text{Part A}} \pm \underbrace{\frac{\sqrt{b_{1,1}^2 + 4 \cdot b_{1,2} \cdot b_{2,1} - 2 \cdot b_{1,1} \cdot b_{2,2} + b_{2,2}^2}}{2}}_{\text{Part B}} \quad (6.30)$$

In all the examined cases in this chapter, the expression under the square root is negative and the above expression represents a pair of poorly-damped complex-conjugate poles with a real part equal to *Part A* and an imaginary part equal to $|\text{Part B}|$, as these are defined in (6.30). Likewise, matrix \mathbf{A}_{22} provides two eigenvalues $\lambda_{3,4}$ as below

$$\lambda_{3,4} = \underbrace{\frac{b_{3,3} + b_{4,4}}{2}}_{\text{Part A}} \pm \underbrace{\frac{\sqrt{b_{3,3}^2 + 4 \cdot (-e) \cdot b_{4,3} - 2 \cdot b_{3,3} \cdot b_{4,4} + b_{4,4}^2}}{2}}_{\text{Part B}} \quad (6.31)$$

In most of examined cases in this chapter, the expression under the square root is negative, with the above expression representing a pair of usually well- or at least better-damped complex-conjugate poles with a real part equal to *Part A* and an imaginary part equal to $|\text{Part B}|$, as these are defined in (6.31). However, in some cases the expression under the square root is positive, leading to two real poles a) (*Part A + Part B*) and b) (*Part A - Part B*).

The same nomenclature as in Section (5.2.1) is going to be used, thus referring to eigenvalues $\lambda_{1,2}$ as "Poorly-damped poles" and to the eigenvalues $\lambda_{3,4}$ as "Well-damped poles".

6.2.2 Convergence of eigenvalue expressions

The accuracy of the results provided by the expressions (6.30)-(6.31) increases with every iteration of the algorithm. However, each additional iteration adds further complexity to the symbolic form of the $b_{i,j}$ terms in the same expressions. A compromise needs to be made between the accuracy of the solutions and the size of the final eigenvalue expressions.

An investigation of the convergence of the *LR* algorithm is performed by applying scenario #4 of Section (6.1.4) where the cable length is swept from 20-600 km, using the data of Table 5.1. As expected from Fig. 6.5, the system will have two a pair of complex-conjugate poorly-damped

Chapter 6. Applications of the analytical approach

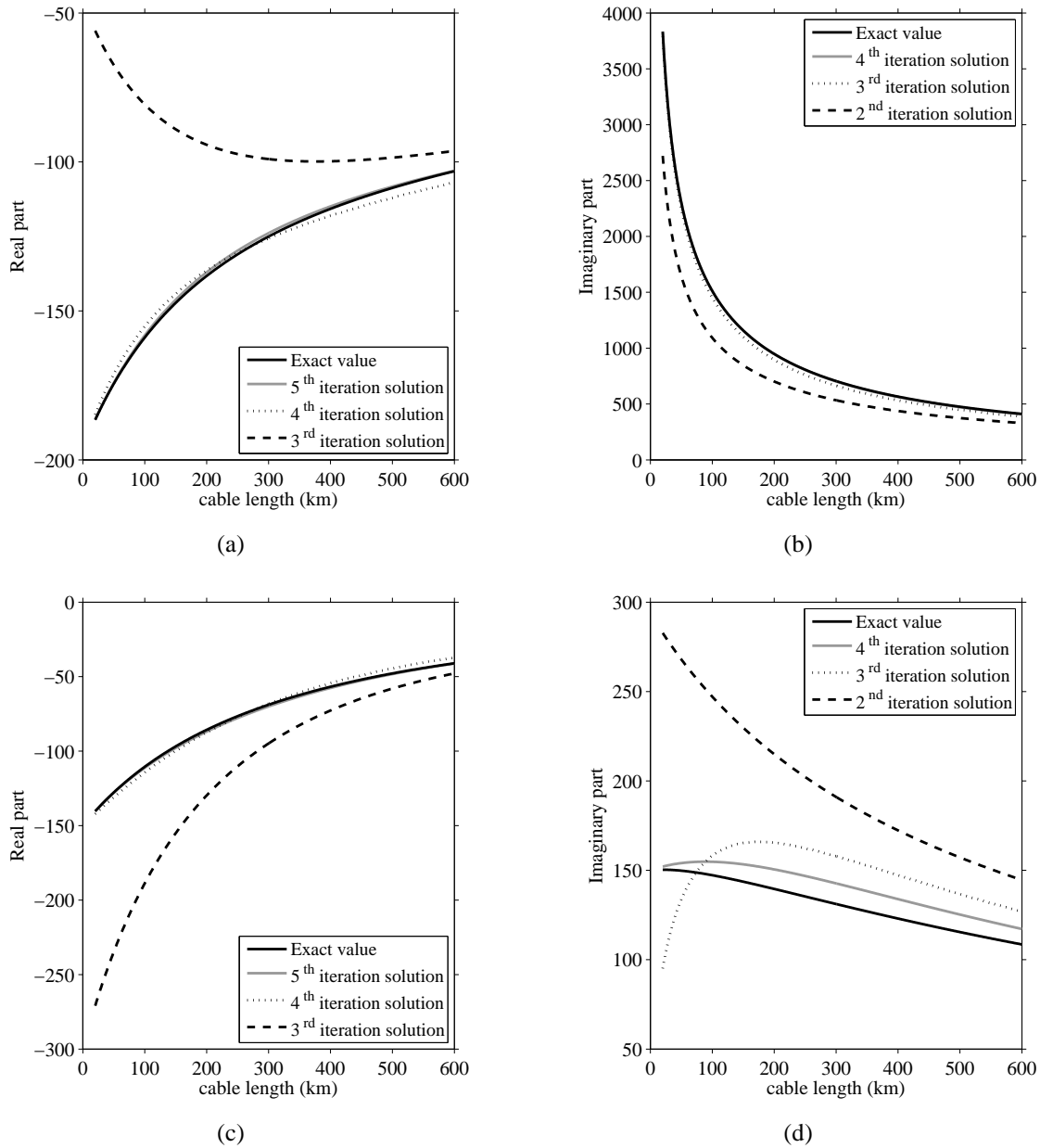


Fig. 6.7 Convergence of the different parts of the eigenvalues for different iterations of the LR algorithm, compared to the exact numerical solution. The cable length is swept from 20-600 km. (a) Real part of $\lambda_{1,2}$, (b) Imaginary part of $\lambda_{1,2}$, (c) Real part of $\lambda_{3,4}$, (d) Imaginary part of $\lambda_{3,4}$

poles and a pair of complex-conjugate well-damped poles; *Part A* and *Part B* in (6.30)-(6.31) are expected to express the real and the imaginary part of their eigenvalues, respectively. Fig. 6.7 presents the results for separately considering the real and imaginary parts of both eigenvalue pairs, as obtained by different iterations of the LR algorithm. Their values are then compared to the exact values, corresponding to the numerical solution of the eigenvalue problem.

6.2. Application of the LR algorithm to a VSC-HVDC system

Figure 6.7(a) and Fig. 6.7(c) show that after the 3rd iteration of the algorithm, the real parts of both eigenvalue pairs quickly converge to their exact numerical values, with the 5th iteration resulting in an almost perfect matching with the exact solutions. The imaginary part of the poorly-damped poles has started to successfully converge even earlier, by the 3rd iteration as seen in Fig. 6.7(b). However, Fig. 6.7(d) shows that the imaginary part of the well-damped poles needs more iterations to converge. After the 2nd iteration, the approximated expression starts approaching the exact solution but will need more than five iterations to get close to matching conditions. The previous observations are consistent with relevant scenarios where other values of the system are swept.

The results of this investigation demonstrate that the LR algorithm can provide reliable results within few repetitions of the algorithm, as well as the fact that the convergence rate of the real and imaginary parts, or to be more precise *Part A* and *Part B* (to include the eigenvalues that become real), of complex poles may vary. This conclusion must be properly utilized, combined with the fact that the symbolic expressions may become overwhelmingly large after only a few iterations.

6.2.3 Analytical eigenvalues expressions

As a reasonable compromise between accuracy and size of the final expressions, the 4 eigenvalues of the system are chosen to be represented by their *Part A* from the 3rd iteration and their *Part B* from the 2nd iteration. Any higher iterations provide expressions so large in size that have no practical value when it comes to symbolic description of eigenvalues. Nevertheless, the chosen iteration results are still large. A simplification procedure must take place during the LR procedure, erasing any terms that have small effect on the final results.

Within the previous context, the final symbolic expressions for the poles of the system will be as described below.

Part A of Poorly-damped poles

The expression for *Part A* of the poorly-damped poles $\lambda_{1,2}$ is

$$\frac{K_1 + K_2}{4eR(a+d)(ad-bc+ce) - 2c[a(6bd-2de) + e(4bc-2ce+d^2)]} \quad (6.32)$$

where

$$K_1 = a^3ce + a^2[6bcd - cef - d(d+eR)(3d+2eR)] - e^2[c^2(-4bR+d+2eR-f) + 2cdeR^2 + d^2eR^3] \quad (6.33)$$

$$K_2 = 3abc[ce + 2d(d+eR)] - ea[c^2e + c(4deR + df + 2e^2R^2) + dR(d+eR)(2d+eR)] \quad (6.34)$$

Chapter 6. Applications of the analytical approach

Part A of Well-damped poles

The expression for *Part A* of the well-damped poles $\lambda_{3,4}$ is

$$\frac{f(ad + ce)^2 - c^2 e^2 (a + d)}{4c^2 e^2} \quad (6.35)$$

Part B of Poorly-damped poles

The expression of *Part B* cannot be easily simplified to a single term but can be represented in the format of (6.30), replacing

$$b_{1,1} = \frac{c [a^2(e - b) + ae(2d + eR) + e(2bc - 2ce + 3d^2 + 2deR)]}{-ce(a + eR) - 2cde + d^3} \quad (6.36)$$

$$b_{1,2} = \frac{c^2 e [a^2(ce - 3d^2) - 2ace(d + eR) + ce(4bc - 2e(c + dR) + d^2)]}{(bc - ad)[(ad - bc + ce)^2 + ce^2 R(a + d)]} \quad (6.37)$$

$$b_{1,3} = \frac{ce^2(bc - ad)(2ad + aeR - 4bc + 2ce)}{(ac(b - e) + 2bcd - 2cde - ce^2 R + d^3)^2} \quad (6.38)$$

$$b_{1,4} = \frac{c^3 e (3b^2 - 4be + 2e^2) (d^2 - ce)}{(ad - bc + ce)^2 [ce(a + eR) + 2cde - d^3]} \quad (6.39)$$

Part B of Well-damped poles

Similarly, the expression of *Part B* cannot be easily simplified to a single term but can be represented in the format of (6.31), replacing

$$b_{3,3} = c \left[\frac{a(d + f) - bc + df}{c(a + d - f)} - \frac{ce^2(a^2 + ad + bc + d^2)}{(a + d)(ad + ce)^2} \right] \quad (6.40)$$

$$b_{4,3} = \frac{c^4 e^3 (bc - ad)^2}{[c^2 e^2 (a + d) - f(ad + ce)^2]^2} \quad (6.41)$$

$$b_{4,4} = \frac{bc - ad}{a + d} \quad (6.42)$$

Practically, all of the terms (6.32)-(6.42) can be further simplified in such a way that sufficient or even improved level of accuracy can be guaranteed in a narrow area of variation of all or selected variables of the system. However, a more general approach is considered for the rest of the analysis, using expressions that are sufficiently accurate in a wide range of variable variation. Thus, the previous terms are going to be used in the complete format that they have been given.

6.2.4 Results

The previously obtained eigenvalue expressions are tested for their accuracy through a series of scenarios where different parameters of the system vary in value. For consistency purposes, the examined scenarios are exactly the same as those in Section (6.1.4) which are summarized as

1. Variation of a_f between 10-600 rad/s
2. Variation of a_d between 10-600 rad/s
3. Variation of $a_d = a_f$ between 10-600 rad/s
4. Variation of the cable length between 20-600 km
5. Variation of $P_{out,0}$ within the interval 0-1000 MW

This approach provides an opportunity to assess the effectiveness of both methods on the same type of model and conditions, while drawing some conclusions from their comparison. Once again, the same type of assessment is used as in Section (6.1.4), where:

- a visual inspection of the approximation of the eigenvalues is performed by plotting the pole movement of the exact and approximated poles of the system for the swept parameter. Both the *LR* and *SMT* results are plotted to highlight how well each method performs.
- the nominal algebraic magnitude error $\varepsilon_{N,nom}$ for each of the poorly- and well-damped complex-conjugate pole pairs are plotted for the *LR* algorithm. The error $\varepsilon_{N,nom}$ is defined in (6.25).
- the real part error $\varepsilon_{N,real}$ and imaginary part error $\varepsilon_{N,imag}$ of the poorly-damped complex-conjugate poles are plotted for the *LR* algorithm. These have been defined in (6.26) and (6.27) respectively.

Variation of a_f

Figure 6.8 presents the results of the parametric sweep of a_f . The *LR*-approximated poorly-damped poles appear to follow in general the track path of their exact counterparts. The associated error $\varepsilon_{N,real}$ reaches a maximum of 10.54% for the maximum value of a_f but constantly lies below 3.7% in the region $a_f \in [10-400]$ rad/s. A smaller error is observed for the imaginary part of the poorly-damped poles which never exceeds 5.05%. It is interesting to notice that all the characteristic errors of these poles are minimized in the area around the nominal value of a_f , with an increasing trend as a_f deviates sharply from 300 rad/s.

A slightly different behavior is observed for the well-damped poles which, even though follow correctly the movement of the exact poles, appear to have a non-negligible magnitude error $\varepsilon_{N,nom}$ for $a_f < 100$ rad/s. This happens because in that region, the absolute value of the exact poles is relatively small and its use in the division within $\varepsilon_{N,nom}$ leads to a numerically high error

Chapter 6. Applications of the analytical approach

as a percentage. However, for the greatest part of the variation region of a_f , the well-damped poles have a small magnitude error (constantly below 3.6% for $a_f \in [115-600]$ rad/s), in fact achieving a better approximation than the *SMT*-derived expressions for great values of a_f .

Variation of a_d

In Fig. 6.9, the movement and relative position of the poles for a variation of the bandwidth of the direct-voltage controller is very similar to the one depicted in Fig. 6.8 for a variation of a_f . Furthermore, all the errors for the *LR*-obtained eigenvalues seem to follow the trends observed for the variation of a_f but are smaller in absolute values. As far as the poorly-damped poles are concerned, their errors $\varepsilon_{N,\text{real}}$ and $\varepsilon_{N,\text{imag}}$ never exceed 3.2% and 2.7% respectively, while the combined error $\varepsilon_{N,\text{nom}}$ takes a maximum value of 2.69% for the maximum value of a_f .

The error $\varepsilon_{N,\text{nom}}$ of the well-damped poles takes, once again, high values for very low values of a_f , but quickly drops and stabilizes below 3.62% throughout the range of [42-600] rad/s. Similarly as in the previous simulation scenario of a_f , the proximity of the accurate pole to the origin of the axes for small values of a_d , causes $\varepsilon_{N,\text{nom}}$ to be relatively high in that region. Overall though, the *SMT*-derived poles seem to converge slightly better to the exact values.

Concurrent variation of a_d and a_f

As observed in Fig. 6.10, increasing the value of parameters $a_d=a_f$ causes the real part of both pole pairs to drastically reduce, while the well-damped poles seem to maintain their damping factor throughout the variation region. Regarding the poorly damped poles, the *LR*-approximated eigenvalues are relatively close to their exact counterparts, even though the corresponding *SMT*-derived eigenvalues appear to have a better convergence. Especially at high and low values of $a_d=a_f$, the *LR*-derived poorly-damped poles show a non-negligible variation in their imaginary part as reflected by their error $\varepsilon_{N,\text{imag}}$. However, the same error becomes very small for a great range around the nominal value of $a_d=a_f=300$ rad/s. Conversely, error $\varepsilon_{N,\text{real}}$ of the same poles remains low for most of the area of parameter variation, with an increasing trend for increasing $a_d=a_f$, reaching the highest value of 5.37% for $a_d=a_f=600$ rad/s.

Regarding the well-damped poles, the detailed view of Fig. 6.10 shows a very good tracking of the exact pole movement for the *LR* method; even better than the one achieved by the *SMT*. In fact the *LR*-approximated poles seem to retain a damping value closer to the one of the exact solutions. The level of approximation in terms of magnitude error $\varepsilon_{N,\text{nom}}$ is also acceptable with the latter lying below 3.7% in the region $a_d=a_f \in [85-600]$ rad/s.

The deviation in the poorly-damped pole approximation accuracy of the imaginary part between the *LR* and *SMT* method, is attributed to the necessary simplification that had to be performed on the terms of *Part B* of these eigenvalues, as these are finally expressed in (6.36)-(6.39). These simplifications were carried out considering an overall good approximation level, without focusing on a specific variable. As shown here, the behavior of the *LR*-approximations is not the optimal for large or very small values of $a_d=a_f$, compared to the *SMT* method results.

6.2. Application of the LR algorithm to a VSC-HVDC system

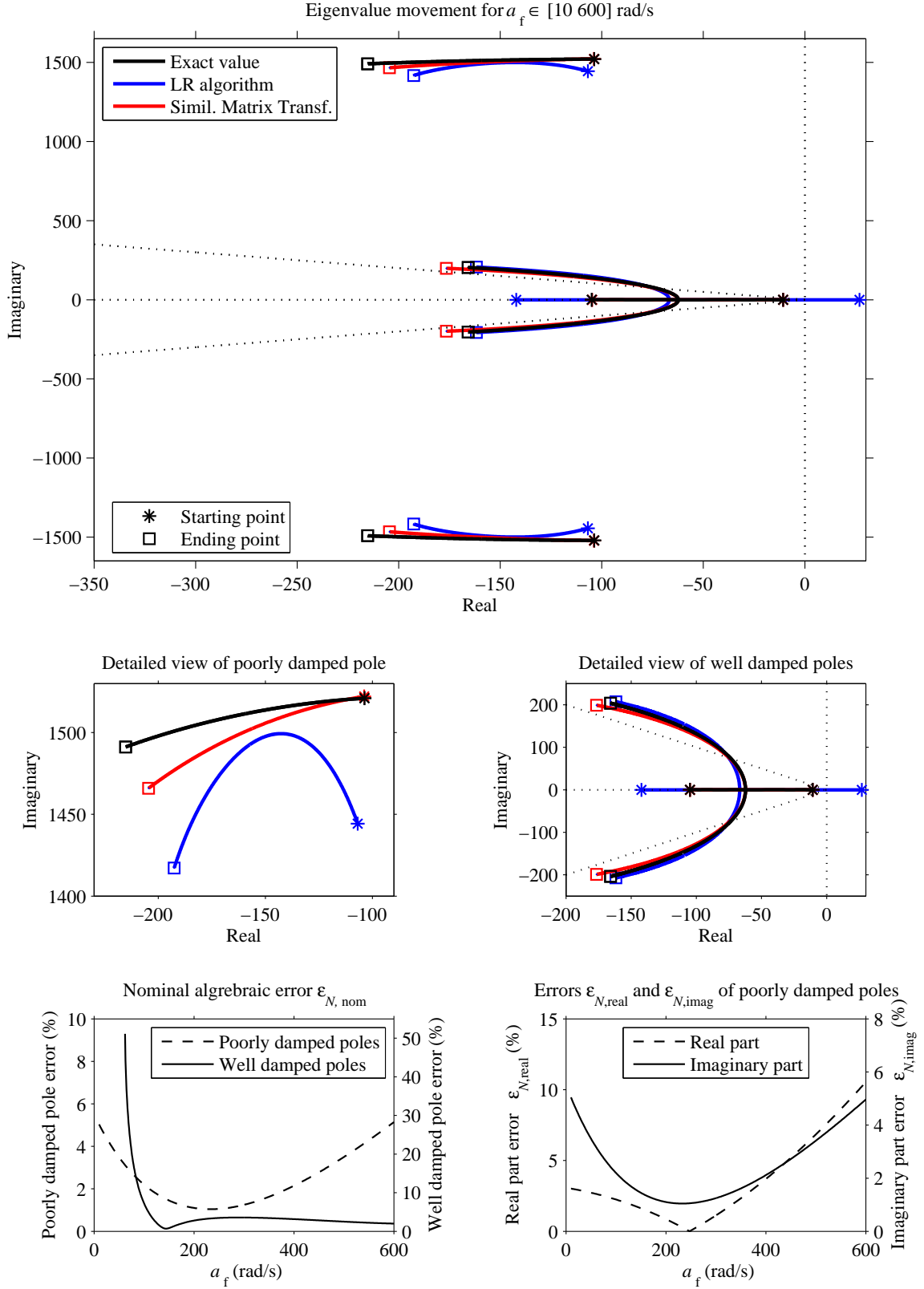


Fig. 6.8 Pole movement and approximation error studies on scenario #1 where a_f is varied.

Chapter 6. Applications of the analytical approach

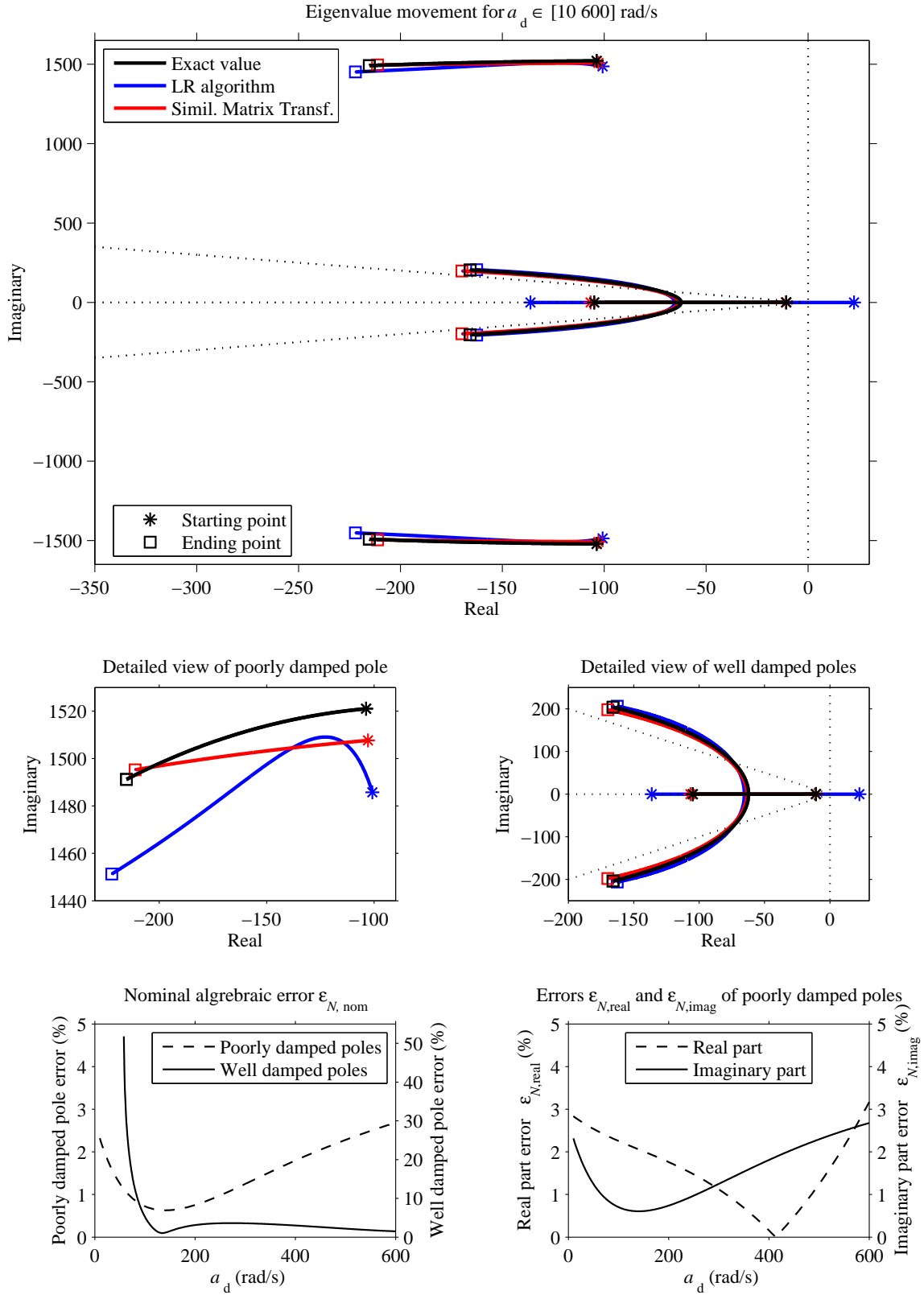


Fig. 6.9 Pole movement and approximation error studies on scenario #2 where a_d is varied.

6.2. Application of the LR algorithm to a VSC-HVDC system

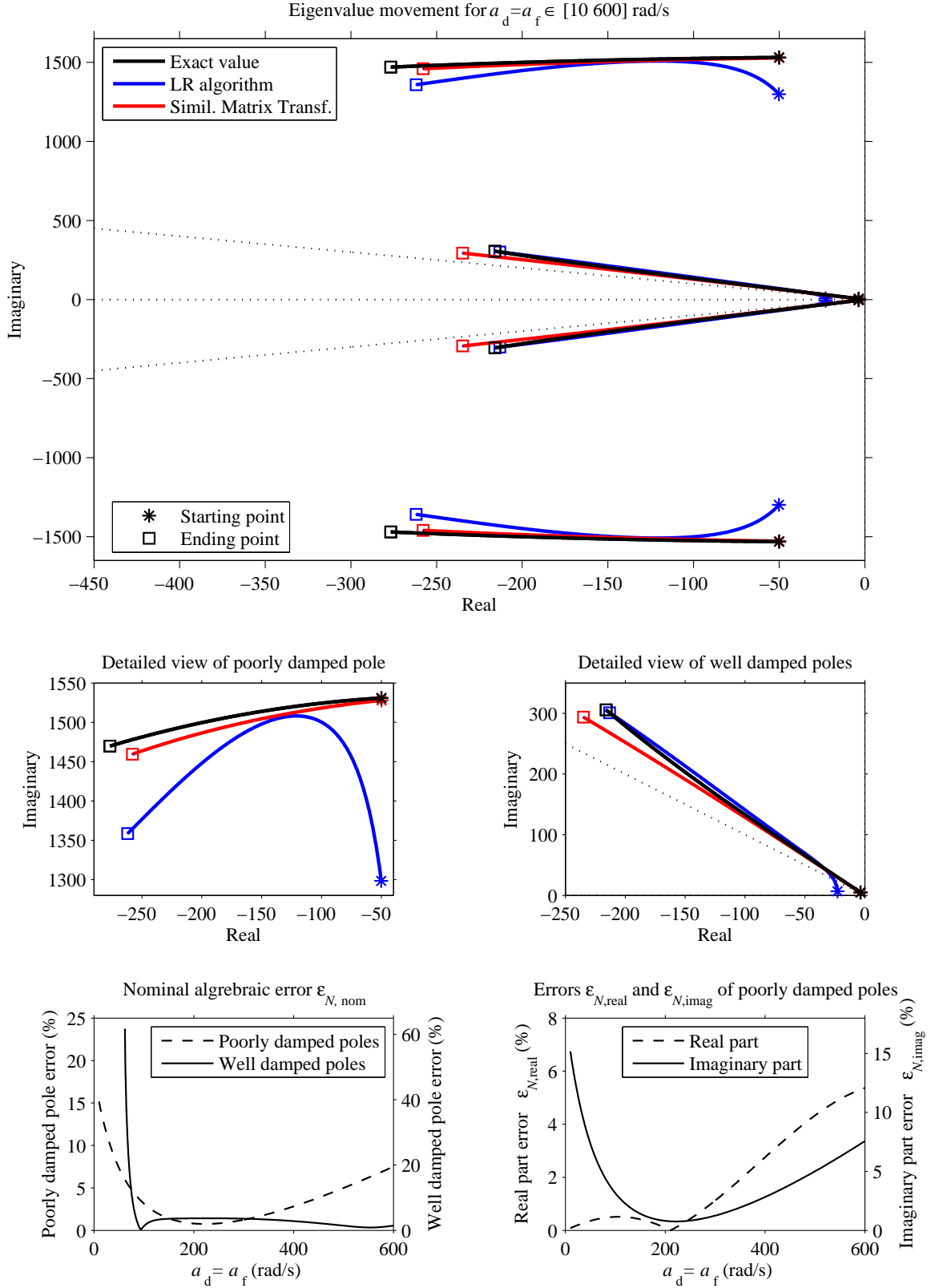


Fig. 6.10 Pole movement and approximation error studies on scenario #3 where a_d and a_f vary.

Chapter 6. Applications of the analytical approach

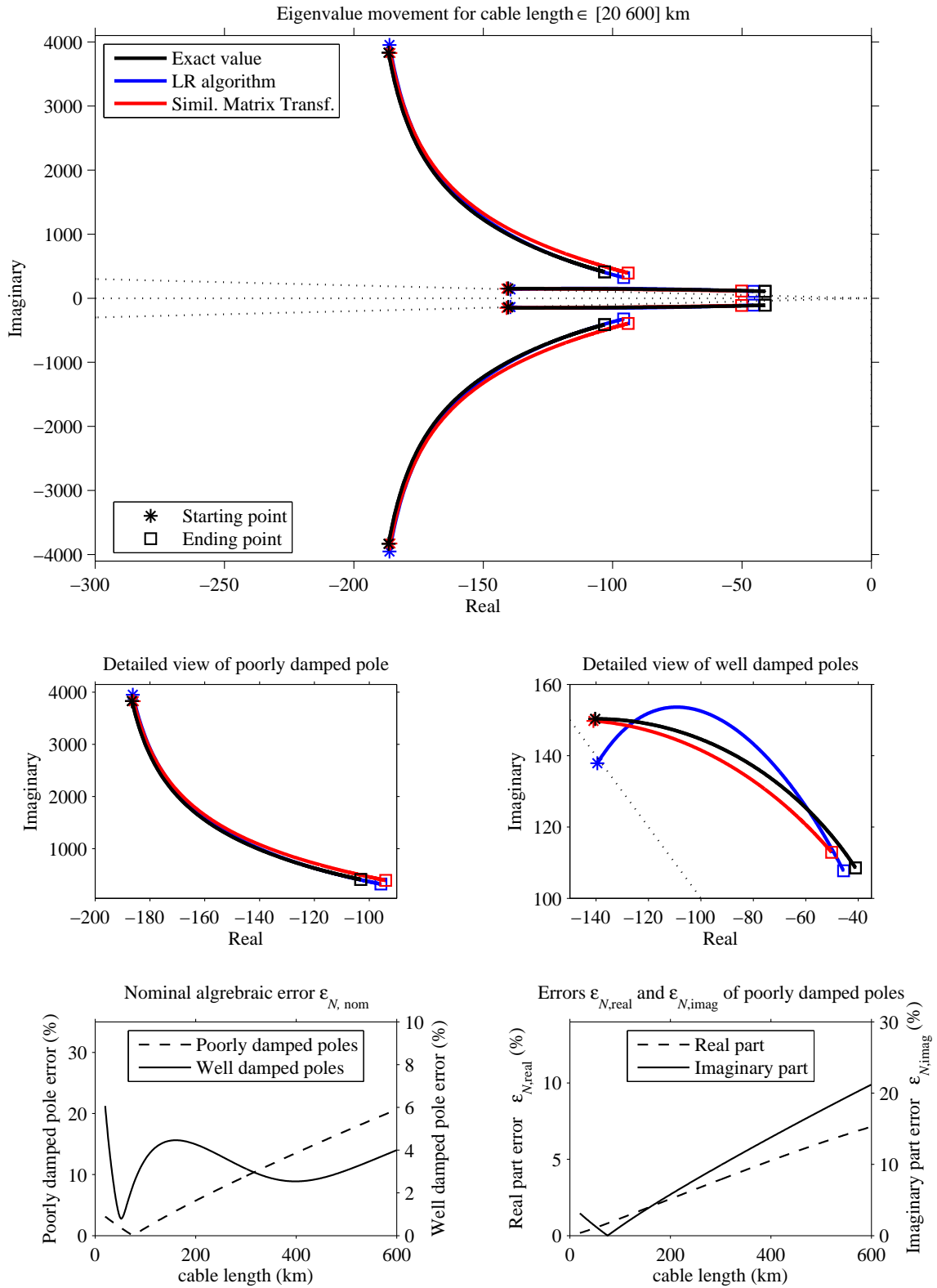


Fig. 6.11 Pole movement and approximation error studies on scenario #4 where the cable length is varied.

6.2. Application of the LR algorithm to a VSC-HVDC system

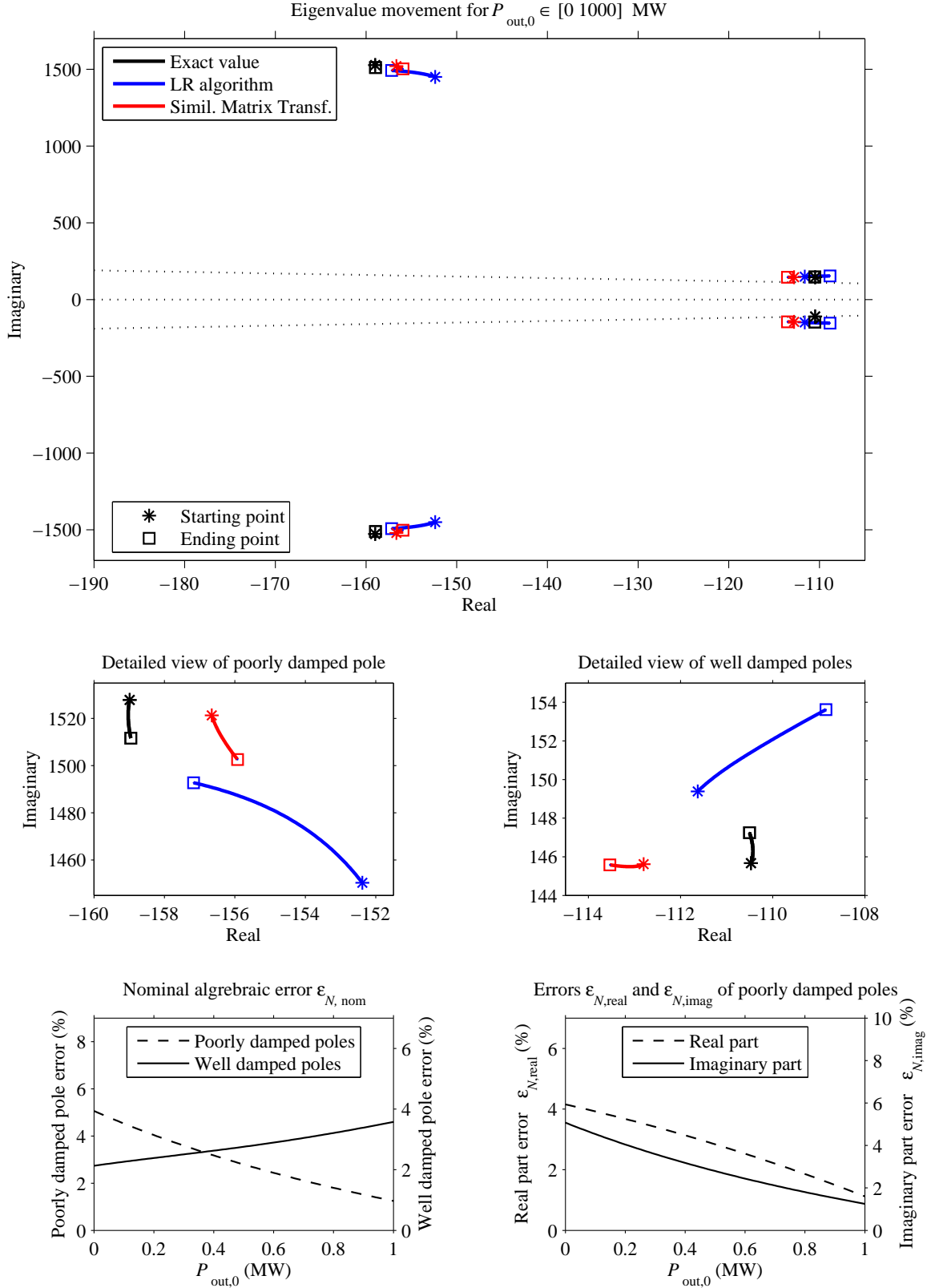


Fig. 6.12 Pole movement and approximation error studies on scenario #5 where $P_{out,0}$ is varied.

Chapter 6. Applications of the analytical approach

Nevertheless, they are still acceptable with a maximum error $\epsilon_{N,\text{imag}}$ of 15.2% for the poorly-damped poles at the lowest value of $a_d=a_f=10$ rad/s.

Variation of cable length

The results shown in Fig. 6.11 show that the *LR*-approximated eigenvalues closely follow the movement trend of the exact eigenvalues, for both pole pairs. The nominal magnitude error $\epsilon_{N,\text{nom}}$ of the well-damped poles is relatively low within the variation range of the cable length, remaining below 6.1%, with the *LR* method achieving even better results than the *SMT* for large cable lengths. A good level of approximation is also achieved for the poorly-damped poles whose real part is approximated with an error $\epsilon_{N,\text{real}}$ which starts at a very low value of 0.17% and keeps increasing until 7.13% for the maximum length of the cable.

However, the error of the *LR*-method on the imaginary part of the same poles is not in the same level. The related error $\epsilon_{N,\text{imag}}$ lies below 5.78% for the first 200 km and then constantly increasing until 21.2% at 600 km. This consequently affects the total nominal magnitude error of the poorly-damped poles considers both the real and imaginary parts of the poles. The description of these poles is better using the *SMT*-method.

Variation of transferred power

The results for varying transfer power in Fig. 6.12 show a relatively good approximation of the exact poles while using the *LR*-method. It should be noted that even though the pole movement is quite minimal for the exact numerical system, the *LR* algorithm tends to derive approximate poles with a slightly wider range of variation, unlike the *SMT*-method which presents a minimal pole movement. Observing the poorly damped poles, the *LR*-method achieves an approximation with constantly declining errors $\epsilon_{N,\text{nom}}$, $\epsilon_{N,\text{real}}$ and $\epsilon_{N,\text{imag}}$, contrary to the *SMT*-method whose respective errors followed a constantly increasing trend as seen in Fig. 6.6. All of these errors are no larger than 5.1% for the *LR*-method at the worst case of zero transferred power.

As far as the well-damped poles are concerned, the *LR*-method approximates the exact poles with a consistently smaller real-part divergence than the *SMT*-method, but a greater imaginary-part divergence. Nevertheless, it correctly shows the increasing trend of its imaginary part for increasing power transfer, unlike the *SMT*-method. The nominal magnitude error $\epsilon_{N,\text{nom}}$ of the well-damped poles for the *LR*-method starts at 2.13% and reaches 3.58% for the maximum amount of power transfer.

6.3 Application of the LR algorithm to an HVDC transmission system

A second example of the *LR* algorithm is demonstrated in this section, by applying it to the 3rd order model of the dc-transmission system described in Section (5.3.2). The objective is to

6.3. Application of the LR algorithm to an HVDC transmission system

analytically describe the physical dynamics of this naturally unstable system, which the direct-voltage controller attempts to stabilize during the operation of the complete VSC-HVDC link. The authors in [14] make an attempt to characterize analytically the poles of the dc-transmission system but can provide symbolic expressions only when there is zero power flow across it, essentially reducing the problem to the estimation of a 2nd order system with the third eigenvalue being real and zero.

It must be noted that, contrary to what expected, the *SMT* method fails to produce approximate expressions for the eigenvalues of this system, even if it is lower in order than the 4th order VSC-HVDC model investigated in Section (6.1). This happens because an approximation similar to (6.15) cannot be made in the case of the dc-transmission system investigation, which would lead to the solution of the non-linear equations that appear.

The initial matrix input \mathbf{A}_1 to the *LR* algorithm is the state matrix of the dc-transmission system model, as described in (5.35) and repeated below.

$$\mathbf{A}_1 = \begin{bmatrix} -\frac{P_{1,0}}{C_1 v_{dc1,0}^2} & -\frac{1}{C_1} & 0 \\ \frac{1}{L_{dc}} & -\frac{R_{dc}}{L_{dc}} & -\frac{1}{L_{dc}} \\ 0 & \frac{1}{C_2} & -\frac{P_{2,0}}{C_2 v_{dc2,0}^2} \end{bmatrix} \quad (6.43)$$

The capacitances used in (6.43) are defined as $C_1 = C_{conv1} + C_{dc}$ and $C_2 = C_{conv2} + C_{dc}$, with reference to Fig. 5.3(b). Given the usual practice in two-terminal VSC-HVDC links, the converter capacitors have the same value. This means that $C_1 = C_2 = C_{link}$ can be considered here. The transmission model is regarded to be part of a stable VSC-HVDC system. This means that the two steady-state electrical values of the system are linked by the relations

$$i_{dc,0} = \frac{v_{dc1,0} - \sqrt{4P_{2,0}R + v_{dc1,0}^2}}{2R_{dc}} \quad (6.44)$$

$$v_{dc2,0} = v_{dc1,0} - i_{dc,0}R_{dc} \quad (6.45)$$

$$P_{1,0} = i_{dc,0}v_{dc1,0} \quad (6.46)$$

$$P_{2,0} = i_{dc,0}v_{dc2,0} \quad (6.47)$$

Consequently, only $P_{2,0}$ and $v_{dc1,0}$ need to be defined externally.

The nominal values of the overall VSC-HVDC link (to which the dc-transmission model (6.43) theoretically belongs) are the same as in Table 5.1 and the *LR* algorithm will investigate the eigenvalue movement of \mathbf{A}_1 for a perturbation of the system's values around the nominal quantities. As described in Section (5.3.3), the convergence of the algorithm is accelerated if the diagonal elements are rearranged in a descending order, as far as their absolute values are concerned. For the nominal values of Table 5.1, it is observed that

$$\left| -\frac{P_{2,0}}{C_2 v_{dc2,0}^2} \right| > \left| -\frac{P_{1,0}}{C_1 v_{dc1,0}^2} \right| > \left| -\frac{R_{dc}}{L_{dc}} \right|$$

Chapter 6. Applications of the analytical approach

Matrix \mathbf{A}_1 is thus pivoted to the expression (6.28), having its diagonal elements in a descending magnitude order

$$\begin{aligned} \mathbf{A}_1 &= \begin{bmatrix} -\frac{P_{2,0}}{C_2 v_{dc2,0}^2} & 0 & -\frac{1}{C_2} \\ 0 & -\frac{P_{1,0}}{C_1 v_{dc1,0}^2} & -\frac{1}{C_1} \\ -\frac{1}{L_{dc}} & \frac{1}{L_{dc}} & -\frac{R_{dc}}{L_{dc}} \end{bmatrix} = \begin{bmatrix} -\frac{P_{2,0}}{C_{link} v_{dc2,0}^2} & 0 & -\frac{1}{C_{link}} \\ 0 & -\frac{P_{1,0}}{C_{link} v_{dc1,0}^2} & -\frac{1}{C_{link}} \\ -\frac{1}{L_{dc}} & \frac{1}{L_{dc}} & -\frac{R_{dc}}{L_{dc}} \end{bmatrix} = \\ &= \begin{bmatrix} a & 0 & c \\ 0 & b & -c \\ -d & d & -R \cdot d \end{bmatrix} \end{aligned} \quad (6.48)$$

where $a = -P_{2,0}/(C_{link} v_{dc2,0}^2)$, $b = -P_{1,0}/(C_{link} v_{dc1,0}^2)$, $c = 1/C_{link}$, $d = 1/L_{dc}$ and $R = R_{dc}$.

6.3.1 General expression of eigenvalues

Using the steps described in Section (5.2.2), a similar matrix \mathbf{A}_{m+1} is produced at the end of the m^{th} iteration of the algorithm, whose general form is given in (5.26). Given the characteristic form of the initial matrix \mathbf{A}_1 in (6.48), matrix \mathbf{A}_{m+1} is observed to have the following form

$$\mathbf{A}_{m+1} = \left[\begin{array}{cc|c} b_{11} & b_{12} & b_{13} \\ b_{21} & b_{22} & b_{23} \\ b_{31} & b_{32} & b_{33} \end{array} \right] = \begin{bmatrix} \mathbf{A}_{11} & \mathbf{A}_{12} \\ \mathbf{A}_{21} & \mathbf{A}_{22} \end{bmatrix} \quad (6.49)$$

where the elements b_{ij} are different in every iteration. Matrix \mathbf{A}_1 has three eigenvalues, which for all the parameter-variation scenarios where observed to be consisting of a real eigenvalue and a complex-conjugate eigenvalue pair. The real approximated eigenvalue λ_1 of \mathbf{A}_1 is found from the diagonal block matrices \mathbf{A}_{22} as below

$$\lambda_1 = \mathbf{A}_{22} = b_{33} \quad (6.50)$$

Matrix \mathbf{A}_{11} provides the approximated complex-conjugate eigenvalue pair $\lambda_{2,3}$ as below

$$\lambda_{2,3} = \underbrace{\frac{b_{11} + b_{22}}{2}}_{\text{Part A}} \pm \underbrace{\frac{\sqrt{b_{11}^2 + 4 \cdot b_{12} \cdot b_{21} - 2 \cdot b_{11} \cdot b_{22} + b_{22}^2}}{2}}_{\text{Part B}} \quad (6.51)$$

The expression under the square root is consistently negative, leading to a pair of complex-conjugate poles with a real part equal to *Part A* and an imaginary part equal to $|Part B|$.

6.3.2 Convergence of eigenvalue expressions

Owing to the nature of the *LR* algorithm, the accuracy of the results provided by the expressions (6.50) and (6.51) increases with every iteration of the algorithm, with each additional iteration

6.3. Application of the LR algorithm to an HVDC transmission system

adding further complexity to the symbolic form of the $b_{i,j}$ terms in the same expressions. Similarly to Section (6.2.2), an investigation of the rate of convergence of (6.50) and (6.51) needs to be performed. The objective is to get an impression of when the algorithm should be terminated, guaranteeing satisfactory convergence at the same time.

A modified scenario #5 of Section (6.1.4) is performed, where the power transfer $|P_{2,0}|$ is swept from 0-1000 MW, using the data of Table 5.1. A difference with the original scenario is that the transmission link is considered to be overhead lines, with a length of 600 km. Such a choice is made because the high inductance of overhead lines causes a great eigenvalue variation of the eigenvalues. This provides more visual data to evaluate the convergence of the LR algorithm.

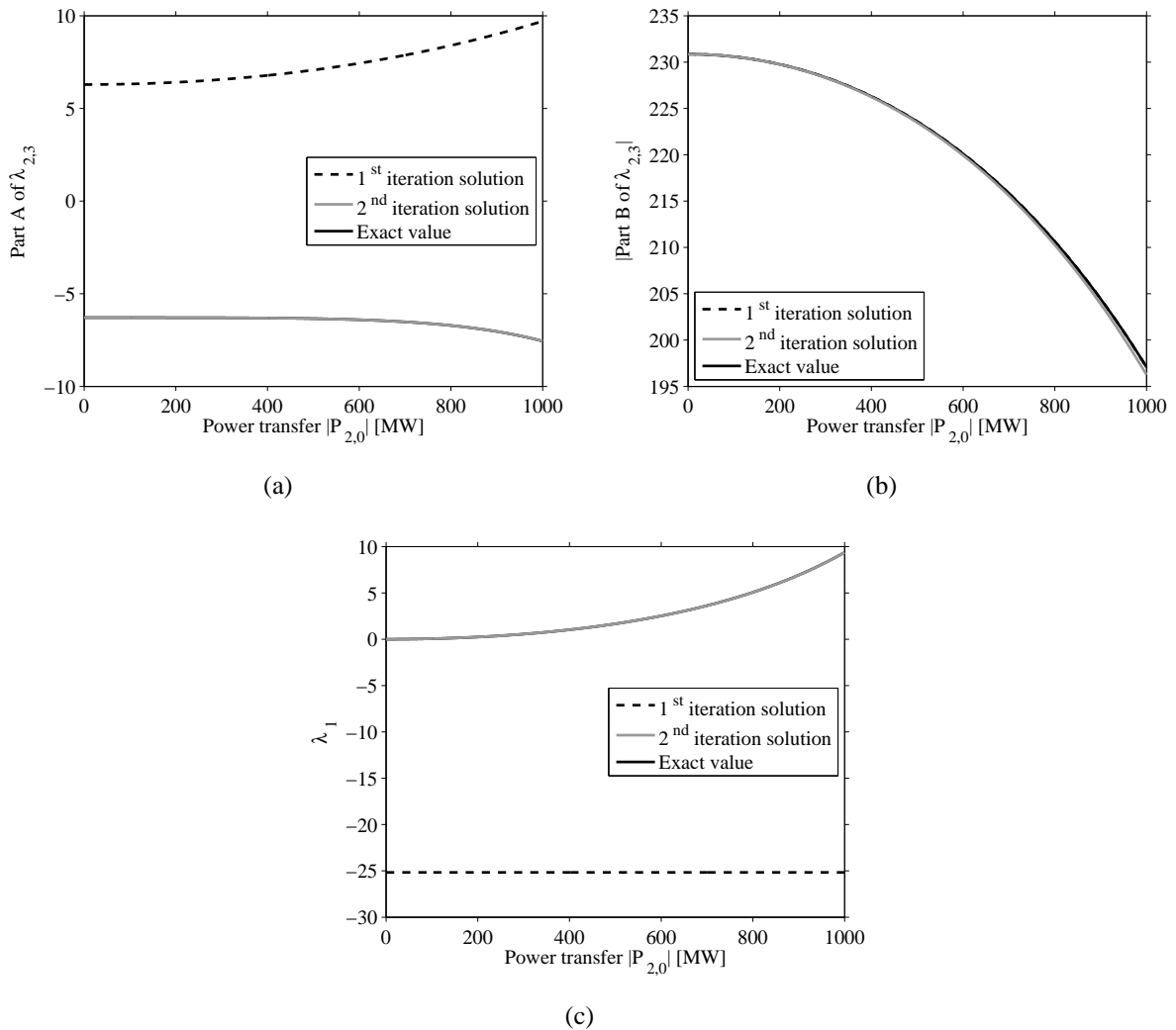


Fig. 6.13 Convergence of the different parts of the eigenvalues for different iterations of the LR algorithm, compared to the exact numerical solution. The cable length is 600 km and $|P_{2,0}|$ is swept from 0-1000 MW. (a) Real part of $\lambda_{2,3}$, (b) Imaginary part of $\lambda_{2,3}$, (c) λ_1 .

Figure 6.13(a) presents the real part of the complex-conjugate eigenvalues $\lambda_{2,3}$. As it can be observed, there is a great leap in the performance of the algorithm between 1st and 2nd iteration, with the real part already converging sufficiently after only 2 iterations. The same comment can be made about Fig. 6.13(c) and the real eigenvalue λ_1 . Interestingly enough, the imaginary part of the complex-conjugate eigenvalues $\lambda_{2,3}$ converges at the first iteration of the algorithm as seen in Fig. 6.13(b).

6.3.3 Analytical eigenvalues expressions

Judging from the results of the previous section, a reasonable compromise between accuracy and size of the final expressions implies that

- the real eigenvalue of the system will be approximated by the expression of the 2nd iteration.
- the real part of the complex-conjugate eigenvalues will be approximated by the expression of Part A from the 2nd iteration.
- the imaginary part of the complex-conjugate eigenvalues will be approximated by the expression of Part B from the 1st iteration.

Within this context, the final symbolic expressions for the poles of the system will be as described below.

Part A of complex-conjugate poles

Regarding, the complex-conjugate pole pair, *Part A* is evaluated as

$$\frac{(a+b)[a^2b^2 - (a^2 + ab + b^2)cd] + (a^2 + b^2)cd^2R}{2a^2b^2 - 2(a^2 + b^2)cd} \quad (6.52)$$

Part B of complex-conjugate poles

Part B of the complex conjugate pole pair is evaluated as

$$\frac{1}{2} \sqrt{(a-b)^2 + \frac{2(a-b)^2cd}{ab} + \frac{(a+b)^2c^2d^2}{a^2b^2}} \quad (6.53)$$

Real eigenvalue λ_1

The real eigenvalue of the dc-transmission system is evaluated as

$$\frac{abd[bc + a(c - bR)]}{-b^2cd + a^2(b^2 - cd)} \quad (6.54)$$

6.3. Application of the LR algorithm to an HVDC transmission system

Observations

Part *B* of the complex-conjugate poles is found to be almost identical to the resonant frequency ω_{res} of the dc-transmission link which is defined as

$$\omega_{\text{res}} = \frac{1}{\sqrt{L_{\text{dc}} \frac{C_{\text{link}}}{2}}} \quad (6.55)$$

Minute deviations in the imaginary part of the complex poles are attributed to the resistance R_{dc} of the lines, which slightly alters the dynamics of the transmission link. This observation was made in all the scenarios examined for the model of the dc-transmission system and to a lesser extent in the poorly-damped poles of the VSC-HVDC model in Section (6.1) and Section (6.2), where the interaction with the direct-voltage controller leads to small but noticeable differences in the imaginary part of these poles.

Without the resistance R_{dc} , the dc-transmission link would be a pure LC-circuit with two marginally -stable complex-conjugate poles at ω_{res} . The presence of the resistance additionally improves the damping of the complex-conjugate poles but at the same time leads to the existence of the unstable pole λ_1 . In fact, an increased value of R_{dc} moves λ_1 further towards the right of the RHP, deteriorating the stability of the closed-loop HVDC system. This effect is however profoundly observed only when overhead transmission lines are used in the HVDC link. As will be shown in the following section, a relatively large movement of the unstable pole is observed only when overhead transmission lines are employed. When a cable is used instead, the unstable pole deviates much less and remains in the vicinity of the axis origin.

Observe that the term $R = R_{\text{dc}}$ may not be visually present in all of the expressions (6.52)-(6.54) but it exists within a and b as part of $P_{1,0}$ and $v_{\text{dc}2,0}$.

6.3.4 Results

In a similar pattern as in Section (6.1.4) and Section (6.2.4), the previously obtained eigenvalue expressions are tested for their accuracy through a series of scenarios where different parameters of the system vary in value. The dc-transmission system under investigation is considered to be under temporary stability (as if it were part of a functioning VSC-HVDC link). The steady-state electrical values of the system are normally $v_{\text{dc}1,0} = 640$ kV and $P_{2,0} = -1000$ MW, with $v_{\text{dc}2,0}$ and $P_{1,0}$ being calculated from (6.44)-(6.47). Four examined scenarios are examined. These are summarized as

1. Variation of $|P_{2,0}|$ between 0-1000 MW with cable type of transmission system
2. Variation of $|P_{2,0}|$ between 0-1000 MW with overhead-line type of transmission system
3. Variation of the transmission-line length between 20-600 km, using cable type of transmission system

Chapter 6. Applications of the analytical approach

4. Variation of the transmission-line length between 20-600 km, using overhead-line type of transmission system

The values of the converter capacitors and cable properties are found in Table 5.1 while the overhead line properties are found in Table 2.1. The same type of assessment is used as in Section (6.1.4), where:

- a visual inspection of the approximation of the eigenvalues is performed by plotting the pole movement of the exact and approximated poles of the system for the swept parameter.
- the nominal algebraic magnitude error $\varepsilon_{N,\text{nom}}$ for each of the complex-conjugate pole pair and the real eigenvalue are plotted. The error $\varepsilon_{N,\text{nom}}$ is defined in (6.25).
- the real part error $\varepsilon_{N,\text{real}}$ and imaginary part error $\varepsilon_{N,\text{imag}}$ of the complex-conjugate pole pair are plotted. These have been defined in (6.26) and (6.27) respectively.

Variation of $P_{2,0}$ with cable type of transmission system

The results in Fig. 6.14 show that the dynamics of the dc-transmission system are practically immune to the level of steady-state power transfer over the lines, especially the complex poles. Furthermore, the real pole is shown to be permanently unstable in non-zero power transfer conditions. This is expected because the transmission line has no natural way to balance the input and output powers after a deviation, leading to an uncontrolled behavior of the voltage of the capacitors. Regarding the effectiveness of the LR algorithm, it is clear that the approximated and numerically derived results cannot be visually distinguished from each other. Indications of the good level of approximation are the errors $\varepsilon_{N,\text{nom}}$ of all poles which are constantly below $3 \times 10^{-3} \%$, with $\varepsilon_{N,\text{real}}$ even lying below $2 \times 10^{-5} \%$.

Variation of $P_{2,0}$ with overhead-line type of transmission system

The same type of power variation as above but using an overhead line, has similar results in terms of restricted pole movement but the complex poles seem to be much more under-damped, as seen in Fig. 6.15. This provides an early information about the stability of the complete VSC-HVDC system. Compared to the cable-type of dc-transmission, a direct-voltage controller with fixed bandwidth settings would now try to stabilize a process with worse damping characteristics. This would cause the closed-loop poles of the overhead-line based system to have worse damping characteristics than with the cable-type of lines.

Once again, the approximation achieved by the LR method are very sufficient with $\varepsilon_{N,\text{nom}}$ of all poles remaining under $4 \times 10^{-3} \%$ for any power transfer. Exceptionally good results are observed for the complex poles of the system with $\varepsilon_{N,\text{imag}}$ and $\varepsilon_{N,\text{real}}$ reaching a maximum value of $9.2 \times 10^{-4} \%$ and $3.4 \times 10^{-4} \%$ for the maximum power transfer, respectively.

6.3. Application of the LR algorithm to an HVDC transmission system

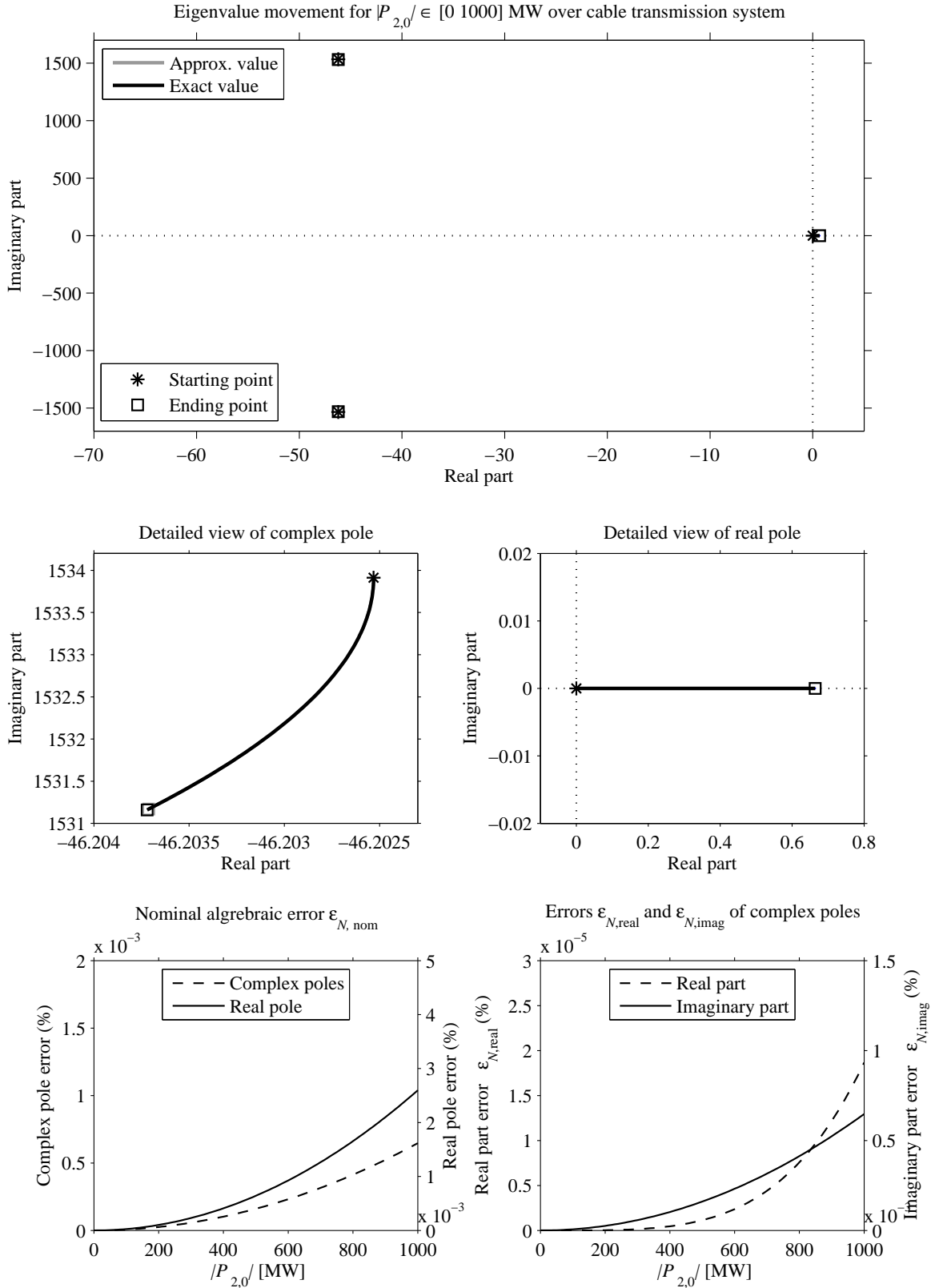


Fig. 6.14 Approximation studies on scenario #1 where $|P_{2,0}|$ is varied over a cable-based system.

Chapter 6. Applications of the analytical approach

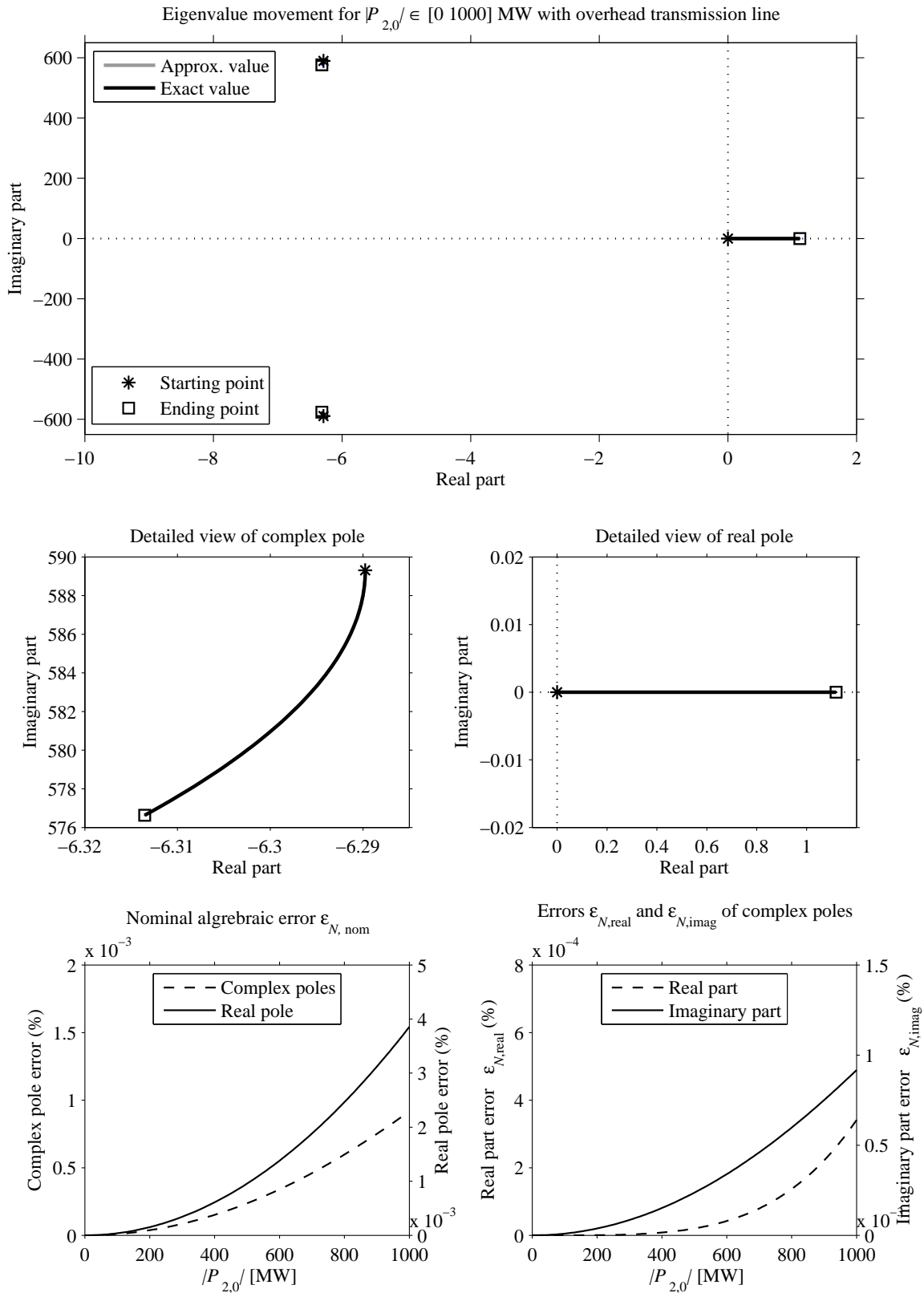


Fig. 6.15 Approximation studies on scenario #2 where $|P_{2,0}|$ is varied in an overhead-line based system.

6.3. Application of the LR algorithm to an HVDC transmission system

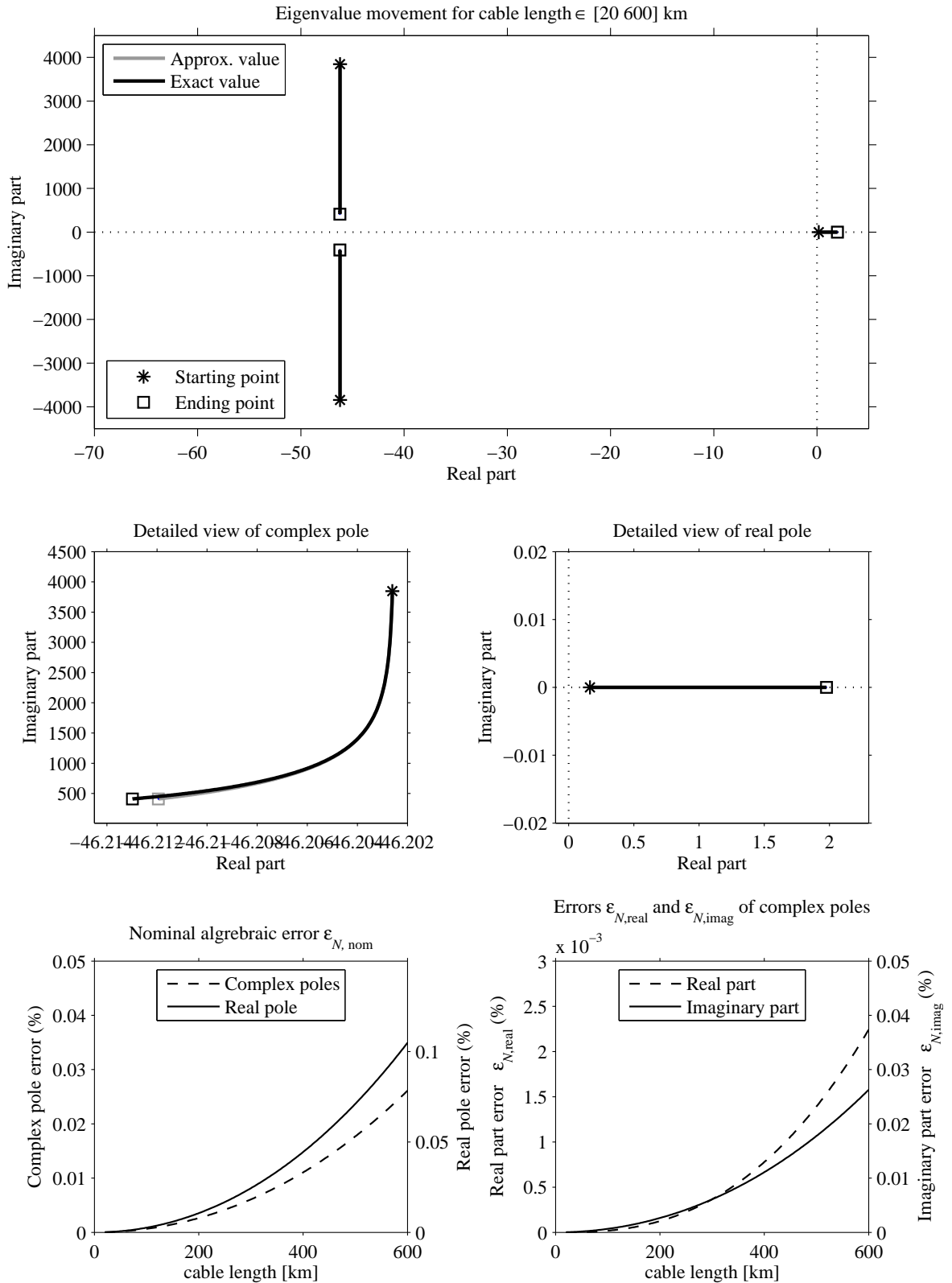


Fig. 6.16 Approximation studies on scenario #3 with cable-transmission lines of varying length.

Chapter 6. Applications of the analytical approach

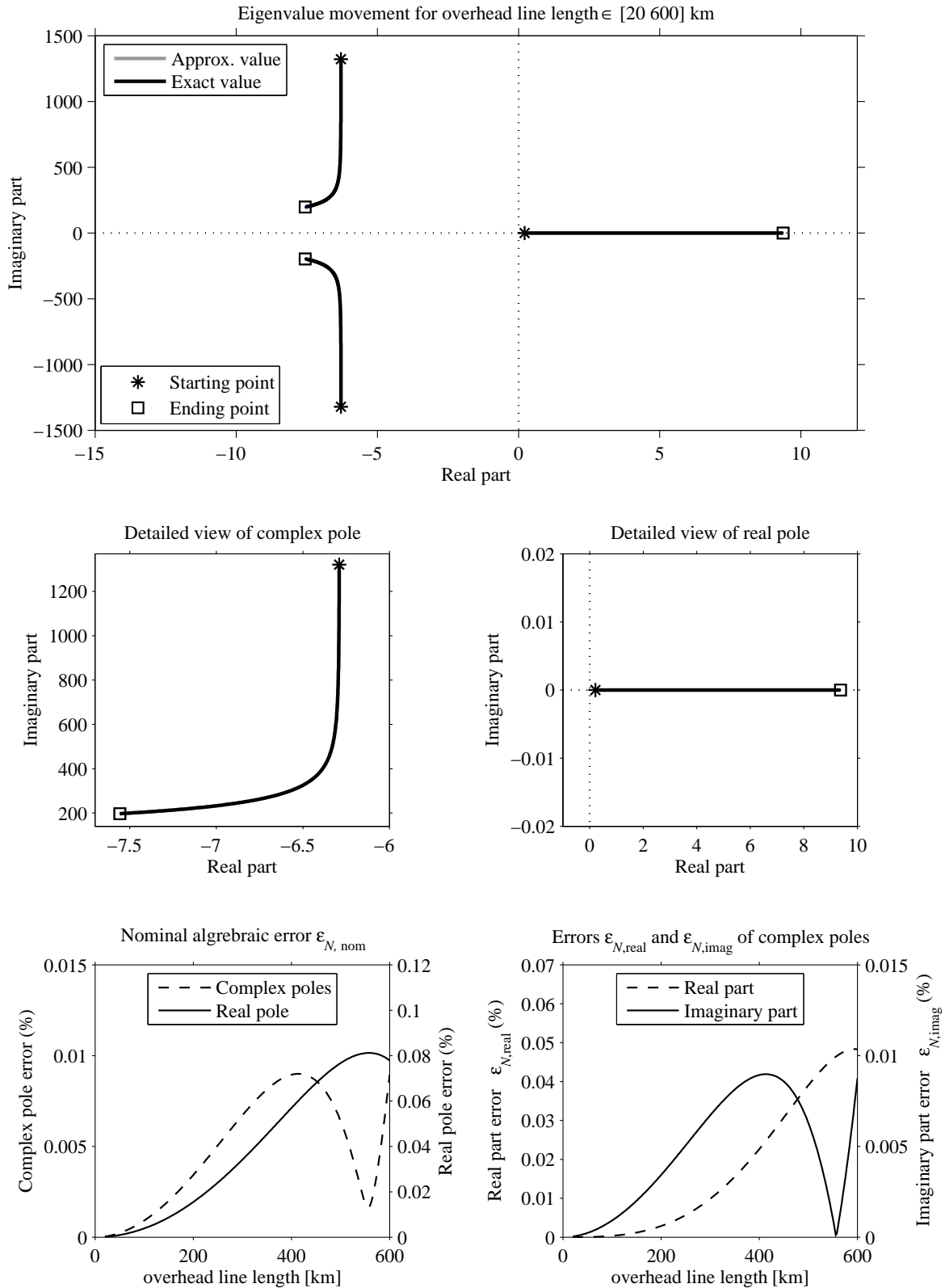


Fig. 6.17 Approximation studies on scenario #4 with overhead-lines of varying length.

6.4. Investigation on the accuracy of the approximating methods

Variation of cable length

In Fig. 6.16, the power transfer is set to its maximum value and the length of the cable is increased. This has a fundamental impact on the complex poles of the line, with an increasing length leading to a constantly decreasing imaginary part of the poles. This is explained because as mentioned earlier, the imaginary part of these poles is very close to the resonant frequency of the transmission system, which depends highly on the length of the line.

As far as the approximation of the poles is concerned, it is still high with the magnitude error $\varepsilon_{N,\text{nom}}$ of the unstable real pole reaching a maximum of 0.105 % at 600 km of length and the same error for the complex poles reaching a maximum of 0.026 % at the same cable length. The high level of accuracy is observed on the real and imaginary parts of the complex-conjugate poles, with $\varepsilon_{N,\text{real}}$ and $\varepsilon_{N,\text{imag}}$ peaking at 2.2×10^{-3} % and 0.027 %, respectively.

Variation of overhead-line length

The impact of the length variation of an overhead dc-transmission line is observed in Fig. 6.17. Compared to the same scenario for a cable-type line, the overhead-line results differ greatly. The complex-conjugate poles are distinctively closer to the imaginary axis while their real part decreasing noticeably for an increasing transmission line length, increasing their damping; a phenomenon that was not observed in the complex poles of the cable-based system, where their real part was stiff for length changes. Another, and possibly the most important, difference is observed on the unstable pole. The shifting of its location towards the right of the RHP is much more profound than the cable-based system, reaching values as high as $\lambda_1=9.37$, compared to a maximum value of 1.98 in the latter. This acutely unstable pole, in combination with complex-conjugate poles being very close to the imaginary axis, lead to a closed-loop VSC-HVDC system with worse dynamic performance when overhead lines are used, rather than cables.

The level of approximation achieved by the *LR* algorithm is very satisfying in this case as well. This is evident by the magnitude errors $\varepsilon_{N,\text{nom}}$ of the unstable real pole and the complex-conjugate poles, peaking at 0.081 % and 9×10^{-3} %, respectively. Furthermore, the errors $\varepsilon_{N,\text{real}}$ and $\varepsilon_{N,\text{imag}}$ of the complex-conjugate poles feature maximum values of 0.048 % and 8.9×10^{-3} %, respectively.

6.4 Investigation on the accuracy of the approximating methods

6.4.1 Accuracy of the Similarity Matrix Transformation

The accuracy of the analytical expressions in closed form for the eigenvalues of the system is directly related to the level of accuracy in approximating (6.15). As mentioned earlier in Section (6.1.3), the factor which determines the level of accuracy in this approximation is the term $\frac{\Phi}{c} = \frac{eRx_{21} - (d+ex_{21})x_{21}}{c}$ which should be the closest possible to a zero value. The more the

Chapter 6. Applications of the analytical approach

factor $\frac{\Phi}{c}$ deviates from zero and becomes comparable to x_{11} and x_{22} , the worse the accuracy of the final eigenvalue expressions.

All the unknown parameters of the system contribute to the final expression of $\frac{\Phi}{c}$, thus affecting the quality of the final symbolic eigenvalue solutions. However, the degree to which each of these parameters affect the resulting expressions varies. The majority of the system unknowns does not seem to have great impact on the approximation accuracy. It was observed that the only unknown which had a significant impact on the final results is the inductance of the dc-transmission link, where the greater its value, the less accuracy in the resulting expressions compared to their numerically extracted values.

A series of parametric scenarios display the effect of an increased inductance in Fig. 6.6, where scenarios 2, 3, 4 and 5 from Section (6.1.4) are repeated with the only difference being that the cable is replaced by an overhead line. Overhead lines typically have much greater inductance per kilometer and much lower capacitance per kilometer than cables of equivalent power and voltage ratings. The overhead line used in this section has values defined in Table 2.1.

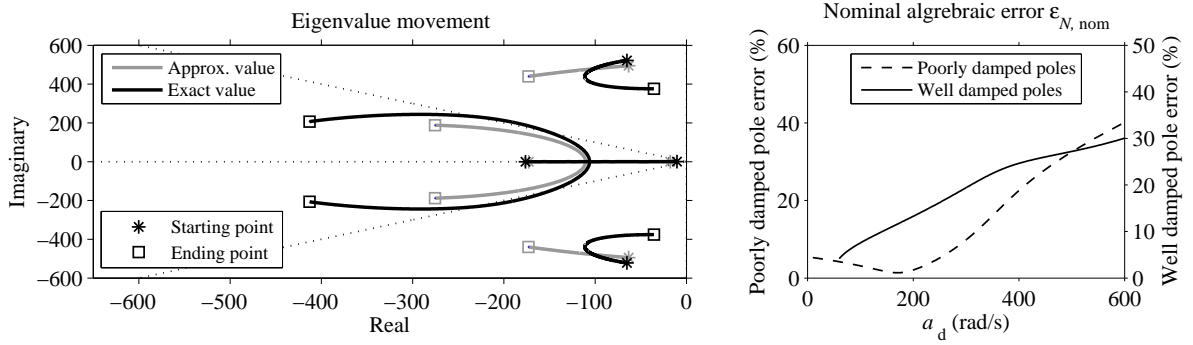
Figure 6.18(a) shows the results from the modified scenario #2 where a_d is varied. The approximated poles closely follow the numerical values and movement trend of the exact poles for small values of a_d but when the latter becomes greater than 300 rad/s, the approximated poles start to deviate, especially considering the real part of the poorly-damped poles. This is because the approximation in (6.15) does no longer hold for large values of a_d . This is however of not significant importance since a_d normally lies close to 4 pu or 300 rad/s [86], [43]. The error $\epsilon_{N,\text{nom}}$ of the poorly- and well-damped poles at $a_d=300$ rad/s is 9.84% and 19.41% respectively.

Figure 6.18(b) presents the results from the modified scenario #3 where a_f and a_f vary. The approximation achieved is sufficiently well for values of the bandwidths up to nominal, mapping the exact eigenvalues in a correct way. However, for larger than nominal values of the bandwidths, the tracking of the poorly-damped poles starts to deteriorate. A representative example of this is when the bandwidths are set to their maximum value of 600 rad/s. The numerically exact solution shows a system which has a pair of unstable complex-conjugate poles, while the approximating algorithm presents the same poles as stable but poorly-damped. Still, this is not an important issue because in practice the related bandwidths do not reach such high values.

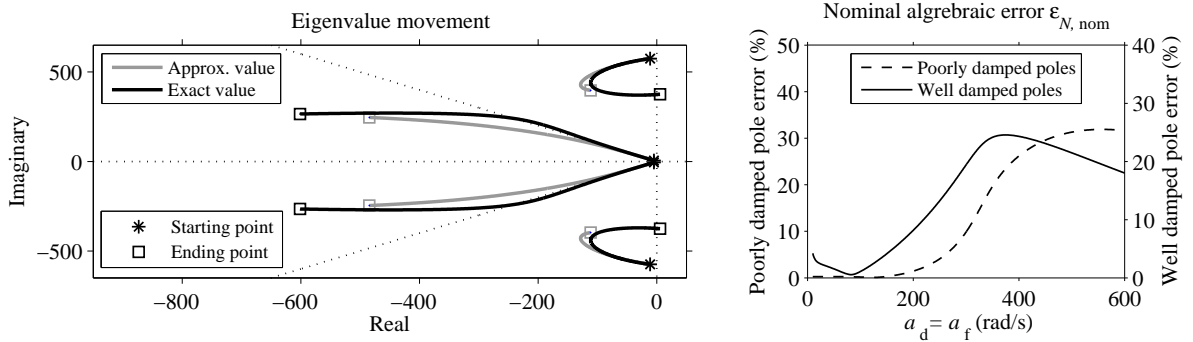
Figure 6.18(c) presents the results from the modified scenario #4 where, in this case, the length of the transmission line length varies. As reflected in the figure, the approximated poles manage to follow the movement path of the exact poles most of the range of the transmission line length but the well-damped pole pair fails to split into two real poles for high values of the length. The error $\epsilon_{N,\text{nom}}$ of the poorly-damped poles reaches a maximum of 30.14% at around 250 km of line length while the same error reaches a local maximum of 23.47% at 140 km, managing to stay below that level until 466 km of line length. For the nominal length of 100 km, the same error for the poorly- and well-damped poles is however much lower at 9.84% and 19.41% respectively.

Finally, Fig. 6.18(d) presents the results from the modified scenario #5 where the amount of the transferred power $P_{\text{out},0}$ varies. Comparing the results to those in Fig. 6.6, a first observation is that the pole movement, when altering $P_{\text{out},0}$, is quite significant in the presence of transmission lines instead of cables, where the poles are almost indifferent to the transmitted power level. The

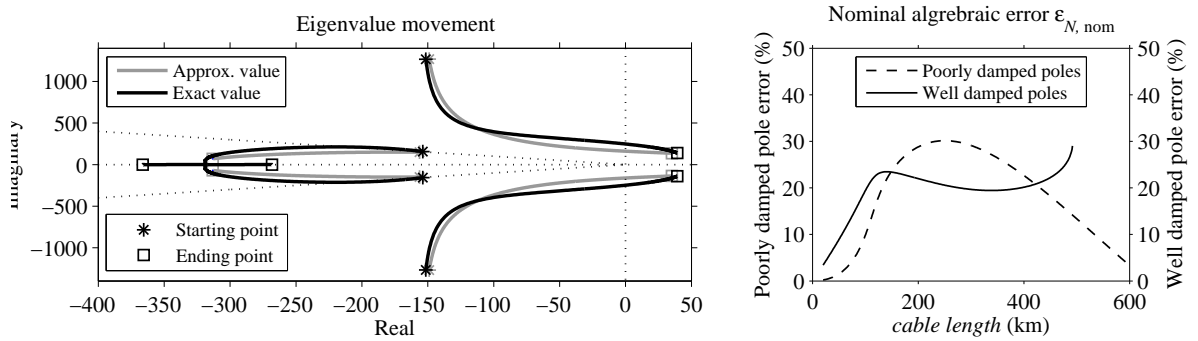
6.4. Investigation on the accuracy of the approximating methods



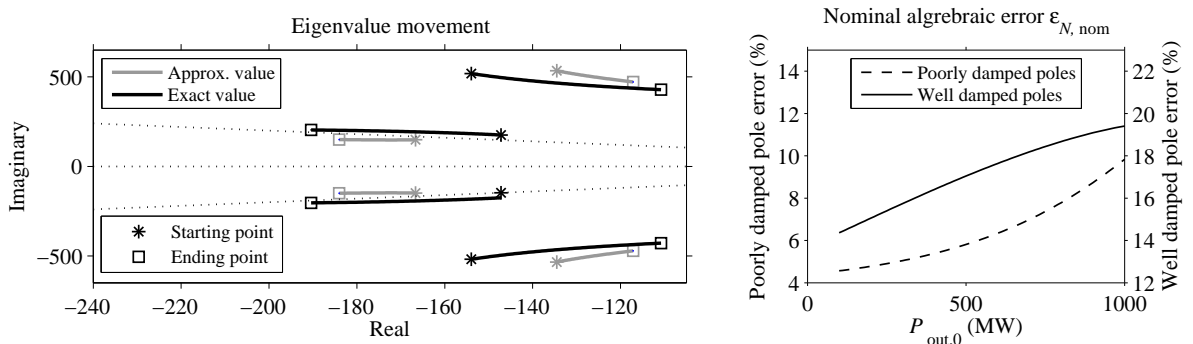
(a) Pole movement and approximation errors when a_d is swept from 10-600 rad/s.



(b) Pole movement and approximation errors when $a_d=a_f$ is swept from 10-600 rad/s.



(c) Pole movement and approximation errors when the the transmission line length is swept from 20-600 km.



(d) Pole movement and approximation errors when the transferred power is swept from 0-1000 MW.

Fig. 6.18 Approximation studies of the system for a change of the cable to overhead transmission lines.

results for varying transfer power in Fig. 6.18(d) show a relatively good approximation of the exact poles with a magnitude error for both the well and poorly damped poles below 20%. The poorly damped poles are in fact approximated with an error $\epsilon_{N,\text{nom}}$ which reaches a maximum of 9.84% for the rated power transfer and keeps dropping for decreasing $P_{\text{out},0}$.

Overall, the *SMT* method seems to be able to provide reliable results for a wide range of variation of the system's unknown parameters around their nominal values. The greatest impact on the accuracy of the method is caused by the inductance of the transmission medium between the stations (cable or transmission line), where it was shown that a large but realistic value of the inductance can raise the approximation errors from the range of 1-5% (in the case of cable) to 10-30% (in the case of transmission line).

6.4.2 Accuracy of the convergence of the LR algorithm

By definition, the derived symbolic expressions for the description of the system's poles using the *LR*-method are created without taking into consideration the numerical values of the symbolic entries. This cannot guarantee, however, the validity or level of accuracy of the same expressions for different values of the system's unknowns. The *LR*-algorithm will usually converge within the first few iterations but it is often the case that for a different parameter-setup of the same system, the method will require a considerable number of additional iterations to converge on specific problematic eigenvalues. It should be reminded that every additional iteration adds further complexity to the symbolic expression of the poles.

A possible solution in these cases is to significantly limit the perturbation margins of the desired unknowns of the system. This implies that the final symbolic expressions are expected to be valid in a very confined area of parameter variation. If this convention is respected, it is possible to attempt a drastic simplification of the intricate eigenvalue expressions into simpler forms, still without any guarantee that the final expressions will be compact enough to be considered useful or presentable.

The application of the *LR*-algorithm in the transmission-line model showed no noticeable effect of the system's parameters and steady-state values on the accuracy of the solutions, which remained at high levels in all of the examined scenarios. The differences between cable and overhead-transmission line had also no impact on the convergence, even though that implied large changes in the considered inductance and capacitance of the dc-link. Unrealistic values of the system's unknowns were not examined but this would be out of the scope of this thesis.

Some considerations on the accuracy of the algorithm are however risen when the complete VSC-HVDC model is regarded. The parameters of the VSC-HVDC model examined in this chapter were varied in an attempt to assess the accuracy and convergence of the algorithm. Just as in the *SMT* method, it was found that the value of the inductance of the dc-transmission link has the greatest impact on the convergence of the *LR*-algorithm. In fact, the greater the value of the inductance, the less accurate the approximation becomes and more iterations are necessary to achieve reliable results.

To demonstrate the effect of an increased inductance, scenario # 4 of Section (6.1.4) and Section (6.2.4) where the transmission link length is varied from 20-600 km is repeated. Only now, just

6.4. Investigation on the accuracy of the approximating methods

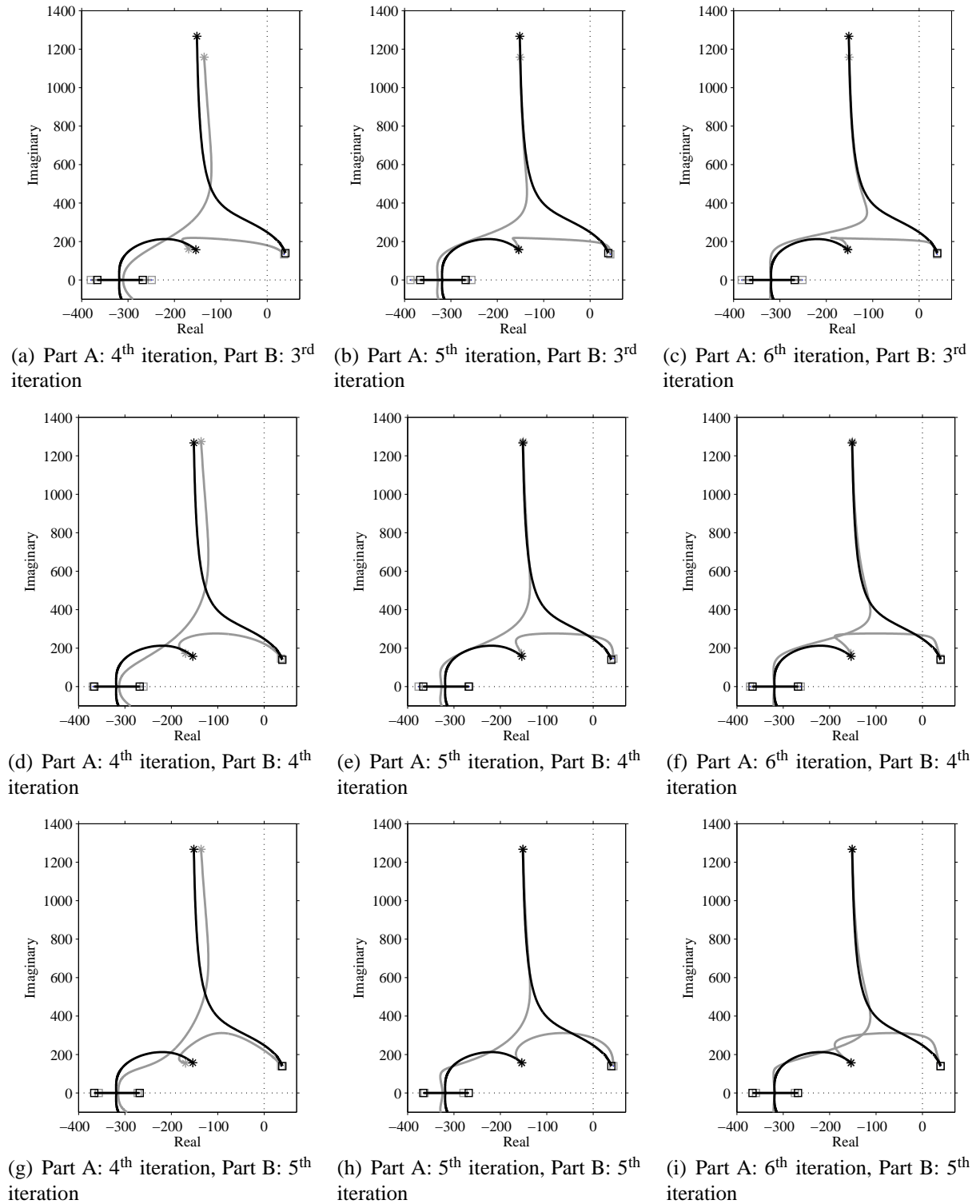


Fig. 6.19 LR-algorithm convergence for a high inductance dc-link whose length is swept from 20-600 km. Different iteration results of Part A and B of the poles are combined. The black line represents the exact poles and the gray line represents the approximated poles. The '*' and '□' markers correspond to the starting and ending position of a pole, respectively.

Chapter 6. Applications of the analytical approach

as applied in Section (6.4.1), the cable is replaced by an overhead line. Overhead lines typically have much greater inductance per kilometer and much lower capacitance per kilometer than cables of equivalent power and voltage ratings. The overhead line used in this section has the same characteristics as the one used in Section (6.4.1).

As mentioned earlier, Part A and Part B of an *LR*-derived eigenvalue expression converge at a different iteration rate. Fig. 6.19 shows a series of results with a combination of Part A and Part B, calculated at different iterations of the algorithm. Each row of figures features Parts B stemming from the same iteration, whereas each column of figures features Parts A of the same iteration. It should be noted that

- the approximated results are based on expressions that have not been subjected to any symbolic simplification.
- the earlier results in Section (6.2.4) are based on the simplified expressions of Parts A of 4th iteration and Parts B of 3rd iteration, as presented in Section (6.2.3).

It is interesting to observe that in all of the Figures 6.19(a)-(i), the approximated poorly- and well-damped poles do not manage to keep a consistent movement trend from their starting point until the ending point. On the contrary, the expression representing the poorly-damped poles shows a good level of approximation for small values of the dc-link length, then diverges and for large length values converges to the location of the exact well-damped poles. The opposite happens for the approximated well-damped poles. There is sufficient approximation for low cable lengths but then follows a great divergence until they start converging to the exact poorly-damped poles for high length values.

Figure 6.19(a) presents the results for a 4th iteration Part A and 3rd iteration Part B of the eigenvalues. Any expression of higher iteration will be difficult to be presented symbolically. Both well- and poorly-damped poles feature the convergence behavior described earlier with nominal magnitude errors $\epsilon_{N,nom}$ below 20% only for approximately 0-100 km and 450-600 km (the latter regards convergence to the opposite type of pole though).

Higher iterations of Part A and Part B show that the convergence improves for both poorly- and well-damped poles but there is always a cable length region where an approximated pole starts to diverge and then follow the path of the other type of pole. This behavior persists even after 100 iterations of the algorithm, but the previously described 'swapping' between poles occurs abruptly at a single dc-link length value. This proves that the *LR*-method, in this case, will finally follow accurately the true eigenvalues of the system, but a single expression in terms of (6.30) or (6.31) is not consistent enough to describe exclusively a single type of pole (either poorly- or well-damped). This is an aspect that did not occur in the *SMT* method, where the consistency is respected but the accuracy of approximation cannot be further improved.

6.5 Summary

In this chapter, the *SMT* and *LR* methods described in Chapter 5, were implemented in the calculation of analytical eigenvalues expressions of VSC-HVDC related state-space models. More

specifically, both methods were applied to a 4th order two-terminal VSC-HVDC transmission system model, while the *LR* method was further applied to the 3rd order model of an HVDC-transmission link.

Regarding the *SMT* method, a number of valid conventions were used to simplify the state-space VSC-HVDC model from its original form, in such a way that several of the state-matrix entries could become identical. This provided more compact final expressions. The solution of the eigenvalue problem requires the solution of non-linear equations, which under a certain convention can be simplified and solved. The accuracy of this simplification was shown to be the key factor determining the accuracy of the derived eigenvalue expressions.

As far as the *LR* method is concerned, the entries of the original state-space models were modified in a similar manner as in the *SMT* method, to possess a plurality of identical terms and provide compact final eigenvalue expressions. Additionally, the order according to which the states were positioned in the state-matrix was re-arranged to facilitate a faster convergence of the iterative algorithm. It was observed that the real and imaginary part of complex conjugate eigenvalues, achieve sufficient accuracy at different convergence rates. This behavior, along with the fact that every additional iteration of the algorithm increases the complexity of the final solutions, led to the practice of separately deriving the analytical real and imaginary part of complex poles from those iterations that provided sufficient accuracy.

Both methods demonstrated satisfactory results, with great accuracy in the expression of the eigenvalues of the examined systems, for a wide variation of control and physical parameters. Nevertheless, in the case of the two-terminal VSC-HVDC model, the *SMT* method appeared to provide consistently increased accuracy than the *LR* method, especially for the poorly-damped complex poles, which are of great concern during the designing of such systems. This implies that in relevant studies on two-terminal configurations, the *SMT* method should be preferred to be used as the tool of choice. The chapter is finalized by an investigation in the convergence of the two methods, showing that the use of dc-transmission lines with large inductance per kilometer (i.e. overhead lines) in the two-terminal VSC-HVDC model, may affect the accuracy of the analytical solutions, with the *SMT* results being less affected than those derived by the *LR*. The same observation was however not made in the case of the dc-transmission link eigenvalues, where the *LR* method seemed to provide accurate expressions.

From an overall perspective, once the desired analytical eigenvalue expressions are obtained by one of the previous methods, it is possible to simplify them to a great extent, in a way that the resulting expressions are valid in a relatively small range of parameter variation around a nominal set of parameter values. Such an analysis may be further extended to a degree that only one critical parameter is allowed to vary, making the simplifications even more drastic. As a result, it may be possible to acquire such simplified forms that design criteria for an HVDC system can be derived. This objective can be part of a future study on the subject.

Chapter 6. Applications of the analytical approach

Chapter 7

Control investigation in Multiterminal VSC-HVDC grids

The expansion of the point-to-point HVDC transmission concept into a multi-terminal arrangement, broadens the possibilities for a more flexible power transfer between ac grids and provides the means for a reliable integration of dispersed, high-capacity renewable power sources to highly interconnected power systems. However, moving from a two-terminal to a multiterminal scale, increases the technical requirements and adds complexity to the control strategies that can be applied.

This chapter functions as an introduction to the ideas, visions and challenges behind the multiterminal concept, focusing on VSC-based MTDC grids. Existing control strategies are presented and new types of controllers are proposed, aiming to enhance the performance of the system or accommodate new power-flow needs that current solutions have difficulty in handling. Examples utilizing four- and five-terminal MTDC grids, demonstrate the effectiveness of the proposed controllers by comparing their performance to that of conventional control concepts, both in steady-state and in cases of large disturbances.

7.1 Multiterminal HVDC grids

The use of HVDC technology has traditionally been restricted to point-to-point interconnections. However in recent years, there has been an increase in the interest for MTDC systems, given the technological advances in power electronics and VSC technology, as well as the challenges that rise from the need for the interconnection of large power systems and the interconnection of remotely located generation sites. An MTDC system can be defined as the connection of more than two HVDC stations via a common dc-transmission network. Just as the concept of a conventional ac grid relies on the connection of multiple generation and consumption sites to a common ac transmission system, the MTDC comprises of stations that inject or absorb power from a dc-transmission system.

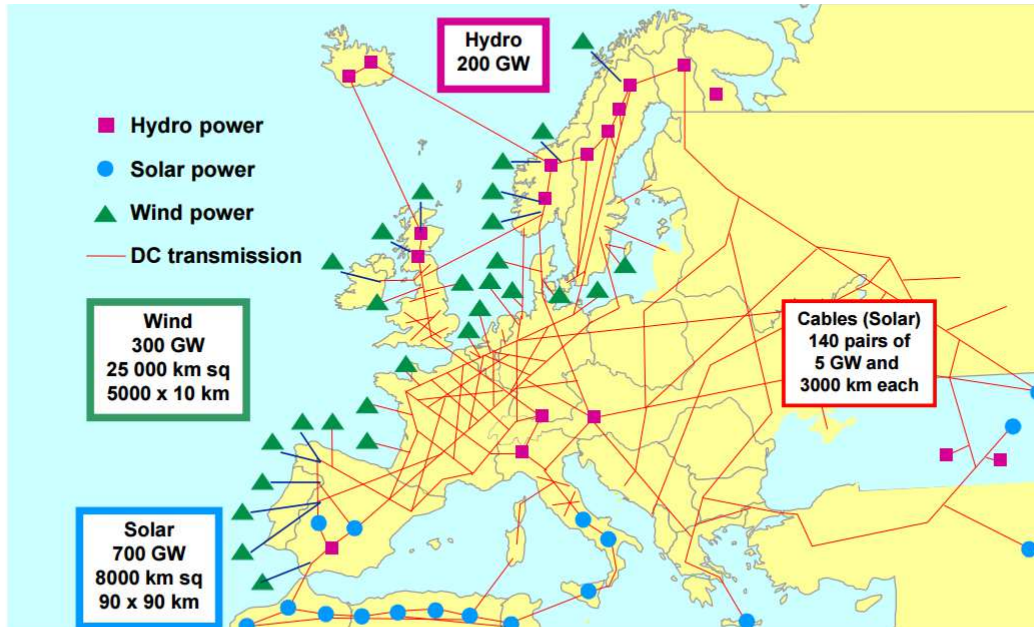


Fig. 7.1 ABB's HVDC grid vision in the 1990's [88].

7.1.1 Technologies and initial projects

Since there are two types of HVDC converters (LCC and VSC), two types of MTDC grids can be realized: an LCC-HVDC based and a VSC-HVDC based MTDC grid. Hybrid versions combining the two technologies have also been introduced as concepts [87], but the operational and protection challenges appear to be hindering factors for a practical realization. The first multi-terminal HVDC was an LCC-based system that was established in Quebec-New England, Canada, in 1990. The existing HVDC line of 690 MW was extended towards north, over a distance of 1100 km to connect a new 2250 MW terminal and also to the south, over a distance of 214 km to connect a 1800 MW terminal. In 1992 a new 2138 MW terminal was added to the already operational multi-terminal system. Nevertheless, despite the potential of transferring large amounts of power compared to the VSC technology, experience has shown that LCC-based MTDC grids appear to have important difficulties from a controllability and flexibility point of view.

The first time that an MTDC was installed using the VSC technology was in 1999 at the Shin-Shinano substation in Japan. The system comprised of three VSC-HVDC terminals in back-to-back connection and has been used for power exchange between the two isolated 50 Hz and 60 Hz ac grids of Japan [36]. However, the lack of dc-transmission lines in the system, do not render it an MTDC grid, in the conventional sense. Even though there is no "true" VSC-based MTDC grid commissioned yet, the VSC technology has been extensively used in point-to-point connections, overcoming the technological limitations and disadvantages of LCC-HVDC and proving that it can constitute the cornerstone of future MTDC grids.

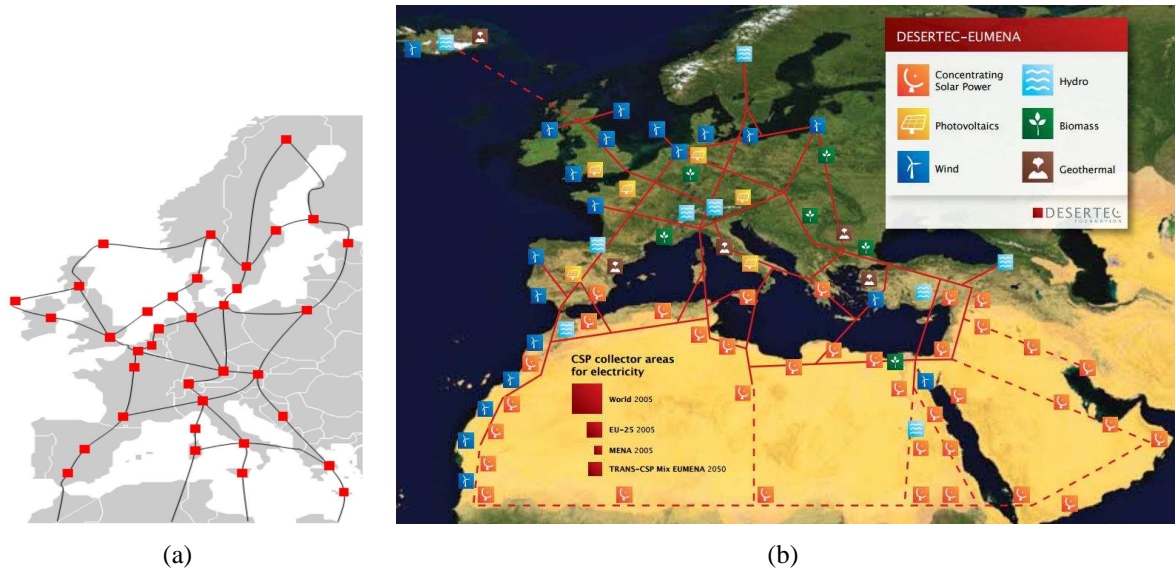


Fig. 7.2 (a) ABB vision for a European DC grid [89], (b) DESERTEC vision from 2009 [90].

7.1.2 Visions

The potential presented by the HVDC technology in bulk energy transfer over long distances, triggered an early interest by the academic and industrial community for highly interconnected, continental-wide, power systems. This was aided by an increased deregulation of the European electricity market and the development and planning of remotely-located renewable power plants, as different visions started rising regarding the future of power systems. In this context, there is a requirement of a flexible system that is able to transfer a large amount of power across the continent.

Inspired by the early advances in multi-terminal HVDC, ABB already in the 1990s presented its vision of the future highly interconnected, European-wide power system as shown in Fig. 7.1. As observed, this plan considered the reliance of the European energy needs on a bulk import of renewable energy (from wind, solar and hydro power plants dispersed around the continent) over a large mainland MTDC grid. The latter would constitute an overlying layer on top of the existing ac-system. However, the available LCC-HVDC technology of the time proved to be a weakening agent, since it could not offer the power-flow and grid flexibility required for the realization of such an ambitious vision. The advances in the VSC-HVDC technology towards the end of the decade, revived the ideas for large MTDC grids. Consequently, similar plans have been re-assessed and further developed by other parties, e.g. the DESERTEC foundation in Fig. 7.2(b), while ABB presented its detailed concept of a European MTDC grid, as in Fig. 7.2(a).

As a step towards the realization of large scale grids, small DC grids are expected to be initially developed and connected to the main ac system. This will test the concept and determine future requirements for an expansion of the grids. Such a proposal has been presented for a three-terminal HVDC grid in Shetland, UK, as shown in Fig. 7.3(a). The North Sea is a location shared by many nations and featuring high wind power potential. These properties make it an ideal

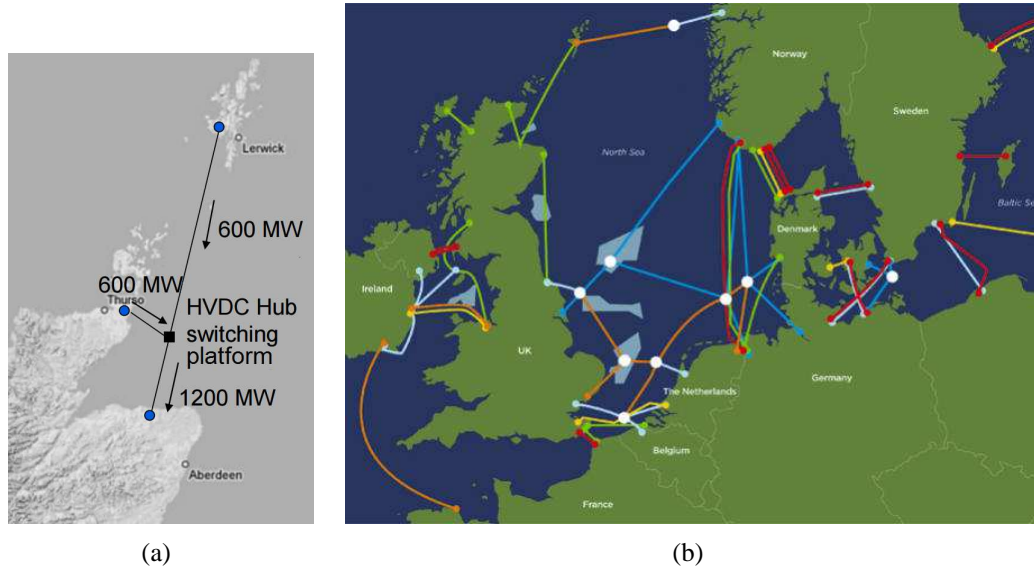


Fig. 7.3 (a) Example of possible three-terminal HVDC grid in UK [89], (b) EWEA vision from 2009 [91].

area to develop small-scale multi-terminal connections with offshore wind power integration. Several relative proposals have been made, as in Fig. 7.3(b).

7.2 Key components for future large scale Multiterminal connections

The realization of MTDC grids presupposes the use of a number of components which are necessary for the operational and safety integrity of the grids. Such devices are either not developed yet or are in the final stages of their development, without having been commissioned yet.

7.2.1 DC-breaker

Devices for switching and protection of dc grids are vital to realize MTDC grids, especially for meshed grids. A dc-fault affects the complete dc-transmission grid and if the faulty segment of the lines is not isolated, the entire MTDC system would have to be taken out of operation. Circuit breakers are widely used in transmission and distribution grids to interrupt short circuit currents.

Figure 7.4(a) shows a schematic representation of a dc grid under where a dc-fault occurs as a short circuit between the dc cables. Due to the terminal capacitor of the VSC station, which is charged at v_{dc} in steady-state operation, the system on the left of the fault can be described by a constant voltage source of v_{dc} voltage, together with the impedance of the cable pair between the converter and the fault location. The latter consists of an equivalent resistance R_{cable} and an

7.2. Key components for future large scale Multiterminal connections

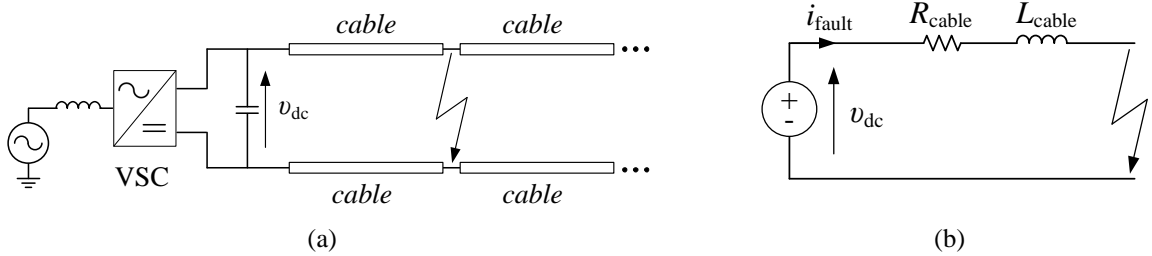


Fig. 7.4 DC-fault conditions: (a) Schematic representation of dc grid under short circuit condition, (b) Equivalent circuit of a dc grid under short circuit condition.

equivalent inductance L_{cable} , as shown in Fig. 7.4(b). Upon occurrence of short-circuit, the full grid voltage appears across the equivalent impedance. Considering a very small value of R_{cable} , this voltage is approximately applied entirely across L_{cable} causing a fault current i_{fault} with a constant rise rate $di_{\text{fault}}/dt = v_{\text{dc}}/L_{\text{cable}}$. The grid inductance does not limit the fault current which will keep increasing as long as v_{dc} is sustained. For very low values of L_{cable} (which is the case for dc-transmission lines), di_{fault}/dt may reach values of hundreds of kA/s [92]. Therefore the fault current would rise to a very high value in a short amount of time and needs to be interrupted quickly.

The important fact for interrupting off short-circuit currents in ac system is the natural zero crossing. Since the natural zero crossing of current does not occur in a dc system, one important question is how to interrupt short-circuit current or load current. In [92], a brief overview of the concept of dc-circuit breakers is provided but no actual designs. The only HVDC breaker whose operational effectiveness has been verified, was presented by ABB [93] and is ready for actual implementation. The principle of operation of this breaker is shown in Fig. 7.5. The hybrid HVDC breaker consists of three essential components: a load commutation switch (LCS), an ultra fast mechanical disconnecter (UFD) and a main breaker with surge arresters in parallel.

In normal operation, the load current flows through the closed UFD and the LCS. When the dc-fault occurs and the control of the system detects it, the main breaker is switched on and the LCS is switched off (with this sequence). As a result, the high fault current can now keep flowing through the main breaker and UFD can be opened safely under virtually zero current and without the fear of an arc across it. Finally, the main breaker is switched off and the fault current flows through the highly resistive surge arresters that quickly limit and finally extinguish it. The complete fault clearing time is in the range of ms ([93] mentions 2 ms).

7.2.2 DC-DC converter

The interconnection of ac systems with different magnitudes of operating voltages is easily performed through the use of transformers. In the future, MTDC grids may be developed without necessarily following the same direct-voltage specifications. Given the benefits of having interconnected power systems, from a power stability and power market perspective, the possibility of interconnecting such grids would prove invaluable. A lack of adequate concepts for transforming direct voltages in high-power dc grids is one of the major challenges for the real-

Chapter 7. Control investigation in Multiterminal VSC-HVDC grids

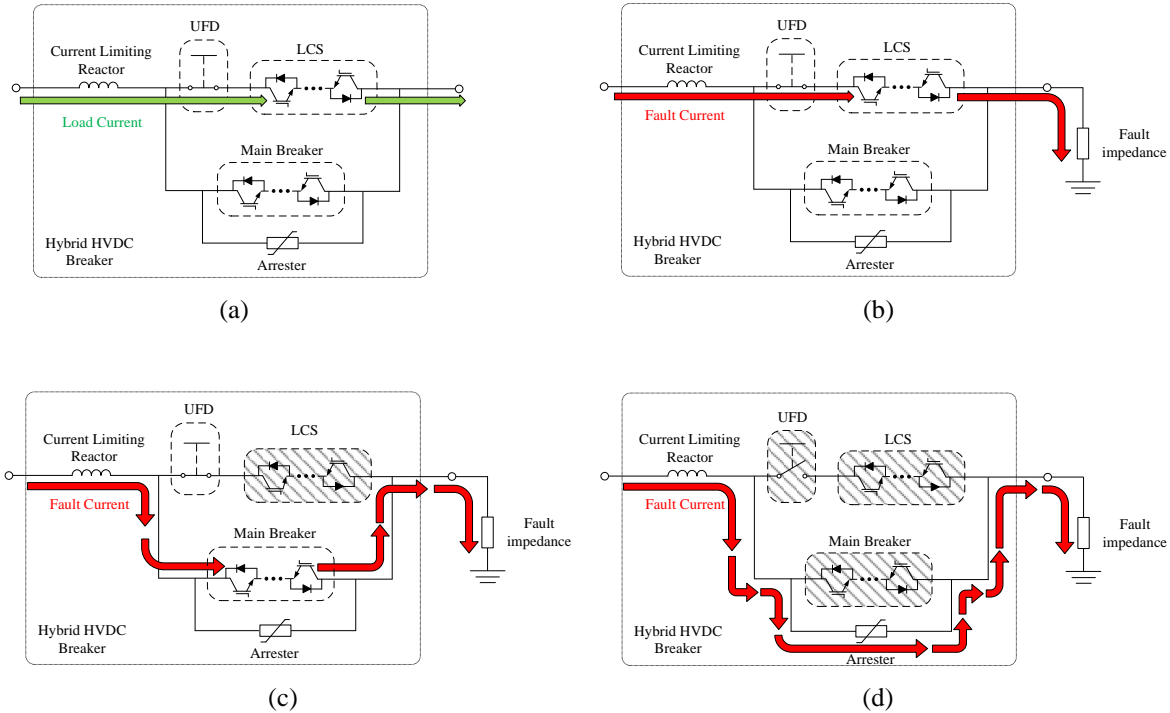


Fig. 7.5 Hybrid HVDC breaker operation principle: (a) normal load current path, (b) fault initiates operation, (c) LCS interrupts and commutates the current to the main breaker, (d) the main breaker interrupts and commutates the current to the arrester.

ization of interconnected MTDC grids of different voltage ratings. This requirement has been highlighted in [94] where a benchmark for future dc-gids has been suggested.

DC/DC converters have extensively been used in various low-voltage/low-power applications such as switched power supplies for electronic appliances. Very simple topologies are usually considered like the classic buck or boost converters. For relatively higher power applications, different topologies have been developed using DC/AC/DC topologies with a medium or high-frequency ac-link as discussed in [95] and [96]. The general structure of these converters is shown in Fig. 7.6. A medium/high frequency ac link includes a transformer to step up or step down the voltage between the dc-input and the dc-output side, resulting in an advantageous galvanic isolation, especially for high power applications. The frequency of the ac link depends on the power level and varies between a few kHz to several MHz.

The galvanic isolated DC/DC converter consists of an inverter at the input side, transforming the direct voltage into an alternating voltage of a certain frequency. In contrast to conventional

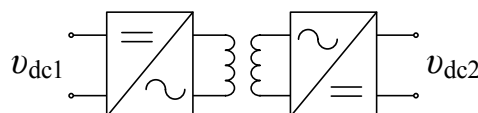


Fig. 7.6 General topology of a galvanic isolated DC/DC converter.

converter applications for grid connections or drives, a sinusoidal output is not needed in this kind of devices. Consequently, the frequency of the output ac voltage is equal to the switching frequency resulting in a rectangular waveform applied to the transformer [97]. This makes filter elements unnecessary. The high operating frequency leads to a significant reduction in the volume of the transformer. Finally at the output side, a rectifier is connected to change the alternating voltage at the output of the transformer into a direct voltage. For a bi-directional power transfer, both converters should have the form of an active rectifier.

Presently, DC/DC converters are available for power levels between a few kW up to 1 or 2 MW [98]. It should be mentioned that although in the work of [98], a total output power of 1.5 MW has been realized, the converter has a modular structure where each module has an output power of only 0.19 MW. This power level of a single module is significantly lower than the requirements in HVDC grids, where the nominal power ranges from several hundreds of MWs up to GWs. Three-phase topologies offer significant advantages for high-power applications [99]. Furthermore, standard three-phase transformer cores are available with various materials, reducing the total volume of the system. Summarizing these aspects, three-phase topologies seem to be the most advantageous concepts when being used in a multi-megawatt DC/DC converter [92].

7.3 MTDC-grid topologies

Several types of MTDC connection concepts are possible to be established in practice, each presenting a number of advantages and drawbacks. The most important of these designs and probable to be actually implemented are summarized below.

Independent HVDC links

This grid configuration, presented in Fig. 7.7(a), follows the concept of having a grid with independent two-terminal HVDC links where a cluster of stations are located in the same geographical area, sharing the same ac busbar. In this case, all the connections are fully controllable without the need of a centralized control to coordinate the stations. It may consist of a mix of LCC- and VSC-HVDC links, operating at potentially different voltages. This setup is ideal to incorporate existing HVDC lines into an MTDC grid and has no need of dc-breakers.

Radial grid

Owing to the simplicity of the design and the possibility to offer a sufficient level of power-flow flexibility between multiple stations, the radial grid topology presented in Fig. 7.7(b), will most likely be applied to the majority of the first MTDC grids. It is designed like a star without closed paths forming. The reliability of this configuration is lower than the other type of connections and in case of a station disconnection, portions of the dc grid could be "islanded".

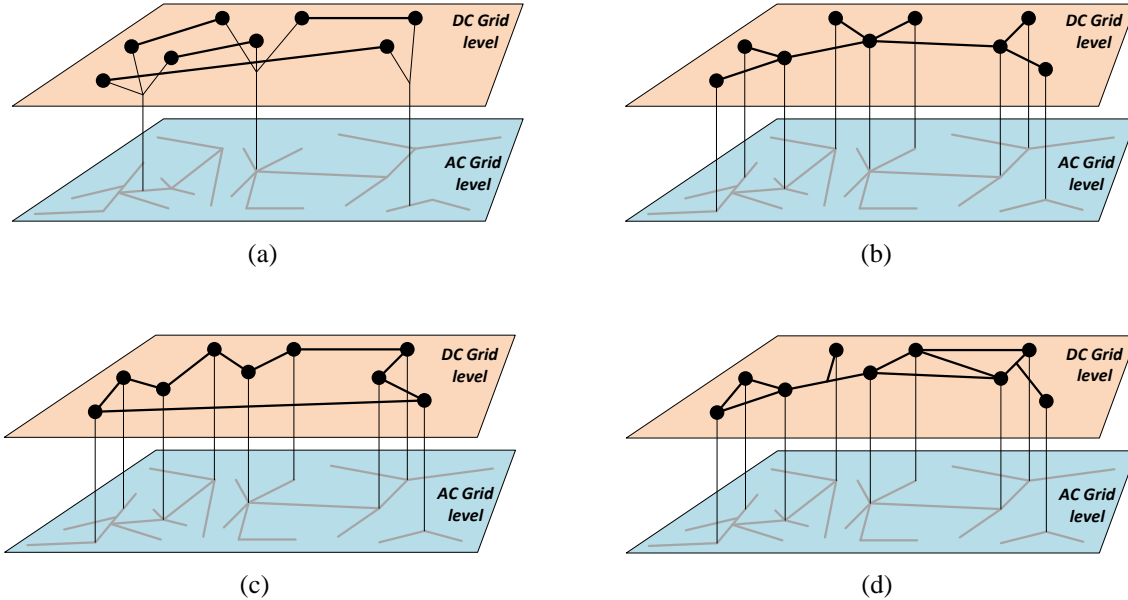


Fig. 7.7 MTDC topologies: (a) independent HVDC links, (b) radial connection, (c) ring connection, (d) meshed connection.

Ring grid

The ring topology, shown in Fig. 7.7(c), connects all converter stations in a closed serial circuit, with each converter featuring two dc-connections to other stations. The advantages of this connection type lie on the simplicity of the construction and operation. However, this type of connection suffers from low reliability and high losses due to the long transmission lines (if the geographical location of the stations is big), which are necessary to close the grid loop. The impact of the latter is intensified in the presence of remote stations which need to be connected to the rest of the grid with two separate dc links.

Meshed grid

The meshed grid topology is presented in Fig. 7.7(d). As it can be observed, this type of grid constitutes a "dc" replica of an "ac" transmission system, introducing redundant paths between dc nodes. An additional advantage of this connection scheme is that a station may be added on certain point of an HVDC link with a separate cable connection, without the need to interrupt the initial HVDC link and introduce the station at the interruption point. The meshed MTDC grid allows multiple power paths between dc nodes, increases the flexibility of power exchange between the respective ac nodes, increases the overall reliability and reduces the shortest connection distance between two nodes in the grid. However, a consequence of these features is the need for advanced power flow controllers and an increase in the cable cost since more (and potentially long) connections need to be established. Furthermore, the use of dc-breakers at every station is considered necessary to ensure the viability of the grid in case of dc-faults.

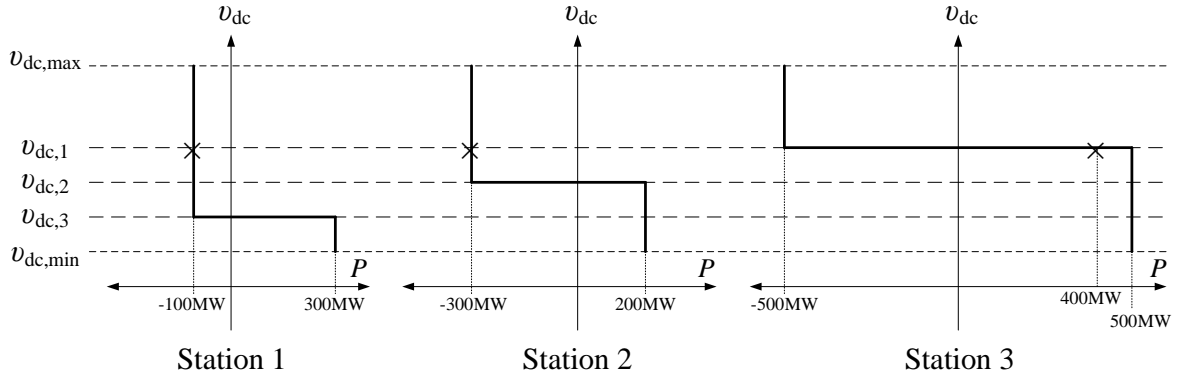


Fig. 7.8 Voltage-margin control in a three-station MTDC grid. The desired operating point is indicated with 'x'.

7.4 Control of MTDC grids

The voltage and power control within a VSC-MTDC grid has been a challenge, given the task of coordinating a large number of stations with the final objective of establishing a desired power flow in the grid. A limited number of solutions have been proposed so far, with the most important of those being the *Voltage-margin* control and the *Voltage-droop* control. Altered versions of these fundamental control strategies are frequently found in the literature, but the core of their philosophy remains the same.

7.4.1 Voltage-margin control

The voltage-margin method presented in [36,37] suggests that each converter follows a voltage-power pattern where, according to the dc-grid voltage level, the converter can be automatically assigned duties of either direct voltage or constant power control. There can only be one direct-voltage controlled station operating in the complete MTDC grid.

An example of the method can be demonstrated in Fig. 7.8, where a grid of three converters is considered. The direct voltage of the grid in steady-state conditions can vary between $v_{dc,min}$ and $v_{dc,max}$. Assume that a power flow plan requires Station 1 to inject 100 MW to its ac-side, Station 2 to inject 300 MW to its ac-side and Station 3 to inject 400 MW to the dc grid (guaranteeing the power balance), while the voltage of the grid is maintained at a level of $v_{dc,1}$ (assuming very small voltage deviations around this value per station terminal to allow dc power flow). Once the stations have been started-up and brought the grid voltage to an initial $v_{dc,min}$, each of them follows their custom voltage-power pattern indicated in Fig. 7.8. The system then reacts in the following steps.

1. Stations 1, 2 and 3 are dictated to inject +300 MW, +200 MW and +500 MW of power to the dc grid, respectively. This gives a net power of 1000 MW transferred to the dc grid, causing the direct voltage to start increasing.
2. When the direct voltage reaches $v_{dc,3}$, Station 1 becomes direct-voltage controlled while

Stations 2 and 3 keep injecting +200 MW and +500 MW to the dc grid, respectively.

3. Station 1 changes its power to maintain the direct voltage and power balance until it reaches -100 MW which is not enough to compensate for the +700 MW injected by the other stations. This causes the direct voltage in the grid to increase, exceeding $v_{dc,3}$, and Station 1 becomes again power controlled injecting 100 MW to its ac side. The net power in the dc grid is now constant at +600 MW and the direct voltage in the grid increases constantly.
4. When the direct voltage reaches $v_{dc,2}$, Station 2 becomes direct-voltage controlled, being able to support a dc power from +200 MW up to -300 MW. This is not enough to compensate for the combined power of +400 MW, injected to the dc grid by Stations 1 and 3. This causes the direct voltage in the grid to increase, exceeding $v_{dc,2}$, and Station 2 becomes again power controlled injecting 300 MW to its ac side. The net power in the dc grid is now constant at +100 MW and the grid voltage increases constantly.
5. When the direct voltage reaches $v_{dc,1}$, Station 3 becomes direct-voltage controlled, being able to support a dc power from +500 MW up to -500 MW. This is enough to compensate for the combined power of -400 MW, injected to the dc grid by Stations 1 and 2.
6. The system stabilizes with Station 1 exporting 100 MW to its ac side, Station 2 injecting 300 MW to its ac side and Station 3 keeping the direct voltage at $v_{dc,1}$ while injecting 400 MW to the dc grid. This matches the desired power flow scenario.

If Station 3 is lost, Stations 1 and 2 keep injecting powers -100 MW and -300 MW, respectively, to the dc grid. This gives a net power of -400 MW, which causes the direct voltage to start decreasing. Once the latter reaches $v_{dc,2}$, Station 2 becomes direct voltage controlled while Station 1 is still in power control mode, injecting -100 MW. Station 2 can provide a power of +100 MW to bring a power balance while maintaining the voltage at $v_{dc,2}$. The system thus stabilizes.

Concluding, the voltage-power curves of the stations can be designed in such a way that in case a station is lost, another station will automatically resume the control of the direct voltage, which is vital for the survival of the MTDC grid. The inherent disadvantage of the method is that the single station which is in direct-voltage control mode, has to bear the possibly large changes of net power that could occur following the loss of a station.

7.4.2 Voltage-droop control

A method sharing some common traits with the voltage-margin control but overcoming its disadvantage of having a single station bear the changes of net power following the loss of a station, is the voltage-droop control. This method follows a similar concept with the frequency-droop control of synchronous generators being simultaneously connected to an ac grid. In this case, the change of grid frequency causes all generators to react in terms of power, with the individual contribution being decided by their frequency-power droop characteristic. In the voltage droop control, the change in the direct voltage in the dc grid causes the MTDC stations to react

with a change of their power transfer. The method was initially demonstrated in LCC-MTDC grids [38] and later adapted for VSC-MTDC grids for offshore wind power integration [39, 40].

An example of the applicability of the method is shown in Fig. 7.9. The scenario is the same as in Section (7.4.1). Once the stations are started up and the direct voltage of the grid reaches $v_{dc,min}$, all three stations inject power into the dc grid, raising the voltage. At a voltage $v_{dc,1}$, Station 1 exports 100 MW to its ac side, Station 2 injects 300 MW to its ac side and Station 3 injects 400 MW to the dc grid. This means that the net power import to the dc grid is zero and the direct voltage is stabilized. Assume now that the voltage momentarily decreases. The stations will then follow their droop curves and as a result, Stations 1 and 2 will decrease their export of power to their ac sides while Station 3 will inject more power to the dc grid. This implies a positive net power injection to the dc grid, causing the voltage to increase. In the same manner, if the direct voltage exceeds $v_{dc,1}$, Stations 1 and 2 will increase their export of power to the ac grid, while Station 3 will decrease its injection of power to the dc grid. This will cause a deficit of net power to the dc grid, causing its voltage to decrease back to its original position.

Assuming for example that Station 3 is lost, Stations 1 and 2 are still extracting power from the dc grid. This implies that the grid voltage will start dropping until a value $v_{dc,new}$ where $P_1(v_{dc,new}) + P_2(v_{dc,new}) = 0$. It is obvious that such a point exists above $v_{dc,min}$ because at that voltage level both surviving stations are already injecting power to the dc grid, stopping any further decrease in v_{dc} and start raising it again. It is evident that in cases of power changes in the grid (such as the loss of a station), all surviving droop controlled stations contribute to the new power distribution instead of just one station as in the voltage margin control.

Voltage-droop controller

The steady-state droop curves illustrated in Fig. 7.9 require a certain type of control in the MTDC stations, with two possible options presented in Fig. 7.10. As it can be seen, the core of each controller can be either a conventional direct-voltage controller (DVC) or an active power controller (APC). In Fig. 7.10(a), the droop control can operate in a way that an error between a power setpoint $P^{setpoint}$ and the actual power flow P^{actual} of the converter (corresponding to P_g

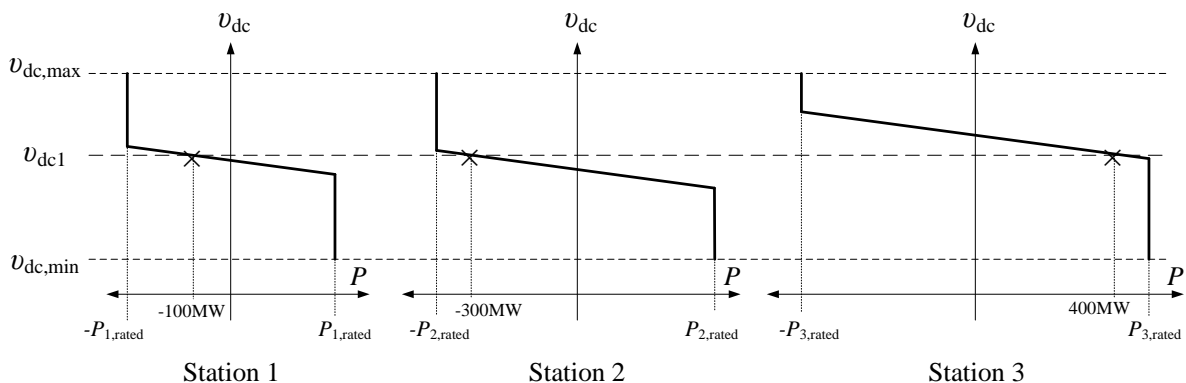


Fig. 7.9 Voltage-droop control in a three-station MTDC grid. The desired operating point is indicated with 'x'.

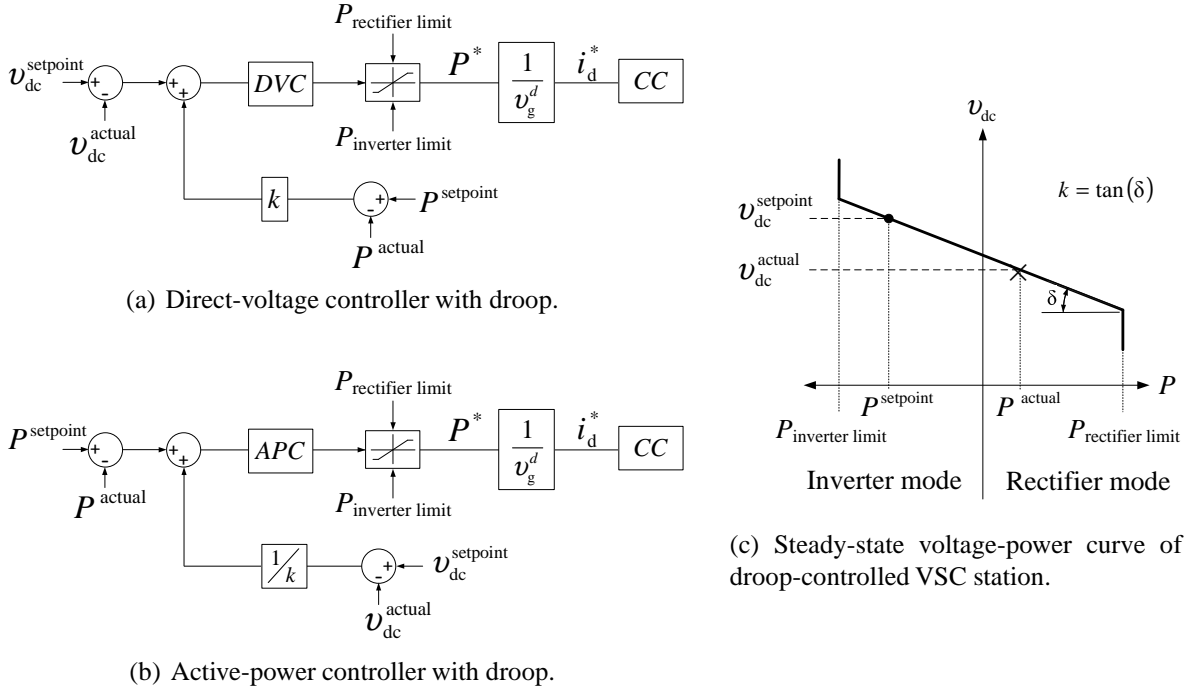


Fig. 7.10 Droop controllers and steady-state voltage-power curve.

that is measured at the phase reactor as defined in Chapter 2) provides a corrective droop signal, weighed by the droop constant k , to a DVC which without the added droop signal tries to follow a direct-voltage setpoint of v_{dc}^{setpoint} as reference. In steady-state, and assuming that the limiter at the output of the DVC has not been saturated, the total input error to the DVC will be zero, or

$$v_{dc}^{\text{actual}} = (P^{\text{setpoint}} - P^*)k + v_{dc}^{\text{setpoint}} \implies$$

$$v_{dc}^{\text{actual}} = (P^{\text{setpoint}} - P^{\text{actual}})k + v_{dc}^{\text{setpoint}} \quad (7.1)$$

This relation expresses the angled droop line in Fig. 7.10(c), where the point $\{P^{\text{setpoint}}, v_{dc}^{\text{setpoint}}\}$ is a point along the droop line and the pair $\{P^{\text{actual}}, v_{dc}^{\text{actual}}\}$ are the actual power and direct voltage conditions at the specific station. At the same time, the tangent of the droop line will be equal to $-k$. What this implies is that once the setpoint pair and the droop constant are defined, if the actual power P^{actual} , the VSC will regulate the voltage at its dc terminals to be equal to v_{dc}^{actual} , which is found by the intersection of the defined droop curve and P^{actual} . From a different perspective, if the power flow is different than P^{setpoint} , the DVC tries to follow the voltage reference v_{dc}^{setpoint} modified by a value of $(P^{\text{setpoint}} - P^*)k$, which is added to the latter. This acts like loosening the action of the integrator in the DVC and instructs the controller to follow a slightly different voltage reference than v_{dc}^{actual} with the choice of k affecting the magnitude of the deviation.

In a similar manner, the same droop action can be achieved by an APC which is trying to follow a reference P^{setpoint} modified by the weighted error $(v_{dc}^{\text{setpoint}} - v_{dc}^{\text{actual}})/k$. This controller is

shown in Fig. 7.10(b) and the steady-state relation between voltages and powers is given again by (7.1). This means that the DVC- and APC-based droop controllers operate on the same droop curve and produce the same steady-state results.

In an MTDC with a number of droop-controlled stations, the choice of setpoints for each converter dictates how the steady-state power flow will be established. If the desired power flow and the direct-voltage at the terminals of a selected converter are known, it is possible to execute a power flow calculation in the MTDC grid so that all the necessary actual powers and direct voltages at the terminals of each station are evaluated. This calculation should take into account losses on the dc lines, the filter inductor, added harmonic filters and the converter itself. If the resulting power and voltage pairs are provided as setpoints to the MTDC converters, the grid will settle with actual power and voltage values being identical to the given setpoints, regardless of the choice of droop constant for each station. This is a powerful tool in the accurate control of the MTDC grid.

Contingencies and secondary control

Once a scheduled power flow has been established in the droop controlled MTDC grid, any unplanned changes to the grid structure and operational conditions will set a new power and direct-voltage balance. As an example, the loss of a station or the unpredictable influx of power by a station which is connected to a wind-farm will cause an initial change in the net injected power to the dc grid. The direct voltage of the grid will thus change and all droop controlled stations will follow their voltage-power droop curves, altering their power outputs until the system reaches a state where the net injected power is zero and the voltage settles. The reaction, in terms of power, of each station to a given voltage change is defined by the slope of its droop curve and therefore its droop constant k . The steeper the curve (large k), the stiffer the station will be in terms of power change. This is an important information regarding the prioritization of stations in the system during contingencies, in case there is a demand for selected stations to preserve their power transfer as much as possible.

Following such unexpected events, it is obvious that the system operator would desire to restore part of the initial power scheduling or establish a totally new planned power pattern. Consequently, there is a need for a secondary, higher level control. This will monitor the conditions of the grid, communicate with all the stations, take into account the needs of the system operator and give localized orders to the stations to adjust their voltage-power curve settings until the complete grid reaches the desired steady-state. Ideally, this controller should solve a new power flow problem in the MTDC grid and provide the stations with new setpoints. The authors in [100, 101] suggest similar types of secondary controllers without the need for an accurate solution of the power flow problem, with sufficiently good results nonetheless.

7.4.3 Control strategy for connections to renewable power plants

An important area of application for MTDC grids includes the connection of distributed and remote renewable power sources to the ac grid. The role of the MTDC grid would consider the

collection of power from the power plants and a planned redistribution of the latter to selected ac grids. However, the power in-feed from intermittent sources, e.g. offshore wind-farms, cannot be accurately predicted. Therefore, it is not possible to set a preselected power flow and an MTDC grid relying entirely on voltage-margin or droop control cannot be established.

An MTDC station that is connected to a cluster of such power sources would have to be operating as a fixed ac voltage source to which the power plants would connect and inject all their available power. This control strategy is exactly the same as the one used in existing two-terminal VSC-HVDC connections to offshore wind-farms [39]. If the amount of neighboring power plants is large, it could be desired to have more than one MTDC converters connected to it. This would provide the MTDC operator with the flexibility to select how the power is going to be shared among the converters for a more efficient power distribution, but also offers redundancy in case a connected converter is lost. In this case, the power plant cluster would not necessarily have to shed its power and shut down but its power could be absorbed by the remaining stations, if the power rating of the latter allows it. If the produced power exceeds the capacity of the remaining connected stations, a portion of the power sources could be shut down but the rest can remain connected.

For such a power flow scenario, the MTDC stations connected to the power source cluster should follow a control strategy similar to the one employed in a conventional ac grid. There, multiple synchronous generators are connected to a common ac grid and each of them is frequency-droop controlled via a governor, sharing the load variations according to their droop setting. In the same manner, the connected MTDC stations would be acting as virtual synchronous machines [102], with a droop setting to control the way the stations share power during variations from the cluster or when an MTDC station is lost.

On the other hand, the stations connecting such an MTDC grid to the external ac networks should operate under the assumption that there is an unpredictable amount of power injected to the MTDC grid. A solution to the problem is suggested in [103], where all these stations are featuring direct-voltage droop control with power setpoints equal to zero and common voltage setpoints. As a result, when there is no influx of power from the power sources, the affected MTDC stations establish a common voltage to the nodes of the dc grid, ensuring zero power flow between the dc lines. When there is power influx, the same stations will react based on their droop curves, sharing the power according to the choice of the droop characteristic at each station.

7.5 Controller offering direct-voltage support in MTDC grids

Within the droop-control context in MTDC grids, a modified droop controller is proposed at this stage that can be utilized by any voltage controlled but also constant-power controlled stations connected to the grid. The benefit of such a controller lies in the fact that contrary to a conventional constant-power controlled station, the use of the proposed controller offers the possibility of controlling the grid voltage during contingencies while ensuring the transfer of the requested power in steady-state conditions. The principles of operation and simulation scenarios proving the effectiveness of the proposed controller are presented in the following sections.

7.5.1 Direct-voltage support in MTDC grids

Abrupt and unscheduled power changes may occur in an MTDC grid. In these cases, the MTDC stations that are droop-controlled will react according to their droop curves, in an effort to support the stiffness of the direct voltage in the grid by altering their power transfer. It is therefore deduced that a plurality of droop controlled stations in the grid increases the direct-voltage support.

Some of the stations in the grid may however operate under constant power control, without the provision for a droop functionality. These stations will try to sustain their power transfer before and after an unexpected power change in the grid. While this is beneficial from the scope of an uninterrupted power transfer, it reduces the ability to quickly support the direct-voltage stiffness of the grid. It is essential that as many stations as possible change their power during such events so that large direct-voltage fluctuations with dangerously high peaks, which could damage the grid equipment, are avoided or quickly damped. The power controlled stations cannot provide such an assistance to the grid.

7.5.2 Controller for direct-voltage support in MTDC grids

A controller, which can be used to solve the problem of providing additional voltage support to an MTDC with droop-controlled and constant-power controlled stations, is proposed in this section. The same type of controller can be used in all stations. Its main design features are shown in Fig. 7.11. It constitutes a cascaded structure which can be divided in two main parts. "Part 1" is a PI-based constant-power controller while "Part 2" is a Droop-based Direct-Voltage Controller (D-DVC). A selector is used to activate or deactivate Part 1, setting the operation of the complete controller to a constant-power or droop-control mode, respectively. When Part 1 is activated, the controller is in its complete form and is addressed to as "Power-Dependent Direct-Voltage Controller" (PD-DVC).

Voltage-droop control mode

In the Voltage-droop control mode, the controller reduces itself to the D-DVC Part 2 of the complete controller of Fig. 7.11. This structure is similar to the standard droop controller as depicted in Fig. 7.10(a), but encapsulates a number of changes. The voltage control is not performed on the direct voltage but rather on the square of the latter. This is in accordance with the description of the direct-voltage controller described in Section (2.4.3) and suggested in [43]. Following the same controller design, a power-feedforward term is included where the dc power P_{dc} of the converter is fed-forward through a low-pass filter $H_f(s) = a_f/(s + a_f)$ of bandwidth a_f .

The direct-voltage controller in Section (2.4.3), which here acts as the core of the complete droop controller, was designed to have only a proportional gain K_p . A key feature in the present controller is the manner in which the droop mechanism is incorporated. Similar to the frequency-droop in synchronous generators connected to ac grids, the droop is here desired to have an

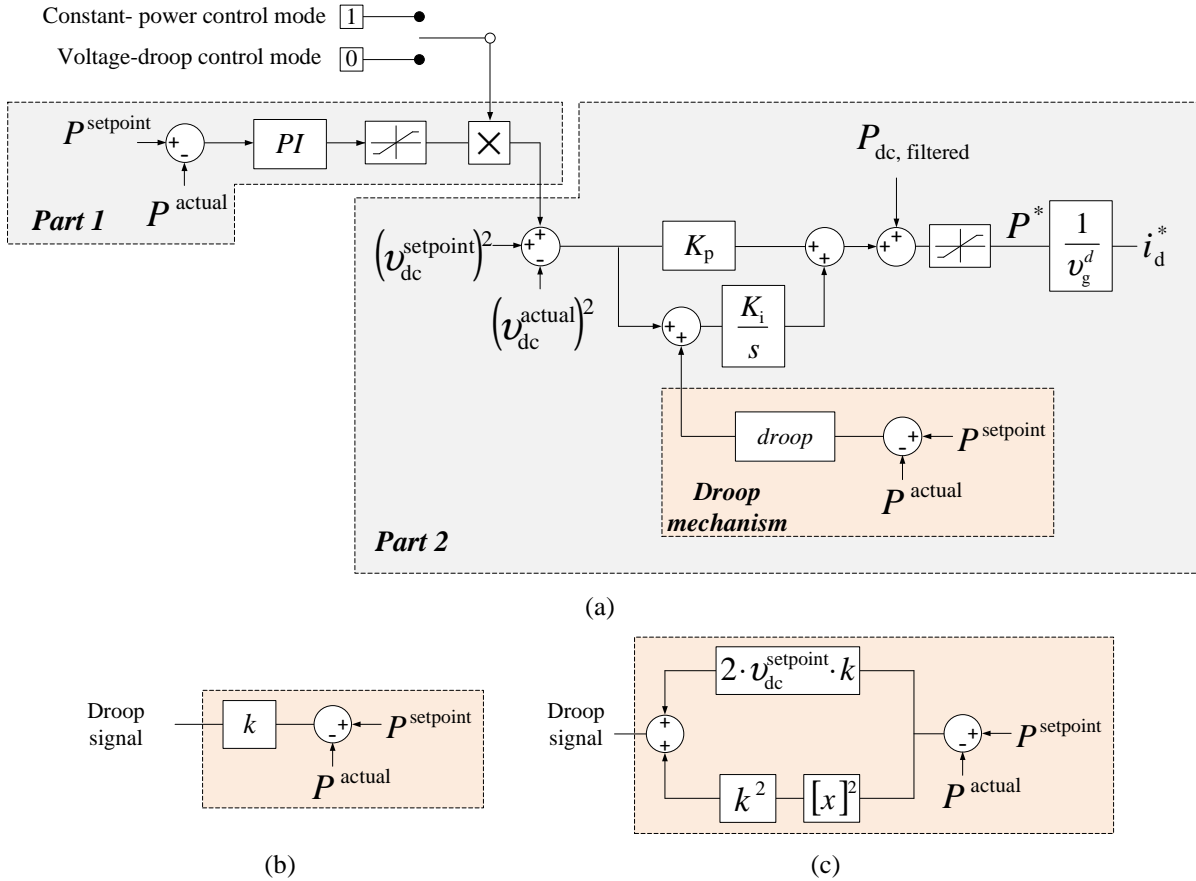


Fig. 7.11 Power-Dependent Direct-Voltage Controller: (a) Complete structure of the controller, (b) Droop mechanism for linear relation between power and square of the voltage, (c) Droop mechanism for linear relation between power and voltage.

impact only on the integral part of the direct-voltage controller, affecting its steady-state output. Therefore, unlike the conventional design in Fig. 7.10(a), the droop signal in the D-DVC is affecting the proportional part of the PI but operates exclusively on the integral part. In this way a great part of the closed-loop dynamics represented by the proportional part (as the controller without the droop was originally designed) remains unaffected.

Regarding the droop mechanism block, there are two options that can be selected. The first is shown in Fig. 7.11(b), with the value amplifying the error $P^{\text{setpoint}} - P^{\text{actual}}$ being a droop constant k , exactly in the same way as in the conventional droop of Fig. 7.10(a). However, if this is applied the controller would impose a linear connection between the steady-state power and the square of the voltage, rather than the power and the voltage as is observed in the conventional droop controller. Instead, the relation between power and the voltage will now be cubic. Nevertheless, given the small deviation region of the direct-voltage in operational conditions, the cubic curve is still close enough to the linear curve and is monotonous. The latter is more important than the linearity for the droop concept to function in a grid application. As such, the

7.5. Controller offering direct-voltage support in MTDC grids

droop mechanism can be still designed with a droop constant.

If the linearity between steady-state direct voltage and active power are to be respected, the droop mechanism should be modified. Starting from the linear droop curve described in (7.1), it is possible to derive the following relation

$$\begin{aligned}
 v_{dc}^{actual} &= - (P^{setpoint} - P^{actual}) k - v_{dc}^{setpoint} \Rightarrow \\
 (v_{dc}^{actual})^2 &= \left[- (P^{setpoint} - P^{actual}) k - v_{dc}^{setpoint} \right]^2 \Rightarrow \\
 (v_{dc}^{actual})^2 &= (v_{dc}^{setpoint})^2 + 2v_{dc}^{setpoint} (P^{setpoint} - P^{actual}) k + (P^{setpoint} - P^{actual})^2 k^2 \Rightarrow \\
 (v_{dc}^{setpoint})^2 - (v_{dc}^{actual})^2 + 2v_{dc}^{setpoint} (P^{setpoint} - P^{actual}) k + (P^{setpoint} - P^{actual})^2 k^2 &= 0 \quad (7.2)
 \end{aligned}$$

This form is now compatible to be used in the droop controller of Fig. 7.11(a) and the droop mechanism is modified to the one presented in Fig. 7.11(c).

Constant-power mode

During this mode, the PD-DVC controller of Fig. 7.11(a) operates in its complete form including Part 1 and Part 2. This is a composite structure consisting of the D-DVC, with the addition of a standard active-power PI controller adding its output signal to the voltage error of the D-DVC. Actively adding a constant to the voltage error is equivalent to manipulating the setpoint $v_{dc}^{setpoint}$. As a result, the voltage-droop characteristic curve would move in a parallel motion to a new position.

Assume that a power-flow solver has calculated the necessary setpoints for the stations of a dc grid, including a constant-power controlled station. Focusing on the latter, its power setpoint $P^{setpoint}$ is set equal to its desired constant power reference P^* , with its direct-voltage setpoint $v_{dc}^{setpoint}$ being provided by the power-flow solution. These values are given to the controller of Fig. 7.11(a) and the station will ideally settle to a steady-state of $P^{actual} = P^{setpoint}$ and $v_{dc}^{actual} = v_{dc}^{setpoint}$ (if all the other stations are provided with setpoints from the power-flow solver). This point is indicated with "x" in Fig. 7.12, located on the droop curve of the station. It is noticed that Part 1 of the controller has not contributed at all in reaching this steady-state and its output is equal to zero.

If a contingency occurs in the MTDC grid (i.e. a station is lost), the droop-controlled stations react by following their droop curves in order to support the voltage stiffness of the grid and, as a result, re-adjust their steady-state power transfers. The station with the PD-DVC would react as well due to its droop characteristics, altering its power momentarily. However, in the new condition of the grid, the setpoint pair $\{P^{setpoint}, v_{dc}^{setpoint}\}$ cannot be followed anymore. Nevertheless, there is a request to respect the power setpoint in order to ensure constant steady-state power transfer. At this stage, Part 1 of the controller calculates a necessary corrective signal, which is added to the error at the input of the droop controller in Part 2. This operation is equivalent to the active calculation of a new voltage setpoint by an external master-level control, with the added advantage that it is performed locally. Consequently, the change in setpoints

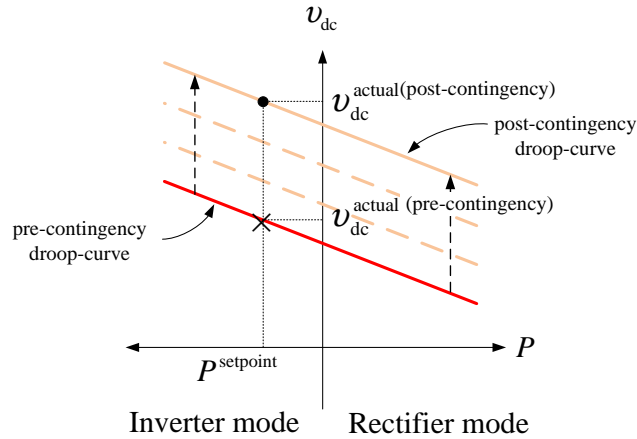


Fig. 7.12 Operation of the PD-DVC before and after a contingency in the MTDC grid. "x" indicates the pre-contingency steady-state point while "•" indicates the post-contingency steady-state point.

caused by the PI controller of Part 1 moves the entire droop characteristic along the voltage axis, as illustrated in Fig. 7.12, until the pair of P^{setpoint} and an adequate voltage setpoint, which will allow the flow of P^{setpoint} in the grid, can be found on it. This new point is indicated with "•" in Fig. 7.12. From the previous analysis it is also clear that the controller will operate seamlessly in pre- and post-contingency conditions, even if a random $v_{\text{dc}}^{\text{setpoint}}$ is originally provided.

7.5.3 Comments on the PD-DVC

Based on the description above, when the selector is set at position "1", the controller is able to

1. accurately maintain a given power reference without the need of communication with other stations
2. retain the ability to provide voltage support during contingencies, in a way dictated by its droop constant.

To achieve such characteristics, it is necessary to design the PI-based power controller of Part 1 so that the active power dynamics are slower than the direct-voltage dynamics, corresponding to the design of Part 2. This allows the droop function to act quickly during a contingency without being in conflict with the slower active-power control, which will restore the correct power flow at a slightly later stage. This is compatible with the conventional design of a two-terminal VSC-HVDC link where the direct-voltage control is designed to be much faster than the active-power control.

Another comment regards the measurement of the actual power P^{actual} input to the controller. It is possible to measure this power either as P_{dc} at the dc-side of the station or as P_{g} at the ac-side of the station, as shown in Fig. 2.16. These quantities will differ due to the system losses. Therefore, depending on the location of measuring P^{actual} , the power setpoint P^{setpoint} should be calculated accordingly, to account for these losses. In this Chapter, it is chosen to identify P^{actual} with P_{g} .

7.5. Controller offering direct-voltage support in MTDC grids

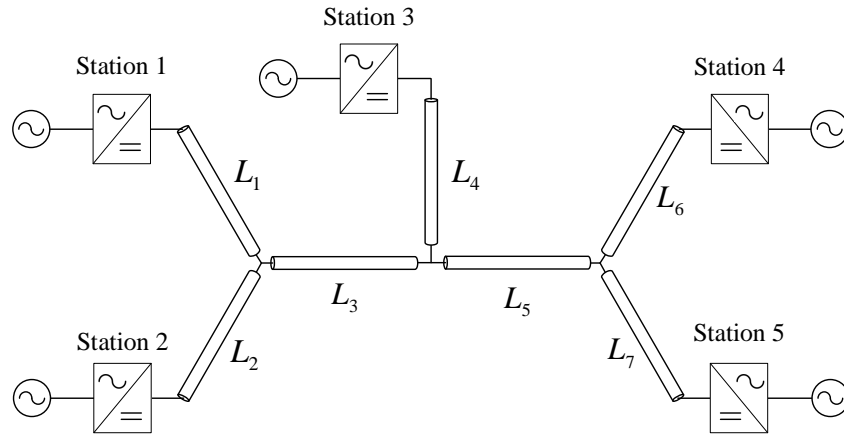


Fig. 7.13 Testing configuration of a five-terminal VSC-MTDC grid.

7.5.4 MTDC model-setup

The effectiveness of the PD-DVC will be verified through scheduled power-flow and contingency-event simulations. For this purpose, a five-terminal MTDC grid is considered. This is an ideal testing platform since it offers the possibility to simultaneously set a plurality of stations in pure droop control and constant-power mode. For simplicity, in all of the simulations the HVDC converters as well as their supplementary components (coupling inductor, transformer, ac-filters and dc-side capacitor) are considered identical in terms of ratings and physical values and their properties are described in Table 2.2. Any converter employing a droop functionality features the same droop characteristic k , equal to 2.5%. The layout of the five-terminal VSC-MTDC grid is presented in Fig. 7.13, where for visual reasons a dc-line pair is shown as a single conductor. The grid is divided into distinct sections L_1 - L_7 of overhead lines with assigned lengths of $L_1=25$ km, $L_2=50$ km, $L_3=100$ km, $L_4=50$ km, $L_5=100$ km, $L_6=70$ km and $L_7=30$ km.

7.5.5 Power-flow studies

At this stage, the functionality of the PD-DVC in establishing a desired power flow to the previously described MTDC grid is demonstrated. The controller of Fig. 7.11(a) is applied to all the stations. Among them, Stations 1, 3 and 4 are selected to operate with the selector in position "0", effectively turning them into pure droop-controlled stations while Stations 2 and 4 have the selector in position "1", being constant-power controlled. The gain values of the PI controller in "Part 1" of the PD-DVC are chosen appropriately to provide a setting time of approximately 1 s for a power-step reference. The droop mechanism is chosen to be the one in Fig. 7.11(c) ensuring a linear relation between voltage and power change. For the purpose of this example, all stations are connected to infinitely strong grids, which are thus represented by 400 kV voltage sources.

A selected power-flow schedule dictates that the active power measured at the PCC of Stations 2, 3, 4 and 5 should be equal to -400 MW, 400 MW, -300 MW and -200 MW, respectively. The direct voltage at the terminals of Station 1 is chosen equal to the rated value of 640 kV.

Chapter 7. Control investigation in Multiterminal VSC-HVDC grids

The reactive-power contribution from the stations is set to 0. Based on these requirements and using performing a dc-power flow calculation, it is possible to calculate the necessary setpoints P^{setpoint} and $v_{\text{dc}}^{\text{setpoint}}$ provided to the stations, such that the desired power flow will be established. These values are presented in Table 7.1.

The performance of the complete system is here evaluated in conditions when there is a predefined power schedule and when unexpected power changes occur due to changes in the demands of constant-power controlled stations. A related power flow pattern is implemented in stages as described below

1. Initially, all stations are provided with $P^{\text{setpoint}}=0$ MW and $v_{\text{dc}}^{\text{setpoint}}=640$ kV so that there is no power flow and the direct voltage of the MTDC is 640 kV at every measured point.
2. Between $t=2$ s and $t=2.3$ s, the setpoints of the stations are linearly ramped from their previous values to the ones in Table 7.1.
3. At $t=4$ s, the power setpoint of the constant-power controlled Station 2 is changed stepwise to $P^{\text{setpoint}}=-600$ MW.
4. At $t=5.5$ s, the power setpoint of the constant-power controlled Station 2 is changed stepwise to $P^{\text{setpoint}}=0$ MW.

The results of the simulation are shown in Fig. 7.14 where the P^{setpoint} references of Stations 2 and 4 are depicted as well.

As expected, when all stations are provided with the calculated setpoints (until $t=4$ s), the steady-state power and voltage match the given setpoints. At $t=4$ s, Station 2 is given a power-setpoint step-change, which follows accurately. At the same time, Station 4 reacts slightly due to the droop functionality within its direct-voltage controller because there is a momentary change in the grid voltage conditions, but quickly settles back to its unchanged power setpoint $P^{\text{setpoint}}=-300$ MW, as dictated by the constant-power setting of its overall controller. The pure droop controlled stations however react based on their droop curves and since there is an unexpected increase in the exported power from the grid, they have to compensate to restore a power balance.

TABLE 7.1. SETPOINTS TO THE STATIONS

Station	P^{setpoint} [MW]	$v_{\text{dc}}^{\text{setpoint}}$ [kV]
Station 1	515.472	640
Station 2	-400	638.166
Station 3	400	639.794
Station 4	-300	634.691
Station 5	-200	635.537

7.5. Controller offering direct-voltage support in MTDC grids

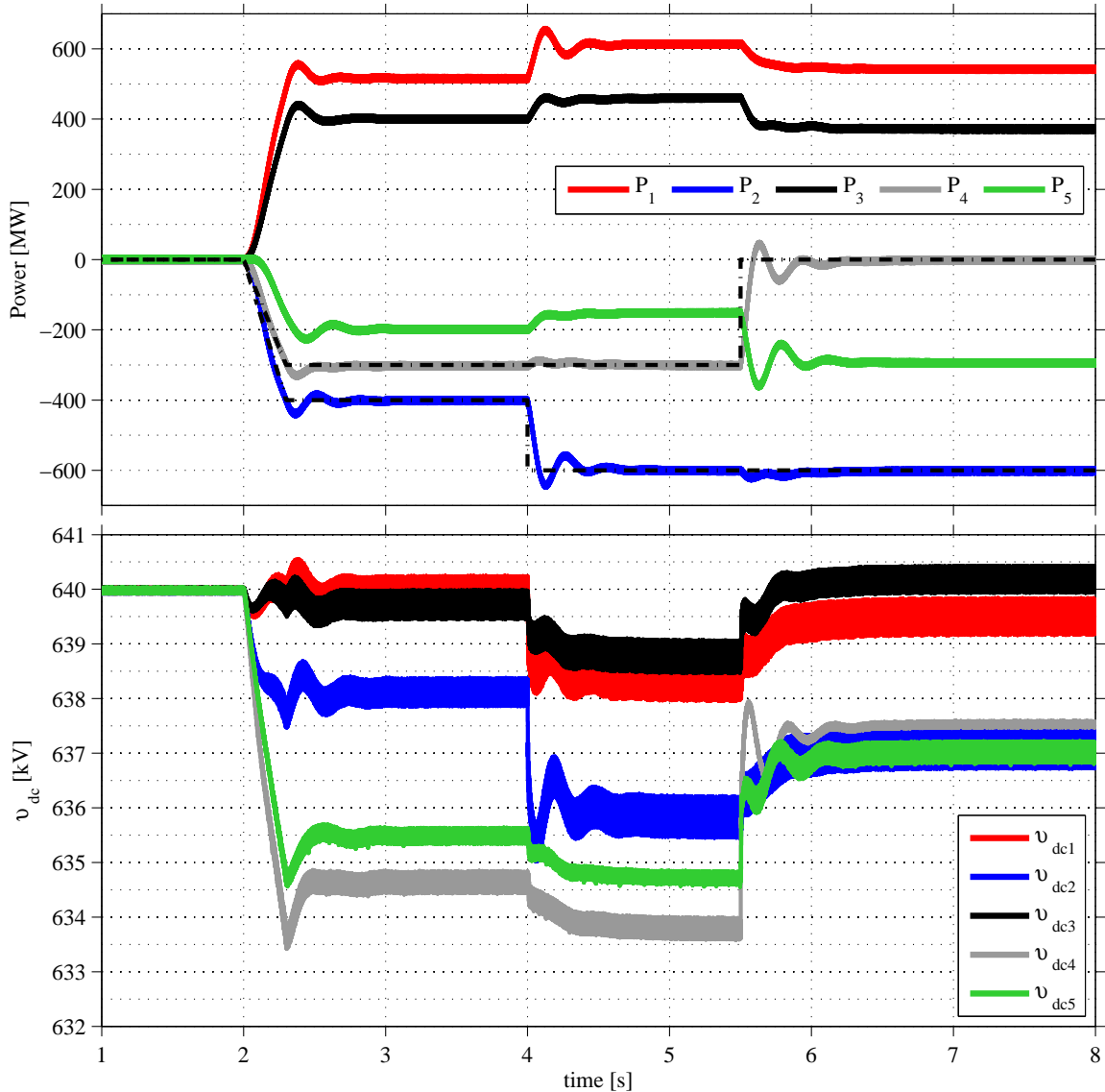


Fig. 7.14 Active-power and direct-voltage response of a five-terminal MTDC grid using the PD-DVC. A preselected power scheduling is applied, followed by consecutive power steps at the constant-power controlled stations.

As a result, Station 5 reduces the power it exports and Stations 1 and 3 increase the power they import to the dc-side.

In the same manner, the power setpoint of Station 4 is changed to zero at $t=5.5$ s and it promptly follows it, with Station 2 briefly reacting to the sudden rise in voltage in the grid (as there was an unexpected reduction in exported power) but quickly settles back to its unchanged $P^{\text{setpoint}} = -600$ MW. The droop controlled stations once again react based on their droop curves to restore the power balance.

Overall, the simulation verifies the functionality of the PD-DVC in an MTDC grid, achieving simultaneous operation of three droop-controlled stations and two constant-power controlled

stations.

7.5.6 Dynamic performance under fault conditions

The performance and direct-voltage supporting properties of the PD-DVC are demonstrated through fault studies on the ac- as well as the dc-side. These studies are performed on the same five-terminal MTDC grid as described in the previous section, featuring three droop-controlled and two constant-power controlled stations. The objective of the fault study is to compare the performance of the PD-DVC to that of an active-power PI controller that would conventionally be used to ensure constant power flow. As such, two types of MTDC-grid control strategies are tested:

- "Control Strategy 1": All stations feature the PD-DVC of Fig. 7.11(a).
- "Control Strategy 2": The constant-power controlled stations feature regular PI control with a rise time that is chosen to be close to the one achieved by the PD-DVC in "Control Strategy 1". The other stations are chosen to operate with the proposed PD-DVC in D-DVC mode (selector in position "0").

For consistency purposes in both the ac- and dc-side fault scenarios, the following common settings are chosen:

1. The stations are set-up exactly as in Section (7.5.5), with Stations 2 and 4 being in constant-power control mode and the setpoints to all the stations provided as in Table 7.1.
2. The ac-sides of all VSC stations are connected to infinite buses apart from the stations close to which the faults occur. These are connected to an ac grid of Short Circuit Ratio (SCR) equal to 2.
3. DC-choppers have been omitted in order to observe the pure dynamics of the fault phenomena.
4. The vector of the reference currents $(i_f^{(dq)})_{\max}^*$ to the current controller of all stations is limited to 1.0 pu.
5. The reactive power reference is set to zero for all stations.

AC-side fault scenario

The distance of the fault location from the VSC station terminals has a large effect on the response of the station. The closer the fault is placed to the VSC station, the more fault current contribution is bound to come from the station rather than the connected ac-network. In the present simulation scenario, the fault is chosen to be located close to Station 2. Namely, the equivalent grid impedance of the associated ac-network (which has been calculated for SCR=2) is split into two parts in series connection. The first one is equal to the 80% of the grid impedance

7.5. Controller offering direct-voltage support in MTDC grids

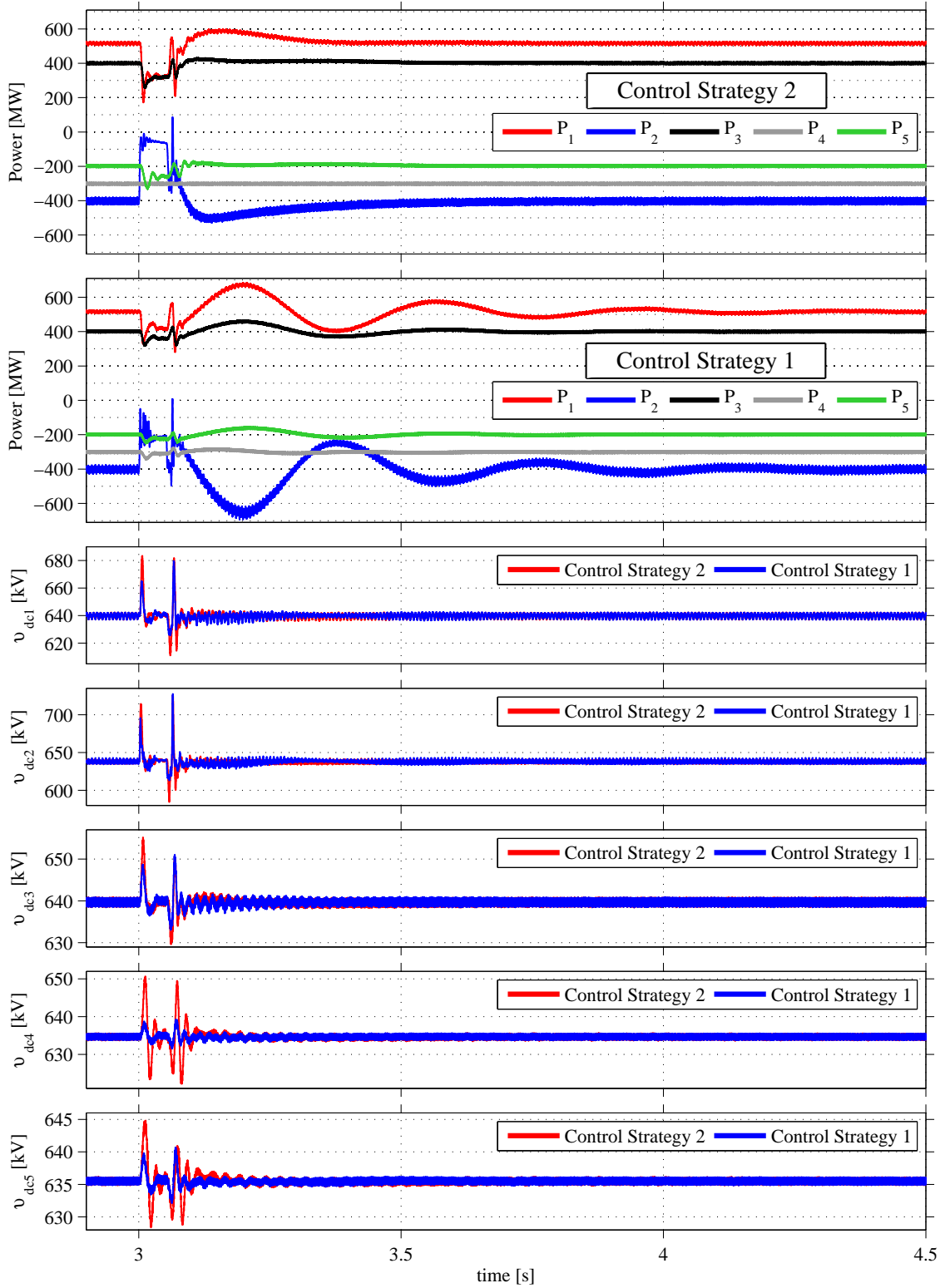


Fig. 7.15 Active-power and direct-voltage response of the five-terminal MTDC grid using the "Control Strategy 1" and "Control Strategy 2" schemes. An ac-side fault is applied close to Station 2 at $t=3$ s.

and is connected to the infinite ac-source while the other part is equated to the rest 20% of the impedance and is finally connected to the VSC station terminals. A small resistor is connected between the connection point of the two impedances and the earth, through a breaker.

While being in steady-state conditions, the breaker closes at $t=3$ s and then opens after 50 ms. This causes the voltage at the fault location to drop to approximately 22% of the original 400kV. The power and direct-voltage response of the system for the two different types of control strategies is presented in Fig. 7.15. For the "Control Strategy 2" control mode, the power references of the inverters are closely followed throughout the event, apart from the immediately affected Station 2 which experiences a great power change. The response of the droop-controlled stations is fast and the initial power flow is quickly restored after the fault is cleared. On the other hand, the direct-voltage, at the beginning and the clearing of the fault, exhibits large magnitude deviations followed by relatively poorly-damped high frequency components.

When the "Control Strategy 1" scheme is used, the power response of all stations is affected. During the fault, the power of the stations seems to change with less severity than in the "Control Strategy 2" scheme. In fact, the immediately affected Station 2 seems to be able to still export almost 200 MW to its ac-side (rather than only 50 MW in the "Control Strategy 2"), implying that the droop controlled stations don't have to significantly alter their contribution. After the fault clearing there is a low-frequency power oscillation until the systems quickly settles again at $t=4.2$ s. This low frequency oscillation is identified to most systems that feature a wide use of direct-voltage droop and reflects the effort of the system to find a new power-voltage settling point, based on the distributed droop curves. Its frequency and magnitude deviation is mostly affected by the droop constant k .

In general, the direct-voltage response is less abrupt and better controlled compared to the one achieved with the "Control Strategy 2" control. The poorly-damped oscillations experienced previously are now slightly better damped but the major difference is identified at the voltage overshoot at the beginning and the duration of the fault, which is significantly reduced. In the same manner, the voltage overshoot at the moment of fault-clearing is generally reduced with the only exception of Station 3 where the "Control Strategy 1" scheme features just slightly higher overshoot than the "Control Strategy 2" control.

Nevertheless, the post-fault power response of the system employing the "Control Strategy 1" scheme exhibits relatively large oscillations, compared to the system with the "Control Strategy 2" scheme. It was further found that their frequency is related to the value of the droop constant k . Despite the fact that these oscillations are quickly damped (approximately 1 s after the clearing of the fault), their magnitude is large enough to consider such a power flow behavior as undesired in an actual MTDC. This calls for modifications in the control algorithms.

DC-side fault and disconnection of a station

In this scenario, a fault is applied at $t=1.5$ s at the point between the upper dc-side capacitor and the positive dc-pole at Station 1, which is connected to earth through a small resistance. The station is provisioned to be equipped with DC-breakers on both of its dc terminals which manage to forcefully interrupt the fault current after 5ms and disconnect the station from the

7.5. Controller offering direct-voltage support in MTDC grids

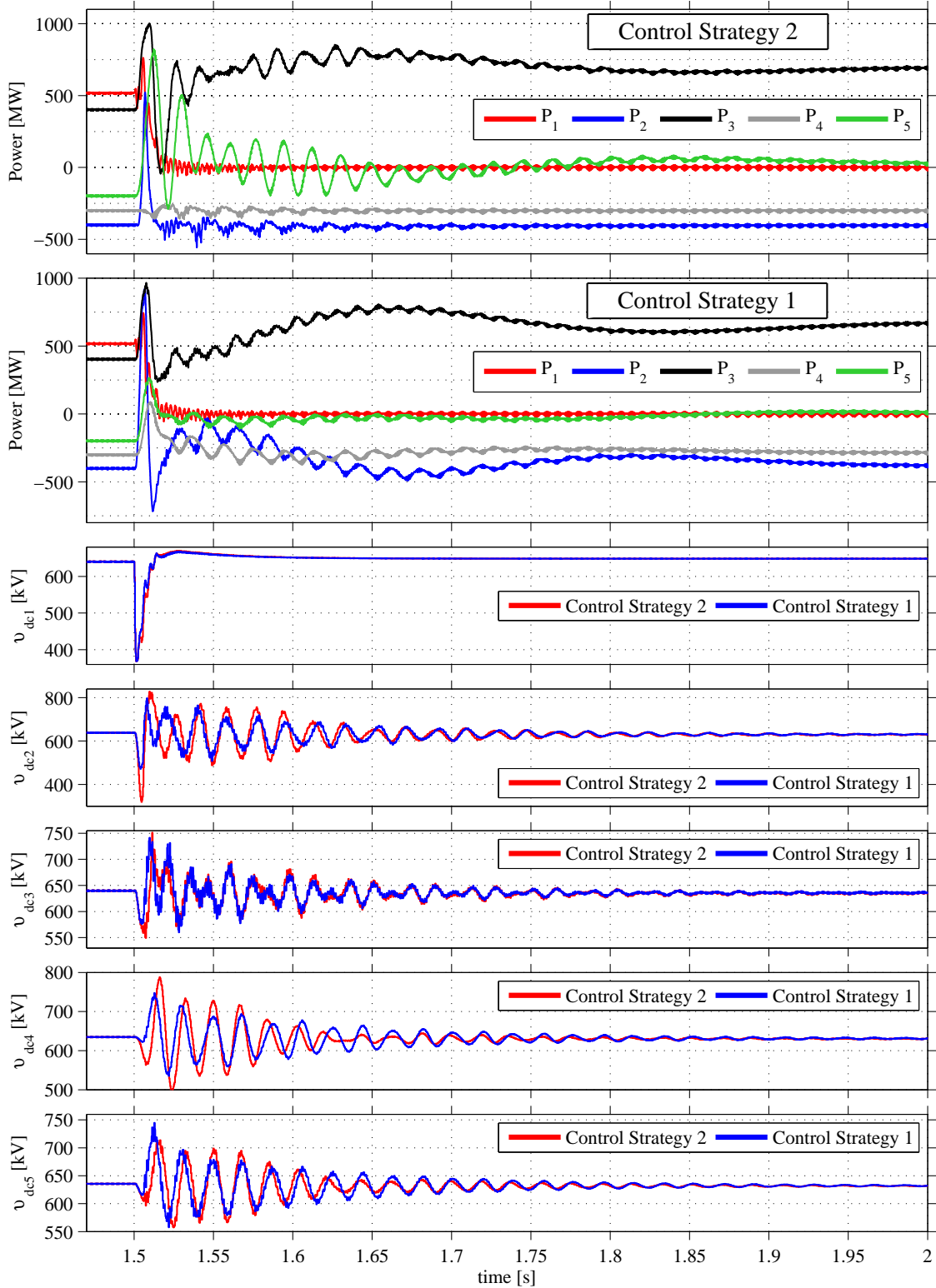


Fig. 7.16 Active-power and direct-voltage response of the five-terminal MTDC grid using the "Control Strategy 1" and "Control Strategy 2" control schemes. A dc-side fault is applied close to Station 1 at $t=1.5$ s, followed by the disconnection of the station.

dc grid. For simulation purposes, after the disconnection of the station, the fault location is also isolated but the station is kept in operating mode. This has no effect on the system, whose response is the main focus of the fault scenario.

The simulation results are presented in Fig. 7.16. During the fault, the surviving droop-controlled Stations 3 and 5 experience a large inrush of active power when the "Control Strategy 2" is used, which quickly reaches and slightly exceeds the rated 1000 MW for Station 3. At the same time, the constant-power Station 3 provides a very stiff power control while Station 5 exhibits a poorly-damped power oscillation. In contrast, the power response under "Control Strategy 1", features contribution from all stations to the voltage support. Station 3 quickly increases its power but never exceed the rated 1000 MW. Station 2 reduces its power extraction from the grid and imports almost the rated power to the MTDC grid. At the same time, the previously stiff power-controlled Station 4 responds by decreasing its power extraction from the grid. This prevents the converter capacitors of the dc grid to quickly discharge and is evident in all the monitored direct-voltages, which are not allowed to dip excessively right after the fault, compared to "Control Strategy 2". This is occurring because the D-DVC part of the proposed controller is operating in all surviving stations (rather than just the pure droop-controlled) and reacts immediately to the change of the direct voltage.

Nonetheless, the long-term direct-voltage response is very similar for both control strategies and in all the remaining stations, mainly characterized by a poorly-damped 53.2 Hz oscillation which is eventually damped after 0.5 s. However for the plurality of the Stations (2, 3 and 4), the direct-voltage overshoot occurring just after the beginning of the fault is always smaller when the "Control Strategy 1" scheme is used. This becomes important in the cases of Stations 2 and 4 that feature the largest voltage peak and the "Control Strategy 1". The sole exception of Station 5 where the "Control Strategy 1" surpasses "Control Strategy 2", in the highest monitored voltage overshoot.

7.6 Control strategy for increased power-flow handling

The control aspect in VSC-MTDC grids is of great importance, with voltage droop based methods considered as the most attractive solutions. This kind of existing strategies are normally designed to maintain the level of voltage in the MTDC grid almost constant during unexpected events, thus sacrificing the power flow. The aim of this section is to introduce a new droop-controller structure which maintains the dc-grid voltage close to the nominal values and at the same time tries to preserve the power flow, following such events as faults or disconnection of stations.

7.6.1 Comparison with standard strategies

In principle, droop-based strategies are designed in a way to secure that the direct voltage of the grid lies within strict boundaries under normal operation. However, in a post-fault scenario where there is a change in the dc-grid layout (i.e. an HVDC station is disconnected), this strategy

7.6. Control strategy for increased power-flow handling

would sacrifice the accuracy of the power flow.

Considering a conventional D-DVC in the form of Fig. 7.10(a), a relatively small value of the droop constant k implies that the controller is restrictive towards voltage and will not allow a large variation of the direct voltage for a large variation of the power. In contrast, a relatively large value of k renders the controller restrictive towards power, allowing a small variation of power in case of large changes of the dc-link voltage. In an MTDC grid, it is necessary to maintain the voltage within a strict margin for proper operation of the system; at the same time it is important to maintain the desired power flow in the different stations not only in steady-state, but also in case of unexpected events such as faults or unplanned disconnection of a station. Droop-controlled converters that are expected to maintain their the power flow to a large extent, require large values of k while converters that are mainly responsible for maintaining the direct voltage and are expected to contribute the most power during unexpected events require low values of k .

However, as investigated in [16], in a MTDC where there are stations using conventional droop control with high values of k (in the range of 60-100% instead of the more conventional 2%) the chances of reaching instability in the grid are very high. Therefore a new controller is here proposed to accommodate the use of large droop constants in order to offer better dynamic response during fault events or power scheduling changes.

7.6.2 Proposed Controller

The proposed controller is presented in Fig. 7.17 and is a modified version of a conventional D-DVC depicted in Fig. 7.17(a), which in turn is practically identical to the one in Fig. 7.11(a) (with the selector in position "0"). The branch that provides the droop-based correcting signal to the voltage controller consists of a PI-based droop controller that operates on the error between the reference power P^{setpoint} for the station of interest and the actual transferred power P^{actual} . The controller's corrective signal is added to the reference $v_{\text{dc}}^{\text{setpoint}}$ of the standard direct-voltage controller.

The version in Fig. 7.17(b) achieves a linear steady-state relation between the actual power and the square of the voltage (or "energy stored in the dc-capacitor") while the version in Fig. 7.17(c) achieves a linear steady-state relation between the actual power and the voltage. This is respectively equivalent to the droop choices in the previously proposed controller of Fig. 7.11(b) and Fig. 7.11(c).

Steady-state properties

The steady-state behavior of the proposed controller can be analyzed in the simpler case of the version in Fig. 7.17(b). Observing the branch generating the droop signal, it is possible to derive the closed-loop transfer function of the combined PI controller with the negative feedback of

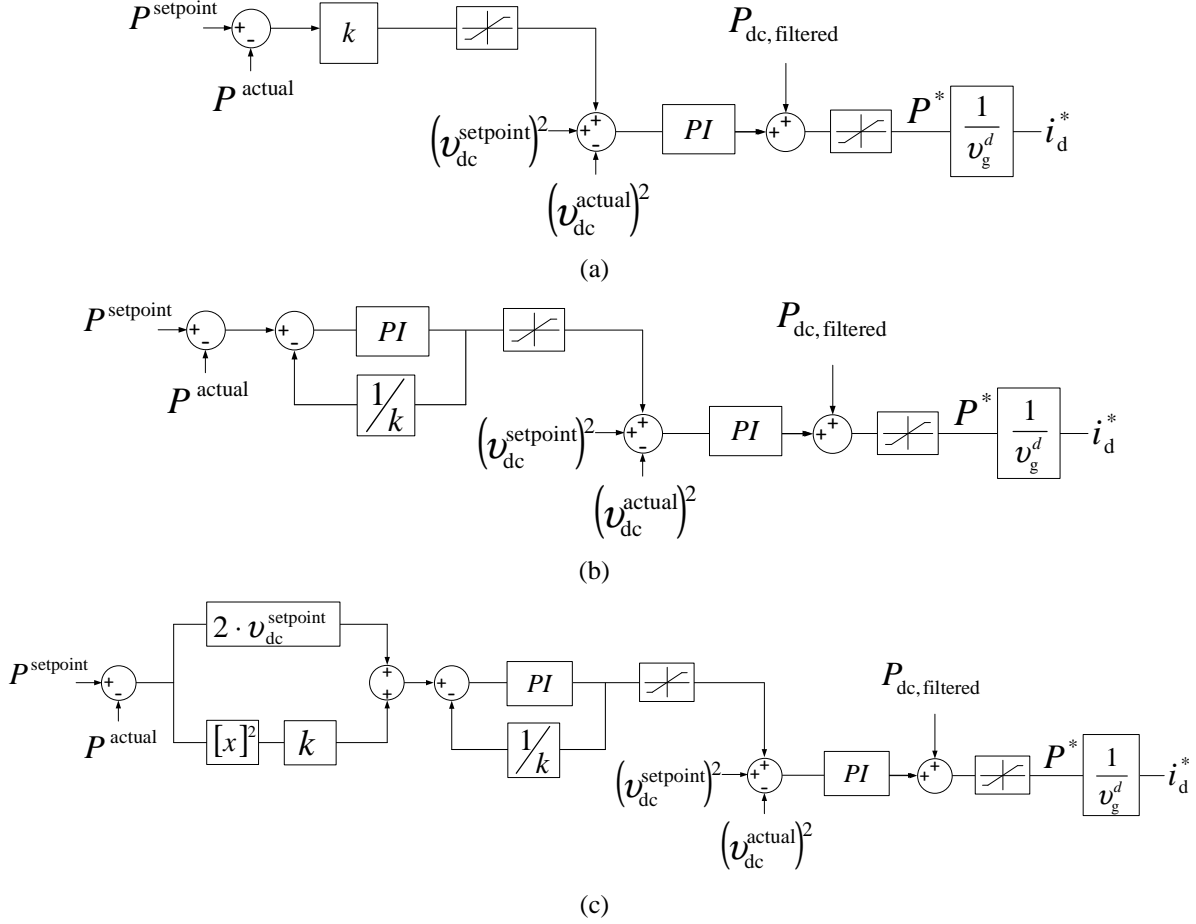


Fig. 7.17 (a) Conventional D-DVC with linear relation between power and square of the voltage, (b) Proposed controller with droop mechanism for linear relation between power and square of the voltage, (c) Proposed controller with droop mechanism for linear relation between power and voltage.

gain $1/k$. This will be equal to

$$G(s) = \frac{K_p + \frac{K_i}{s}}{1 + \left(K_p + \frac{K_i}{s}\right) \frac{1}{k}} = \frac{\frac{sK_p + K_i}{s}}{\frac{sk + sK_p + K_i}{sk}} = \frac{sK_pk + K_ik}{sk + sK_p + K_i} = \frac{sK_pk + K_ik}{s(k + K_p) + K_i} \quad (7.3)$$

The steady-state gain, or *dc-gain*, of this transfer function is

$$G(s)|_{s=0} = \frac{sK_pk + K_ik}{s(k + K_p) + K_i} \Big|_{s=0} = \frac{K_ik}{K_i} = k \quad (7.4)$$

This means that in steady-state, the investigated controller behaves exactly like the conventional D-DVC with droop constant k of Fig. 7.17(a). Analyzing in a similar way, the suggested controller in Fig. 7.17(c) behaves exactly as the conventional droop controller, portrayed in Fig. 7.11 with the selector at positions "0" and the droop selection of Fig. 7.11(c). Therefore,

7.6. Control strategy for increased power-flow handling

the use of the conventional or the suggested controller has no effect on the final power flow that will be established in the MTDC grid, as long as the same setpoints and droop constants are provided to the respective stations.

Dynamic properties

In the conventional droop controller of Fig. 7.17(a), the droop signal is created by comparing the given power setpoint P^{setpoint} of a station to the actual transferred power P^{actual} , amplified by the droop constant k and then added to the voltage setpoint $v_{\text{dc}}^{\text{setpoint}}$. This means that whenever there is a difference between the power setpoint and its actual value, the voltage controller will try to set the direct voltage equal to the voltage represented by the predetermined voltage setpoint, corrected by the value of the droop signal. When k is relatively large, rapid and large power flow changes in the system could lead to a large droop signal passing directly to the voltage controller. This explains from a macroscopic point of view the instabilities observed in [16].

Conversely, the proposed controller features a PI-based droop signal mechanism. Even if in steady-state the droop part of the controller reduces to a proportional gain k (in the case of Fig. 7.17(b)), during transients it provides a filtering action, preventing large and rapid droop signals from reaching the voltage controller. This allows improved dynamic performance when changing setpoints, as well as in fault or station disconnection events.

7.6.3 Application of the proposed controller

The properties of the proposed controller are verified through power-flow and contingency-event simulations. A four-terminal MTDC grid is considered as shown in Fig. 7.18. This choice instead of the five-terminal grid of Section (7.5.4) is performed because it was found that dynamic phenomena involving poor damping, can be better observed in this configuration. The design of this grid follows the pattern used in Section (7.5.4), where for simplicity purposes, the HVDC converters as well as their supplementary components (coupling inductor, transformer, ac-filters and dc-side capacitor) are considered identical in terms of ratings and physical values and are the same as in Table 2.2. The grid is divided into distinct sections L_1 - L_5 of overhead lines with assigned lengths of $L_1=100$ km, $L_2=100$ km, $L_3=100$ km, $L_4=160$ km and $L_5=40$ km. All stations are connected to infinitely strong grids, which are represented by 400 kV voltage sources.

Two different types of droop controllers will be utilized in the simulations: the conventional D-DVC of Fig. 7.17(a) (addressed to as "Classic") and the proposed controller in its version of Fig. 7.17(b) (addressed to as "Proposed"). In a conventional D-DVC as the one in Fig. 7.10(a), where the voltage controller acts on v_{dc} , the droop constant k is defined by a percentage value e.g. 3%. This implies that if for zero power transfer the controlled station has a direct voltage at its terminals equal to $v_{\text{dc},0}$, for rated power transfer the same voltage will drop by 3%. Additionally the connection between transferred power and direct voltage at the terminals of the station is linear. When the voltage controller, instead, acts on v_{dc}^2 , there is no longer linear correlation between power and voltage but k can still be defined as earlier, corresponding to the percentage

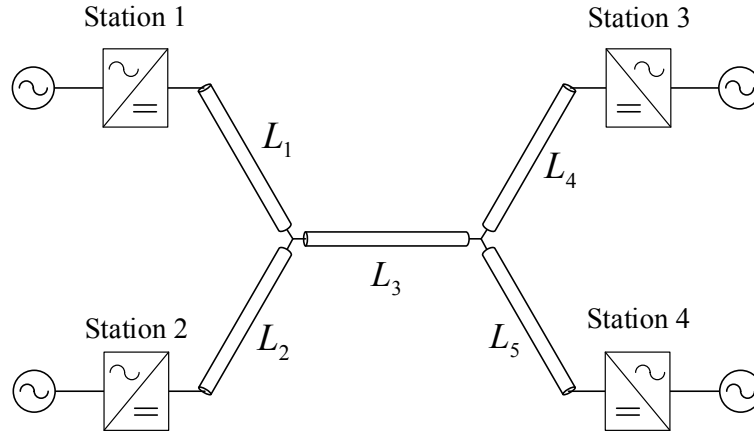


Fig. 7.18 Testing configuration of a four-terminal VSC-MTDC grid.

of dc-voltage change between zero and rated power transfer conditions.

Post-fault performance

After unexpected events in the system, such as faults, changes in the layout of the grid may occur e.g. disconnection of certain portions of the dc grid. In this case, the new physical characteristics of the grid will no longer be able to support the pre-fault scheduled power flow and all droop controlled stations will have to re-adjust their power outputs according to their droop curves and hence k values. High values of k cause the associated station to be very restrictive on power variations for any voltage variations in the dc grid. This means that the affected station will try to retain its power exchange very close to its power setpoint at all times and try to maintain its assigned power flow.

The four-terminal MTDC grid shown in Fig. 7.18 is simulated with all stations operating with the same type of controller at the same time (either "Proposed" or "Classic"). The selected strategy dictates that

- When the "Classic" control is used, all stations have the same droop constant $k=2.5\%$.
- When the "Proposed" control is applied, Stations 1, 2, 3 and 4 have droop constants $k_1=2.5\%$, $k_2=20\%$, $k_3=20\%$ and $k_4=80\%$, respectively. This indicates that Station 1 is expected to maintain the direct voltage at its terminals close to its setpoint under most conditions, while the rest of the stations exhibit stiffness on the change of their power transfer, with the highest degree of stiffness observed in Station 4.

A selected power-flow schedule dictates that the active power measured at the PCC of Stations 2, 3 and 4 should be equal to -600 MW, -700 MW and 700 MW, respectively. The direct voltage at the terminals of Station 1 is chosen equal to the rated value of 640 kV. The reactive-power contribution from the stations is set to 0. Based on these requirements and performing a dc-power flow calculation, it is possible to calculate the necessary setpoints P^{setpoint} and $v_{\text{dc}}^{\text{setpoint}}$

7.6. Control strategy for increased power-flow handling

provided to the stations, such that the desired power flow will be established. These values are presented in Table 7.2.

A sequence of events is implemented in consecutive stages, as described below

1. Initially, all stations are provided with $P^{\text{setpoint}}=0$ MW and $v_{\text{dc}}^{\text{setpoint}}=640$ kV so that there is no power flow and the direct voltage of the MTDC is 640 kV at every measured point.
2. Between $t=1$ s and $t=1.4$ s, the setpoints of the stations are linearly ramped from their previous values to the ones in Table 7.2.
3. At $t=2.0$ s, a fault is applied at the point between the upper dc-side capacitor and the positive dc-pole at Station 3, which is connected to earth through a small resistance. The station is provisioned to be equipped with DC-breakers on both of its dc-terminals which manage to forcefully interrupt the fault current after 5 ms and disconnect the station from the dc grid. For simulation purposes, after the disconnection of the station, the fault location is also isolated but the station is kept in operating mode.

The results of the simulation are shown in Fig. 7.19. After the disconnection of Station 3, the "Proposed" controller manages to restrain the power at Station 4 at 655 MW, from the pre-fault 700 MW, while under the "Classic" control it reaches 366 MW in steady-state. Additionally, Station 2 transmits a power of -693 MW under the "Proposed" control, instead of the pre-fault -600 MW, but deviates to -781 MW under "Classic" control. Given that only Station 1 was provided with a low droop constant in the "Proposed" control strategy, it now bears the total power that needs to be injected to the grid to restore a power balance. On the contrary, in the "Classic" control strategy, all the remaining stations share equally the burden of changing their power to restore a power balance, causing a significant deviation in the power transfer of them all. Consequently, Station 1 decreases its power, under "Proposed" control, from 615.2 MW to 49.6 MW, unlike the "Classic" control scenario where it only decreases to 425.2 MW.

The changes in steady-state direct voltage are in any case relatively limited and are formulated according to the droop gains of the remaining stations and the new power flow. The results show that under the "Proposed" control with a combination of droop constant values according to which station is needed to preserve its power transfer after contingencies, the power flow is better preserved while keeping the voltages in the MTDC grid close to the nominal value.

TABLE 7.2. SETPOINTS TO THE STATIONS

Station	P^{setpoint} [MW]	$v_{\text{dc}}^{\text{setpoint}}$ [kV]
Station 1	615.245	640
Station 2	-600	633.204
Station 3	-700	630.202
Station 4	700	638.166

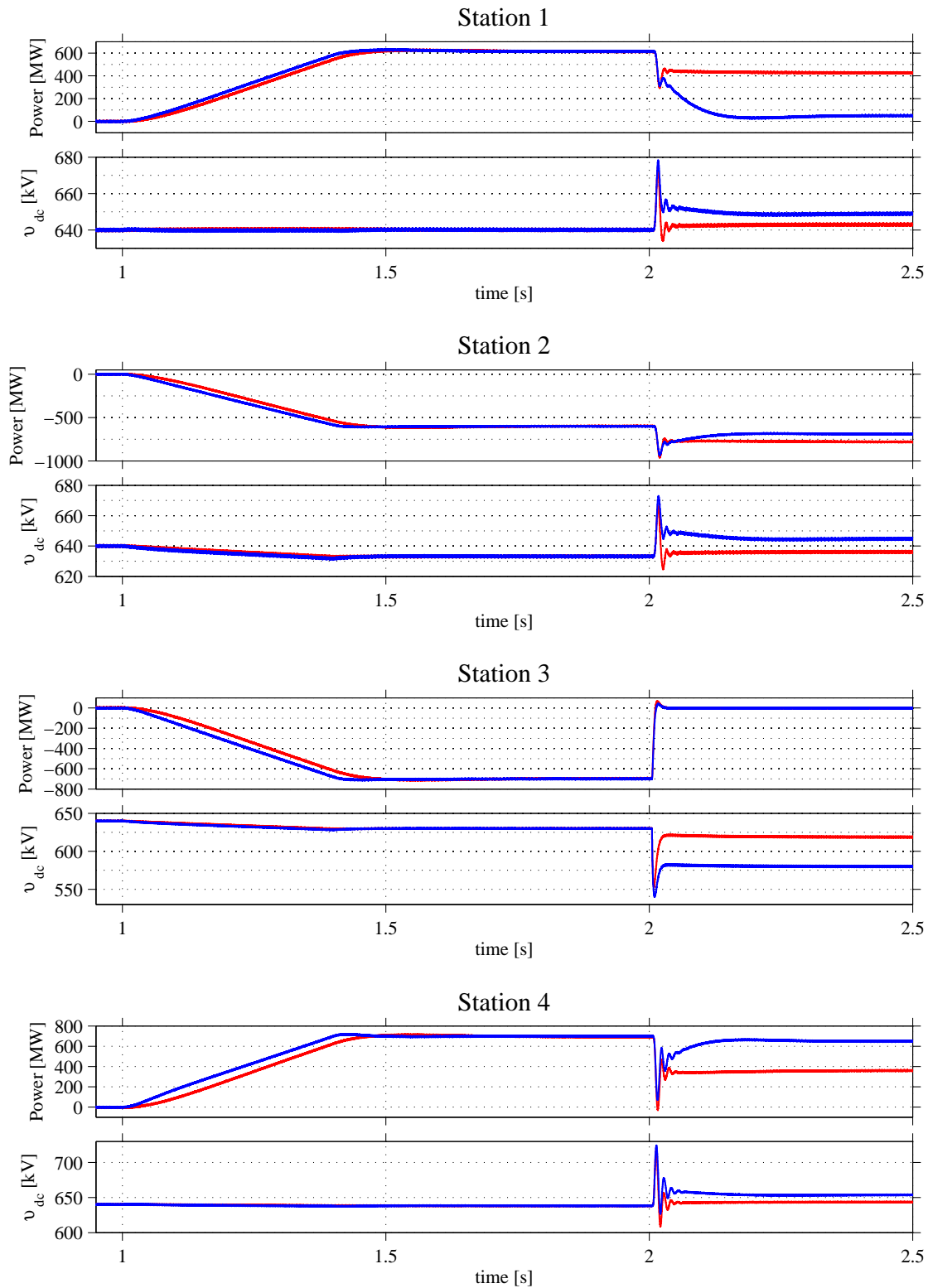


Fig. 7.19 Power and direct voltage of all stations in the four-terminal MTDC, after the disconnection of Station 3. Blue color represents "Proposed" control while red color represents "Classic" control.

7.6. Control strategy for increased power-flow handling

Dynamic performance during power-flow changes

Poorly-damped conditions might appear in droop controlled MTDC grids [41]. Such events may appear when high values of k are applied [16], as will be demonstrated in the current simulation scenario. The four-terminal MTDC grid used in the previous section, is simulated with all stations operating with the same type of controller at the same time (either "Proposed" or "Classic"). In both cases, the controllers of Stations 1, 2, 3 and 4 have $k_1=2.5\%$, $k_2=20\%$, $k_3=20\%$ and $k_4=80\%$, respectively. This is exactly the same as in the strategy for the "Proposed" control strategy of the previous section, but now the same droop constants are applied to conventional droop controllers as well.

A sequence of events is implemented in consecutive stages, as described below

1. Initially, all stations are in steady-state, following the setpoints of Table 7.2.
2. At $t=2$ s, new values of setpoints are provided to the stations. These are calculated based on a demand for an increase in power at Station 4 from the initial 700 MW to 950 MW, while Stations 2 and 3 maintain their power and Station 1 should still regulate the direct voltage at its terminals at 640 kV. The new setpoints are provided in Table 7.3.

The effect of the application of a new set of set-points to the stations is presented in Fig. 7.20 where the power and direct voltage of each station is provided over time. Even though both types of control manage to establish the requested power flow changes in steady-state, the configuration using the "Classic" control appears to suffer from poorly-damped oscillations. This oscillation appears in the voltage and power of Station 4 and is located at approximately 298 Hz. It should be reminded that this station features the highest value of droop constant. The performance on the other stations, which feature a smaller value of k , does not seem to be affected by the oscillation.

On the other hand, when the "Proposed" type of control is applied, there is no issue with the 298 Hz voltage and power oscillation, which does not appear at all. Additionally, all stations (including Stations 2, 3 and 4 that feature relatively high values of k), demonstrate a smooth power and voltage response, ensuring the dynamic integrity of the system. Furthermore, all stations exhibited a high overshoot peak when the "Classic" control was chosen. This type of control appears to have a fast response, which in turn leads to high overshoots in the voltage response during the application of the new setpoints. On the contrary, the "Proposed" type of control seems to perform in a smoother manner, maintaining the voltage very close to the nominal values with insignificant overshoots and no poor damping issues.

TABLE 7.3. UPDATED SETPOINTS TO THE STATIONS

Station	P^{setpoint} [MW]	$v_{\text{dc}}^{\text{setpoint}}$ [kV]
Station 1	364.948	640
Station 2	-600	634.604
Station 3	-700	633.007
Station 4	950	641.415

Chapter 7. Control investigation in Multiterminal VSC-HVDC grids

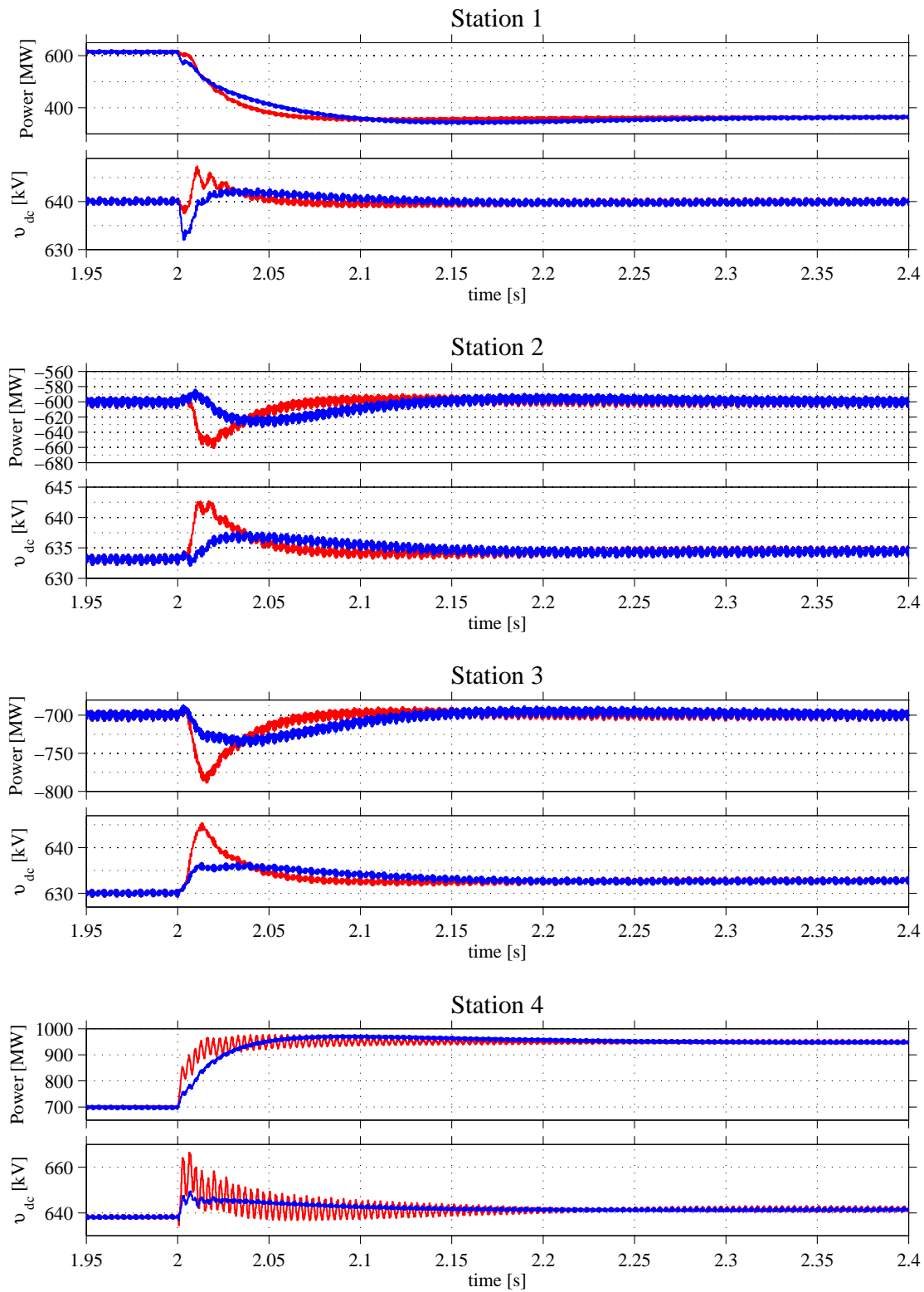


Fig. 7.20 Power and direct voltage response in the four-terminal MTDC during a change of setpoints at $t=2$ s. Blue color represents "Proposed" control while red color represents "Classic" control

7.6.4 Dynamic performance during ac-faults

The behavior of the PD-DVC controller in Section (7.5.6) demonstrated satisfactory results, restricting the deviations in the direct voltage of the dc grid after an ac-fault, but at the expense of relatively large power fluctuation in all stations. The "Proposed" controller is here tested in exactly the same conditions as those in Section (7.5.6), in an attempt to evaluate whether the performance of the system can be improved in the case of ac-faults.

In this sense, the power flow scenario of Section (7.5.6) is repeated on the same five-terminal MTDC grid, with the same setpoints given to the converters. Two types of MTDC-grid control strategies are tested:

- "Proposed" control: Identical to the "Control Strategy 1" control of Section (7.5.6) but Stations 2 and 4 feature the "Proposed" controller proposed in this section with a droop constant equal to $k=80\%$. Even though this strategy does not provide constant-power control to Stations 2 and 4, the selected value of their droop constants imply that any deviations from the power setpoints, in case of station disconnection in the grid, would be minimal. The other stations of the grid keep using the PD-DVC controller of Section (7.5.2) in its standard-droop mode (or D-DVC mode), with droop constants equal to 2.5%.
- "Control Strategy 2" control scheme: Same as the strategy of the same name in Section (7.5.6).

The results of the ac-fault simulation are presented in Fig. 7.21. As it can be observed, the use of "Proposed" control has improved the power response of the stations not only compared to the "Control Strategy 1" control of Section (7.5.6) but also compared to the "Control Strategy 2" control. In the duration of the fault, all stations seem to restrict the deviation of their pre-fault power, with the exception of Station 4, which nonetheless presents only as minor oscillation in the power transfer. Furthermore, after the fault is cleared and the stations try to restore the original power flow, the power response with the "Proposed" control appears to be faster and more accurate with minimal overshoots, compared to the "Control Strategy 2" scheme. In particular, the power at Stations 1 and 2 never exceed 564 MW and -472 MW under "Proposed" control, respectively. The same quantities for the "Control Strategy 2" have values of 598 MW and -529 MW.

As far as the voltage response is concerned, the "Proposed" control shows impressive results compared to the "Control Strategy 2" scheme, very similar to those obtained by the "Control Strategy 1" in Fig. 7.15. Despite the fact that Stations 2 and 4 are controlled so that their power transfer is maintained as close to the designated power setpoint, the droop characteristics of their "Proposed" controllers still allows them to support the dc-grid voltage.

Concluding, the "Proposed" controller offers the similar benefits as the PD-DVC control in terms of direct-voltage support to the grid, but with the advantage of a great improvement in its power response during system disturbances, while providing almost constant power control to selected stations.

Chapter 7. Control investigation in Multiterminal VSC-HVDC grids

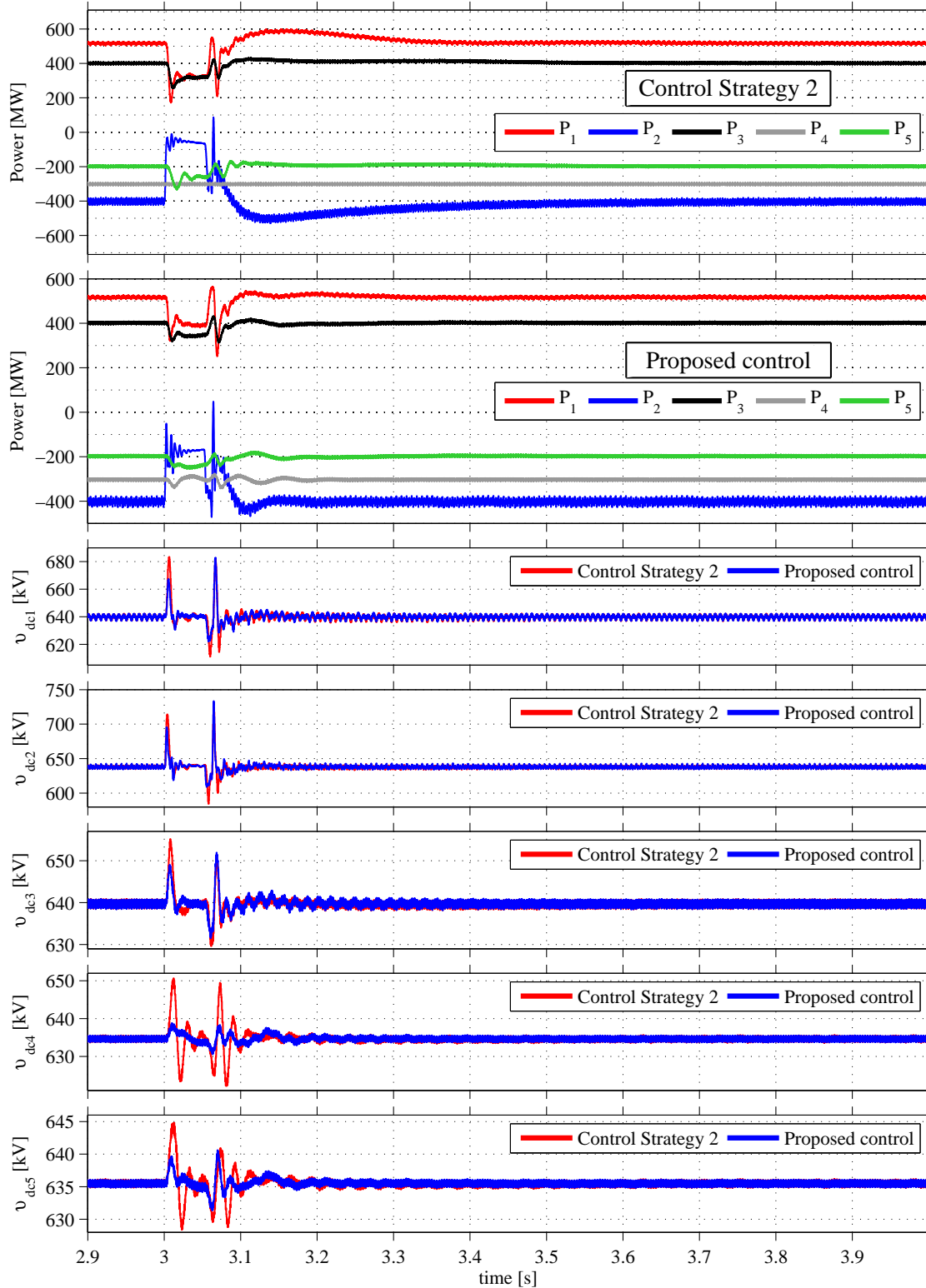


Fig. 7.21 Active-power and direct-voltage response of the five-terminal MTDC grid using the "Proposed" controller and "Control Strategy 2" scheme. An ac-side fault is applied close to Station 2 at t=3s.

7.7 Summary

This chapter presented the concept of VSC-MTDC grids and focused on their structural and control features. Having provided a brief description of the history and visions in the MTDC area, the possible future topologies and key components were described, along with the main types of control that are considered for implementation. Among the latter, the voltage-droop control appeared to be the dominant solution and the main objective of the chapter was to introduce new droop-based controllers that offer improved power-flow handling capabilities and provide voltage support to the dc grid under disturbances.

An initial proposal involved the PD-DVC controller, capable of providing constant power control to stations that require it, under all circumstances, including a change in the dc grid e.g. station disconnection. Simulation results in a five-terminal MTDC grid showed that the controller provided much better voltage support than a conventional active-power PI controller, but at the cost of relatively high power-fluctuations in the grid. A second type of controller, addressed to as "Proposed", was later introduced, designed specifically for cases where a station is required to be in droop-control mode but also retain its power flow as much as possible during grid contingencies. The results in a four-terminal MTDC grid demonstrated improved power-handling capabilities and increased the damping of the system, compared to a conventional droop controller. Furthermore, its voltage support capabilities were almost identical to those of the PD-DVC controller, but with the added benefit that previously observed acute power-flow fluctuations during fault conditions were now greatly diminished.

Chapter 7. Control investigation in Multiterminal VSC-HVDC grids

Chapter 8

Conclusions and future work

8.1 Conclusions

In this thesis, the dc-network dynamics of VSC-HVDC systems were thoroughly investigated in two-terminal connections and new perspectives were introduced to the control of VSC-MTDC grids. As an introductory part, Chapter 3 set the background for poorly-damped conditions in dynamic systems. It was shown in an explicit way that a VSC station operating as a constant-power provider in a VSC-HVDC or in motor drives, introduces the effect of a negative resistance. This has a degrading effect on the damping of the complex poles of the system, whose frequency is usually related to the characteristic frequency of the LC filter between the VSC and its dc source in drive applications, or the dc-transmission link natural frequency in a two-terminal VSC-HVDC connection.

In Chapter 4, a two-terminal VSC-HVDC system was modeled as a SISO feedback system, where the VSC-transfer function $F(s)$ and the dc-grid transfer function $G(s)$ were defined and derived. The implemented direct-voltage control had a direct impact on the transfer function $F(s)$ while $G(s)$ relied entirely on the passive components of the dc-transmission link and the operating conditions. Furthermore, if no power-feedforward term is used in the direct-voltage control, $F(s)$ is completely decoupled from the dynamics of the dc-transmission link. This is a major advantage when analyzing the SISO system in the frequency domain because it is possible to observe the separate contribution to instability by the VSC and the dc grid. This feature was exploited when using the passivity approach, where it was shown that as long as $G(s)$ can be successfully replaced by a marginally stable and incidentally passive transfer function $G'(s)$, the passivity characteristics of the VSC via its transfer function $F(s)$, will, to a certain degree, determine the stability of the closed-loop system. Indeed, it was shown that when the direct-voltage controlled VSC station imports power to the dc grid, the dc-grid resonant peak might coincide with a negative $\text{Re}[F(j\omega)]$, meaning that instead of being damped, the resonance is amplified; the more negative $\text{Re}[F(j\omega)]$ is, the greater the risk of instability. As an example, a factor that caused such conditions to appear was an increasing bandwidth a_d of the closed-loop direct-voltage control.

Nevertheless, it was shown that a direct-voltage controller with power-feedforward leads to an

Chapter 8. Conclusions and future work

$F(s)$ that is no longer decoupled from the dc-grid dynamics and is unstable and non-passive. Since the passivity approach could no longer be used, the net-damping criterion was utilized as an alternative frequency-domain approach. It was shown that the criterion could explain most conditions of potential instability, simply by focusing on the open-loop resonant frequencies of the VSC and dc-grid transfer functions and determining whether the cumulative damping of these functions was positive at the resonant points (and therefore stability was ensured). Additionally, the open-loop resonances could be defined in unstable subsystem transfer functions, showing that unstable subsystems did not prohibit the application of the criterion to derive conclusions for the closed-loop stability. It was also found that the absolute amount of net-damping in the system measured at the frequency where the Nyquist plot crosses the real axis closest to -1, is directly related to the existence of poorly-damped dominant poles and their damping factor. A net-damping approaching zero at that frequency, indicates the existence of poorly-damped poles with constantly decreasing damping factor.

In Chapter 5, the *SMT* analytical method was developed and presented in conjunction with the already known *LR* method, which had nevertheless never been implemented in the analysis of power systems or control related processes. A benefit of the *SMT* focused on the fact that is not iterative, meaning that the form and complexity of the final analytical eigenvalue expressions is known from the beginning, in contrast to the iterative *LR* where each additional iteration theoretically improves the accuracy but dramatically worsens the compactness of the expressions. A two-terminal VSC HVDC system was successfully minimized to a 4th order state-space representation and both methods were applied on it in Chapter 6. It was discovered that when using the *LR* method, the imaginary part of the expressions for complex-conjugate poles was converging at less iterations of the algorithm than the real part. Thus, it was suggested that the *LR* could be interrupted while executing, in order to extract a sufficiently accurate expression of the imaginary part and then be allowed to execute until the real part was sufficiently accurate as well. The final eigenvalue expression comprised of the two separately extracted real and imaginary parts. Both methods showed impressive results in approximating the actual values of the VSC-HVDC model, but the *SMT* showed a consistent increase in accuracy compared to the *LR*. A concluding investigation revealed that a high inductance per kilometer of the dc lines, adversely affected the accuracy of the results; in this case, the *SMT* showed a better tolerance, being able to show the way the eigenvalues would move for the change of a system parameter and still provide a good estimation of the absolute location of the poles. The *LR* was further applied to calculate the eigenvalues of the dc-transmission link portion of the previous two-terminal connection, demonstrating excellent results for any parameter variation.

Finally, Chapter 7 focused on the development of droop-based controllers for the use in MTDC grids. In the beginning, a controller was proposed for use in cases where a VSC station required to maintain its designated power flow after unexpected contingencies in the grid, such as the loss of a station following a dc-side fault, while maintaining voltage-droop characteristics during transients in the grid. The concept was tested in a five-terminal MTDC, where the performance of the controller was compared to that of a conventional PI-based power controller. It was shown that the use of the proposed controller caused a smaller direct-voltage variation in the grid during and after ac faults, but at the expense of significant but quickly damped power oscillations at all the stations. The performance after the disconnection of a station showed com-

parable behavior to that of having a pure PI controller to regulate the power, but with a slight improvement in reducing the direct-voltage oscillations that occurred within the MTDC. A second droop-controller variation was proposed for use in MTDC grids where a droop-controlled station requires a very high droop constant, meaning that it should maintain its power flow almost constant under all grid conditions, but still provide direct-voltage support as a conventional droop-controlled station would during grid contingencies. The proposed controller was tested in a four-terminal MTDC and compared to the performance of conventional droop-controllers, with the same droop constants being used for the same stations in both scenarios. It was shown that following a rapid change of power and voltage setpoints, the two controllers had no difference in steady-state performance (as desired), but the proposed control provided a smooth power and direct-voltage reaction from the stations that used it, compared to the conventional control that even exhibited poorly-damped oscillations. Finally, the controller was tested in the five-terminal MTDC of the earlier scenario and showed very good results for the ac-side fault scenario with almost negligible power oscillations compared to the first controller that was proposed.

8.2 Future work

The main focus of this thesis has been on the stability and control studies in the area of VSC-HVDC, with most of the efforts being concentrated around the two-terminal arrangement but later expanded to MTDC as well. Several future steps can be considered for the improvement of the acquired results and the investigation of related but unexplored areas of interest.

In the frequency-domain analysis of the two-terminal VSC-HVDC model, it was shown that the passivity approach can be applied only within specific boundaries. In particular, the unstable pole of the dc-grid transfer function $G(s)$ must be sufficiently close to the origin, so that $G(s)$ can be replaced by the marginally stable $G'(s)$, as shown in Chapter 4. Furthermore, the VSC-transfer function $F(s)$ must also be stable, limiting the choices on the direct-voltage control strategy. In general, a higher complexity of the model increases the chances of having unstable subsystem transfer functions. Contrary to the passivity approach, the net-damping approach not only does not seem to suffer from such restrictions but can also give far more consistent and direct information on the system's stability and the system's poorly-damped poles. As such, a future consideration is to apply the net-damping criterion methodology to higher complexity models and MTDC grids that can be represented by SISO models.

The analytical expressions that were derived by the *SMT* and *LR* methods, constitute a leap in acquiring useful and relatively compact eigenvalue descriptions. However, if it is desired to establish design specifications from these expressions, their final form should be further simplified. A future step could therefore consider studies on minimizing the analytical expressions, to the extent that their validity is sufficient for a small variations of only some, or preferably just one of the system's parameters. Since the derived eigenvalues would no longer need to have a complicated form in order to express the cumulative effect of all the parameters on the pole movement, the eigenvalue expressions could be substantially reduced and provide design criteria and specifications.

Chapter 8. Conclusions and future work

Additionally, in this thesis, the *SMT* and *LR* methods were applied to system models up to the 4th order. Systems of higher order could either increase the complexity of the final eigenvalue expressions (at least in the case of the *LR*), or may not even be solvable (considering the *SMT*). It could be useful to modify the *LR* method so that the maximum possible simplifications could be performed while creating the assisting matrices at each iteration step. In this way, it could be possible to produce final expressions for higher-order models, that are valid within a small variation margin of a nominal set of system parameters. Similarly, it could be useful to investigate whether it is theoretically possible to apply the *SMT* method on 5th or 6th order models, or whether a specific structure of the model's state-matrix can assist the solution of the eigenvalue problem.

Regarding the MTDC grid investigation, it could be desirable to develop a procedure for the tuning of the proposed controllers, based on a strict dynamic description of the system's model. This step, as well as improvements to the functionality of the controllers, could definitely be considered for future research.

A following step in the investigation of poorly-damped resonances in VSC-HVDC systems is the consideration of the input admittance of the VSC-stations. A relevant analysis has been performed in [43] for a single two-level VSC that is normally equipped with a lumped dc-side capacitor, without considering the impact of a dc-transmission link dynamics connected to the converter. The MMC has already been tested in HVDC applications and the current indications seem to consider this type of converter as dominant for future commissioned projects [2]. Each of the submodule cells of the MMC has a small capacitor bank and a unique switching pattern inserts or disconnects this capacitor to the rest of the converter circuit. This implies that the effective dc-side capacitance of the MMC, depends on the type of cell-switching and will inevitably impact the input admittance of the converter (especially on its dc-side) and the dynamics of the VSC-HVDC system to which the converter is connected. A future consideration for the expansion of the results of this thesis would consider the calculation of the input admittance of the MMC converter and investigate its impact to the development of poorly-damped conditions and instability in two-terminal HVDC and MTDC grids.

References

- [1] G. Asplund, K. Eriksson and K. Svensson, “Dc transmission based on voltage source converters,” in *presented at CIGRE Colloquium, SC14, South Africa*, 2011.
- [2] ABB, “It’s time to connect,” Technical brochure, December 2012.
- [3] V. A. N. Flourentzou and G. Demetriades, “Vsc-based hvdc power transmission systems: An overview,” *IEEE Power Electron.*, vol. 24, no. 3, pp. 592–602, March 2009.
- [4] S. Danielsen, “Electric traction power system stability,” Ph.D. dissertation, Norwegian University of Science and Technology, Norway, April 2010.
- [5] B.-H. Bae, B.-H. Cho and S.-K. Sul, “Damping control strategy for the vector controlled traction drive,” in *Proc. of the 9th European Conference on Power Electronics and Applications*, 2001.
- [6] S.D. Sudhoff, K.A. Corzine, S.F. Glover, H.J. Hegner and H. Robey, “Dc link stabilized field oriented control of electric propulsion systems,” *IEEE Trans. Energy Convers.*, vol. 13, no. 1, pp. 27–33, March 1998.
- [7] K. Pietilainen, L. Harnefors, A. Petersson and H.-P. Nee, “Dc-link stabilization and voltage sag ride-through of inverter drives,” *IEEE Trans. Ind. Electron.*, vol. 53, no. 4, pp. 1261–1268, June 2006.
- [8] M.P. Bahrman, E.V. Larsen, R.J. Piwko and H. Patel, “Experience with hvdc - turbine-generator torsional interaction at square butte,” *IEEE Trans. Power App. Syst.*, vol. PAS-99, no. 3, pp. 966–975, May 1980.
- [9] S.D. Sudhoff, S.F. Glover, P.T. Lamm, D.H. Schmucker and D. Delisle, “Admittance space stability analysis of power electronic systems,” *IEEE Trans. Aerosp. Electron. Syst.*, vol. 36, no. 3, pp. 965–973, July 2000.
- [10] M.P. Bahrman, G.C. Brownell, T. Adielson, K.J. Peterson, P.R. Shockley and R. Lasseter, “Dc system resonance analysis,” *IEEE Trans. Power Del.*, vol. 2, no. 1, pp. 156–164, Jan. 1987.
- [11] W. Zhang, G. Asplund, A. Aberg, U. Jonsson and O. Loof, “Active dc filter for hvdc system - a test installation in the konti-skan dc link at lindome converter station,” *IEEE Trans. Power Del.*, vol. 8, no. 3, pp. 1599–1606, July 1993.

References

- [12] M. Pereira, G. Wild, H. Huang and K. Sadek, "Active filters in hvdc systems: actual concepts and application experience," in *Proc. of International Conference on Power System Technology, PowerCon 2002*, vol. 2, 2002, pp. 989–993.
- [13] N.L. Shore, K. Adamson, P. Bard, R.S. Burton, C.D. Clarke, A. Coutu, S.C. Kapoor, K.L. Kent, F.P. Pereira, C. Pincella and K. Sadek, "Dc side filters for multiterminal hvdc systems," *IEEE Trans. Power Del.*, vol. 11, no. 4, pp. 1970–1984, Oct. 1996.
- [14] L. Zhang, L. Harnefors and H.-P. Nee, "Interconnection of two very weak ac systems by vsc-hvdc links using power-synchronization control," *IEEE Trans. Power Syst.*, vol. 26, no. 1, pp. 344–355, Feb. 2007.
- [15] F. Mura, C. Meyer and R. D. Doncker, "Stability analysis of high-power dc grids," *IEEE Trans. Ind. Appl.*, vol. 46, no. 2, pp. 584–592, March 2010.
- [16] P. Rault, F. Colas, X. Guillaud and S. Nguefeu, "Method for small signal stability analysis of vsc-mt dc grids," in *Proc. of IEEE Power and Energy Society General Meeting*, July 2012, pp. 1–7.
- [17] G.O. Kalcon, G.P. Adam, O. Anaya-Lara, S. Lo and K. Uhlen, "Small-signal stability analysis of multi-terminal vsc-based dc transmission systems," *IEEE Trans. Power Syst.*, vol. 27, no. 4, pp. 1818–1830, Nov. 2012.
- [18] S.D. Sudhoff, S.F. Glover, S.H. Zak, S.D. Pekarek, E.J. Zivi, D.E. Delisle and D. Clayton, "Stability analysis methodologies for dc power distribution systems," in *Proc. of the 13th International Ship Control System Symposium*, April 2003.
- [19] G. Pinares, "On the analysis of dc network dynamics of vsc-based hvdc systems," Chalmers University of Technology, Gothenburg, Sweden, Licentiate Thesis, Apr. 2014.
- [20] G. Pinares, L.A. Tuan, L. Bertling-Tjernberg and C. Breitholtz, "Analysis of the dc dynamics of vsc-hvdc systems using a frequency domain approach," in *Proc. of Power and Energy Engineering Conference (APPEEC), 2013 IEEE PES Asia-Pacific*, Dec. 2013, pp. 1–6.
- [21] I. Canay, "A novel approach to the torsional interaction and electrical damping of the synchronous machine part i: Theory," *IEEE Trans. Power App. Syst.*, vol. PAS-101, no. 10, pp. 3630–3638, Oct. 1982.
- [22] —, "A novel approach to the torsional interaction and electrical damping of the synchronous machine part ii: Application to an arbitrary network," *IEEE Trans. Power App. Syst.*, vol. PAS-101, no. 10, pp. 3639–3647, Oct. 1982.
- [23] A. Tabesh and R. Iravani, "On the application of the complex torque coefficients method to the analysis of torsional dynamics," *IEEE Trans. Energy Convers.*, vol. 20, no. 2, pp. 268–275, June 2005.
- [24] L. Harnefors, "Proof and application of the positive-net-damping stability criterion," *IEEE Trans. Power Syst.*, vol. 26, no. 1, pp. 481–482, Feb. 2011.

- [25] T. Tanaka, S. Fujikawa and S. Funabiki, "A new method of damping harmonic resonance at the dc link in large-capacity rectifier-inverter systems using a novel regenerating scheme," *IEEE Trans. Ind. Appl.*, vol. 38, no. 4, pp. 1131–1138, July 2002.
- [26] I. Kawaguchi, A. Okui, H. Ikeda and K. Matsuse, "Harmonic resonance phenomenon in the dc circuit of inverter to drive lsm," in *Proc. of Power Conversion Conference (PCC), Osaka 2002*, vol. 3, 2002, pp. 1009–1014.
- [27] L. Harnefors, N. Johansson, L. Zhang and B. Berggren, "Interarea oscillation damping using active-power modulation of multiterminal hvdc transmissions," *IEEE Trans. Power Syst.*, vol. 29, no. 5, pp. 2529–2538, Sept. 2014.
- [28] E. Hennig, R. Somme and M. Wiese, "Approximate symbolic pole/zero extraction using equation-based simplification driven by eigenvalue shift prediction," in *Proc. of the 1998 IEEE International Symposium on Circuits and Systems, ISCAS '98*, vol. 6, May 1998, pp. 25–28.
- [29] E. Hennig, "Symbolic approximation and modeling techniques for analysis and design of analog circuits," Ph.D. dissertation, University of Kaiserslautern, Germany, 2000.
- [30] O. Guerra, J.D. Rodriguez-Garcia, F.V. Fernandez and A. Rodriguez-Vazquez, "A symbolic pole/zero extraction methodology based on analysis of circuit time-constants," *Analog Integrated Circuits and Signal Processing*, vol. 31, no. 2, pp. 101–118, May 2002.
- [31] F. Constantinescu, M. Nitescu, M. Iordache and L. Dumitriu, "A program for the computation of the approximate symbolic pole/zero expressions," in *Proc. of European Conference on Circuit Theory and Design (ECCTD)*, vol. 1, August 2001, pp. 197–200.
- [32] A. Gheorghe and F. Constantinescu, "Pole/zero computation for linear circuits," in *Proc. of European Symposium on Computer Modeling and Simulation (EMS), 2012 Sixth UK-Sim/AMSS*, Nov. 2012, pp. 477–480.
- [33] A.G. Gheorghe, F. Constantinescu and M. Nitescu, "Improved lr algorithm for computation of the approximate symbolic pole/zero expressions," in *Proc. of AFRICON, 2013*, Sept. 2013, pp. 1–4.
- [34] D.G. Chapman, J.B. Davies, J.R. McNichol, E.M. Gulachenski, S. Doe and N. Balu, "Test experience with multiterminal hvdc load flow and stability programs," *IEEE Trans. Power Del.*, vol. 3, no. 3, pp. 1173–1181, Jul. 1988.
- [35] J. Reeve, "Multiterminal hvdc power systems," *IEEE Trans. Power App. Syst.*, vol. PAS-99, no. 2, pp. 729–737, Mar. 1980.
- [36] T. Nakajima and S. Irokawa, "A control system for hvdc transmission by voltage sourced converters," in *Proc. of IEEE Power Engineering Society Summer Meeting*, vol. 2, July 1999, pp. 1113–1119.

References

- [37] Y. Tokiwa, F. Ichikawa, K. Suzuki, H. Inokuchi, S. Hirose and K. Kimura, "Novel control strategies for hvdc system with self-contained converter," *Electrical Engineering in Japan*, vol. 113, no. 5, pp. 1–13, 1993.
- [38] H. Jiang and A. Ekstrom, "Multiterminal hvdc systems in urban areas of large cities," *IEEE Power Del.*, vol. 13, no. 4, pp. 1278–1284, Oct. 1998.
- [39] J. Liang, O. Gomis-Bellmunt, J. Ekanayake and N. Jenkins, "Control of multi-terminal vsc-hvdc transmission for offshore wind power," in *Proc. of the 13th European Conference on Power Electronics and Applications, EPE '09*, Sept. 2009, pp. 1–10.
- [40] T. Haileselassie, T. Undeland and K. Uhlen, "Multiterminal hvdc for offshore wind farms-control strategy," in *Wind Power to the Grid- EPE Wind Energy Chapter-2nd Seminar*, April 2009.
- [41] L. Tang, "Control and protection of multi-terminal dc transmission systems based on voltage-source converters," Ph.D. dissertation, University of McGill, Montreal, Quebec, Canada, Jan. 2013.
- [42] ABB, "It's time to connect," Technical brochure, December 2008.
- [43] L. Harnefors, M. Bongiorno and S. Lundberg, "Input-admittance calculation and shaping for controlled voltage-source converters," *IEEE Trans. Ind. Electron.*, vol. 54, no. 6, pp. 3323–3334, Dec. 2007.
- [44] J. Arrillaga, *High Voltage Direct Current Transmission*. London: The Institution of Electrical Engineers, 1998.
- [45] Y. Jiang, "Active and reactive power control of transmission systems with voltage source converters," Ph.D. dissertation, Royal Institute of Technology, KTH, Stockholm, Sweden, 1997.
- [46] C. Du, "Vsc-hvdc for industrial power systems," Ph.D. dissertation, Chalmers University of Technology, Gothenburg, Sweden, 2007.
- [47] S.G. Johansson, G. Asplund, E. Jansson and R. Rudervall, "Power system stability benefits with vsc dc-transmission systems," in *Proc. of CIGRE Conference in Paris, Session B4-204*, 2004.
- [48] B. Bijlenga, "Hvdc device for converting between alternating voltages and direct current voltages," U.S. Patent 6 480 403, 2002.
- [49] A. Lesnicar and R. Marquardt, "An innovative modular multi-level converter topology for a wide power range," in *Proc. of IEEE Power Tech Conference, Bologna, Italy*, June 2009, pp. 1–7.
- [50] C. Davidson and D. Trainer, "Innovative concepts for hybrid multi-level converters for hvdc power transmission," in *Proc. of 9th IET International Conference on AC and DC Power Transmission*, Oct. 2010, pp. 1–5.

- [51] ALSTOM, “Hvdc-vsc: transmission technology of the future,” *http://www.alstom.com/*, brochure.
- [52] L. Harnefors, *Control of Variable-Speed Drives*. Västerås, Sweden: Applied Signal Processing and Control, Dept. of Electronics, Mälardalen University, 2002.
- [53] L. Harnefors and H.-P. Nee, “Model-based current control of ac machines using the internal model control method,” *Industry Applications, IEEE Transactions on*, vol. 34, no. 1, pp. 133–141, Jan./Feb. 1998.
- [54] M. Beza, “Control of energy storage equipped shunt-connected converter for electric power system stability enhancement,” Chalmers University of Technology, Gothenburg, Sweden, Licentiate Thesis, May 2011.
- [55] L. Ängquist and M. Bongiorno, “Auto-normalizing phase-locked loop for grid-connected converters,” in *Energy Conversion Congress and Exposition, 2009. ECCE 2009. IEEE*, Sept. 2009, pp. 2957–2964.
- [56] M. Carpita, H. Zueger, M. Pellerin and P. Stefanutti, “Transformer used as a dc link filter inductance in dc high power traction applications,” in *Proc. of 2005 European Conference on Power Electronics and Applications*, June 2005.
- [57] J. Xu, H. Mori and Y. Sato, “An investigation of damping control method of power converters to suppress resonance in dc power network,” in *Proc. of Power Electronics Conference (IPEC), 2010 International*, June 2010, pp. 3093–3098.
- [58] P. Magne, B. Nahid-Mobarakeh and S. Pierfederici, “Dc-link voltage large signal stabilization and transient control using a virtual capacitor,” in *Proc. of Industry Applications Society Annual Meeting (IAS), 2010*, Oct. 2010, pp. 1–8.
- [59] J. Willems, “Dissipative dynamical systems part i: General theory,” *Arch. Ration. Mech. Anal.*, vol. 45, no. 5, pp. 321–351, 1972.
- [60] L. Harnefors, L. Zhang and M. Bongiorno, “Frequency-domain passivity-based current controller design,” *Power Electronics, IET*, vol. 1, no. 4, pp. 455–465, Dec. 2008.
- [61] L. Harnefors, “Modeling of three-phase dynamic systems using complex transfer functions and transfer matrices,” *IEEE Trans. Ind. Electron.*, vol. 54, no. 4, pp. 2239–2248, Aug. 2007.
- [62] ———, “Analysis of subsynchronous torsional interaction with power electronic converters,” *IEEE Trans. Power Syst.*, vol. 22, no. 1, pp. 305–313, Feb. 2007.
- [63] W. Press and W. Vetterling, *Numerical Recipes in Fortran 77: The Art of Scientific Computing*. Cambridge University Press, 1992.
- [64] R. Nickalls, “Viète, descartes and the cubic equation,” *The Mathematical Gazette*, no. 518, pp. 203–208, July 2006.

References

- [65] E. L. Rees, “Graphical discussion of the roots of a quartic equation,” *The American Mathematical Monthly*, vol. 29, no. 2, pp. 51–55, Feb. 1922.
- [66] R. Sommer, E. Hennig, M. Thole, T. Halfmann and T. Wichmann, “Analog insydes 2-new features and applications in circuit design,” in *Proc. SMACD2000, Lisbon*, Oct. 2000.
- [67] F. Constantinescu, M. Nitescu and C. Marin, “Computation of approximate symbolic pole/zero expressions,” *Analog Integrated Circuits and Signal Processing*, vol. 40, no. 3, pp. 255–264, Sept. 2004.
- [68] R. Horn and C. Johnson, *Matrix Analysis*. Cambridge University Press, 1985.
- [69] D. Watkins and L. Elsner, “Convergence of algorithms of decomposition type for the eigenvalue problem,” *Linear Algebra Appl.*, vol. 143, pp. 19–47, 1991.
- [70] J. Wilkinson, *The Algebraic Eigenvalue Problem*. Oxford: Oxford University Press, 1965.
- [71] A. Bunse-Gerstner, V. Mehrmann and D. Watkins, “An sr algorithm for hamiltonian matrices based on gaussian elimination,” *Methods Oper. Res.*, vol. 58, pp. 339–358, 1989.
- [72] A. Bunse-Gerstner, “An analysis of the hr algorithm for computing the eigenvalues of a matrix,” *Linear Algebra Appl.*, vol. 35, pp. 155–178, 1981.
- [73] D. Watkins and L. Elsner, “Chasing algorithms for the eigenvalue problem,” *SIAM Journal on Matrix Analysis and Applications*, vol. 12, no. 2, pp. 374–384, 1991.
- [74] D. Watkins, “Understanding the qr algorithm,” *SIAM Review*, vol. 24, no. 4, pp. 427–440, Oct. 1982.
- [75] H. Rutishauser, “Une methode pour la determination des valeurs propres d’une matrice,” *Comptes Rendus Acad. Sci. Paris*, vol. 240, pp. 34–36, 1955.
- [76] ———, “Solution of eigenvalue problems with the lr-transformation,” *J. Res. Nat. Bur. Standards, App. Math. Ser.*, vol. 49, pp. 47–81, 1958.
- [77] J. Francis, “The qr transformation, i,” *The Computer Journal*, vol. 4, no. 3, pp. 265–271, 1961.
- [78] ———, “The qr transformation, ii,” *The Computer Journal*, vol. 4, no. 4, pp. 332–345, 1961.
- [79] V. Kublanovskaya, “On some algorithms for the solution of the complete eigenvalue problem,” *USSR Comput. Math. Math. Phys.* vol. 1, no. 3, pp. 637–657, 1963.
- [80] G. Golub, *Matrix Computations, 3rd ed.* Baltimore: Johns Hopkins University Press, 1996.
- [81] J. Wilkinson, “Convergence of the lr, qr, and related algorithms,” *Comput. J.*, vol. 8, pp. 77–84, Sept. 1965.

- [82] ———, “Stability of the reduction of a matrix to almost triangular and triangular forms by elementary similarity transformations,” *J. Assoc. Comput. Mach.*, vol. 6, no. 3, pp. 336–359, July 1959.
- [83] B. Parlett, “The development and use of methods of Ir type,” *SIAM Review*, vol. 6, no. 3, pp. 275–295, July 1964.
- [84] Siemens, “Hvdc-high voltage direct current transmission,” Siemens AG, Energy Sector, Erlangen, Germany, technical brochure, 2012.
- [85] T.G. Magg, M. Manchen, E. Krige, H.D. Mutschler and J. Wasborg, “Caprivi link hvdc interconnector: The first vsc hvdc power transmission with overhead lines,” in *CIGRE Study Committee B4 Colloquium, Brisbane, Australia*, Oct. 2004.
- [86] B. Bose, *Power Electronics and Variable Frequency drives*. New York: IEEE Press, 1997.
- [87] Z. Zhao, M.R., and Iravani, “Application of gto voltage source inverter in a hybrid hvdc link,” *IEEE Power Del.*, vol. 9, no. 1, pp. 369–377, Jan. 1994.
- [88] E. Koldby and M. Hyttinen, “Challenges on the road to an offshore hvdc grid,” in *Proc. of Nordic Wind Power Conference*, Sep. 2009.
- [89] M. Dahlgren, “Abb-technology providers perspective,” in *Presentation at Energidagen-Chalmers Energy Initiative*, Dec. 2011.
- [90] D. Foundation, *Clean Power from Deserts: The DESERTEC Concept for Energy, Water and Climate Security*. Bonn, Germany: Protex Verlag, 2009.
- [91] N. Fichaux, J. Wilkes, F. Van Hulle and A. Cronin, *Oceans of opportunity. Harnessing Europe’s largest domestic energy resource*. EWEA, 2009.
- [92] C. Meyer, “Key components for future offshore dc grids,” Ph.D. dissertation, Electrical Engineering Department, RWTH, Aachen, Germany, July 2007.
- [93] J. Häfner and B. Jacobson, “Proactive hybrid hvdc breakers - a key innovation for reliable hvdc grid,” in *Proc. of Cigresymposium*, Sept. 2011.
- [94] T.K. Vrana, Y. Yang, D. Jovcic, S. Dennetire, J. Jardini and H. Saad, “The cigre b4 dc grid test system,” Working Group B4.57 and B4.58, Study, 2013.
- [95] R. L. Steigerwald and R. E. Tompkins, “A comparison of high frequency link schemes for interfacing a dc source to a utility grid,” in *Proc. of Industry Applications Society Annual Meeting (IAS’82)*, vol. 17, Oct. 1982, pp. 759–766.
- [96] V.T. Ranganathan, P.D. Ziogas and V. Stefanovic, “A regulated dc-dc voltage source converter using high frequency link,” *IEEE Trans. Ind. Appl.*, vol. IA-18, no. 3, pp. 279–287, May 1982.

References

- [97] S. Kenzelmann, A. Rufer, D. Dujic, F. Canales and Y. D. Novaes, “Isolated dc/dc structure based on modular multilevel converter,” *IEEE Trans. Power Electron.*, vol. 30, no. 1, pp. 89–98, Jan. 2015.
- [98] B. Engel, M. Victor, G. Bachman and A. Falk, “15kv/16.7 hz energy supply system with medium frequency transformer and 6.5 kv igbts in resonant operation,” in *Proc. of the 10th European Conf. on Power Electronics and Applications (EPE)*, Sept. 2003.
- [99] J. Jacobs, “Multi-phase series resonant dc/dc converters,” Ph.D. dissertation, Electrical Engineering Department, RWTH, Aachen, Germany, 2006.
- [100] C. Barker and R. Whitehouse, “Autonomous converter control in a multi-terminal hvdc system,” in *Proc. of the 9th IET International Conference on AC and DC Power Transmission*, Oct. 2010, pp. 1–5.
- [101] T. Haileselassie, “Control, dynamics and operation of multi-terminal vsc-hvdc transmission systems,” Ph.D. dissertation, Department of Electric Power Engineering, Norwegian University of Science and Technology (NTNU), Trondheim, Norway, Dec. 2012.
- [102] S. D’Arco and J. Suul, “Operation of power electronic converters in offshore wind farms as virtual synchronous machines,” in *Presentation at the 11th Deep Sea Offshore Wind R&D Conference, EERA DeepWind 2014*, Jan. 2014.
- [103] L. Xu, L. Yao and M. Bazargan, “Dc grid management of a multi-terminal hvdc transmission system for large offshore wind farms,” in *Proc. of International Conference on Sustainable Power Generation and Supply (SUPERGEN ’09)*, April 2009, pp. 1–7.

Appendix A

Transformations for three-phase systems

A.1 Introduction

In this appendix, the necessary transformations from three-phase quantities into vectors in stationary $\alpha\beta$ and rotating dq reference frames and vice versa will be described.

A.2 Transformation of three-phase quantities to vectors

A three phase system constituted by three quantities $v_a(t)$, $v_b(t)$ and $v_c(t)$ can be transformed into a vector $\underline{v}^{(\alpha\beta)}(t)$ in a stationary complex reference frame, usually called $\alpha\beta$ -frame, by applying the following transformation

$$\underline{v}^{(\alpha\beta)}(t) = v^\alpha(t) + jv^\beta(t) = K_{\text{tran}} \left(v_a(t) + v_b(t) e^{j\frac{2}{3}\pi} + v_c(t) e^{j\frac{4}{3}\pi} \right) \quad (\text{A.1})$$

The transformation constant K_{tran} can be chosen to be $\sqrt{2/3}$ or $2/3$ to ensure power invariant or amplitude invariant transformation respectively between the two systems. This thesis considers a power invariant transformation. Equation (A.1) can be expressed in matrix form as

$$\begin{bmatrix} v^\alpha(t) \\ v^\beta(t) \end{bmatrix} = \mathbf{T}_{32} \begin{bmatrix} v_a(t) \\ v_b(t) \\ v_c(t) \end{bmatrix} \quad (\text{A.2})$$

where the matrix \mathbf{T}_{32} is given by

$$\mathbf{T}_{32} = K_{\text{tran}} \begin{bmatrix} 1 & -\frac{1}{2} & -\frac{1}{2} \\ 0 & \frac{\sqrt{3}}{2} & -\frac{\sqrt{3}}{2} \end{bmatrix}$$

The inverse transformation, assuming no zero-sequence, i.e. $v_a(t) + v_b(t) + v_c(t) = 0$, is given by the relation

$$\begin{bmatrix} v_a(t) \\ v_b(t) \\ v_c(t) \end{bmatrix} = \mathbf{T}_{23} \begin{bmatrix} v^\alpha(t) \\ v^\beta(t) \end{bmatrix} \quad (\text{A.3})$$

where the matrix \mathbf{T}_{23} is given by

$$T_{23} = \frac{1}{K_{\text{tran}}} \begin{bmatrix} \frac{2}{3} & 0 \\ -\frac{1}{3} & \frac{1}{\sqrt{3}} \\ -\frac{1}{3} & -\frac{1}{\sqrt{3}} \end{bmatrix}$$

A.2.1 Transformation between fixed and rotating coordinate systems

For the vector $\underline{v}^{(\alpha\beta)}(t)$ rotating in the $\alpha\beta$ -frame with the angular frequency $\omega(t)$ in the positive (counter-clockwise) direction, a dq -frame that rotates in the same direction with the same angular frequency $\omega(t)$ can be defined. The vector $\underline{v}^{(\alpha\beta)}(t)$ will appear as fixed vectors in this rotating reference frame. A projection of the vector $\underline{v}^{(\alpha\beta)}(t)$ on the d -axis and q -axis of the dq -frame gives the components of the vector on the dq -frame as illustrated in Fig. A.1.

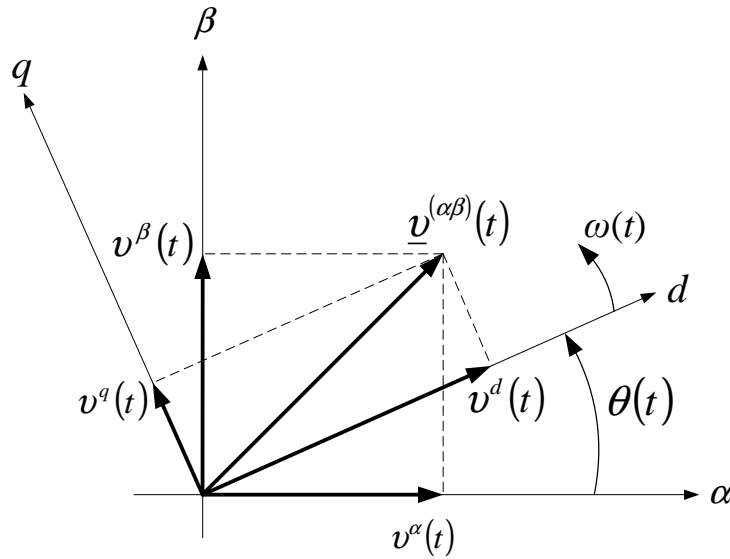


Fig. A.1 Relation between $\alpha\beta$ -frame and dq -frame.

The transformation can be written in vector form as follows

$$\underline{v}^{(dq)}(t) = v^d(t) + jv^q(t) = \underline{v}^{(\alpha\beta)}(t) e^{-j\theta(t)} \quad (\text{A.4})$$

with the angle $\theta(t)$ in Fig. A.1 given by

$$\theta(t) = \theta_0 + \int_0^t \omega(\tau) d\tau$$

The inverse transformation, from the rotating dq -frame to the fixed $\alpha\beta$ -frame, is provided as

$$\underline{v}^{(\alpha\beta)}(t) = \underline{v}^{(dq)}(t) e^{j\theta(t)} \quad (\text{A.5})$$

A.2. Transformation of three-phase quantities to vectors

In matrix form, the transformation between the fixed $\alpha\beta$ -frame and the rotating dq -frame can be written as

$$\begin{bmatrix} v^d(t) \\ v^q(t) \end{bmatrix} = \mathbf{R}(-\theta(t)) \begin{bmatrix} v^\alpha(t) \\ v^\beta(t) \end{bmatrix} \quad (\text{A.6})$$

$$\begin{bmatrix} v^\alpha(t) \\ v^\beta(t) \end{bmatrix} = \mathbf{R}(\theta(t)) \begin{bmatrix} v^d(t) \\ v^q(t) \end{bmatrix} \quad (\text{A.7})$$

where the projection matrix is

$$\mathbf{R}(\theta(t)) = \begin{bmatrix} \cos(\theta(t)) & -\sin(\theta(t)) \\ \sin(\theta(t)) & \cos(\theta(t)) \end{bmatrix}$$

Chapter A. Transformations for three-phase systems

Appendix B

Per-unit Conversion

The use of the per-unit system in the analysis of Chapter 2, requires the establishment of base values for the conversion of entities from natural to per-unit values. This section provides the definition of all the necessary base values for both ac- and dc-side quantities.

B.1 Per-unit conversion of quantities

The base values for the electrical variables (current and voltage), as well as entities that correspond to electrical properties (impedance, inductance, capacitance, frequency) are provided in Table B.1, for both ac- and dc-side quantities. As, an example, Table B.2 presents the numerical form of the derived base values for the system with characteristics described in Table 2.2.

TABLE B.1. BASE VALUES

Base value	Definition
Base frequency (ω_{base})	$2\pi f_{\text{nominal}}$
Base time (t_{base})	$(2\pi f_{\text{nominal}})^{-1}$
Base power ($S_{\text{ac-base}}$)	$S_{\text{VSC-rated}}$
ac side - Base voltage ($v_{\text{ac-base}}$)	$u_{\text{ac-rated}}$
ac side - Base current ($i_{\text{ac-base}}$)	$\frac{S_{\text{ac-base}}}{\sqrt{3}v_{\text{ac-base}}}$
ac side - Base impedance ($Z_{\text{ac-base}}$)	$\frac{v_{\text{ac-base}}^2}{S_{\text{ac-base}}}$
ac side - Base inductance ($L_{\text{ac-base}}$)	$\frac{Z_{\text{ac-base}}}{\omega_{\text{base}}}$
ac side - Base capacitance ($C_{\text{ac-base}}$)	$(Z_{\text{ac-base}}\omega_{\text{base}})^{-1}$
dc side - Base power ($S_{\text{dc-base}}$)	$S_{\text{VSC-rated}}$
dc side - Base voltage ($v_{\text{dc-base}}$)	$u_{\text{dc-rated}}$
dc side - Base current ($i_{\text{dc-base}}$)	$\frac{S_{\text{dc-base}}}{v_{\text{dc-base}}}$
dc side - Base impedance ($Z_{\text{dc-base}}$)	$\frac{v_{\text{dc-base}}}{i_{\text{dc-base}}}$
dc side - Base inductance ($L_{\text{dc-base}}$)	$\frac{Z_{\text{dc-base}}}{\omega_{\text{base}}}$
dc side - Base capacitance ($C_{\text{dc-base}}$)	$(Z_{\text{dc-base}}\omega_{\text{base}})^{-1}$

Chapter B. Per-unit Conversion

TABLE B.2. BASE VALUES

Base value	Numerical value
ω_{base}	314.16 rad/s
$S_{\text{ac-base}}$	1000 MVA
$v_{\text{ac-base}}$	320 kV
$i_{\text{ac-base}}$	1.8 kA
$Z_{\text{ac-base}}$	102.4 Ω
$L_{\text{ac-base}}$	325.9 mH
$C_{\text{ac-base}}$	31.08 μF
$S_{\text{dc-base}}$	1000 MW
$v_{\text{dc-base}}$	640 kV
$i_{\text{dc-base}}$	1.563 kA
$Z_{\text{dc-base}}$	409.6 Ω
$L_{\text{dc-base}}$	1304 mH
$C_{\text{dc-base}}$	7.77 μF